Computer Simulation Studies of Minerals

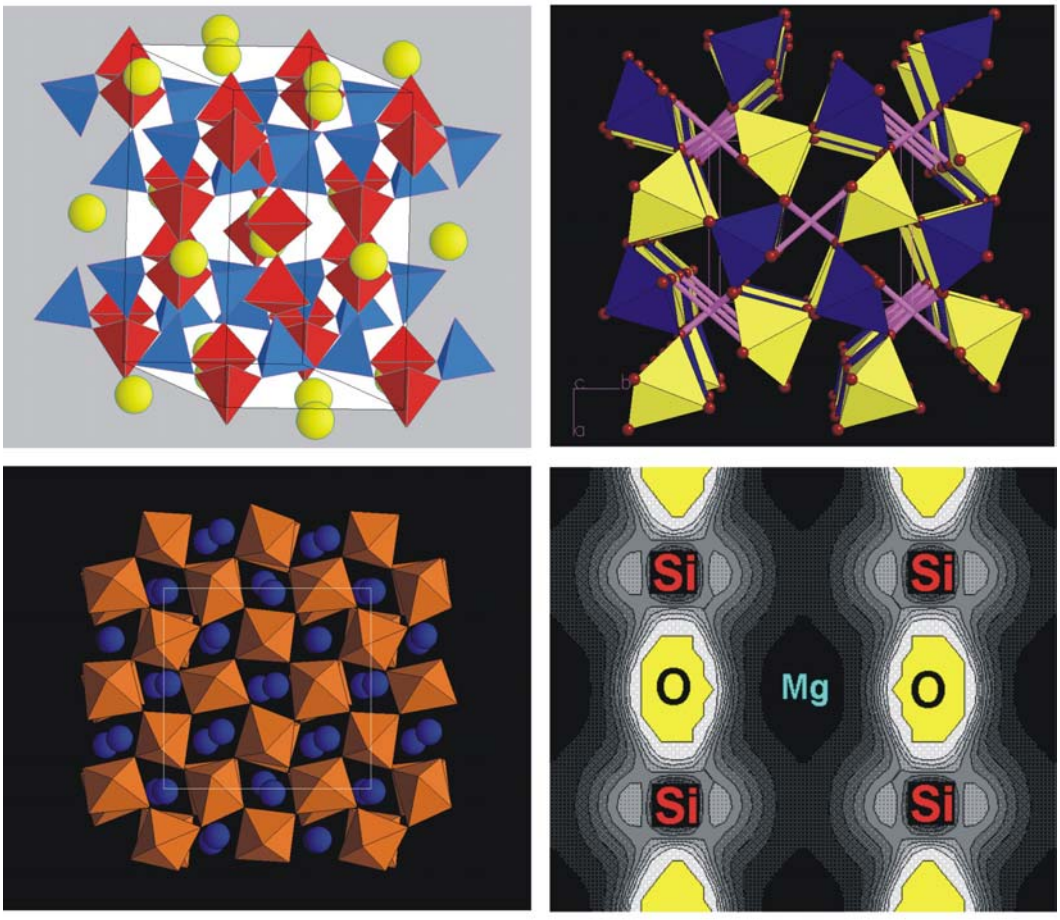

ARTEM R. OGANOV

Computer Simulation Studies of Minerals

Artem Romaevich Oganov
University College London

Thesis submitted in fulfilment of the requirements
for the degree of Doctor of Philosophy
to the
University of London
2002

Abstract.

Applications of state-of-the-art computer simulations to important Earth- and rock-forming minerals (Al_2SiO_5 polymorphs, albite ($NaAlSi_3O_8$), and $MgSiO_3$ perovskite) are described. Detailed introductions to equations of state and elasticity, phase transitions, computer simulations, and geophysical background are given.

A new general classification of phase transitions is proposed, providing a natural framework for discussion of structural, thermodynamic, and kinetic aspects of phase transitions. The concept of critical bond distances is introduced. For Si-O bonds this critical distance is 2.25 Å.

Using atomistic simulations, anomalous Al-Si antiordering in albite is explained. A first-order isosymmetric transition associated with a change in the ordering scheme is predicted at high pressures.

A quantum-mechanical study is presented for the Al_2SiO_5 polymorphs: kyanite, andalusite, sillimanite, and hypothetical pseudobrookite-like and V_3O_5-like phases (the latter phase was believed to be the main Al mineral of the lower mantle). It is shown that above 11 GPa all the Al_2SiO_5 phases break down into the mixture of oxides: corundum (Al_2O_3) and stishovite (SiO_2). Atomisation energies, crystal structures and equations of state of all the Al_2SiO_5 polymorphs, corundum, stishovite, quartz (SiO_2) have been determined. Metastable pressure-induced transitions in sillimanite and andalusite are predicted at ~30-50 GPa and analysed in terms of structural changes and lattice dynamics. Sillimanite (*Pbnm*) transforms into incommensurate and isosymmetric (*Pbnm*) phases; andalusite undergoes pressure-induced amorphisation.

Accurate quantum-mechanical thermal equation of state is obtained for $MgSiO_3$ perovskite, the main Earth-forming mineral. Results imply that a pure-perovskite mantle is unlikely. I show that $MgSiO_3$ perovskite is not a Debye-like solid, contrary to a common assumption. First ever *ab initio* molecular dynamics calculations of elastic constants at finite temperatures are performed for $MgSiO_3$ perovskite. These for the first time allowed a physically sound interpretation of seismic tomography maps in terms of the temperature distribution in the lower mantle of the Earth.

To my brother for his wedding;
To my mother for the wedding of her son.

Acknowledgements.

I am very grateful to the Russian President Scholarship for Education Abroad, UCL Graduate School Research Scholarship, and the Overseas Research Scholarship of the UK Government for the support of my studies at UCL.

My supervisors, J.P. Brodholt and G.D. Price, have provided me with their supervision, support, and encouragement throughout my PhD course. They have made my PhD experience very enjoyable, and I am much indebted to them for this and for the many scientific discussions that we had. The whole Department of Geological Sciences of UCL proved to be a very inspiring scientific community, where I had learnt much from D. Alfé, L. Vočadlo, and I. Wood. I am grateful to my colleagues in the Department of Physics and Astronomy – especially M. Gillan, J. Harding, L. Kantorovich, J. Gavartin. For inspiring discussions I thank M. Catti (Milano), J. Gale (Imperial College London), G. Kresse (Vienna), P. Ballone (Messina), B. Karki (Minneapolis), H. Barron (Bristol), P. Dorogokupets (Irkutsk), O. Kuskov and V. Polyakov (Moscow), M. Hostettler (Lausanne), T. Balič-Zunič (Copenhagen), R. Angel (Blacksburg), and many others.

My teachers - T. Shakhova, B. Glybin, M. Maryashin, N. Cherkasskaya, G. Litvinskaya, V. Urusov, and D. Pushcharovsky - have formed my scientific interests and skills. I am infinitely grateful to my mother Galina for everything; my uncle Felix has always remained for me an example. I am indeed very fortunate to have met so many remarkable people in my life.

Contents.

LIST OF FIGURES AND TABLES

Figures:

Tables:

Chapter 1. Introduction.

Quantum-mechanical and atomistic simulations play an increasingly important role in understanding the behaviour and properties of materials. On one hand, such simulations provide a detailed microscopic picture of condensed-matter phenomena (phase transitions, atomic motion and diffusion), which is difficult or impossible to obtain experimentally. On the other hand, macroscopic properties (thermodynamics, elasticity, equation of state, phase diagram) can be calculated and linked to the microscopic picture and, in case of Earth- and planet-forming materials, to the global planetary processes.

The main objective of this thesis is to show how solid state physics and computer simulations of materials can be applied to geological problems. Enormous progress has been made in this field since 1980-s; many important results in this field were obtained at UCL, and some of the most recent major results will be discussed in this thesis. Both theoretical background and examples from my recent works are presented.

The first four chapters, 'Earth's models', 'Thermoelastic properties', 'Simulation methods', and 'Phase transitions' are largely introductory and contain most of the theoretical background and equations used in later chapters, which will be dedicated to particular systems of interest. Much of this theory can be found in well-known books and reviews, but some was developed by myself. References to the original or review literature are given throughout, although often (especially when the original publications were too old) I preferred to cite later reviews or books that can be consulted on each particular topic.

Subsequent chapters deal with results obtained for several particular mineral systems, including albite ($NaAlSi_3O_8$), the Al_2SiO_5 polymorphs, and $MgSiO_3$ perovskite. Both geological and physical implications of the results are discussed. Most of the results presented here have been published and extensively presented at a number of conferences and research seminars. Appendix gives a list of these publications and presentations. Chapter 11 gives some concluding remarks and outlines directions of future work. Some parts of this thesis (especially in Chapters 3, 4, 5, and 7) were taken from my MSc thesis (1997, University of Moscow), often with only few changes.

A number of abbreviations have been introduced and used in many parts of this thesis. For convenience, here I list some of them:

BM – Birch-Murnaghan equation of state (BM2 – 2^{nd}-order, BM3 – 3^{rd}-order)

DFT – Density Functional Theory

DM – Debye Model

DOS – Density Of States

EOS – Equation Of State

GEA – Gradient Expansion Approximation

GGA – Generalised Gradient Approximation

HF – Hartree-Fock approximation

LAPW – Linearised Augmented Plane Wave method

LCAO – Linear Combination of Atomic Orbitals

LD – Lattice Dynamics

LDA – Local Density Approximation

LSDA – Local Spin Density Approximation

MD – Molecular Dynamics

MEG – Modified Electron Gas method

Mg-pv – $MgSiO_3$ perovskite

PAW – Projector Augmented-Wave method

PBE – functional of Perdew, Burke, Ernzerhof (1996)

PIB – Potential-Induced Breathing

PREM – Preliminary Reference Earth Model

PW91 – Perdew and Wang (Wang & Perdew, 1991) functional

QHA – Quasiharmonic Approximation

RGT – Renormalisation Group Theory

SIC – Self-Interaction Correction

ZSISA – Zero Static Internal Strain Approximation

Chapter 2. Models of the Earth.

2.1. Overview.

The Earth is one of the 9 planets in the Solar System. It is the largest of the 4 planets (Mercury, Venus, Earth, Mars) known as terrestrial (or rocky) planets; the other 5 planets are known as gas planets. Like any other terrestrial planet, the Earth 1) is believed to have a nearly chondritic composition, and 2) is deeply chemically differentiated (into the metallic Fe-rich and silicate-oxide fractions) and stratified (metallic Fe forms the core, while oxides and silicates form the mantle and crust).

Further stratification of the planet is determined by phase transitions in the mantle and core minerals – these are responsible for the discontinuities of elastic properties, observed in seismological studies. Spherically averaged seismological models of the Earth (e.g., PREM – Preliminary Reference Earth Model), in view of the lack of direct sampling, comprise the central piece of information on the deep regions of the planet. Such models will eventually allow us to determine the precise composition and temperature of deep regions of the Earth as a function of depth. This requires the knowledge of the physical properties of minerals as a function of both temperature and pressure.

It is essentially not known whether the Earth was formed hot (and is cooling down now) or cold (and is warming up now). Both scenarios are plausible, but lead to slightly different geochemical consequences (e.g., on the K content in the core). The energy balance of the Earth is known only very approximately, the main items being heat flux, gravitational energy, and the energy of radioactive decay. The main mechanism of the heat transport in the Earth is thermal convection. Convection of the liquid outer core also generates the magnetic field of the Earth, which shields the planet from the solar wind. Solid-state convection in the mantle is responsible for plate tectonics, and is the ultimate cause of the continental drift, earthquakes, and volcanism. Seismic tomography enables a visualisation of this convection and can in principle give information on the underlying temperature anomalies. Seismic tomography correlates the surface tectonic structure with large-scale dynamical processes occuring in the Earth's interior, thus providing a fundamental basis for classical geology.

This chapter will consider in detail the current picture of the structure and dynamics of the Earth, sketched above. Some of the physical quantities and equations, used here, will be clarified in the next two chapters.

2.2. Origin and energetics of the Earth.

The most popular cosmogonic theory (the Safronov theory – see Anderson (1989)) associates the formation of the Earth and other planets in the Solar System with a disk-shaped gas-dust cloud rotating around the Sun. The formation of planets is estimated to have begun 4.6 billion years ago (e.g., Allègre et al., 1995a). At the first stage of planetary formation, the protoplanetary gas, initially very hot, condensed on cooling into small dust particles. There are indications that the first (the most refractory) condensates, which form the 'white inclusions' in carbonaceous CI chondrites (see below), were formed within the first few million years. At the second stage, the dust material accreted into small macroscopic bodies (planetesimals), which increased in size and stuck together during collisions, forming several large planets orbiting the Sun. Most planets have one or more satellites orbiting them. In the Safronov theory, most of the present mass of the Earth (97-98%) had accreted within the first ~100 million years; other theories give shorter times of the order of a few million or several hundred thousand years. There is also some evidence that within these first 100 million years chemical differentiation of the Earth was already underway.

The four planets closest to the Sun – Mercury, Venus, Earth, and Mars – are similar in many ways, and are known as terrestrial (or rocky) planets. The other 5 planets – Jupiter, Saturn, Uranus, Neptune, Pluto – are known as gas planets, because their composition is dominated by gas-forming molecules (H_2, CH_4, NH_3, H_2O) in the fluid and (in deeper parts of these planets) solid state. Condensation of such volatile compounds could occur only at <200 K.

It is believed that the Sun, containing almost all the mass of the Solar System, gives a good model of the primordial gas cloud. The composition of the Sun's outer spheres can be studied spectrocopically; it is assumed to be close to the average composition of the Universe, since the Sun is an 'average' star in its size and stage of evolution. H and He are by far the most abundant elements in the Sun and in the Universe.

The first condensates appear at ~1750-1600 K and are represented by refractory oxides, silicates, and titanates of Ca and Al (corundum Al_2O_3, anorthite $CaAl_2Si_2O_8$, perovskite $CaTiO_3$, melilite $Ca_2Al_2Si_2O_7$, spinel $MgAl_2O_4$, diopside $CaMgSi_2O_6$, hibonite $CaAl_{12}O_{19}$, and Al-Ti pyroxene, fassaite). At ~1471 K metallic Fe begins to condense, followed at ~1400 K by the condensation of the

bulk of Mg silicates (forsterite Mg_2SiO_4 and enstatite $MgSiO_3$). At 700 K Fe oxidises into Fe^{2+}, and FeS condenses. Hydrous silicates appear at 500 K. Since the Earth contains some volatiles (especially H_2O and CO_2), it is likely that it was formed from the material condensed below 500 K. Carbonaceous chondrites CI (undifferentiated meteorites), formed at 300-400 K, represent the most convenient and relatively likely model of the composition of the Earth and other terrestrial planets.

It appears, therefore, that the Earth was formed from a relatively cold (300-400 K) dust cloud. However, due to the gravitational energy released during accretion and kinetic energy released during collisions and impacts, the Earth is likely to have been hot in its initial stages, even if it was formed from cold planetesimals. Release of the gravitational energy during accretion of the Earth and radioactive decay of U, Th and other elements (in particular, ^{40}K and now completely extinct ^{26}Al) are the main sources of the Earth's heat. An estimated $2.49*10^{32}$ J worth of gravitational energy was released during accretion (most of it radiated into the space, but some is still stored in the Earth); 10^{31} J of it was solely due to the formation of a dense metallic core. This latter figure would be sufficient to raise the temperature of the whole Earth by ~1500 K (Verhoogen, 1980). The total amount of radiogenic heat presently generated within the Earth is estimated to be $2.42*10^{13}$ W if there is no K in the Earth's core. Combined with the fact that now radiogenic energy is almost the only source of the Earth's heat (accretion being long over) and the total surface heat flux is $\sim 4*10^{13}$ W, this would mean that the Earth is cooling at present time (possible cooling rate for the mantle ~100 K per 10^9 years – Verhoogen, 1980). It has been suggested, however, that most of the Earth's K is stored in the core. This is consistent with the measured depletion of the surface rocks in K and the fact that at high pressures K behaves increasingly like a 3d-element, and might have significant chemical affinity to Fe. Early LDA calculations of McMahan (1984) concluded that the $s \rightarrow d$ electronic transition in metallic K is completed at 60 GPa (for Rb and Cs this pressure is 53 GPa and 15 GPa, respectively), which is well below the core-mantle boundary pressure of 136 GPa. High-pressure crystallographic experiments and theoretical studies (starting from M.S.T. Bukowinski's early work in 1976) confirm that at high pressures K becomes a d-element with new complicated crystal structures with directional bonding and

significant populations of the 3d-electronic levels. For more discussion see Katsnelson et al. (2000), Sherman (1990), and McMahan (1984).

Models including K (~0.1%) in the core would result in ~$3.8*10^{13}$ W of radiogenic heat generated presently within the Earth (Verhoogen, 1980). This is close to the estimated Earth's heat flux of $4*10^{13}$ W, and leaves some possibility that the Earth is heating up at present time.

2.3. Elemental abundances.

The cosmic abundances of the elements can be explained on the basis of the relative stability of their isotopes during nucleosynthesis. In this way it is possible to explain the predominance of light elements, well-known low abundances of odd-number elements relative to their even-number neighbours in the Periodic Table (e.g., Al relative to Mg and Si), and anomalously large abundance of Fe. The abundances of some elements in the Universe, in the Earth and its crust and mantle, are given in Table 2-1.

Chondritic model is the starting point of all models of the bulk composition of the Earth (see Anderson, 1989; Allègre et al., 1995b) and is believed to be valid to a large extent for other terrestrial planets. Carbonaceos CI chondrites, the most primitive of all chondrites, possibly represent the best model, apart from the fact that carbonaceous chondrites are richer in volatiles than terrestrial planets. It is the relative proportions of refractory elements (e.g., Ca, Al, Sr, Ti, Ba, U, Th, Mg, Si) that are very similar in the chondritic meteorites, Earth (and other terrestrial planets), Sun, and the Universe. The Earth is moderately depleted in moderately volatile elements (e.g., K, Na, Rb, Cs, S) and heavily depleted in very volatile ones (e.g., H, He and other noble gases, C, N). There is a significant depletion in O, due to the tendency of O to form volatile compounds. The proportion of the main elements in the bulk composition of the Earth is estimated to be 3.7O: 1.06Mg: 1Si: 0.9Fe: 0.09Al: 0.06Ca: 0.06Na. This ratio predetermines one of the most important characteristics of the Earth – its chemical differentiation and stratification. Mg, Ca, Al, and Si are lithophile elements, i.e. have a strong chemical affinity to O and readily form oxides and silicates; Fe less easily forms such compounds. There is simply not enough O in the Earth to oxidise all Fe and other metal atoms available,

Table 2-1. Data on abundances of some chemical elements (in atoms per 1 atom Si).

Element	The Universe [a]	Whole Earth[b]	Earth's Crust[c]	Upper Mantle [c]	Lower Mantle[c]	Pyrolitic Homogeneous Mantle[d]
O	20.10	3.73	2.9	3.63	3.63	3.68
Na	0.06	0.06	0.12	0.03	$2*10^{-3}$	0.02
Mg	1.08	1.06	0.09	0.97	1.09	1.24
Al	0.08	0.09	0.36	0.17	0.06	0.12
Si	1	1	1	1	1	1
P	0.01	-	$4*10^{-3}$	$6*10^{-4}$	$4*10^{-5}$	$4*10^{-4}$
S	0.52	-	$8*10^{-4}$	$6*10^{-4}$	$5*10^{-5}$	$2*10^{-3}$
Ca	0.06	0.06	0.14	0.12	0.05	0.09
Cr	0.01	-	$1*10^{-4}$	$5*10^{-3}$	0.01	0.01
Fe	0.9	0.9	0.11	0.14	0.14	0.16
Ni	0.05	-	$3*10^{-5}$	$3*10^{-3}$	$4*10^{-3}$	$3*10^{-5}$

a – Estimates of Anders and Ebihara (1982).

b - Simple model based on cosmic abundances (Anderson, 1989).

c - Recalculated from data of Anderson (1989).

d - Recalculated from (Ringwood, 1991).

and most Fe will be bound to form a residual metallic phase. This heavy metallic fraction is concentrated in the centre of the Earth, forming its core. The presence of two almost immiscible fractions: silicate+oxide crust and mantle and metallic core results in strong partitioning of elements between them. Siderophile (e.g., Ni, platinoids, Au, Re) elements go almost exclusively into the core, while lithophiles (e.g., Al, Mg, Ca, Na) fractionate into the mantle and crust. Chalcophile elements (e.g., Cu, Pb) are distributed between the core and mantle, but are more easily incorporated into the core. Some of the fractionation trends (e.g., mantle and crust depleted in Fe and Ni, but enriched in Ca and Al) can be seen in Table 2-1.

It is worth noting that at different p/T-conditions many elements change their behaviour: e.g., K may become a chalcophile or siderophile element, and Si almost certainly acquires some siderophile properties at very high pressures. This would imply that these elements can be partitioned into the core; fractionation of K into the core would create an important source of radiogenic energy (due to the radioactive ^{40}K isotope) within the core.

In the mantle, Mg, Si, and O are by far the most important elements, and their ratio is close to 1:1:3. At high pressures (>24 GPa) $MgSiO_3$ with the perovskite structure is stable; elemental abundances and phase equilibria indicate that this mineral should be the most abundant mineral in the mantle – in fact, even the most abundant mineral in the Earth. This mineral will be studied extensively in Chapter 10. In the pyrolitic model of the mantle, the Mg/Si ratio is 1.24, resulting in the mantle enriched (compared to the chondritic model) in MgO and other magnesium-rich minerals (especially the Mg_2SiO_4 polymorphs - forsterite, wadsleyite, and ringwoodite). If the mantle is pyrolitic, the deficit of Si in it may be due to a large Si content in the Earth's core, or due to a non-chondritic bulk Earth's composition.

2.4. Geophysical observations: stratification of the Earth.

In the previous section, it was shown how a simple geochemical consideration already suggested the presence of a dense metallic Fe-rich core in the Earth (and other terrestrial planets). To prove this hypothesis, some observations are needed. The simplest of them is the measured density of the Earth. The average density of the Earth is 5.5. g/cm^3, much higher than that of the crustal rocks (~3.4 g/cm^3). The high average density of the Earth cannot be explained just by adiabatic self-compression of a chemically homogeneous material.

The second observation is the moment of inertia of the Earth. For a perfect sphere made of a homogeneous incompresible material, the moment of inertia $I=0.4MR^2$ (Landau & Lifshits, 2001a), where M is the mass of the sphere, and R- its radius. Including the compressibility of the Earth's materials and slight non-sphericity of the Earth would not change this result sufficiently. The observed $I=0.33MR^2$ implies a significant mass concentration in the centre of the planet, which is best explained by the presence of a large dense metallic core (core radius = 3480 km, the Earth's radius = 6371 km). For the Moon $I=0.393MR^2$, indicating a small core (upper bound – 500 km in radius for a dense core; the Moon's radius is 1737 km); for Mars $I=0.365MR^2$, suggesting an intermediate situation.

It is interesting to mention an early hypothesis, proposed by W.H. Ramsey in 1949, that the Earth's dense core is not chemically different from the mantle and is made of the usual silicates of Mg, Al, Ca, and other elements - the idea being that at very high pressures of the Earth's core (~3 Mbar) these silicates will transform into superdense modifications and (in order to explain the magnetic field) will become metallic. Geochemically this would mean no chemical stratification – hence, no

energy of the core formation. This would also contradict the expected abundance of Fe in the Earth. Early shock-wave experiments of L.V. Altshuler's group in Russia, subsequently reproduced in other groups and reinforced by theoretical calculations (e.g., Cohen, 1991; Bukowinski, 1994), definitively refuted this hypothesis. Silicate minerals remain insulating at core pressures, never adopt superdense structures or become metallic at the Earth's core conditions. The core must be Fe-rich.

Detailed information on the density and size of the dense core is obtained from seismological observations. Following an earthquake, the arrival times of seismic waves are recorded at numerous seismic stations located all over the surface of the Earth. Earthquakes generate three types of response in the Earth: surface waves (periods 200-10,000 s), body waves (they travel along ray-like paths through the Earth's interior and have periods up to 200 s), and free oscillations (standing waves, in which the whole Earth vibrates as a giant bell with periods 200-10,000 s). In seismological studies, body waves with periods <0.1 s are unusable due to seismic attenuation. Arrival data are inverted (with the use of Snell's law of refraction) to give the trajectories of body wave propagation. Body waves can be reflected from seismic boundaries, where large discontinuous changes in the elastic properties and density occur. It is possible to locate the depths of these boundaries, and obtain the depth profiles of seismic wave velocities. Apart from first-order seismic boundaries (where velocities jump discontinuously), there are also second-order boundaries, where velocity gradients are discontinuous without any discontinuities in the velocities.

The most popular global seismological model – PREM (Preliminary Reference Earth Model – Dziewonski & Anderson, 1981) will be considered in the next section. This and all other existing seismological models heavily rely on the locations of seismic discontinuities and distinguish the following regions in the Earth separated by major first-order seismic boundaries: crust (0-24.4 km, but the depth strongly varies geographically); mantle (24.4-2891 km): upper mantle (24.4-410 km), transition zone (410-660 km), lower mantle (660-2891 km); core (2891-6371 km): outer core (2891-5150 km) and inner core (5150-6371 km). Fig. 2-1 shows a scheme of the Earth's structure.

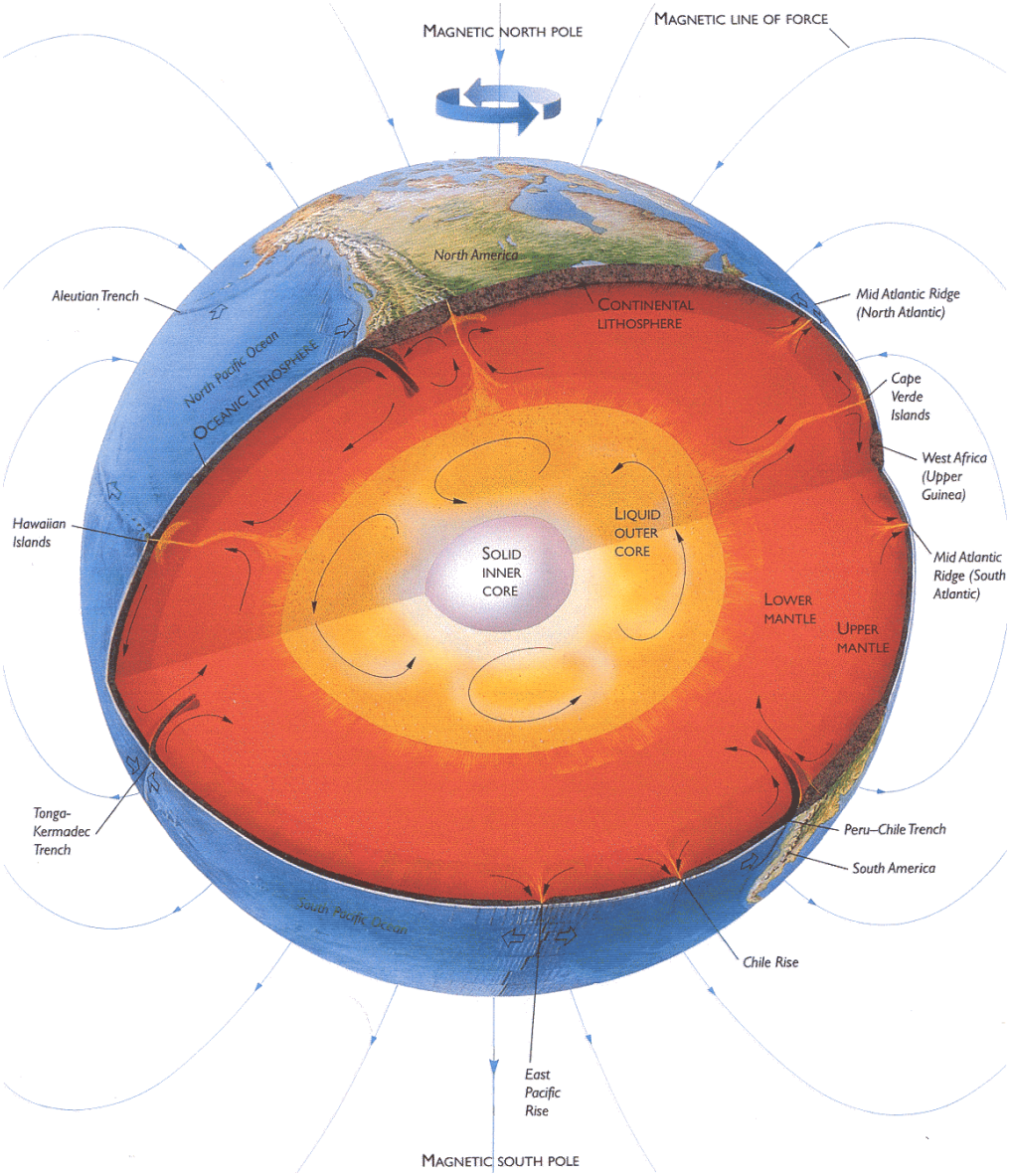

Fig. 2-1. Scheme of the Earth's internal structure. Earth's mantle and outer core convection are shown here. Mantle convection is responsible for plate tectonics, core convection – for the the generation of the Earth's magnetic field (whose force lines are also shown). From http://geoweb.princeton.edu/faculty/Duffy/MineralPhy/index.htm (taken from the book Lamb S., Sington D. Earth story: the shaping of our world. London : BBC Books, 1999, 240 pp.)

It is noteworthy that there are other models of the Earth's internal structure, differing in the stratification of the mantle – see, e.g., Pushcharovsky and Pushcharovsky (1999), who distinguish 6 layers in the mantle and consider both major and minor discontinuities as region boundaries (layers 30-400 km, 400-670

km, 670-850 km, 850-1700 km, 1700-2200 km, 2200-2900 km). However, this and other similar schemes can be accepted only when the global nature and first-order character of the minor discontinuities are proved.

Seismic observations detect these minor discontinuities only in some regions, but it must be kept in mind that even global discontinuities may become seismically unobservable if they are small enough and/or spread over a large depth interval. As a rule of thumb (Helffrich, 2000), they become undetectable if their thickness exceeds ¼ of the wavelength of the incident seismic wave. The finite thicknesses of the discontinuity zones are primarily due to lateral variations of temperature (Helffrich, 2000) and the dependence of the phase transition pressures (and depths) on temperature via the Clapeyron relation: $dp/dT=\Delta S/\Delta V$. Finite thickness of phase transition boundaries in the mantle is also due to the multicomponent composition of the mantle. In effect, the discontinuities related to phase transitions with large Clapeyron slopes and/or having large two-phase coexistence regions on the phase diagram may become locally or globally seismically invisible. This is the case for the global 520-km discontinuity related to the wadsleyite-ringwoodite transition: this discontinuity is small and only locally observable (Shearer, 1990); it is not included in current seismological models.

2.5. PREM and other spherical models.

PREM is the most frequently used seismological model of the Earth. Other models (e.g., ak135 – Kennett et al., 1995) generally agree with PREM within 1-2% on seismic velocities (Fig. 2-2). The parameters given by all these models as a function of depth are: pressure (p), compressional and shear seismic velocities (V_P and V_S), density (ρ), acceleration due to gravity (g), adiabatic bulk and shear moduli (K_S and G), seismic parameter ($\Phi=K_S/\rho$), Poisson ratio (ν), attenuation Q-factors for the compressional and shear velocities (Q_P and Q_S), and Bullen parameter (η). PREM velocity profiles are shown in Fig. 2-3, while Fig. 2-4 and Fig. 2-5 show profiles of the density and pressure, respectively.

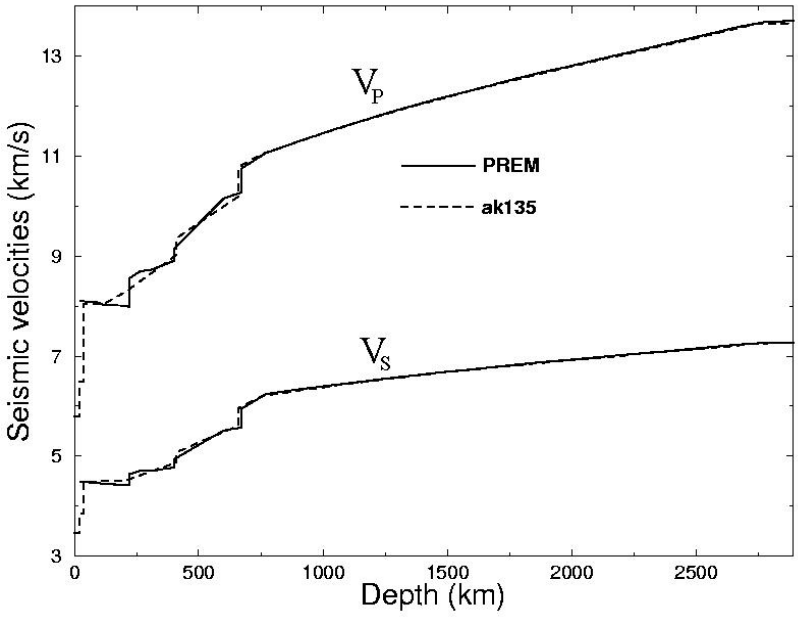

Fig. 2-2. Comparison of the PREM and ak135 profiles of seismic wave velocities in the Earth's mantle and crust. Generally, the agreement is good. Serious differences are in the ultralow velocity zone (~220 km depth); gradients of seismic wave velocities in the upper 670 km are significantly different. In the lower mantle, the velocity profiles of the two models practically coincide.

Within PREM there are a number of observables: 1) mass of the Earth, 2) geometrical parameters of the Earth (geoid data), 3) moment of inertia of the Earth, and 4) seismic data – arrival times of seismic waves, from which it is possible to obtain the trajectories of propagation of the seismic waves including locations where reflection of seismic waves occurs, in particular 5) locations of seismic boundaries. Studying reflection and refraction of seismic waves in the Earth's interior, it is possible to locate seismic discontinuities quite precisely (Helffrich, 2000).

In constructing PREM (Dziewonski and Anderson, 1981; see also Poirier, 2000), measured geometry, mass and moment of inertia of the Earth were used, and it was assumed that in each continuous region below 670 km the Adams-Williamson equation:

$$\mathrm{d}\rho/\mathrm{d}r=-g\rho\Phi_S^{-1} \quad , \tag{2.5.1}$$

describing adiabatic self-compression of a chemically homogeneous material, is valid. For the upper mantle, the Birch's law density-velocity systematics (V_P=

a($\bar{M}$) + bρ, where a and b are constants – see section 3.13) was assumed to apply. At the start, values for the density of the Earth's surface rocks (3.32 g/cm^3), at the core-mantle boundary (5.5 g/cm^3) and the density jump at the inner-outer core boundary (0.5 g/cm^3) were supplied, and subsequently refined. The provisional density distribution thus obtained was then refined in a general fitting procedure (fitted parameters: profiles of V_P, V_S, ρ, Q_P, and Q_S) with added observables (free oscillation periods and travel times for the 1s-period P- and S-waves). The uppermost 200 km were treated as an elastically anisotropic region.

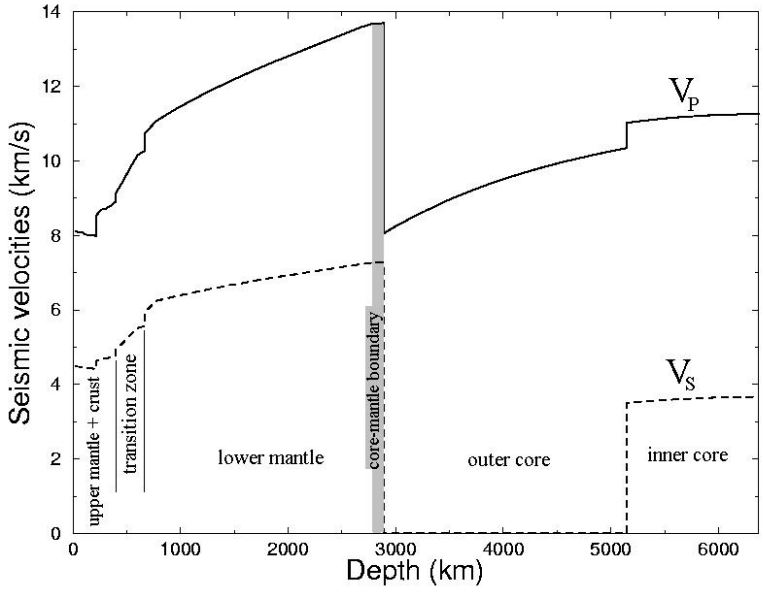

Fig. 2-3. PREM seismic velocity profile. Major regions of the Earth are specified. The core-mantle boundary region D'' (grey shading) is the major seismic boundary in the Earth and has many anomalous and poorly understood properties.

Pressure distribution can be calculated using the following equation:

$$dp/dr = -4\pi G\rho r^{-2} \int_0^r \rho\, r^2 dr = -g\rho, \qquad (2.5.2)$$

where G is the gravitational constant, and r is the radius.

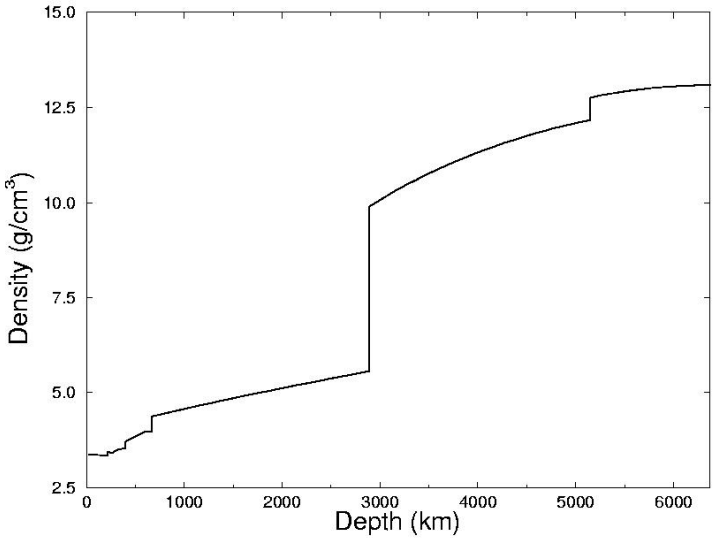

Fig. 2-4. PREM density profile.

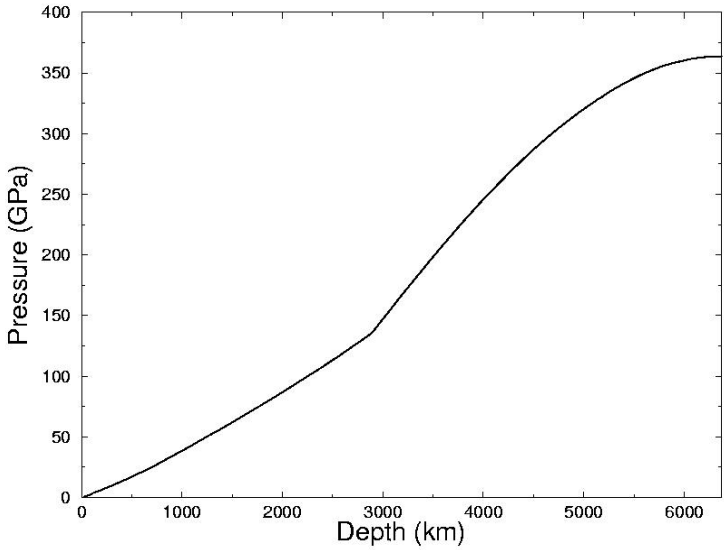

Fig. 2-5. PREM pressure profile. Pressure is continuous, but there is a large kink in its slope at the core-mantle boundary due to the large density jump occurring there.

2.6. Interpretation of PREM. Composition, mineralogy, and temperature.

It is straightforward (eq. 2.5.2) to calculate the pressure distribution from the density distribution provided by seismological models. Derivation of a temperature profile is much more complicated, and there is still no commonly accepted thermal profile of the Earth. Determination of the composition of each region of the Earth from seismological models is another non-trivial, yet fundamentally important, problem.

As we saw, the core must be mainly made of Fe, with minor siderophile (particularly Ni) content. Its density, however, is too low compared to pure Fe at the core conditions (by ~6-10% in the outer core). This is explained by the presence of lighter alloying elements. From Birch's law (see section 3.13), the average atomic mass $\bar{M}$ =49.3 (Poirier, 2000), supporting the presence of lighter elements (the atomic mass of Fe is 55.8). On the basis of the latest theoretical work (Vočadlo et al., 2000) and experiments, it is believed that the phase of Fe stable at the inner core conditions, is hcp-Fe. From seismic observations it follows that the inner core is highly seismically anisotropic, with the fastest direction of seismic waves along the axis of the Earth's rotation. This anisotropy implies a high degree of crystal alignment, whose cause is unknown. Using *ab initio* molecular dynamics simulations, Alfé et al. (1999) calculated the melting curve of pure Fe and concluded that for a pure-Fe core the temperature at the inner-outer core boundary is 6700 ± 600 K. Using the density jump at this boundary as a constraint, Alfé et al. (2000 and private communication) were able to put forward a compositional model for the Earth's core (inner core: 8.5% Si+S and 0.2% O; outer core: 10% Si+S and 8% O); this composition has $\bar{M}$ =49.38. The temperature at which these compositions are at equilibrium, is 5500 K. This is the best currently available estimate of the core temperatures.

Convection of the outer core generates the Earth's magnetic field. The giant dynamo-mechanism is, most probably, powered by the energy released on cooling of the core: $2.6*10^{12}$ from cooling itself, $0.34*10^{12}$ W from crystallisation of the inner core, and $0.66*10^{12}$ W of gravitational energy due to the convective rise of Fe-depleted liquid during crystallisation of the Fe-rich inner core (Verhoogen, 1980). By constructing an adiabatic temperature profile for the outer core, Alfé et al. (private communication) obtained T~4300 K at the core-mantle boundary.

The Earth's mantle consists mainly of Mg-silicates. Birch's law gives $\bar{M}$ = 21.3 for the mantle. Compared to $\bar{M}$ = 20.12 for $MgSiO_3$, 20.15 for MgO, and 20.13 for Mg_2SiO_4, this implies an ~10% substitution of Mg by Fe. Fe is mainly in the form of Fe^{2+}, which is in a high-spin state at low pressures, but may transform into low-spin Fe^{2+} at high pressures. This 'magnetic collapse' has attracted much attention in both theoretical (Sherman, 1991; Isaak et al., 1993; Cohen et al., 1997; Cohen, 1999; Fang et al., 1999; Gramsch et al., 2001) and experimental (Pasternak et al.,

1997; Badro et al., 1999) literature. Despite many interesting implications of the possible presence of low-spin Fe^{2+} in the mantle and a large number of studies, it remains highly unclear whether the low-spin Fe^{2+} exists in the mantle. Phase transitions of Mg-silicates determine the seismic stratification within the mantle (Fig. 2-6; Helffrich, 2000; Chudinovskikh & Boehler, 2001). Whether there is a compositional stratification, related to the phase transition boundaries, is an open question. From phase diagrams of the Mg_2SiO_4-Fe_2SiO_4 system, Ito & Katsura (1989) determined T=1673 K at 350 km and 1873 ± 100 K at 660 km depths.

If the mantle were chemically homogeneous and had a pyrolitic composition, the lower mantle would consist of $(Mg,Fe)SiO_3$ perovskite (~75 vol. %), magnesiowustite (Mg,Fe)O (~20 vol. %), and $CaSiO_3$ perovskite (~5 vol. %). Atomistic simulations of Watson et al. (2000) have demonstrated that the solubility of Ca in $MgSiO_3$ perovskite is negligible; therefore, $CaSiO_3$ perovskite must be present as a distinct phase. There has been some experimental evidence (Meade et al., 1995; Saxena et al., 1996, 1998) that at high mantle temperatures and

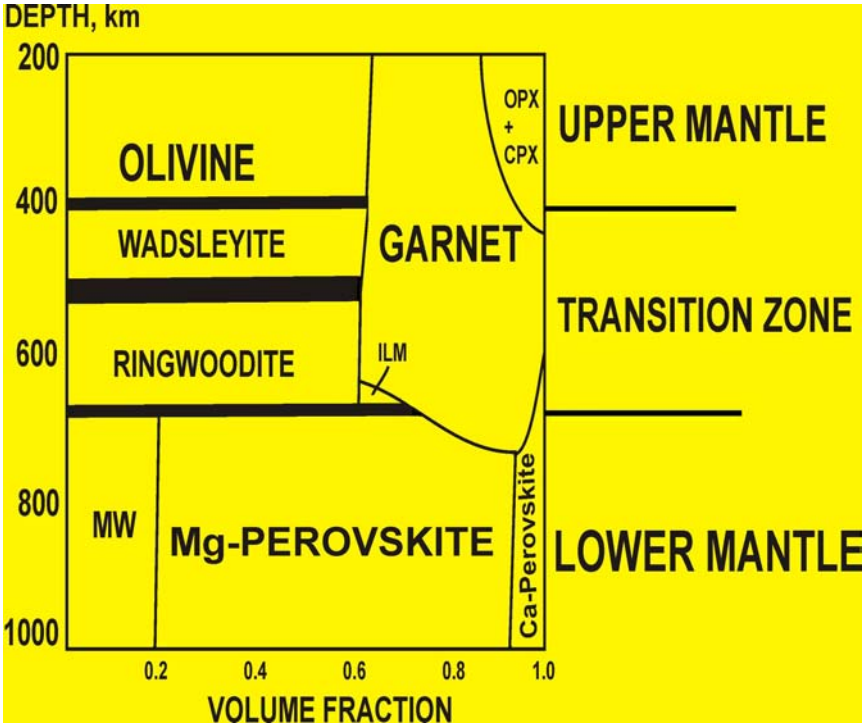

Fig. 2-6. Schematic phase relations in pyrolite (after Ringwood, 1991). OPX and CPX are ortho- and clinopyroxene, ILM is $MgSiO_3$ ilmenite (akimotoite), MW is magnesiowüstite (Mg,Fe)O, 'Mg-perovskite' and 'Ca-perovskite' stand for $MgSiO_3$ and $CaSiO_3$ perovskites.

pressures >75 GPa, $MgSiO_3$ perovskites breaks down into the mixture of oxides, periclase (MgO) and post-stishovite phase of SiO_2. However, there seems to be more evidence (Shim et al., 2001; Serghiou et al., 1998; see also a technical discussion in Dubrovinsky et al., 1999 and Serghiou et al., 1999) that $MgSiO_3$ perovskite remains stable at mantle conditions. Knowledge of the thermoelastic properties of $(Mg,Fe)SiO_3$ perovskite is crucial for constructing thermal and compositional models of the mantle. Stixrude et al. (1992), on the basis of first measurements of thermoelastic parameters of $(Mg,Fe)SiO_3$ perovskite (Knittle & Jeanloz, 1986; Mao et al., 1991) with very high thermal expansion coefficient, arrived at the conclusion that the lower mantle must be ~100% $(Mg,Fe)SiO_3$ perovskite. This would imply a compositional difference between the lower mantle and pyrolitic upper mantle, absence of chemical mixing between different parts of the mantle and layered, rather than whole-mantle, convection. The total mantle composition would be chondritic (e.g., in Mg/Si ratio), rather than pyrolitic. Later measurements of thermal expansion of this mineral (Wang et al., 1994; Funamori et al., 1996; Fiquet et al., 2000) yielded much lower values, strongly supported by *ab initio* simulations of Oganov et al. (2001a). To have a pure-perovskite lower mantle with these values, one must have temperatures ~2500 K at the top of the lower mantle, inconsistent with the value of 1873 K determined by Ito & Katsura (1989). Whole-mantle or intermediate convection models are currently preferred, being also consistent with seismic tomography images (see next two sections). The main support of the layered convection model comes from geochemical studies, which indicate two chemically distinct sources of mantle magmas with different degrees of depletion in volatiles. This geochemical observation can be explained by either intermediate style of convection (i.e., with partial mixing) or by layered convection taking place at earlier stages of the Earth's evolution and then replaced by whole-mantle convection, possibly about 1 billion years ago (see Poirier, 2000).

The temperature gradient in a convecting system must be adiabatic or higher. The adiabatic temperature gradient can be calculated from the thermodynamic equality:

$$(\partial T/\partial p)_S=\gamma T/K_S=\alpha V T/C_P \quad , \qquad (2.6.1)$$

where V is the molar volume, and takes the form:

$$(dT/dr)_S = -M\alpha g T/C_P \quad , \qquad (2.6.2)$$

where M is the molar mass. For the lower mantle the adiabatic temperature gradient is equal to ~0.3-0.4 K/km (Verhoogen, 1980).

A fundamental geophysical relation (see Jackson, 1998) exists:

$$1-g^{-1}\partial\Phi/\partial r = (\partial K_S/\partial p)_S + (\tau\alpha\Phi/g)\{1+(\partial K_S/\partial T)_P/\alpha K_S\}, \quad (2.6.3)$$

which describes self-compression of a chemically homogeneous layer characterised by a superadiabatic temperature gradient τ; α is the thermal expansion coefficient. If the temperature distribution is adiabatic, the following relation must be obeyed:

$$\eta = (\mathrm{d}K_S/\mathrm{d}p)_S + g^{-1}\mathrm{d}\Phi/\mathrm{d}r = \Phi\mathrm{d}\rho/\mathrm{d}p = 1\ , \quad (2.6.4)$$

where η is known as the Bullen parameter. If its values deviate from 1, it indicates that either the temperature gradient is non-adiabatic, or the chemical composition varies with depth. The Bullen parameter can be calculated from seismological models.

The superadiabatic gradient τ is related to the deviations of η from unity:

$$\tau = (g/\alpha)[\Phi^{-1}-\mathrm{d}\rho/\mathrm{d}p] = (g/\alpha\Phi)(1-\eta) \quad (2.6.5)$$

The effects of changing chemical composition can also be included, yielding the following equation:

$$\mathrm{d}\rho/\mathrm{d}p = \Phi^{1} - \alpha\tau/g + (\xi/\rho g)(\partial\rho/\partial X)_{p,T}\ , \quad (2.6.6)$$

where X is a compositional variable, and ξ its gradient. It should be noted that possible compositional heterogeneity and non-adiabatiity in the mantle have opposite effects on η (Jackson, 1998).

In PREM, η=0.99±0.01 throughout the lower mantle, supporting the view that the lower mantle is adiabatic and chemically homogeneous. However, in ak135 model η=0.94±0.02, which implies very large superadiabatic gradients, 0.3-0.7 K/km (Jackson, 1998).

According to Verhoogen (1980), the core-mantle boundary layer D'' is essentially a thermal boundary layer with a temperature jump of ~1200 K. This mysterious layer is highly variable in its thickness, is highly heterogeneous and elastically anisotropic, and has very small or in some places even negative velocity gradients. An intriguing possibility is the partial melting of this region. Solidus of the pyrolite mantle was determined experimentally by Zerr et al. (1998); at core-mantle boundary melting would start at 4300 K. As this is remarkably similar to the temperatures of the core near this boundary, partial melting of the lower mantle in the D'' seems very likely. The presence of a melt would imply a high electrical conductivity due to ionic diffusivity. The electrical conductivity of the lower mantle is indeed very high (~1-10 S/m – Xu et al., 2000); apart from partial melting it could be explained (O'Keeffe & Bovin, 1979; Matsui & Price, 1991) by a

hypothetical temperature-induced phase transition of $MgSiO_3$ perovskite from the orthorhombic to a disordered and superionically conducting cubic phase. Knittle and Jeanloz (1991) considered the D'' as a chemical reaction zone between the core and mantle. They experimentally observed a reaction, which can be schematically written as follows:

$$(Mg,Fe)SiO_3 + Fe = MgSiO_3 + SiO_2 + FeO + FeSi \qquad (2.6.7)$$

Iron oxide and silicide at the high pressure of the core-mantle boundary are metallic and should be soluble in the core. The reaction of Knittle and Jeanloz (1991) might drive Fe (as well as Si and O) from the mantle into the core. This opens an interesting possibility of the still growing core.

Another interesting question is the nature of minor seismic discontinuities in the lower mantle. E.g., the locally observed 1200-km discontinuity (Vinnik et al., 1998; Le Stunff et al. (1995) suggested that discontinuities at 785-950 km and 1200 km might be global) has been attributed to a tetragonal-to-cubic transition in $CaSiO_3$ perovskite (Stixrude et al., 1996; Chizmeshya et al., 1996) found in linear-response all-electron LAPW calculations. More approximate pseudopotential calculations of Karki (1997) and Warren et al. (1998), however, did not find this transition, and the stable phase of $CaSiO_3$ perovskite in their simulations was always cubic. Improved experimental and theoretical techniques can or soon will be able to resolve such these questions.

Closely related to the (still unknown) composition is the problem of the lower mantle mineralogy. Mineralogical models significantly differ in mineral proportions; essentially nothing certain is known about the mineralogy of Al. This question may have far-reaching consequences, and it will be considered in detail in Chapter 8.

Our understanding of the mantle mineralogy can be greatly increased by studies of mantle inclusions – e.g., Harte et al. (1999) found several lower-mantle minerals (among others, they found $MgSiO_3$ inclusions with up to 10% Al_2O_3) in inclusions in diamonds. Most inclusions studied so far have upper-mantle or transition-zone origin, however.

The transition zone (410-660 km) is quite diverse mineralogically, and might possess exotic properties. This region can host large amounts of water: both wadsleyite and ringwoodite can contain up to 2-3 wt.% H_2O (see Fiquet, 2001 and references therein). It has also been suggested (Angel et al., 1996 and references

therein) that unusual for inorganic compounds five-coordinate Si can play an important role in the transition zone, determining its transport properties.

The upper mantle consists predominantly of olivine, garnet, and pyroxenes. There are four particularly important features of the upper mantle: 1) Ultralow velocity zone at variable depths, roughly between 50-100 km and 220 km (Anderson, 1989), 2) A seismic discontinuity (Lehmann discontinuity) at the base of the ultralow velocity zone, 220 km depth, 3) Strong elastic anisotropy above the 220 km depth, and 4) Strong compositional heterogeneity in the upper 150 km (see Ringwood, 1991). The Lehmann discontinuity is, possibly, due to the *Pbca-C*2/*c* transition in pyroxenes (see Mendelssohn & Price, 1997). The ultralow velocity zone is interpreted as a region of partial melting and low viscosity (asthenosphere) beneath the rigid lithosphere. Anisotropy in this region is a consequence of preferred orientation of crystals caused by nearly horizontal convective flow of the mantle. The uppermost parts of the upper mantle consist mainly of peridotites, while the pyrolitic composition is believed to be characteristic of its deeper regions (Ringwood, 1991).

A comprehensive review of mantle mineralogy can be found in Fiquet (2001). Overall, mantle mineralogy is rather poor: only a handful of mineral species are stable there, and all these minerals have quite dense structures. Very large (e.g., Na, K, Rb, Cs, Ca, Sr, Ba, Cl, Br, I, S, Se, Te, U, Th) and very small (e.g., Li, Be, B) atoms cannot enter these minerals, and concentrate in mantle magmas and fluids, rising to the surface of the Earth and forming its crust. This is why the rich mineral list of the crust is dominated by rare mantle-incompatible elements. The most abundant minerals of the crust are feldspars $(Na,K,Ca)(Al,Si)_4O_8$. The chemical and mineralogical composition as well as the thickness of the crust are very different under oceans and continents. Basaltic oceanic crust is much younger; it is richer in Mg and Fe and poorer in mantle-incompatible elements, denser, and only ~10 km thick. Continental crust is sometimes very old (up to 3-4 billion years), very rich in mantle-incompatible elements, and very rigid and thick (up to ~100 km). The variable thickness and rigidity of the lithosphere (which includes the crust and the rigid uppermost part of the upper mantle) and convection in the deeper mantle result in plate tectonics. Depending on the rheological properties of the lithosphere, there could be other dynamical regimes: e.g., rigid-lid regime (Tackley, 2000), where the lithosphere is not perturbed by deeper convection (this regime is possible for Mars).

2.7. The Dynamic Earth: plate tectonics and mantle convection.

Plate tectonics theory, that appeared in the 1960s, was a revolutionary step in geology. It explained for the first time the strong localisation of earthquakes in continental margins (plate boundaries), the existence of volcanic mid-ocean ridges (rift zones), and continental drift. It is firmly established that it is the mantle convection that drives plate tectonics mechanism.

Convection can occur only when the temperature gradient is equal to or higher than the adiabatic gradient, eq. (2.6.2), or, in other words, when Bullen parameter $\eta \leq 1$ (see eq. 2.6.5). Another very important criterion is that the Rayleigh number *Ra*, which measures the ratio of the buoyant force to the viscosity drag force, be higher than the critical value, Ra_c. For the case of a liquid heated from below,

$$Ra = g\alpha h^3 \Delta T / \nu\kappa \quad , \tag{2.7.1}$$

where h is the thickness of the layer, ΔT is the temperature difference between the top and bottom, ν is the kinematic viscosity, and κ is the thermal diffusivity (which is related to the thermal conductivity, K, via: $\kappa = K/\rho C_P$).

For the liquid heated from within,

$$Ra = g\alpha\rho q h^5 / \nu\kappa K \quad , \tag{2.7.2}$$

where q is the rate of internal heat production.

For both cases of heating from within and from below, the critical values $Ra_c \approx 2*10^3$. Inserting values characteristic of the mantle into (2.7.1) and (2.7.2), one gets highly supercritical values, $\sim 10^9$ for heating within and $\sim 10^6$ for heating from below (Poirier, 2000; Anderson, 1989).

Among other important physical parameters is the Péclet number, which measures the ratio of the convected heat to the conducted heat:

$$Pe = vl/\kappa \quad , \tag{2.7.3}$$

where v is a characteristic velocity and l is a characteristic length. For the Earth $Pe \approx 10^3$, indicating that convection dominates overall (Anderson, 1989). At the boundary of two separately convecting layers, where there is no vertical convective velocity, no heat is transported by convection. A thermal boundary layer must exist between separately convecting layers; across this layer heat is transported by conduction, and temperature gradient is highly superadiabatic.

The Prandtl number:

$$Pr = \nu/\kappa \tag{2.7.4}$$

is ~10^{24} for the mantle, indicating that the viscous response to a perturbation is much faster than thermal response (Anderson, 1989).

The numbers defined above are important in understanding results of numerical modelling of the mantle convection (for a discussion of early results, see Verhoogen, 1980). Rayleigh numbers significantly exceeding the critical value imply time-dependent (rather than steady) convection with many convective cells (when Ra is comparable to Ra_c, only one convective cell would develop[1]). At such high Rayleigh numbers convective flow may become intermittent; the period of interittency for the Earth's mantle is calculated to be ~100 million years. The estimated horizontal wavelength of mantle convection is ~ 700 km (Verhoogen, 1980).

The Earth's mantle is convecting with velocities of several mm/year. These velocities are highly variable, and may be a few times lower in the lower mantle due to its higher viscosity. Microscopically, this solid-state convection is not well understood. It is possible that in different parts of the Earth it occurs by different mechanisms – plastic flow, dislocational or diffusional creep.

Hot ascending plumes are born at thermal boundary layers (especially D''). They may be depleted in Fe as a result of the reaction (2.6.7) with the core. Depletion in Fe would increase buoyancy of the plumes. Cold downgoing slabs consist of basaltic oceanic crust and peridotitic upper-mantle rocks (Kesson et al., 1998). Excess silica in the form of stishovite (SiO_2) in the basaltic part of the slabs may be removed as a result of partial melting (Ringwood, 1991). According to Kesson et al. (1998), the slab material is intrinsically less dense than the pyrolitic lower mantle; its negative buoyancy would be entirely due to the lower T. Even if this material is able to sink to the core-mantle boundary, it will eventually rise again when sufficiently heated up. This has led Kesson et al. (1998) to conclude that slabs cannot reside at the D'' for much longer than 500 million years. It is possible that the basaltic component of the slab, being much less dense than the lower mantle at ~600-800 km depths, is delaminated and left in the transition zone (Kesson et al., 1998). However, below 800-1000 km basalts should be significantly denser than the pyrolitic mantle (Ringwood, 1991). Generally, slabs may have a difficulty in penetrating the 670-km discontinuity due to the large increase of viscosity and

[1] I.e. convection is described by a spherical harmonic with l=1. Higher-order harmonics appear on increasing the Ra/Ra_c ratio. These conclusions were reached for a convecting

density at this depth. It is possible that slab material accumulates at this depth and from time to time falls through the discontinuity in 'avalanches' – this picture was obtained in numerical simulations of convection (see Poirier, 2000 and references therein).

Cold slabs would have a different mineralogy from the rest of the mantle, because of the lower temperatures and different bulk chemical composition. An aluminous phase (possibly, $MgAl_2O_4$ in the $CaTi_2O_4$ or $CaFe_2O_4$ structures – Kesson et al., 1994, 1998) would be present in the lower-mantle slabs. H_2O, liberated from hydrous silicates at high pressures, might form ice VII in sufficiently cold slabs (e.g., at 700 K and 15 GPa – Bina & Navrotsky, 2000).

Subduction zones with downgoing slabs are strongly correlated with seismically active areas (e.g., Japan); hot plumes are situated below volcanic 'hot spots' (such as Hawaii or Iceland). It is important to understand the 3D-thermal structure of the mantle, in particular how cold are the cold slabs and how hot are the hot plumes relative to the normal mantle. The temperature contrast between the slabs and the hot regions must be related to the driving force of convection. Knowledge of the lateral temperature variations can shed a new light on the mantle, its structure and composition.

Studying topography of major seismic discontinuities, it is possible to get some ideas on the lateral temperature varations (Helffrich, 2000), knowing the Clapeyron slopes of the corresponding phase transitions. Most slabs turn out to be ~400-700 K colder than the average mantle at 660 km; Tonga slab seems to be ~1200 K colder. The temperature anomaly below the Iceland hot spot is estimated to be +180 K at the 660 km depth (Helffrich, 2000). Studies of this kind are very important, but restricted to the seismic discontinuity zones. It is possible to extract the same information and many other important characteristics of the mantle, but without such restrictions, from seismic tomography. The first physically sound attempt to solve this problem was made by Oganov et al. (2001b; see Chapter 10), who found the maximum temperature contrast between the cold and hot regions increasing from ~800 K at 1000 km depth to ~1500 K at 2000 km and, possibly, over 2000 K at the core-mantle boundary. The following section is dedicated to a brief discussion of seismic tomography.

---

sphere. In a slab-shaped convecting layer, convection with $Ra \approx Ra_c$ follows hexagonal

2.8. Seismic tomography.

In seismic tomography, a large number of seismological measurements are inverted to give 3D-distributions of seismic wave velocities. It is common to represent results in terms of perturbations of seismic velocities relative to the average velocity at each depth: e.g., $\Delta V_S/V_S$. Various types of tomographic inversions exist, including regional and global. Technical details of seismic tomography inversion techniques can be found in (Anderson, 1989; Kennett et al., 1998; Masters et al., 2000). The most recent tomography maps have similar qualitative features and give the absolute velocity perturbations within ~25% uncertainty. Perhaps, the most reliable global seismic tomography maps currently available are those of Masters *et al*. (2000). Older higher-resolution maps of Kennett *et al*. (1998) realistically give much narrower cold (high-velocity) zones, but strongly underestimate amplitudes of the velocity variations (see Masters et al., 2000). Tomographic images obtained in these works are shown in Fig. 2-7 and 2-8.

It is very difficult to obtain a reliable 3D-distribution of the density (Romanowicz, 2001), therefore the interpretation must concentrate on the velocities. In the first approximation, low velocities can be attributed to high temperatures, and high velocities – to low-temperature slabs. This interpretation is generally consistent with the expected convective flow patterns. There is a remarkable correlation between surface tectonics and tomographic images down to the core-mantle boundary. Most slabs penetrate the 660-km boundary and even seem to reach the core-mantle boundary (Masters et al., 2000), although in some tomographic images (Kennett et al., 1998) most slabs seem to disappear somewhere between 1000 km and 2000 km depths.

From PREM, the relative perturbation of shear and compressional seismic wave velocities due to pressure alone:

$$R_T=\left(\frac{\partial \ln V_S}{\partial \ln V_P}\right)_T \qquad (2.8.1)$$

is 0.7 (Anderson, 1989). A similarly defined parameter,

$$R_p=\left(\frac{\partial \ln V_S}{\partial \ln V_P}\right)_p \qquad (2.8.2)$$

measuring the same ratio, but due to temperature effects alone, is much larger: it increases from 1.7 to 2.6 between the depths of 1,000 km and 2,000 km as determined by seismic tomography (Robertson & Woodhouse, 1996).

---

honeycomb-like patterns (called Benard patterns).

The large difference between R_T and R_p has been a puzzle for geophysicists over the last 15 years. The seismological values of R_T are well reproduced in the laboratory (see Anderson, 1989) and in theoretical simulations (Oganov et al., 2001b; Parker & Wall, 1991); it is the large seismologically measured value of R_p that needs to be

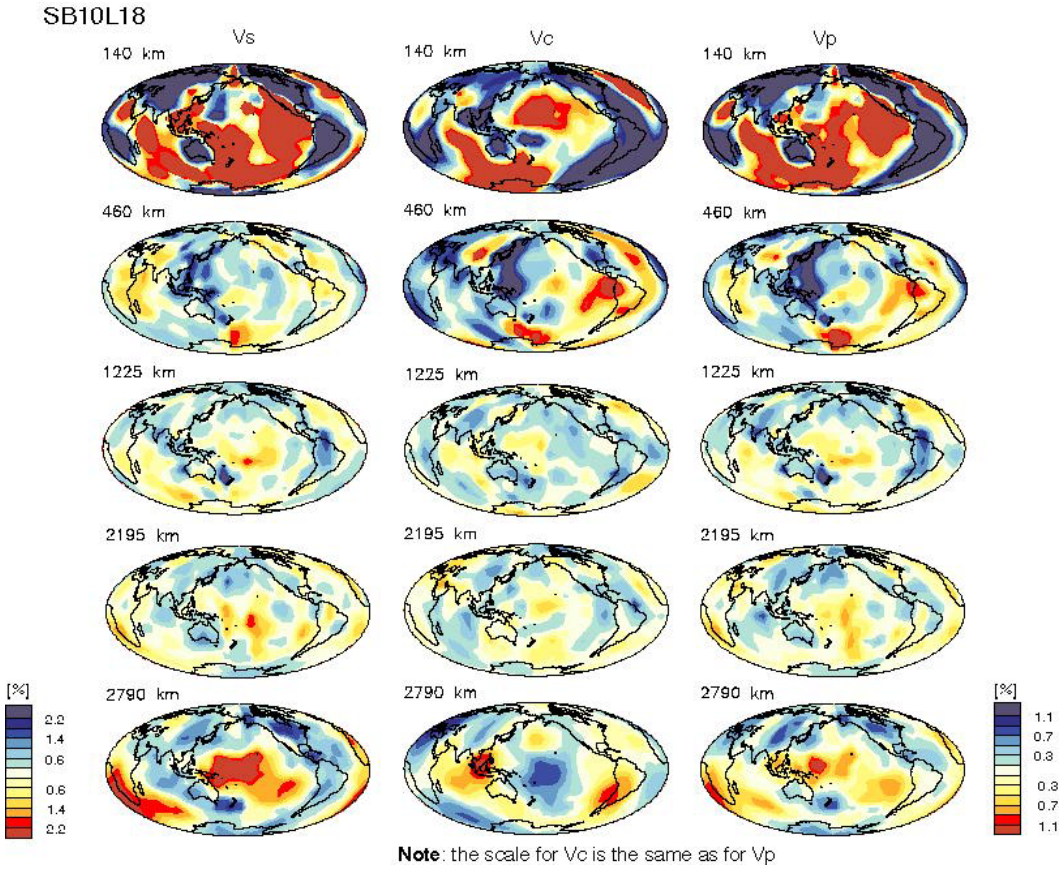

Fig. 2-7. Seismic tomography images of Masters et al. (2000). V_C (more often denoted as V_ϕ) is the bulk sound velocity: $V_\phi = (K_S/\rho)^{1/2} = (V_P^2\text{-}4/3V_S^2)^{1/2}$. This velocity is not directly observed, but is easily obtained from the observable V_S and V_P and is often more convenient for analysis.

explained. Three possible explanations exist: 1) Intrinsic anharmonicity (Anderson, 1989), 2) Anelastic effects (Karato, 1993), and 3) Large-scale compositional heterogeneity (e.g., Masters et al., 2000). The first two effects must be present; the question is how important these effects are. Intrinsic anharmonicity contribution is difficult to analyse experimentally; in theoretical work, one must go beyond the quasiharmonic approximation and apply molecular dynamics or Monte-Carlo simulations. This has been done (Oganov et al., 2001b; see Chapter 10); the

resulting R_p is still lower than the seismological values, implying significant anelastic and/or compositional contributions.

Anelastic attenuation springs from the dissipation of the energy of the seismic wave passing through the rock. This effect is highly frequency-dependent, and has a maximum at the frequencies similar to the frequency of some process (e.g., defect migration) in the solid. Details of the complicated theory of attenuation can be found in Anderson (1989); here I consider it briefly.

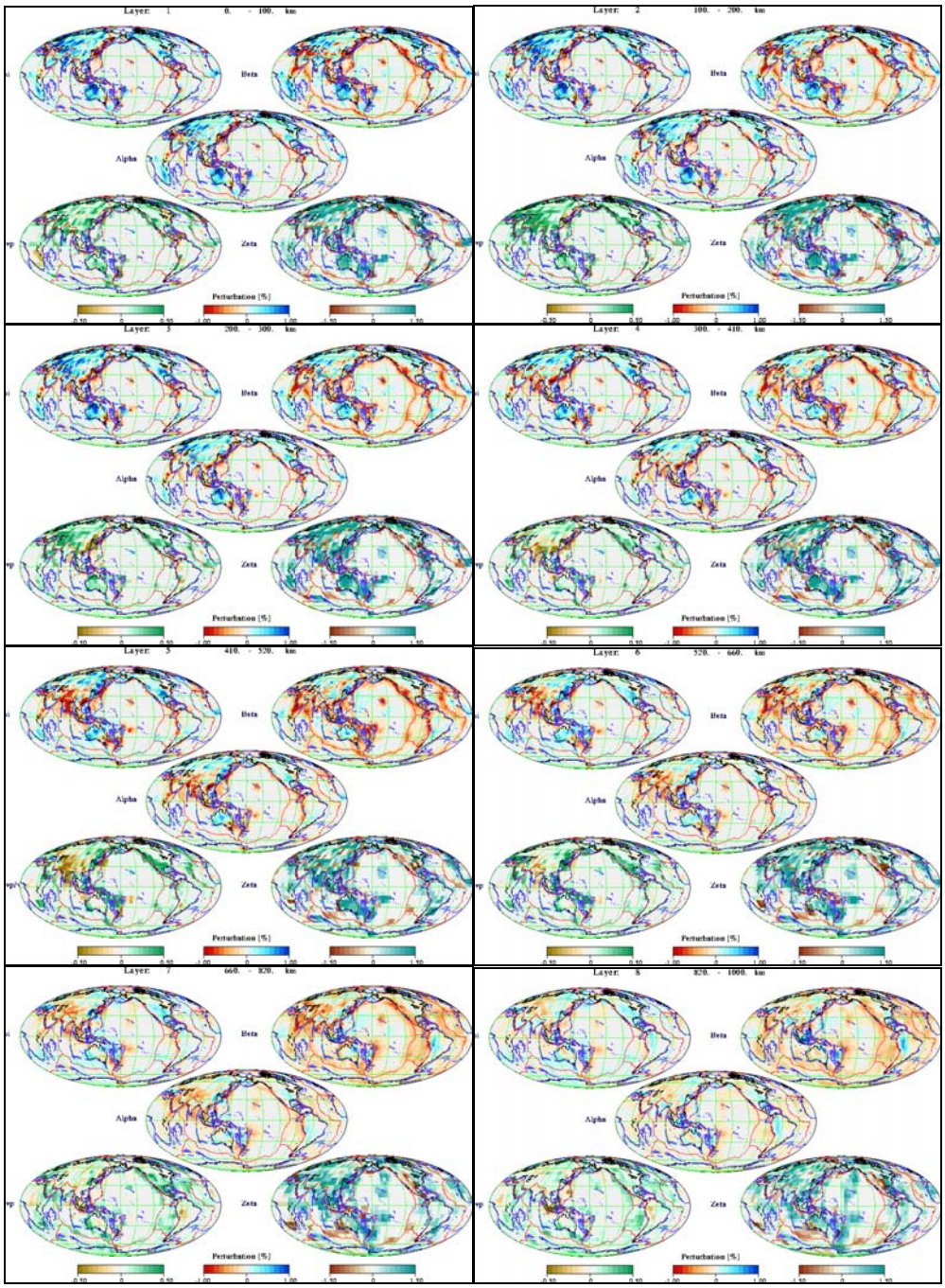

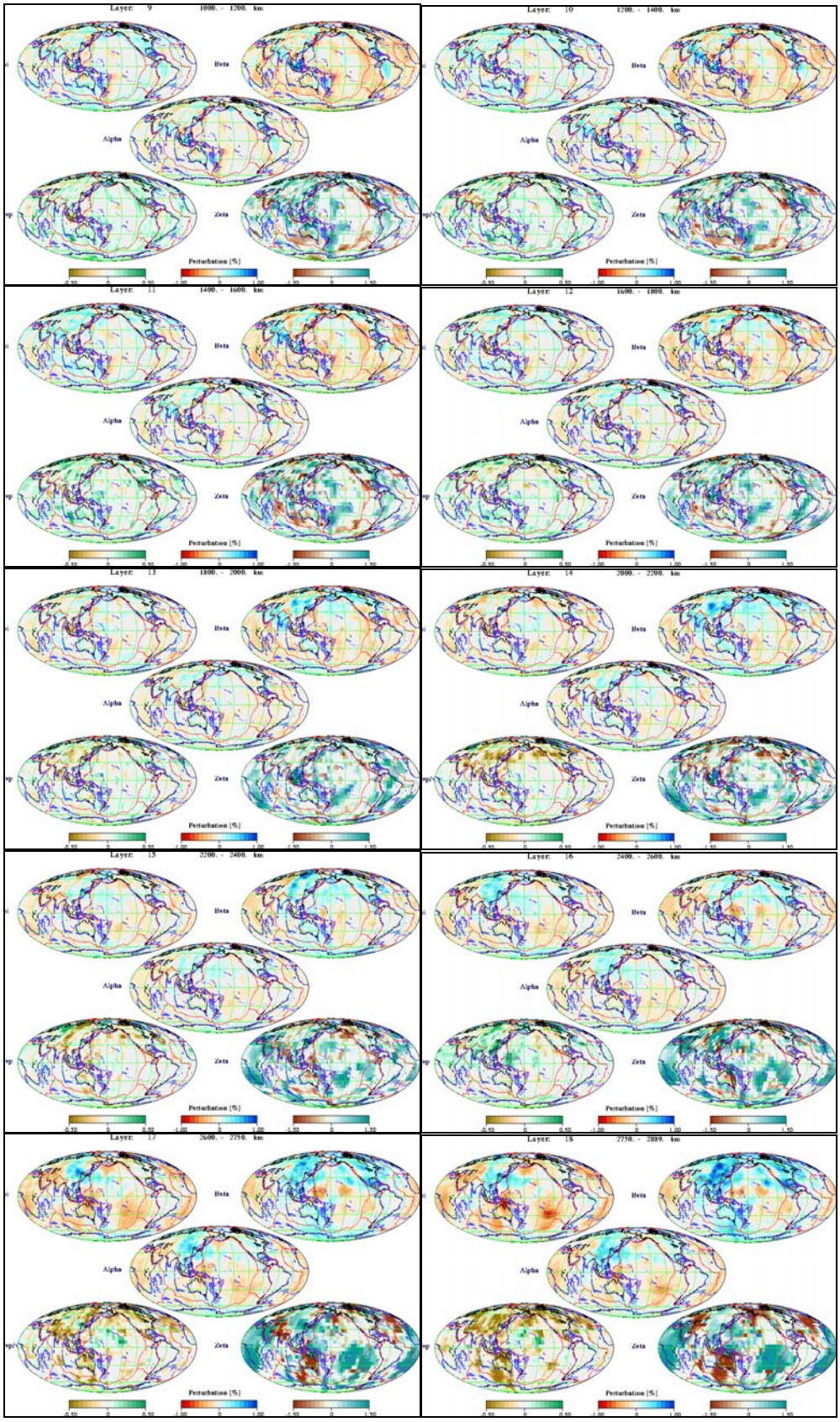
Layer: 9 1000. - 1200. km
Layer: 10 1200. - 1400. km
Layer: 11 1400. - 1600. km
Layer: 12 1600. - 1800. km
Layer: 13 1800. - 2000. km
Layer: 14 2000. - 2200. km
Layer: 15 2200. - 2400. km
Layer: 16 2400. - 2600. km
Layer: 17 2600. - 2750. km
Layer: 18 2750. - 2889. km
Beta
Alpha
Zeta
Perturbation [%]

Fig. 2-8. Seismic tomography images of Kennett et al. (1998). In each box: top left picture, V_ϕ perturbation; top right V_S; centre V_P perturbation; bottom left and bottom right – distributions of $(\frac{\partial \ln V_P}{\partial \ln V_S})_p$ and $(\frac{\partial \ln V_\phi}{\partial \ln V_S})_p$, respecively.

A wave travelling through an anelatic rock can be described by the following wave equation:

$$A = A_0 \exp[i(\omega t - kx)] \exp(-k^* x) \quad , \tag{2.8.3}$$

where the wavenumber is complex, and k^* is its imaginary part. For an anelastic rock, the elastic constants are also complex (in Chapter 3 I shall consider in detail the case of a perfectly elastic solid, where the elastic constants are real):

$$\hat{C} = C + iC^* \quad , \tag{2.8.4}$$

where C^* is the imaginary part of a given elastic constant. The dimensionless specific quality factor is

$$Q_M^{-1} = C^*/C \tag{2.8.5}$$

The Q-factor is related to the energy dissipation $\Delta\varepsilon$ per vibrational cycle:

$$Q = 4\pi \langle \varepsilon \rangle / \Delta\varepsilon \quad , \tag{2.8.6}$$

were $\langle \varepsilon \rangle$ is the average energy of the wave. A model analytical expression for $Q(\omega)$, taking into account its resonance nature, is:

$$Q^{-1}(\omega) = 2Q_{max}^{-1} \frac{\omega\tau}{1+(\omega\tau)^2} \quad , \tag{2.8.7}$$

where τ is the relaxation time:

$$\tau = \tau_0 \exp(H^*/RT), \tag{2.8.8}$$

where H^* is the activation enthalpy. Eq. (2.8.8) explicitly introduces the temperature dependence into the Q-factors. The frequency dependence of the seismic wave velocities is approximately

$$V(\omega) = V_0(1+Q_{max}^{-1} \frac{\omega\tau}{1+(\omega\tau)^2}) \quad , \tag{2.8.9}$$

where V_0 is the zero-frequency velocity. The high-frequency (elastic) velocity is simply

$$V\infty = V_0(1+Q_{max}^{-1}) \tag{2.8.10}$$

Attenuation effects are usually negligble for the bulk modulus, but often are strong for the shear modulus and shear seismic waves. Using PREM values of the Q-factors in the lower mantle, $(V_\infty - V_0)/V_0$ is ~0.32% and ~0.13% for the shear and

compressional velocities, respectively (for the bulk velocities it would be only 0.002%). Dewaele and Guyot (1998) argued that PREM underestimates the contribution of attenuation to the shear velocities in the lower mantle (i.e., PREM values of Q are overestimated).

Karato (1993) proposed a method to estimate the contribution of anelasticity to the seismologically measured R_p. Instead of (2.8.7) he used simpler expressions, justifying it by the fact that in real solids there are usually several possible defect relaxation mechanisms, rather than just one. The resulting $Q^{-1}(\omega)$ function would have many maxima and yield a smaller ω-dependence of the velocities than in the model (2.8.9).

Karato (1993) considered two models. Assuming that Q is independent of ω, one has

$$V(\omega) = V_\infty[1+(Q^{-1}/\pi)\ln\omega\tau] \quad , \tag{2.8.11}$$

from which Karato obtained

$$\frac{\partial \ln V}{\partial T} = \frac{\partial \ln V_\infty}{\partial T} - [Q^{-1}/\pi][H^*/RT^2] \qquad \text{for } Q>>1 \tag{2.8.12}$$

In the second model, Karato allowed a small frequency dependence of Q:

$$Q(\omega) \sim \omega^\alpha \qquad \text{with } \alpha\sim 0.1\text{-}0.3 \ , \tag{2.8.13}$$

in which case

$$V(\omega) = V_\infty[1- \tfrac{1}{2}\cot(\pi\alpha/2)Q^{-1}(\omega)] \tag{2.8.14}$$

and

$$\frac{\partial \ln V}{\partial T} = \frac{\partial \ln V_\infty}{\partial T} - (\pi\alpha/2)\cot(\pi\alpha/2)[Q^{-1}(\omega)/\pi][H^*/RT^2] \qquad \text{for } Q>>1 \tag{2.8.15}$$

Karato estimated the anelastic contribution to R_p using H^* for olivine. It became clear from these estimates that the anelastic contribution is very important throughout the mantle. Although no self-consistent analysis of the problem has been reported for the lower mantle, it seems that the anharmonic and anelastic effects would not be sufficient to account for the R_p values only in the D'' layer. Some other features of this layer (e.g., anticorrelation of the bulk and shear velocities – see Fig 2-7) suggest that this region is significantly chemically heterogeneous on large scales. This is hardly surprising if one views this layer as a chemical reaction zone (Knittle & Jeanloz, 1991).

Forte and Mitrovica (2001) attempted to analyse seismic tomography data for the core-mantle boundary. They took into account anharmonic, anelastic, and

compositional effects. Among other results, they reported on the temperature contrast up to 1,200 K and maximum contrast in the Fe content of 2% (with hot regions depleted in Fe). Unfortunately, their compositional derivative of the shear wave velocity was almost certainly wrong by up to an order of magnitude, which casts doubt on their results.

In the next chapter I shall consider in detail the elastic properties of crystals, their equations of state, and thermodynamic properties. Theory presented in Chapter 3 plays a central role in the interpretation of seismological data.

Chapter 3. Thermodynamics, equations of state, and elasticity of crystals.

In this chapter I shall discuss some of the most important properties of crystals – their equations of state, elastic properties, and thermodynamic functions. As thermodynamics is in the very heart of this whole area of solid state physics, I begin the discussion with thermodynamic properties of crystals.

3.1. Thermodynamic properties of crystals.

Thermodynamic properties are, perhaps, the most important properties of a crystal – they define its stability field; their derivatives with respect to pressure, temperature, and volume describe the behaviour of the crystal at changing conditions, its equation of state and response functions such as elastic constants and thermal expansion.

In thermodynamic theory of condensed matter, a fundamental role is played by the partition function:

$$Z = \sum_i e^{-E_i / k_B T} \quad , \tag{3.1.1}$$

where the summation is carried out over all discrete energy levels of the system. Once Z is known, all thermodynamic properties can be obtained straightforwardly, e.g. the Helmholtz free energy:

$$F = E_0 - k_B T \ln Z \, , \tag{3.1.2}$$

where E_0 is the ground-state energy (at 0 K) including the energy of zero-point motion.

However, it is extremely difficult to obtain all energy levels experimentally or theoretically, and their number is overwhelmingly large for solids. This is where simplified models (such as the harmonic approximation) come into play. The harmonic approximation plays a key role in the theory of thermodynamic properties of crystals. It gives a first approximation to the distribution of the energy levels E_i, which is usually accurate for the most-populated lowest excited vibrational levels. The key concept here is that of a non-interacting (ideal) gas of quasiparticles called phonons, and the key quantity – the phonon density of states, g(ω), which defines the number of phonons with energies in an infinitely narrow energy interval between $\hbar\omega$

and $\hbar\omega$+d($\hbar\omega$). The effects not accounted for by this simplified picture can often be included as additive corrections to the harmonic results.

3.2. Harmonic approximation.

In the harmonic approximation it is assumed that all interatomic interactions are analogous to perfectly elastic springs connecting atoms, the energy of any displacement being proportional to the square of the displacement, x, and the force induced by the displacement is proportional to the displacement itself:

$$\Delta E = 1/2kx^2 \quad \text{or} \quad E(R) = E(R_0) + 1/2kx^2 \ , \ f = -kx \ , \tag{3.2.1}$$

where R_0 is the equilibrium distance between two atoms connected by a 'spring' with a force constant k.

Quantum mechanics stipulates that energy levels be discrete, and for the harmonic oscillator the solution of the Schrödinger equation yields the following energy levels:

$$E_n = \hbar\,(1/2+n)\omega, \tag{3.2.2}$$

where n is the quantum number and ω the frequency of the vibration. For n=0 (ground state) there is a quantum energy $\hbar\omega/2$ called the zero point vibrational energy. For n=2,3,… we have doubly, triply,… excited vibrations – such vibrations are called overtones, and due to high energies such excited states have low populations p_n, increasing with temperature according to the Boltzmann statistics: $p_n \sim e^{\frac{-E_n}{k_B T}}$. Energy levels in a true vibrational system are well described by (3.2.2) only for the lowest quantum numbers n, but these represent the most populated, and thus the most important vibrational excitations.

In the harmonic model all atoms vibrate around their equilibrium positions. Diffusion cannot occur as the energy required to remove an atom or for an atom to become unbound to its original position, is infinite. Such high-temperature phenomena as melting and diffusion in real materials cannot be accounted for by the harmonic approximation. These phenomena are essentially anharmonic; the harmonic potential (3.2.1) becomes inaccurate at large displacements (or, in other words, high-order overtones are poorly described by the harmonic approximation). These large displacements become accessible at high temperatures, where the harmonic approximation breaks down. At not too high temperatures, however, the harmonic approximation is valid.

In this approximation, the vibrational energy of the crystal can be determined via the frequencies ω of the normal lattice vibrations (also known as vibrational modes

or phonons) and temperature T. Each normal mode contributes to the vibrational energy according to a famous formula first derived by Einstein for the harmonic oscillator:

$$E_{\mathrm{vib}}(\omega, T) = \frac{1}{2}\hbar\omega + \frac{\hbar\omega}{\exp(\frac{\hbar\omega}{k_{\mathrm{B}}T})-1}, \qquad (3.2.3)$$

where $\hbar$ is the Planck constant, and k_{B} the Boltzmann constant. The first term in (3.2.3) is the zero-point energy originating from quantum motion of atoms; in the harmonic approximation it is independent of temperature. Zero-point energy dominates E_{vib} at temperatures between zero and roughly half the Debye temperature. The second, temperature-dependent term, gives the thermal energy of the mode according to the Bose-Einstein distribution. The thermal energy (or heat content) gives the energy absorbed by the crystal upon heating from 0 K to the temperature T. At room temperature, the zero-point energy is usually significantly larger than the heat content. Differentiating (3.2.3) with respect to the temperature, produces the heat capacity of a harmonic oscillator :

$$C_{\mathrm{V,vib}}(\omega, T) = (\frac{dE_{\mathrm{vib}}(\omega, T)}{dT})_{\mathrm{v}} = k_{\mathrm{B}}(\frac{\hbar\omega}{k_{\mathrm{B}}T})^2 \frac{\exp(\frac{\hbar\omega}{k_{\mathrm{B}}T})}{(\exp(\frac{\hbar\omega}{k_{\mathrm{B}}T})-1)^2} \qquad (3.2.4)$$

In the harmonic approximation the isochoric (C_{V}) and isobaric (C_{p}) heat capacities are equal: $C_{\mathrm{V}} = C_{\mathrm{p}}$, and for the contribution of a normal mode to the vibrational entropy of the crystal, we have:

$$S_{\mathrm{vib}}(\omega, T) = \int_0^T \frac{C_{\mathrm{p}}(\omega, T)}{T} dT = -k_{\mathrm{B}} \ln[1-\exp(-\frac{\hbar\omega}{k_{\mathrm{B}}T})] + \frac{1}{T}\frac{\hbar\omega}{\exp(\frac{\hbar\omega}{k_{\mathrm{B}}T})-1} \qquad (3.2.5)$$

In a crystal with n atoms in the primitive unit cell, there are $3n$ different normal modes. The Helmholtz free energy of a harmonic oscillator is then:

$$F_{\mathrm{vib}}(\omega, T) = \frac{1}{2}\hbar\omega + k_{\mathrm{B}}T\ln[1-\exp(-\frac{\hbar\omega}{k_{\mathrm{B}}T})] \qquad (3.2.6)$$

If all of them had the same frequency (the assumption of the Einstein model), then, multiplying the right-hand sides of (3.2.3)-(3.2.6) by the total number of vibrations ($3n$), all thermodynamic properties would be obtained immediately. However, normal mode frequencies form a spectrum; most modes are in the infrared range of frequencies. The highest frequencies are determined by the strongest bonds

in the structure. This spectrum of frequencies (energies) of phonons is called the phonon spectrum, or phonon density of states $g(\omega)$.

As in the harmonic approximation the normal modes are independent of each other and non-interacting, all thermodynamic properties can be obtained as a natural generalisation of (3.2.3)-(3.2.6) by integration over all frequencies:

$$E_{\mathrm{vib}}(T) = \int_0^{\omega_{\max}} E_{vib}(\omega, T) g(\omega) \mathrm{d}\omega =$$

$$= \int_0^{\omega_{\max}} \frac{1}{2} \hbar \omega \, g(\omega) \mathrm{d}\omega + \int_0^{\omega_{\max}} \frac{\hbar\omega}{\exp(\frac{\hbar\omega}{k_B T}) - 1}] g(\omega) \mathrm{d}\omega \qquad (3.2.7)$$

$$C_V(T) = \int_0^{\omega_{\max}} C_v(\omega, T) g(\omega) \mathrm{d}\omega = k_B \int_0^{\omega_{\max}} (\frac{\hbar\omega}{k_B T})^2 \frac{\exp(\frac{\hbar\omega}{k_B T})}{(\exp(\frac{\hbar\omega}{k_B T}) - 1)^2} \mathrm{g}(\omega) \mathrm{d}\omega \qquad (3.2.8)$$

$$S(T) = \int_0^{\omega_{\max}} S(\omega, T) \, g(\omega) \mathrm{d}\omega =$$

$$= \int_0^{\omega_{\max}} [-k_B \ln[1-\exp(-\frac{\hbar\omega}{k_B T})] + \frac{1}{T} \frac{\hbar\omega}{\exp(\frac{\hbar\omega}{k_B T}) - 1}] g(\omega) \mathrm{d}\omega \qquad (3.2.9)$$

$$F(T) = E_0 + \int_0^{\omega_{\max}} F(\omega, T) \mathrm{g}(\omega) \mathrm{d}\omega =$$

$$E_0 + \int_0^{\omega_{\max}} \frac{1}{2} \hbar \omega \, \mathrm{g}(\omega) \mathrm{d}\omega + k_B T \int_0^{\omega_{\max}} \ln[1-\exp(-\frac{\hbar\omega}{k_B T})] g(\omega) \mathrm{d}\omega \, , \qquad (3.2.10)$$

where E_0 is the energy of the static lattice.

3.3. Models of the phonon spectrum: Debye, Agoshkov, Kieffer.

Once the density of states $g(\omega)$ is known, the application of equations (3.2.7)-(3.2.10) is straightforward. IR- or Raman spectra probe only some of the vibrations which have wavevectors close to zero (e.g., have the wavelengths of the scale of the whole crystal; however, most vibrations have shorter wavelengths), and therefore do not give the full information on the phonon spectrum. The $g(\omega)$ can be determined experimentally by inelastic neutron scattering (e.g., Dove, 1993), or theoretically using lattice dynamics or molecular dynamics simulations. All these methods are complicated. Often one can obtain a reasonable approximation of $g(\omega)$ using the

easily obtained IR- and/or Raman spectra and/or elastic properties of the material. Here I briefly describe such models.

Debye model. For the acoustic modes the phonon spectrum can be described, to a first approximation, as a parabolic function truncated at the maximum frequency $\omega_D = \frac{k\theta_D}{\hbar}$. The Debye model assumes the same distribution for all phonon modes:

$$g(\omega) = 9n(\frac{\hbar}{k_B\theta_D})^2\omega^2 , \qquad (3.3.1)$$

where n is the number of atoms per unit cell of the volume V_0, and θ_D is the characteristic Debye temperature, the only parameter in this model.

With (3.3.1) for g(ω) the thermodynamic functions take the following forms :

$$E_{vib} = \frac{9}{8}k_B n\theta_D + 3k_B nTD(\frac{\theta_D}{T}) , \qquad (3.3.2)$$

$$C_V(T) = (\frac{dE_{vib}}{dT})_v = 3k_B n\,[4D(\frac{\theta_D}{T}) - \frac{3(\theta_D/T)}{e^{\theta_D/T}-1}], \qquad (3.3.3)$$

$$S(T) = \int_0^T \frac{C_p}{T}dT = k_B n\,[4D(\frac{\theta_D}{T}) - 3\ln(1-e^{\theta_D/T})], \qquad (3.3.4)$$

where $D(x) = \frac{3}{x^3}\int_0^x \frac{x^3dx}{e^x-1}$, $x = \frac{\theta_D}{T}$.

The first term in (3.3.2) is the zero-point energy in the Debye model, the second term is the heat content. The Debye temperature is determined by the elastic properties of the solid – or, more precisely, its average sound velocity <*v*>:

$$\theta_D = \frac{\hbar}{k_B}(\frac{6\pi^2 n}{V_0})^{1/3} <v> \qquad (3.3.5)$$

The mean sound velocity can be accurately calculated from the elastic constant tensor (Robie & Edwards, 1966). Usually, however, an approximate formula is used:

$$<v> = (\frac{1}{V_P^3} + \frac{2}{V_S^3})^{-1/3} , \qquad (3.3.6)$$

where V_P and V_S are the longitudinal and transverse sound velocities, respectively. Later in this chapter, when discussing elastic constants, I shall discuss how to calculate these velocities.

The Debye model is very effective in application to chemically and structurally simple crystals, but in more complicated cases (particularly, in molecular crystals and compounds with complex anions, e.g. silicates) it becomes too crude. Deep theoretical analyses of this model and its critique can be found in (Seitz, 1949;

Kieffer, 1979a). Some more details of this model will be discussed in Chapter 10. As will be also discuss later, the thermal equation of state can be formulated within the Debye model – the roots and consequences of such approaches will be considered for $MgSiO_3$ perovskite.

Kieffer model. The most complete critical review of the Debye model can be found in the paper by S.W. Kieffer (Kieffer, 1979a), who in the same seminal cycle of papers proposed a new model (Kieffer, 1979b, 1979c, 1980, 1982). This much more accurate model is based on the following main points: 1) Three acoustic modes have a sinusoidal dispersion law $\omega(\mathbf{k})$ (not linear, as assumed in the Debye model) and are described by three different densities of states, 2) Optic modes are divided into two groups: high-frequency (e.g., Si-O stretching modes in silicates) and low-frequency modes (e.g., cation-oxygen stretching modes and deformational modes). Low-frequency vibrations are represented by an 'optic continuum' – a constant density of states between some lowest ω_l and highest ω_u frequencies. In estimating these limiting frequencies one is guided by the corresponding IR- and Raman frequencies and the ratio of the masses of the cation and the complex anion – this approximately takes into account the dispersion. The high-frequency modes are described by one or more monochromatic ('Einstein') peaks of the density of states or another optic continuum. The predictive power of this model is limited: the results critically depend on the limiting frequencies ω_l and ω_u of the low-frequency optic continuum. These frequencies differ greatly from crystal to crystal and therefore cannot be transferred. Either an experiment or accurate calculations of the phonon spectrum are required. At the same time, the Einstein frequencies are usually quite transferable: e.g., the Si-O stretching modes in orthosilicates have an average frequency of 28.5 THz.

Agoshkov model. One of the possible simplifications was introduced by V.M. Agoshkov (Agoshkov, 1985; Agoshkov *et al.*, 1994). This model was used in my early work (Urusov *et al.*, 1998). In brief, all the acoustic and low-frequency optic modes are described by a single Debye-like parabolic density of states $g(\omega)$ (3.3.1), but truncated (such truncation was also present in Kieffer's model) at a lower frequency; this maximum frequency ω_D^* is now:

$$\omega_D^* = \frac{k_B \theta_D}{\hbar} \sqrt[3]{\frac{3+M}{3n}} \quad , \tag{3.3.7}$$

where M is the number of the low-frequency optic modes, included in the parabolic g(ω). The high-frequency modes, like in the Kieffer model, are described as Einstein oscillators.

The zero-point energy of the Agoshkov model is easily obtained:

$$E_{zp} = \frac{9}{8} k_B n \theta_D \left(\frac{3+M}{3n}\right)^{4/3} + \sum_{i=M+1}^{3n-3} \frac{1}{2} \hbar \omega_i \ , \qquad (3.3.8)$$

where the first term gives the contribution of the 'Debye distribution', and the second term is a sum over all the high-frequency optic modes. Expressions for other thermodynamic functions were given in the original work (Agoshkov, 1985). Very accurately describing heat capacity at room and higher temperatures, the model gives serious errors at low temperatures; this affects the entropy. The same shortcoming is possessed, but to a smaller extent, by the Kieffer model. The advantage of the Agoshkov model is in its suitability for the *a priori* estimates of thermodynamic properties. Anharmonic corrections can be easily incorporated into both models (for the Debye model this is even easier – I shall discuss this in Chapter 10) by assigning different values of the mode Grüneisen parameter to each group of vibrations.

It is possible to construct other approximate thermodynamic models – an example is the Komada-Westrum model (Komada & Westrum, 1997), which, like the Debye model, has only one parameter, but is comparable in its accuracy to more complicated models.

3.4. Shortcomings of the harmonic approximation.

The harmonic approximation, neglecting third- and higher-order terms in the interatomic potential, leads to a number of fundamental errors. First, within this approximation, all vibrational modes are independent – there is no exchange of energy and momentum between them. This leads to a simple interpretation of experimentally observed vibrational spectra and greatly simplifies the calculation of thermodynamic properties (3.2.7)-(3.2.10), but at high temperatures errors become serious.

Non-interacting phonons can freely travel within the crystal, leading to the infinite thermal conductivity of the harmonic crystal. In real crystals, thermal conductivity is finite due to phonon-phonon collisions (especially Umklapp processes – see Elliott, 1998), scattering on defects, and finite size of samples.

As it was mentioned, diffusion and melting cannot be explained within the harmonic approximation. The same can be said about displacive phase transitions – although the harmonic approximation can indicate such a transition by showing a soft mode, no properties can be calculated for the dynamically disordered phase.

In the harmonic approximation there is no thermal expansion, which obviously contradicts experiment. This is particularly important for geological applications. Related to this is the equality $C_V=C_p$, whereas experiment indicates $C_V < C_p$.

From general thermodynamics, we have:

$$C_p = C_V(1+\alpha^2 K_T V/C_V) , \qquad (3.4.1)$$

where α is thermal expansion coefficient, K_T isothermal bulk modulus, and V the molar volume. When $\alpha = 0$, $C_V=C_p$.

Also, experiment indicates (Gillet *et al.*, 1999) that at high temperatures the isochoric heat capacity increases beyond $3n$R (the Dulong-Petit limit): $C_V>3n$R, while in the harmonic approximation $3n$R is the maximum value. Similarly, the vibrational energy can exceed the harmonic quota of $3k_BT$ per atom. Consider a single anharmonic oscillator, whose potential is given by a polynomial expansion in terms of displacements x from the minimum energy position:

$$E_{pot} = 1/2kx^2 + 1/3ax^3 + 1/4bx^4 + 1/5cx^5 + \ldots \qquad (3.4.2)$$

Applying the virial theorem (Landau & Lifshitz, 2001a, 1980): $\frac{1}{2}<\frac{\partial E_{pot}}{\partial x} x> = <E_{kin}>$, we find for the expectation value of the kinetic energy:

$$<E_{kin}> = 1/2k<x^2>+1/2a<x^3>+1/2b<x^4>+1/2c<x^5>+\ldots, \qquad (3.4.3)$$

which is $k_BT/2$ at high temperatures – just like in the case of the ideal gas. Obvously from (3.4.2), the potential energy is:

$$<E_{pot}> = 1/2k<x^2>+1/3a<x^3>+1/4b<x^4>+1/5c<x^5>+\ldots, \qquad (3.4.4)$$

and the total vibrational energy is:

$$<E> = <E_{kin}> + <E_{pot}> = 2\frac{k_BT}{2} - (a/2-a/3)<x^3>-(b/2-b/4)<x^4>-(c/2-c/5)<x^5>-\ldots =$$

$$=k_BT -1/6a<x^3>-b/4<x^4>-3c/10<x^5>-\ldots \qquad (3.4.5)$$

To the lowest order,

$$<E> = k_BT -1/6a<x^3>, \qquad (3.4.6)$$

which should be $>k_BT$ since usually $a<0$ and $<x^3> > 0$. Obviously, the second term in (3.4.6) would be absent in the harmonic approximation, and we would recover the Dulong-Petit value of k_BT for the energy per mode at high temperatures.

Perhaps, the most spectacular failure of the harmonic approximation is its wrong conclusion that vibrational frequencies do not depend on temperature and pressure. To account for such experimentally observed strong dependences, one has to use more realistic interatomic potentials. The first approximation, combining the simplicity of the harmonic approximation and correcting its most serious errors, is the quasiharmonic approximation.

3.5. Quasiharmonic approximation (QHA).

In this approximation, it is assumed that the solid behaves like a harmonic solid at each volume, but the phonon frequencies depend on volume. It is assumed that they depend only on volume – i.e., heating at constant volume does not change the frequencies.

In the QHA phonon modes are still independent and non-interacting. Thermodynamic functions at constant volume, as before, are given by (3.2.7)-(3.2.10). Isochoric heat capacity C_V still cannot exceed $3n$R. Melting, diffusion, and dynamically disordered phases are beyond the scope of this approximation, which breaks down at high temperatures. Thermal conductivity is still infinite.

However crude, this approximation heals the biggest errors of the harmonic approximation. Introducing a volume dependence of the frequencies is enough to create non-zero thermal expansion and account for $C_V < C_p$ (*cf* 3.4.1). Thermal pressure contributes to all constant-pressure thermodynamic functions (enthalpy H, Gibbs free energy G, isobaric heat capacity C_p, etc.). This is the first approximation for the thermal equation of state of solids, which can be effectively used in conjunction with realistic interatomic potentials (Parker & Price, 1989; Kantorovich, 1995; Gale, 1998) or quantum-mechanical approaches (Baroni *et al.*, 1987, 2001; Karki *et al.*, 1999, 2000a,b). It leads to some fundamental results, which remain almost intact in more accurate theories. I shall concentrate on these issues later in this chapter.

3.6. Beyond the QHA: intrinsic anharmonicity.

At temperatures roughly below one half to two thirds of the melting temperature, QHA is quite accurate. Only at higher temperatures do its errors become significant. All the effects beyond the QHA are termed *intrinsic anharmonic effects*. To the lowest order, intrinsic anharmonic contribution to the free energy F_a is proportional

to T^2 (Zharkov & Kalinin, 1968; Gillet et al., 1999; Dorogokupets, 2000) at high temperatures:

$$F(V,T) = F_{qha}(V,T) + 3nk_B[\frac{1}{2}a(V)T^2+\ldots] \ , \qquad (3.6.1)$$

from which

$$E(V,T) = E_{qha}(V,T) - 3nk_B[\frac{1}{2}a(V)T^2+\ldots],$$

$$S(V,T) = S_{qha}(V,T) - 3nk_B[a(V)T+\ldots],$$

$$C_V(T)= C_{V,qha}(T) - 3nk_B[a(V)T+\ldots] \qquad (3.6.2)$$

The use of (3.6.1) and (3.6.2) is restricted to high temperatures only, because at low temperatures these equations will dramatically overestimate heat capacity (linear instead of T^3 temperature dependence) and lead to large errors in the entropy. An exponential term better describes the effects of intrinsic anharmonicity in the whole temperature range (Dorogokupets, 2001):

$$F(V,T) = F_{qha}(V,T) - 3nk_B[k(V)T\exp(-Q/T)+\ldots] \ , \qquad (3.6.3)$$

where k is a constant, and Q parameter equal to or exceeding the melting temperature. From (3.6.3) obtain:

$$E(V,T) = E_{qha}(V,T)+ 3nk_B[k(V)Q\exp(-Q/T)+\ldots] \ ,$$

$$S(V,T) = S_{qha}(V,T) + 3nk_B[k(V)(1+Q/T)\exp(-Q/T)+\ldots] \ ,$$

$$C_V(T)= C_{V,qha}(T) + 3nk_B[k(V)(Q/T)^2\exp(-Q/T)+\ldots] \qquad (3.6.4)$$

The exponential term is explicitly related to the premelting processes, involving atomic diffusion and formation of thermal defects. These processes are linked to melting in the Lennard-Jones and Devonshire model (Poirier, 2000), and are essentially anharmonic. The exponential expression for the intrinsic anharmonic effects leads to an excellent description of thermodynamic properties and thermal equation of state of NaCl (Dorogokupets, 2001) at temperatures between 10-20 K and the melting temperature.

One important consequence of intrinsic anharmonicity is that vibrational frequencies depend not only on the volume; identical volume changes, produced by changing pressure and temperature, result in different changes in the frequencies. This is clearly demonstrated by precise experiments (see, e.g., Gillet *et al.*, 2000; 1999) and computer simulations (Winkler & Dove, 1992). The intrinsic anharmonicity parameter of an i-th phonon mode at a wavevector **k** is given by:

$$a_{\mathbf{ik}} = \left(\frac{\partial \ln \omega_{ik}}{\partial T}\right)_V = \alpha(\gamma_{\mathbf{ik}}{}^T - \gamma_{\mathbf{ik}}{}^p), \qquad (3.6.5)$$

where α is the thermal expansion coefficient, and $\gamma_{\mathbf{ik}}{}^T$ and $\gamma_{\mathbf{ik}}{}^p$ are constant-temperature and constant-pressure mode Grüneisen parameters (see below), respectively. Intrinsic anharmonic parameters $a_{\mathbf{ik}}$ (3.6.5) are equal to the coefficients a previously used in the expressions (3.6.1) and (3.6.2) for the anharmonic thermodynamic properties (a expresses the total anharmonicity, while $a_{\mathbf{ik}}$ are the mode anharmonic parameters). Since these parameters are measurable, the anharmonic corrections can be directly evaluated from experiment. Soft modes are the most anharmonic ones (above the critical temperature they are essentially anharmonic), hence no wonder that thermodynamic functions of crystals near phase transitions have anomalously large anharmonic contributions.

The full anharmonic theory of thermodynamic properties of crystals is very complicated (for more details see Wallace, 1998); some details of phonon-phonon interactions and their influence on thermal conductivity can be found in (Elliott, 1998). Computationally, all intrinsic anharmonic effects can be fully accounted for by the use of Monte Carlo or molecular dynamics simulations (Allen & Tildesley, 1987): these methods involve a full sampling of the potential hypersurface without any assumptions regarding its shape or the magnitude of atomic vibrations; these methods are also applicable to liquids and gases. Free energies of significantly anharmonic systems can be calculated using thermodynamic integration technique (e.g., Allen & Tildesley, 1987; Alfé *et al.*, 1999, 2000). An approximate method for calculating anharmonic free energies was suggested by Wallace (1998) and used by P. Gillet and co-workers (e.g., 1999; 2000). As Wallace has shown using perturbation theory, the entropy S in the first approximation is given by the harmonic result (3.2.9) when the actual frequencies are used (i.e. not quasiharmonically extrapolated; one must take explicitly into account the temperature dependence of the frequencies – eq. (3.6.5)). Other thermodynamic properties follow from this: e.g., $C_V(V,T)=T(\partial S/\partial T)_V$; note that only for the entropy can the original harmonic expression be justified. Since the actual frequencies in this approach are anharmonically corrected, so are the entropy, all other thermodynamic properties, and the EOS.

We shall come back to anharmonic effects several times in this thesis. Now we turn to the discussion of the thermal equations of state of solids.

3.7. Equation of state (EOS) – general thermodynamic formulation.

An equation of state (i.e., the p-V-T relationship) is one of the most important characteristics of the Earth's materials. Indeed, accurate EOSs of minerals are necessary for the interpretation of seismological observations.

Generally, thermodynamics gives:

$p = -(\frac{\partial F}{\partial V})_T$ and $V = (\frac{\partial G}{\partial p})_T$ isothermal EOS

$T = (\frac{\partial H}{\partial S})_p$ and $S = -(\frac{\partial G}{\partial T})_p$ isobaric EOS

$p = -(\frac{\partial E}{\partial V})_S$ and $V = -(\frac{\partial H}{\partial p})_S$ adiabatic EOS

An explicit analytical EOS can only be written for an ideal gas (where interatomic interactions are absent: in this case there are no problems in the analytical representation of the interatomic potential, and entropy can be easily and exactly calculated using the Sackur-Tetrode relation). The classical ideal gas EOS is: $pV_m = RT$, where V_m is the molar volume.

For solids and liquids interatomic interactions are essential, and all existing analytical EOSs are by necessity approximate. Even worse, interactions between atoms make phase transitions possible, and EOS becomes discontinuous (i.e., non-analytical) at phase transitions. All the approximate EOS formulations are valid only for one phase, and generally the accuracy of the EOS is best at conditions far from phase transitions.

To advance further, consider the isothermal EOS: $p = -(\frac{\partial F}{\partial V})_T$, taking the QHA as the starting point. Using indices i and **k** to denote the number of the phonon branch and the wavevector **k**, we have:

$$F(T) = E_0 + \frac{1}{2}\sum_{i,\mathbf{k}} \hbar\omega_{i\mathbf{k}} + k_B T \sum_{i,\mathbf{k}} \ln\,[1-\exp(-\frac{\hbar\omega_{i\mathbf{k}}}{k_B T})]$$

and

$$p = -(\frac{\partial E_0}{\partial V})_T - \frac{1}{2}\sum_{i,\mathbf{k}} \hbar\,(\frac{\partial \omega_{i\mathbf{k}}}{\partial V})_T - k_B T \sum_{i,\mathbf{k}} (\frac{\partial(\ln[1-\exp(-\frac{\hbar\omega_{i\mathbf{k}}}{k_B T})])}{\partial V})_T \,, \qquad (3.7.1)$$

where the first term is the static (athermal) pressure, the second one counts the pressure of the zero-point vibrations; and the third term represents the pressure component associated with heating the crystal (thermal pressure). Simple

mathematical manipulations give the zero-point pressure $p_{zp} = -\frac{1}{2}\sum_{i,\mathbf{k}}\hbar(\frac{\partial\omega_{i\mathbf{k}}}{\partial V})_T = \frac{1}{2}\sum_{i,\mathbf{k}}\hbar\frac{\gamma_{i\mathbf{k}}\omega_{i\mathbf{k}}}{V} = <\gamma_{i\mathbf{k}}>E_{zp}/V$, where we defined the mode Grüneisen parameter $\gamma_{i\mathbf{k}} = -(\frac{\partial \ln\omega}{\partial \ln V})_T$ (in the QHA the constant-temperature and constant-pressure Grüneisen parameters are equal). For the third term in (3.7.1) we similarly have:

$$p_{th} = -k_B T\sum_{i,\mathbf{k}}(\frac{\partial(\ln[1-\exp(-\frac{\hbar\omega_{i\mathbf{k}}}{k_B T})])}{\partial V})_T = \sum_{i,\mathbf{k}}\frac{\gamma_{i\mathbf{k}}}{V}\frac{\hbar\omega_{i\mathbf{k}}}{\exp(\frac{\hbar\omega_{i\mathbf{k}}}{k_B T})-1} = \sum_{i,\mathbf{k}}\frac{\gamma_{i\mathbf{k}}E_{th,ik}}{V},$$

where $E_{th,i\mathbf{k}}$ denotes the mode contributions to the thermal energy.

The total pressure is then:

$$p(V,T) = p_{st}(V) + \frac{1}{2}\sum_{i,k}\hbar\frac{\gamma_{i\mathbf{k}}\omega_{i\mathbf{k}}}{V} + \sum_{i,\mathbf{k}}\frac{\gamma_{i\mathbf{k}}E_{th,ik}}{V} \qquad (3.7.2)$$

Defining average Grüneisen parameters, re-write eq. (3.7.2):

$$p(V,T) = p_{st}(V) + <\gamma_{i\mathbf{k}}(V)>E_{z.p.}(V)/V + \Gamma(V,T)E_{th}(V,T)/V \ , \qquad (3.7.3)$$

where $<\gamma_{i\mathbf{k}}>$ denotes the arithmetic average of the mode Grüneisen parameters $\gamma_{i\mathbf{k}}$, and Γ is the so called thermodynamic Grüneisen parameter defined as a weighted average of the mode Grüneisen parameters:

$$\Gamma = \frac{\sum_{i,\mathbf{k}}\gamma_{i\mathbf{k}}E_{th,i\mathbf{k}}}{\sum_{i,\mathbf{k}}E_{th,i\mathbf{k}}} = \frac{\sum_{i,\mathbf{k}}\gamma_{i\mathbf{k}}E_{th,i\mathbf{k}}}{E_{th}} = \frac{\sum_{i,\mathbf{k}}\gamma_{i\mathbf{k}}C_{V,i\mathbf{k}}}{\sum_{i,\mathbf{k}}C_{V,i\mathbf{k}}} = \frac{\sum_{i,\mathbf{k}}\gamma_{i\mathbf{k}}C_{V,i\mathbf{k}}}{C_V}, \qquad (3.7.4)$$

where $C_{V,i\mathbf{k}}$ is the contribution of the i-th mode (at the **k**-wavevector) to the total isochoric heat capacity (3.2.4).

From (3.7.3) and (3.7.4) one can derive thermal expansion:

$$\alpha = \Gamma\frac{C_V}{K_T V} \qquad (3.7.5)$$

Gathering the first two terms of (3.7.3), both describing the pressure at 0 K, and neglecting the temperature dependence of Γ, one obtains the famous Mie-Grüneisen thermal EOS:

$$p(V,T) = p_{0\,K}(V) + p_{th}(V,T) = p_{0\,K}(V) + \Gamma(V)E_{th}(V,T)/V \qquad (3.7.6)$$

Note from (3.7.4) that at high temperatures, where all phonons are practically fully excited, partial heat capacities $C_{V,i\mathbf{k}}$ of all the phonon modes are very close to their high-temperature limit (k_B), and (3.7.4) reduces to a constant high-temperature

limit, which is just an arithmetic mean over all mode Grüneisen parameters: $\Gamma \to \langle\gamma_{i\mathbf{k}}\rangle$.

In the classical approximation, which is put in the basis of the standard molecular dynamics and Monte Carlo simulations, thermodynamic Grüneisen parameter will always be close to $\langle\gamma_{i\mathbf{k}}\rangle$ (Welch et al., 1978), but also including a temperature-dependent correction due to intrinsic anharmonic effects. Generally, Γ is a function of not only volume, but also temperature – e.g. (3.7.4), where the weight of each $\gamma_{i\mathbf{k}}$ is given by the temperature-dependent $C_{V,i\mathbf{k}}$. Often Γ is a non-monotonic function of the temperature (Oganov *et al.*, 2000; Price *et al.*, 1987). However, temperature variations of Γ are usually small, rendering the original Mie-Grüneisen approximation that $\Gamma(V)$ is temperature-independent, rather accurate. The best value to be accepted as Γ is $\langle\gamma_{i\mathbf{k}}\rangle$, which is correct in the high-temperature limit, and which also appears in the expression (3.7.3) in the pressure of zero-point vibrations.

Setting $\Gamma = \langle\gamma_{i\mathbf{k}}\rangle = \gamma$, we can re-write the Mie-Grüneisen EOS as follows:

$$p(V,T) = p_{\text{stat}}(V) + \langle\gamma_{i\mathbf{k}}\rangle(V)E_{\text{vib}}(V,T)/V = p_{\text{stat}}(V) + \gamma(V)E_{\text{vib}}(V,T)/V \ , \qquad (3.7.7)$$

which is more convenient for computer simulations than (3.7.6) due to the explicit separation of the static pressure from the vibrational terms. Mie-Grüneisen EOS in form (3.7.6) or (3.7.7) is the basis of most studies of thermal EOSs of minerals. Despite being derived within the QHA, the Mie-Grüneisen EOS can be formulated at any level of theory. Generally speaking, (3.7.4) will become invalid due to a correction for intrinsic anharmonicity. For a general case it is convenient to define the Grüneisen parameter via phonon pressure:

$$\gamma = \frac{[p(V,T) - p_{\text{stat}}(V)]V}{E_{\text{vib}}} \qquad (3.7.8)$$

Thermodynamic Grüneisen parameter can be defined via thermal pressure or thermal expansion (cf. (3.7.5)):

$$\Gamma = \frac{[p(V,T) - p_{0\,\text{K}}(V)]V}{E_{\text{th}}} = \alpha K_T V/C_V \qquad (3.7.9)$$

The volume dependence of γ (or Γ) is usually described by a power law:

$$\gamma(V)=\gamma_0(V/V_0)^q \ , \qquad (3.7.10)$$

where parameter $q = \left(\frac{\partial \ln\gamma}{\partial \ln V}\right)_T$ is usually assumed to be constant, partly because of the experimental difficulties in estimating q (Shim & Duffy, 2000). In many studies, including mine (Oganov *et al.*, 2000), it was found that q varies strongly with

volume; Oganov *et al.* (2001a) proposed a more accurate form, which seems to be sufficient in the whole range of mantle pressures:

$$\gamma(V) = \gamma_0 (V/V_0)^{q_0+q_1 \ln(V/V_0)} \qquad (3.7.11)$$

In (3.7.8)-(3.7.11) the intrinsic anharmonic effects are included implicitly within the formalism derived within the QHA. Other approaches are possible.

Dorogokupets (2000, 2001) has proposed a model for fitting (and, possibly, extrapolating) thermodynamic functions and equations of state of minerals in a broad range of temperatures and pressures; in this model he explicitly separated quasiharmonic and intrinsically anharmonic terms. Added to the quasiharmonic thermal pressure from (3.7.8) (calculated with the quasiharmonic $E_{\rm th}$), is the anharmonic thermal pressure $p_{\rm a}=-(\frac{\partial F_{\rm a}}{\partial V})_{\rm T}$, where $F_{\rm a}$ is given by (3.6.1) or (3.6.3); this pressure can also be recast in the Mie-Grüneisen-like form $p_{\rm a}=\gamma_{\rm a}(V)E_{\rm a}(V,T)/V$.

Expressing the anharmonic corrections to thermodynamic properties by (3.6.1) and (3.6.2), i.e. making use of the approximate high-temperature result for each mode $F_{\rm a}(\omega,V,T) = \frac{1}{2} a_{\rm i}(V) k_{\rm B} T^2$, the anharmonic thermal pressure per mode is:

$$p_{\rm a} = -\frac{1}{2} m_{\rm i} a_{\rm i} k_{\rm B} T^2 / V \ , \qquad (3.7.12)$$

where $m_{\rm i}=(\frac{\partial \ln a_{\rm i}}{\partial \ln V})_{\rm T}$. This result implies that when intrinsic anharmonic parameters $a_{\rm i}$ are volume-independent, the anharmonic thermal pressure will be negligible.

So far I have considered in detail the general construction of a thermal EOS. It has not taken any analytical form yet. Various analytical formulations of the EOS are the topic of next section.

3.8. Analytical representations of the equation of state.

The material discussed in this section can be found in several literature sources. I mention here Poirier (1999, 2000), Poirier & Tarantola (1998), O.L. Anderson (1995), Holzapfel (1996), Sutton (1993), Cohen *et al.* (2000), Vinet *et al.* (1986, 1989), and Angel (2001). The latter document is the manual to the program EOSFIT, which I used for fitting pV-data to various EOSs.

Elasticity theory is used to construct the simplest EOSs. The simplest EOS is just the definition of the bulk modulus: $K_{\rm T}=-V(\partial p/\partial V)_{\rm T}$. This EOS is valid only in a very

narrow pressure range, because the bulk modulus K changes rapidly with pressure. The pressure variation of K is determined by the interatomic forces acting within the solid – these forces must be accounted for by accurate EOS formulations.

Assuming that K varies linearly with pressure and denoting $K_0' = (\partial K/\partial p)_{T,p=0}$, we obtain the Murnaghan EOS:

$$p = K_0/K_0'[(V/V_0)^{-K0'} - 1] \tag{3.8.1}$$

This simple EOS works well in the compression range $|(V-V_0)/V_0|<0.1$-0.2. At larger compressions higher-order derivatives of K become important. Of course, these non-linearities can be formally incorporated as well, resulting in a more complicated EOS. Better convergence is obtained if, instead of K as a function of pressure, we construct an approximate model for the energy as a function of $x=V_0/V$ or some other measure of strain. Using this method, some of the most popular EOSs are obtained – families of Birch-Murnaghan and logarithmic EOSs of different orders. Vinet EOS will follow from a general scaled interatomic potential.

Birch-Murnaghan EOSs. These EOSs are based on the polynomial expansion of the energy:

$$E=E_0+af^2+bf^3+cf^4+\ldots \tag{3.8.2}$$

in powers of the Eulerian strain f_E:

$$f_E = \tfrac{1}{2}[1-(V_0/V)^{2/3}] \tag{3.8.3}$$

It is advantageous to use the Eulerian finite strain rather than the Lagrangian strain:

$$f_L = \tfrac{1}{2}[(V/V_0)^{2/3}-1] , \tag{3.8.4}$$

because Eulerian strain leads to a better description of the correct $E(V)$ dependence with fewer terms in the expansion (3.8.2). At infinite pressure, Eulerian strain is infinite, whereas Lagrangian strain remains finite. However, for infinitesimal strains both definitions become equivalent, and

$$df_E = df_L = da/a_0 = -1/3(dV)/V_0 \tag{3.8.5}$$

It can be shown that generally

$$9V_0K_0 = (1/f)(\partial E/\partial f)_T \tag{3.8.6}$$

Truncating (3.8.2) on the second-order term:

$$E=E_0+af^2, \tag{3.8.7}$$

and, noting that

$$a=(9/2)K_0V_0, \tag{3.8.8}$$

it is easy to obtain (see Poirier, 2000) the second-order Birch-Murnaghan EOS:

$$p = 3K_0f(1+2f)^{5/2} \tag{3.8.9}$$

Or, in a different form:

$$p = (3/2)K_0[(V_0/V)^{7/3}-(V_0/V)^{5/3}] \quad (3.8.10)$$

$$E = E_0 + (9/8)K_0V_0[(V_0/V)^{2/3}-1]^2 \quad (3.8.11)$$

Third-order BM EOS is

$$p(V)=3/2K_0[(V_0/V)^{7/3}-(V_0/V)^{5/3}]\{1+\xi[(V_0/V)^{2/3}-1]\}, \quad (3.8.12)$$

$$E(V) = E(V_0) + \\ +3/2K_0V_0[3/2(\xi-1)(V_0/V)^{2/3}+3/4(1-2\xi)(V_0/V)^{4/3}+1/2\xi(V_0/V)^{6/3}-(2\xi-3)/4], \quad (3.8.13)$$

where $\xi=3/4(K_0'-4)$.

Note that when $K_0'=4$, the third-order Birch-Murnaghan EOS (BM3) automatically reduces to the second-order one (BM2). In other words, BM2 EOS implicitly assumes $K_0'=4$. It is remarkable that this estimate of the lowest order of the finite strain theory is often very close to experimental values of K_0' of many crystals (especially with close-packed structures). This is why BM2 EOS, although very simple, works well in many cases. The main problem of all BM EOSs is rather poor convergence with respect to the number of terms beyond the second order for large strains: it turns out that the fourth-order energy term in (3.8.2) is often larger than the third-order one. The third-order BM EOS is very accurate when K_0' is close to 4; when it is significantly different, this EOS gives poor results at high compressions. For $K_0'<4$ at large compressions (e.g., for $V/V_0\sim0.5$ and $K_0'=2$) BM3 can give even negative pressures (Poirier & Tarantola, 1998)! Being based on a polynomial expansion of the interatomic potential (of the type $\sum_{n=1,2,3,\ldots} a_n R^{-2n}$), this EOS must be used with caution when extrapolations are needed – outside the range of fitting the truncated polynomial expansion (3.8.2) may become invalid (Cohen *et al.*, 2000).

It is possible to derive systematically higher-order BM EOS, but this appears to be of little use since the number of parameters involved will be too large; only fourth-order BM EOS:

$$p = 3K_0f_E(1+2f_E)^{5/2}\{1+3/2(K_0'-4)f_E+3/2(K_0K_0''+(K_0'-4)(K_0'-3)+35/9)f_E^2\} \quad (3.8.14)$$

is sometimes used when ultra-high pressures are studied. This EOS is equivalent to the BM3 EOS when $K_0''=-1/K_0\{(3-K_0')(4-K_0')+35/9\}$ – the value implied by the BM3 EOS. BM4 EOS seems to be very accurate in a wide range of compressions – insofar as can be judged from the limited number of its applications available.

Logarithmic EOSs. Drawbacks of the Birch-Murnaghan EOSs leave much room for other possible EOSs. Poirier and Tarantola (1998) have derived the logarithmic EOS, based on the polynomial expansion (3.8.2) in terms of natural, or logarithmic (also called Hencky) strain:

$$f_H = \ln(l/l_0) = 1/3\ln(V/V_0), \quad (3.8.15)$$

where l is the length of the sample (l_0 in the unstrained sample). The second-order logarithmic EOS is:

$$p = K_0(V_0/V)\ln(V_0/V), \quad (3.8.16)$$

implicitly assuming K_0'=2. The third-order logarithmic EOS is:

$$p = K_0(V_0/V)[\ln(V_0/V)+1/2(K_0'-2)(\ln(V_0/V))^2], \quad (3.8.17)$$

which implicitly takes $K_0'' = -(1/K_0)[1+(K_0'-2)+(K_0'-2)^2]$. In the fourth order, the logarithmic EOS is:

$$p=K_0\frac{V_0}{V}\ln(\frac{V_0}{V})[1+\frac{1}{2}(K_0'-2)\ln(\frac{V_0}{V})+\frac{1}{6}\{1+K_0K_0''+(K_0'-2)+(K_0'-2)^2\}\ln^2(\frac{V_0}{V})] \quad (3.8.18)$$

For the instructive case of hcp-Fe, Vočadlo et al (2000) have shown that the third-order logarithmic EOS fits *ab initio* pV-data worse than third-order BM EOS (BM3) or third-order Vinet EOS. Fourth-order logarithmic EOS is superior to BM3, but involves more parameters. In the case of MgO examined in Table 1, the third-order logarithmic EOS also shows a very poor performance compared to BM3 or Vinet EOS. It can be expected that this EOS can work well in the rare cases where K_0'~2.

Logarithmic EOS corresponds to an unphysical interactomic potential of the type $\sum_{n=1,2,3,...} a_n(\ln R)^n$ (Cohen *et al.*, 2000). Even though it can be expanded as – $a/R+bR^{-3(K_0'-7)}$ (Poirier & Tarantola, 1998), one can note that the repulsion exponent is too small (5 for K_0'=4) compared to the usual values ~9-12. This is why, although based on a potentially powerful idea of the Hencky finite strain, the logarithmic EOS is not successful. Like the BM3 EOS, the logarithmic EOS has an unphysical behaviour on expansion (V/V_0>1): the potential corresponding to BM3 behaves non-monotonically, and the one corresponding to the logarithmic EOS diverges. Vinet EOS is the best choice of an EOS for solids – it combines simplicity, high accuracy, and universal applicability to solids with any character of chemical bonding, and up to extremely high compressions (at least compression by 2-3 times).

Vinet EOS (Vinet et al., 1986, 1989). This EOS, also known as the Universal EOS, is sometimes considered as one of the most impressive recent achievements of solid

state physics (Sutton, 1993). In fact, just like BM and logarithmic EOSs, Vinet EOS is a whole family of EOSs of different orders. The most remarkable feature is very fast convergence with respect to the order of EOS – one seldom needs to use higher than third order Vinet EOS.

The third-order Vinet EOS is:

$$p = 3K_0 \frac{1-(V/V_0)^{1/3}}{(V/V_0)^{2/3}} \exp[\frac{3}{2}(K_0^{'}-1)(1-(V/V_0)^{1/3}] , \quad (3.8.19)$$

$$E(V) = E(V_0) + \frac{4K_0V_0}{(K_0^{'}-1)^2} -$$

$$-2V_0K_0(K_0^{'}-1)^{-2}(5+3K_0^{'}\{(\frac{V_0}{V})^{1/3}-1\}-3(\frac{V_0}{V})^{1/3})\exp(-3/2(K_0^{'}-1)\{(\frac{V_0}{V})^{1/3}-1\})$$

(3.8.20)

The value of $K_0^{''}$ following is (Vinet *et al.*, 1989): $K_0^{''}=-1/K_0[(K_0^{'}/2)^2+(K_0^{'}/2)-19/36]$. The bulk modulus can be expressed as (Vinet *et al.*, 1989):

$$K=(K_0/(\frac{V_0}{V})^{2/3})[2-(\frac{V_0}{V})^{1/3}+\{(\frac{V_0}{V})^{1/3}-3/2(\frac{V_0}{V})^{2/3}(K_0^{'}-1)\}]\exp(\frac{3}{2}(K_0^{'}-1)\{1-(\frac{V_0}{V})^{1/3}\})$$

(3.8.21)

This EOS is based on a universal scaled binding curve:

$$E = E_0(1+a)\exp(-a), \quad (3.8.22)$$

where E_0 is the bond energy at equilibrium, $a=(R-R_0)/l$, $l=\sqrt{E_0/(\frac{\partial^2 E}{\partial R^2})}$ being a scaling length roughly measuring the width of the potential well, and R the Wigner-Seitz radius (the average radius of a sphere in the solid containing 1 atom). The potential (3.8.19) was first used in 1930s by Rydberg for fitting potential curves of molecules and obtaining their anharmonic coefficients; it turned out (see Sutton, 1993) that it describes very accurately systems with different types of chemical bonding in solids, molecules, adsorbates, etc. The Vinet EOS proved to be very accurate for fitting EOS of solid hydrogen (Loubeyre *et al.*, 1996; Cohen *et al.*, 2000) throughout the whole experimentally studied pressure range 0-120 GPa, roughly to the 8-fold compression. The universal binding curve (3.8.22), however, does not describe long-range forces in ionic and van der Waals crystals. This means that for such material Vinet EOS will not give accurate description of expansion ($V_0/V<1$). For compression, however, it should be sufficiently accurate, since compression behaviour is dominated by interatomic repulsion, well accounted for by (3.8.22).

In very rare cases a higher-order Vinet EOS may be needed; such higher-order versions of the Vinet EOS already exist (Vinet *et al.*, 1989); fourth-order Vinet EOS has been successfully applied to solid H_2 at extreme compressions (Cohen *et al.*, 2000) and has lead to significant improvements of the description of experimental *p-V* data. At extreme compressions (V/V_0<0.1), where solids approach the free electron regime, other EOSs are required (Cohen *et al.*, 2000). Such EOSs, manifesting the Thomas-Fermi behaviour at extreme compressions, are developed and discussed in detail by Holzapfel (1996) and Hama and Suito (1996); some discussion can also be found in (Cohen *et al.*, 2000).

Table 3-1 gives a summary of the EOSs discussed, while Table 3.2 gives a comparison of several EOSs fitted to theoretical data on MgO. Fits were performed in different pressure ranges. For a reliable (i.e., applicable for extrapolations) EOS, fitted parameters (V_0, K_0, and K_0') should be independent of the pressure range of fitting and consistent with zero-pressure values of these parameters. Zero-pressure unit cell volume was fixed in our fitting; K_0 and K_0' were determined from the independently calculated elastic constants at zero and other pressures. The best results can be obtained with the BM3 and Vinet EOS. For MgO BM3 slightly outperforms Vinet EOS. However, there are more examples of the dramatically opposite behaviour, and the overall performance of the Vinet EOS is better. Logarithmic EOS is unreliable. In a finite pressure range the values of the EOS parameters (especially K_0') can strongly depend on the EOS used. Note that as the pressure range of fitting tends to zero, all EOSs recover the correct zero-pressure parameters – the fastest convergence is for BM3 and Vinet EOSs. At small compressions all EOSs become equivalent.

Table 3-1. Summary of analytical equations of state.

Murnaghan EOS

EOS: $p = K_0/K_0'[x^{K0'} -1]$ $(x = V_0/V)$

Other relations: $K_0'' = 0$

Comments: valid for $0.9<x<1.1$

Birch-Murnaghan

BM2. EOS: $p = (3/2)K_0[x^{7/3}-x^{5/3}]$ $(x = V_0/V)$

Other relations: $E=E_0+ (9/8)K_0V_0[x^{2/3}-1]^2$

$K_0' = 4$

BM3. EOS: $p(V)=3/2K_0[x^{7/3}-x^{5/3}]\{1+\xi(x^{2/3}-1)\}$, $\xi=3/4(K_0'-4)$, $x = V_0/V$

Other relations: $E=E_0+3/2K_0V_0[3/2(\xi -1)x^{2/3}+3/4(1-2\xi)x^{4/3}+1/2\xi x^{6/3}-(2\xi-3)/4]$,

$K_0'' = -1/K_0\{(3-K_0')(4-K_0')+35/9\}$

Comments: usually accurate for x up to 1.5

BM4. Strain: $f_E = ½[(V_0/V)^{2/3}-1]$

EOS: $p = 3K_0f_E(1+2f_E)^{5/2}\{1+3/2(K_0'-4)f_E+3/2(K_0K_0''+(K_0'-4)(K_0'-3)+35/9)f_E^2\}$

Comments: accurate in a wide range of compressions (x up to 2-3)

Logarithmic

2nd order. EOS: $p = K_0x\ln x$ $(x = V_0/V)$

Other relations: $K_0' = 2$

Comments: very poor in most cases

3rd order. EOS: $p = K_0x[\ln x+1/2(K_0'-2)\ln^2 x]$ $(x = V_0/V)$

Other relations: $K_0'' = -(1/K_0)[1+(K_0'-2)+(K_0'-2)^2]$

Comments: worse than BM3

4th order. *EOS:* $p=K_0x\ln x[1+1/2(K_0'-2)\ln x+1/6(1+K_0K_0''+(K_0'-2)+(K_0'-2)^2)\ln^2 x]$

Comments: can be accurate in a wide range of compressions, but has too many parameters

Vinet

EOS: $p = 3K_0 \dfrac{1-x^{-1/3}}{x^{-2/3}} \exp[\dfrac{3}{2}(K_0'-1)(1-x^{-1/3})]$ $(x = V_0/V)$

Other relations:

$E(V) = E(V_0) + \dfrac{4K_0V_0}{(K'-1)^2} -2V_0K_0(K_0'-1)^{-2}(5+3K_0'\{x^{-1/3}-1\}-3x^{-1/3})\exp(-3/2(K_0'-1)\{x^{-1/3}-1\})$

$K=(K_0x^{2/3})[2-x^{-1/3}+\{x^{-1/3}-3/2x^{-2/3}(K_0'-1)\}]\exp(3/2(K_0'-1)\{1-x^{-1/3}\}$

$K_0'' = -1/K_0[(K_0'/2)^2+(K_0'/2)-19/36]$

Comments: universal, usually accurate for x up to at least 2-3.

Table 3-2. Analytical equations of state fitted to theoretical *p-V* data on periclase (MgO). Murnaghan, Birch-Murnaghan (2nd and 3rd order), logarithmic (3rd-order) and Vinet (3rd-order) EOS are listed. Zero-pressure volume V_0 was fixed at the theoretical value 77.64 Å^3. These data were obtained by pseudopotential plane wave calculations within the generalised gradient approximation (GGA). This table shows EOS parameters obtained for a pressure range 0-p_{max} with N data points. The last row gives independent calculations based on the elastic constants tensor at several pressures. The table shows that: 1)At small compressions, all EOS formulations become equivalent, 2)Only Vinet and BM3 give consistent parameters in the whole pressure range, 3) K_0' crtically depends on the EOS used – again, BM3 and Vinet give the best results.

p_{max} (N)	**MUR**		**BM2** (K_0'=4)	**BM3**		**Logarithmic third-order**		**Vinet**	
	K_0	K_0'	K_0	K_0	K_0'	K_0	K_0'	K_0	K_0'
165 GPa (12)	159.18	3.588	158.53	151.66	4.213	138.42	5.594	146.61	4.653
150 GPa (11)	158.66	3.605	158.13	151.79	4.208	140.02	5.477	147.25	4.624
105 GPa (8)	156.55	3.688	156.86	151.74	4.210	144.16	5.157	148.75	4.545
60 GPa (5)	154.70	3.788	155.29	152.12	4.186	148.43	4.781	150.67	4.416
30 GPa (3)	154.03	3.846	154.13	152.96	4.110	151.32	4.448	152.41	4.246
0 GPa	K_0=153.23 ; K_0'= 4.2±0.1 (from elastic constants)								

Since both K' and γ come from anharmonic interactions, an intriguing possibility arises to establish a general relation between these parameters. This possibility was widely discussed since 1939, when J. Slater suggested the first solution of the problem:

$$\gamma_s = \frac{1}{2}K' - \frac{1}{6} \qquad (3.8.23)$$

Later approaches resulted in very similar equations, the difference being in the value of the constant subtracted from ½ K': $^1/_2$, $^5/_6$, or 0.95. If any of the relations of the type (3.8.23) were accurate, it would greatly simplify the construction of thermal EOS. Although some linear correlation between γ and K' does exist, the correlation is too poor to be useful (Wallace, 1998). Vočadlo *et al.* (2000) have examined all approximate theories of this kind (for more details see Poirier, 2000), and confirmed the conclusion of Wallace (1998). Vočadlo *et al.* (2000) also found that pressure dependence of K' critically depends on which analytical EOS formulation is used.

3.9. EOS, internal strain, and phase transitions.

All the EOSs discussed in the previous section were based on the assumption that crystal structures compress uniformly, and there is no relaxation of the unit cell shape or atomic relaxation. For some solids (e.g., MgO) this is definitely true: there

are no internal degrees of freedom, and the unit cell shape is fixed by symmetry. For most crystals and all glasses, however, this is an approximation, sometimes crude. Effects of atomic relaxation (or, internal strain) lead to renormalized values of the EOS parameters within the fitting range – extrapolations outside this range can become risky. As emphasized by Angel and Ross (1996), all the classical EOSs are less successful for crystals with internal degrees of freedom. These EOSs perform particularly poorly in the vicinity of phase transitions.

Here I propose a simplified static model taking atomic relaxation into account and resulting in a simple additive correction. Lattice strains and thermal effects (ignored in the present model) can be systematically included in a similar way. Homogeneous compression leads to a configuration with atoms generally off their equilibrium positions. I denote these displacements Q_i to emphasize that they can be expressed via specific mode eigenvectors. Denoting the energy of the crystal without atomic relaxation as E_0, in the lowest order (i.e., in the harmonic approximation) the energy E with positional relaxation will be:

$$E = E_0 - \tfrac{1}{2}\sum_i k_i Q_i^2 ,$$

where k is the force constant. Recalling that for the static pressure $p = -(\frac{\partial E}{\partial V})$ we find

$$p(V) = -(\frac{\partial E_0}{\partial V}) + \tfrac{1}{2}\Sigma(\frac{\partial (k_i Q_i^2)}{\partial V}) =$$

$$= p_{\text{unrelaxed}}(V) + \Sigma k_i Q_i(\frac{\partial Q_i}{\partial V}) + \tfrac{1}{2}\Sigma Q_i^2(\frac{\partial k_i}{\partial V}) , \qquad (3.9.1)$$

where $p_{\text{unrelaxed}}$ is the pressure corresponding to the homogeneous compression.

To advance further, we need to introduce some approximations. First, let us represent Q as a linear function of volume and take the reference $Q_i=0$ at $V=V_0$. Then,

$$Q_i = -a_i(V-V_0) \qquad (3.9.2)$$

The volume derivative of the force constant k is related to the Grüneisen parameter, and we can write:

$$k_i = k_{0i}(V/V_0)^{2\gamma_i} \qquad (3.9.3)$$

$$(\frac{\partial k_i}{\partial V})_T = -2\gamma_i k_{0i}/V \qquad (3.9.4)$$

Substituting (3.9.2)-(3.9.4) into (3.9.1), we get:

$$p(V) = p_{\text{unrelaxed}}(V) + \Sigma a_i^2 k_{0i}[(V/V_0)^{2\gamma_i}(V-V_0) - \gamma_i/V(V-V_0)^2] \qquad (3.9.5)$$

or, neglecting the volume dependence of the force constant, a simplified formula:

$$p(V) = p_{\text{unrelaxed}}(V) + \sum a_i^2 k_{0i}(V - V_0) \qquad (3.9.6)$$

The term $p_{\text{unrelaxed}}(V)$ is well described by the conventional EOSs, e.g., Vinet EOS, whereas the total EOS is not necessarily so (see below). The bulk modulus $K = -V(\frac{\partial p}{\partial V})_T$ is always lowered by the relaxation effects, in the simplest approximation (3.9.6):

$$K(V) = K_{\text{unrelaxed}}(V) - \sum a_i^2 k_{0i} V\,, \qquad (3.9.7)$$

whereas K' is predicted to increase:

$$K'(V) = K'_{\text{unrelaxed}}(V) + \sum a_i^2 k_{0i} V/K = K'_{\text{unrelaxed}}(V) + (\delta K_{\text{unrelaxed}}(V))/K(V) \qquad (3.9.8)$$

This simple model explains qualitatively correctly the real effects of internal strain. Complex structures are usually relatively 'soft' and usually have large K_0' (often significantly exceeding 'normal' $K_0'=4$), in agreement with the prediction (3.9.8). E.g., quartz SiO_2, despite consisting of extremely rigid SiO_2 tetrahedra, has a very low bulk modulus $K_0 = 37.12$ GPa and high $K_0'=5.99$ (Angel *et al.*, 1997). This is because the structure is very flexible due to relaxation of the internal degrees of freedom. Perhaps, the highest known $K_0'=13$ was found in amphibole grunerite (Zhang *et al.*, 1992), whose structure has very many degrees of freedom.

Some new ideas spring from two series of calculations on sillimanite, Al_2SiO_5. Compression behaviour of this mineral is very interesting, and will be considered in detail in Chapter 9. Calculations were based on density functional theory within the generalised gradient approximation (GGA: Wang & Perdew, 1991); for more details see Chapters 5 and 9. In one series of calculations, all structural parameters were optimised to give the minimum-enthalpy structures for a number of pressures. This gives the correct EOS comparable to experiment; all effects of internal strains are included in this EOS. In the other series, I took the optimised zero-pressure structure, and calculated pressure, which would result from a simple isotropic scaling of the lattice (without atomic relaxation) at several volumes. This gives the unrelaxed EOS. The BM3 EOS parameters fitted to the $p(V)$ data are $V_0 = 339.57$ A^3 (fixed), K_0= 199.7 GPa (160 GPa), K_0'= 4.0 (2.7) for unrelaxed (relaxed) equations of state. In agreement with the prediction (3.9.7), the bulk modulus is lowered by relaxation. In the unrelaxed structure, fitting results in K_0'= 4.0 typical of crystals without internal degrees of freedom (e.g., close-packed oxides and metals). For the relaxed EOS K_0'= 2.7, but in fitting in a narrower pressure range, up to 15 GPa, $K_0'=3.7$ results. At

pressures up to 5 GPa, the EOS of sillimanite is well described by $K_0' = 4.25$[2]. The apparent failure of the prediction (3.9.8) at higher pressures is understandable: a soft longitudinal acoustic mode develops, leading to a volume collapse and an isosymmetric phase transition at p~38 GPa. This explains low K_0' (even negative near the transition) at higher pressures.

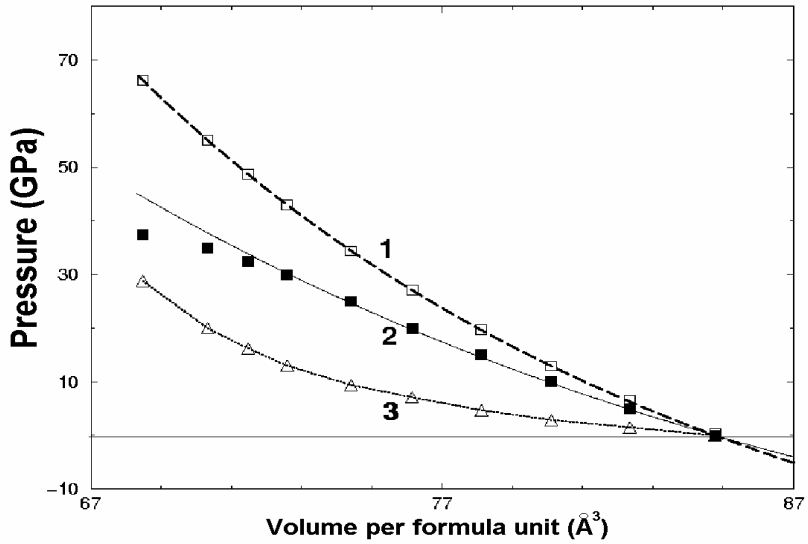

Figure 3-1. Effects of internal strains on equation of state. At the lowest volumes depicted, the structure is on the verge of an isosymmetric phase transition. 1 - unrelaxed EOS (symbols – calculated points; line – BM3 fit), 2 – correct EOS including relaxation (symbols – calculated points; line – BM3 fit for points outside the pre-transition region), 3 – the difference caused by relaxation. Note that in the pre-transition region the correct EOS is poorly fit, while the unrelaxed EOS is very well represented by BM3 throughout. Also note that the relaxational correction is very large.

It is well known that internal strains always soften elastic constants (e.g., Catti, 1989) and, in particular, the bulk modulus. In extreme cases (like the case of sillimanite), the softening can be complete, leading to a phase transition. In such cases the simplified model (3.9.6) is not sufficient. To study EOS in the vicinity of the phase transition, one needs to go beyond the harmonic approximation built in this model. It can be done using the Landau expansion of the internal energy in powers of Q including the full elastic constants tensor and allowed couplings of the order parameter and lattice strains.

[2] This value results from fitting BM3 EOS to theoretical pV-data with fixed zero-pressure volume. When this volume is fitted as well, K_0'= 3.35 is obtained, with a slight improvement of the EOS.

3.10. Elastic constants.

The importance of elastic constants for the Earth sciences springs from the fact that most of the information about the deep Earth is obtained seismologically, by measuring the velocities of seismic waves passing through the Earth. Seismic wave velocities, in their turn, are related to the bulk and shear moduli of the Earth-forming rocks and minerals forming these rocks. Acoustic anisotropy of the Earth, also measurable seismologically, is related to the elastic anisotropy of the Earth-forming minerals and the degree of their alignement caused, e.g., by convective flow. Knowing the full elastic constants tensors of Earth-forming minerals at relevant *p-T*-conditions, it is straightforward to calculate seismic wave velocities and estimate their anisotropy in the Earth. A number of excellent books and reviews exist; I would emphasize Nye (1998), Sirotin & Shaskolskaya (1975), Wallace (1998), Alexandrov & Prodaivoda (1993), Born & Huang (1954), Belikov *et al.* (1970), Barron & Klein (1965), Fedorov (1968).

Elastic constants characterise the ability of a material to deform under any small stresses. They can be described by a fourth-rank tensor C_{ijkl}, relating the second-rank stress tensor σ_{ij} to the (also second-rank) strain tensor e_{kl} via the generalised Hooke's law:

$$\sigma_{ij} = C_{ijkl} e_{kl} , \qquad (3.10.1)$$

where multiplication follows the rules of tensor multiplication (see Nye, 1998). Equation (3.10.1) can be simplified using the Voigt notation (Nye, 1998), which represents the fourth-rank tensor C_{ijkl} by a square 6*6 matrix C_{mn}. In these notations, indices '11', '22', '33', '12', '13', '23' are represented by only one symbol – 1, 2, 3, 6, 5, and 4, respectively. These notations significantly simplify all equations. So we write instead of (3.10.1):

$$\sigma_i = C_{ij} e_j \qquad (3.10.2)$$

Note that infinitesimal strains are being used; in this limit all definitions of strain (e.g., Eulerian, Lagrangian, Hencky, etc.) become equivalent. Under a small strain, the lattice vectors matrix a_{ij}' of the strained crystal is obtained from the old lattice matrix a_{ij}^0 and the strain tensor e_{ij} using the relation:

$$a_{ij}' = (\delta_{ij} + e_{ij}) a_{ij}^0 \quad . \qquad (3.10.3)$$

In the original tensor notation and in the Voigt notation (Nye, 1998), the $(\delta_{ij}+e_{ij})$ matrix is represented as follows:

$$\begin{pmatrix} 1+e_{11} & e_{12} & e_{13} \\ e_{12} & 1+e_{22} & e_{23} \\ e_{13} & e_{23} & 1+e_{33} \end{pmatrix} = \begin{pmatrix} 1+e_1 & +e_6/2 & e_5/2 \\ e_6/2 & 1+e_2 & e_4/2 \\ e_5/2 & +e_4/2 & 1+e_3 \end{pmatrix} \qquad (3.10.4)$$

Voigt notation allows one to write elastic constants conveniently as a symmetric 6*6 matrix. Voigt notation is adequate for most situations; for some cases, e.g., for a general transformation of the coordinate system, only the original fourth-rank tensor representation can be used to derive the transformed elastic constants.

The number of components of a fourth-rank tensor is 81; Voigt notation reduces this to 36. The thermodynamic equality C_{ij}=C_{ji} makes the 6*6 matrix of elastic constants symmetric relative to its main diagonal. This reduces the number of independent elastic constants to the well-known maximum number: 21, possessed by triclinic crystals. Symmetry results in further reductions of this number: 13 for monoclinic, 9 for orthorhombic, 6 or 7 (depending on the point group symmetry) for trigonal and tetragonal, 5 for hexagonal, and 3 for cubic crystals; for isotropic (amorphous) solids there are only 2 independent elastic constants. Elastic constants and their anisotropy are closely related to crystal structures. E.g., for andalusite and sillimanite (Al_2SiO_5) this relation was clearly demonstrated by Vaughan & Weidner (1978).

One can define the inverse tensor S_{ijkl} (or, in Voigt notations, S_{ij} [3]), often called the elastic compliance tensor:

$$\{S_{ijkl}\} = \{C_{ijkl}\}^{-1} \text{ or } \{S_{ij}\} = \{C_{ij}\}^{-1} \qquad (3.10.5)$$

For an orthorhombic crystal, this matrix inversion leads to the following explicit relations between C_{ij} and S_{ij} (Belikov *et al.*, 1970):

$$S_{11} = (C_{22}C_{33} - C^2_{23})/D$$
$$S_{22} = (C_{11}C_{33} - C^2_{13})/D$$
$$S_{33} = (C_{11}C_{22} - C^2_{12})/D$$
$$S_{44} = 1/C_{44}$$
$$S_{55} = 1/C_{55}$$
$$S_{66} = 1/C_{66}$$
$$S_{12} = -(C_{12}C_{33} - C_{13}C_{23})/D$$
$$S_{13} = (C_{12}C_{23} - C_{13}C_{22})/D$$

[3] Note that in Voigt notation $C_{ijkl} = C_{mn}$, but $S_{ijkl} = S_{mn}$ only when m and n = 1,2, or 3; when either m or n = 4,5, or 6: $2S_{ijkl} = S_{mn}$; when both m and n = 4,5, or 6: $4S_{ijkl} = S_{mn}$ (Nye, 1998).

$$S_{23} = -(C_{11}C_{23} - C_{13}C_{12})/\mathrm{D}\,, \qquad (3.10.6)$$

where $\mathrm{D} = C_{11}C_{22}C_{33} + 2C_{12}C_{13}C_{23} - C^2_{23}C_{11} - C^2_{12}C_{33} - C^2_{13}C_{22}$. Relations (3.10.6) are automatically valid for tetragonal and cubic crystals.

The S_{ij} tensor can be defined via the generalised Hooke's law in its equivalent formulation:

$$e_i = S_{ij}\sigma_j \qquad (3.10.7)$$

Linear compressibilities can be easily derived from the S_{ij} tensor. Full expressions for an arbitrary direction in a triclinic crystal can be found in Nye (1998); along the coordinate axes linear compressibilities are:

$$s_x = -\frac{1}{a}\left(\frac{\partial a}{\partial p}\right)_T = \sum_{j=1}^{3} S_{1j} = S_{11} + S_{12} + S_{13}$$

$$s_y = -\frac{1}{b}\left(\frac{\partial b}{\partial p}\right)_T = \sum_{j=1}^{3} S_{2j} = S_{22} + S_{12} + S_{23}$$

$$s_z = -\frac{1}{c}\left(\frac{\partial c}{\partial p}\right)_T = \sum_{j=1}^{3} S_{3j} = S_{33} + S_{13} + S_{23}\,, \qquad (3.10.8)$$

where *a, b, c* are linear dimensions along the axes of the coordinate system[4]. For the bulk compressibility have:

$$\beta = -\frac{1}{V}\left(\frac{\partial V}{\partial p}\right)_T = s_x + s_y + s_z = \sum_{j=1}^{3}\sum_{j=1}^{3} S_{ij} = S_{11} + S_{22} + S_{33} + 2(S_{12} + S_{13} + S_{23}), \qquad (3.10.9)$$

where V is the volume (e.g., unit cell volume).

The values of the elastic constants depend on the orientation of the coordinate system. There are two particularly important invariants of the elastic constants tensor – bulk modulus K and shear modulus G. These invariants are obtained by special averaging of the individual elastic constants. There are several different schemes of such averaging. Reuss averaging is based on the assumption of a homogeneous stress throughout the crystal. This leads to the Reuss bulk modulus:

$$K_R = \{S_{11} + S_{22} + S_{33} + 2(S_{12} + S_{13} + S_{23})\}^{-1} = \frac{1}{\beta} \qquad (3.10.10)$$

and shear modulus:

$$G_R = 15\{4(S_{11} + S_{22} + S_{33}) - 4(S_{12} + S_{13} + S_{23}) + 3(S_{44} + S_{55} + S_{66})\}^{-1} \qquad (3.10.11)$$

[4] These axes may not coincide with the lattice vectors for non-orthogonal crystal systems. Coordinate systems used in crystal physics are always orthogonal, on the other hand.

Expressions (3.10.7-3.10.11) are valid for crystals of any symmetry (Nye, 1998). It is important to realise that it is the Reuss bulk modulus, explicitly related to compressibility, which is used in constructing EOSs. This is also the modulus appearing in all thermodynamic equations involving the bulk modulus.

Another popular scheme of averaging is due to Voigt. It is based on the assumption of a spatially homogeneous strain, and leads to the following expressions for the Voigt bulk and shear moduli:

$$K_V = \frac{1}{9}\{C_{11} + C_{22} + C_{33} + 2(C_{12} + C_{13} + C_{23})\} \quad (3.10.12)$$

$$G_V = \frac{1}{15}\{C_{11} + C_{22} + C_{33} - (C_{12} + C_{13} + C_{23}) + 3(C_{44} + C_{55} + C_{66})\} \quad (3.10.13)$$

These equations are also general, valid for crystals of any symmetry. For an isotropic polycrystalline aggregate Voigt moduli give upper, and Reuss moduli lower bounds for the corresponding moduli. More accurate estimates can be obtained from Voigt-Reuss-Hill averages:

$$K_{VRH} = 1/2(K_V + K_R)$$
$$G_{VRH} = 1/2(G_V + G_R) \quad (3.10.14)$$

The most accurate results (and tighter bounds) are given by Hashin-Shtrikman variational scheme, which is much more complicated, but leads to results similar to the Voigt-Reuss-Hill scheme.

There are two groups of experimental methods of measurement of the elastic constants - 1) static and low-frequency methods (based on determination of stress-strain relations for static stresses) and 2) high-frequency, or dynamic, methods (e.g., ultrasonic methods, Brillouin spectroscopy, etc.). Static methods are not used anymore, because of their poor accuracy. Experiments are very complicated and require high-quality samples; experimental uncertainties until recently were very large, even for high-frequency measurements often 10-15% and up to 30% in some cases (Alexandrov & Prodaivoda, 1993). During the last decade the typical uncertainty of high-level experiments was reduced to a few percent.

Static measurements yield isothermal elastic constants (timescale of the experiment allows thermal equilibrium to be attained within the sample), high-frequency measurements give adiabatic constants (Belikov *et al.*, 1970). The difference is entirely due to anharmonic effects (see below) and vanishes at 0 K. Adiabatic C_{ij} are larger, usually by a few percent. The following thermodynamic equation gives the difference in terms of thermal pressure tensor b_{ij} (Wallace, 1998):

$$C_{ijkl}{}^{S} = C_{ijkl}{}^{T} + (TV/C_V)b_{ij}b_{kl}\,, \qquad (3.10.15)$$

where $b_{ij}=(\partial\sigma_{ij}/\partial T)_V$ is related to the thermal expansion tensor. Equation (3.10.13) implies for the bulk moduli:

$$K_S = K_T(1+\alpha\gamma T) = K_T(1+\alpha^2 K_T V/C_V), \qquad \text{[compare with (3.4.1)]} \qquad (3.10.16)$$

where α and γ are the thermal expansion and Grüneisen parameter, respectively. Adiabatic and isothermal shear moduli are strictly equal for cubic crystals and usually practically indistinguishable for crystals of other symmetries.

Acoustic wave velocities measured in seismological experiments and ultrasonic determinations of elastic constants are related to the adiabatic elastic constants. Isothermal constants, on the other hand, are related to the compressibility and EOS.

The general equation for the calculation of velocities of acoustic waves with an arbitrary propagation direction, the Christoffel equation (Sirotin & Shaskolskaya, 1975), is:

$$C_{ijkl}{}^{S} m_j m_k p_l = \rho v^2 p_i \quad , \qquad (3.10.17)$$

where p is the polarisation vector of the wave (of unit length), m unit vector parallel to the wave vector, and ρ the density of the crystal. It can be also represented in a form of a secular equation:

$$\det\|C_{ijkl}{}^{S} m_j m_k - \rho v^2 \delta_{il}\| = 0 \qquad (3.10.18)$$

There are 3 acoustic modes – 1 longitudinal (or compressional) and 2 shear ones. Their average velocities are given by famous equations (Belikov *et al.*, 1970):

$$V_P = \sqrt{\frac{3K+4G}{3\rho}} \qquad (3.10.19)$$

and

$$V_S = \sqrt{\frac{G}{\rho}}\,, \qquad (3.10.20)$$

where the adiabatic Voigt-Reuss-Hill (or Hashin-Shtrikman) values are used for the bulk and shear moduli.

The energy change (per unit volume) due to a deformation can be described by the adiabatic elastic constants:

$$\Delta E/V = \tfrac{1}{2}\, C_{ijkl}{}^{S} e_{ij} e_{kl} \qquad (3.10.21)$$

An analogous relation exists between the Helmholtz free energy and isothermal constants:

$$\Delta F/V = \tfrac{1}{2}\, C_{ijkl}{}^{T} e_{ij} e_{kl} \qquad (3.10.22)$$

These relations enable the calculation of elastic constants via the second derivatives of thermodynamic potentials at zero pressure.

It is well known (Barron & Klein, 1965; Wallace, 1998) that under non-zero stresses there can be several different definitions of elastic constants. Consider a solid at a non-zero initial hydrostatic pressure. For the stress tensor we have:

$$\sigma_{ij} = -p\delta_{ij} + C_{ijkl}e_{kl} \tag{3.10.23}$$

Instead of the zero-stress equation (3.10.21), the energy density becomes:

$$\Delta E/V = -pe_{ii} + \tfrac{1}{2}[C_{ijkl}{}^{S} - p/2(2\delta_{ij}\delta_{kl} - \delta_{il}\delta_{jk} - \delta_{jl}\delta_{ik})]e_{ij}e_{kl} - p/2\,\omega_{ik}\omega_{ik}\ , \tag{3.10.24}$$

where ω_{ik} corresponds to a pure rotation of the crystal (rotation tensor), while e_{ij} corresponds to a pure strain. This gives (Barron & Klein, 1965) in the case of a hydrostatic pressure:

$$C_{ijkl}{}^{S} = \frac{1}{V}\left(\frac{\partial^2 E}{\partial e_{ij}\partial e_{kl}}\right)_S + p/2(2\delta_{ij}\delta_{kl} - \delta_{il}\delta_{jk} - \delta_{jl}\delta_{ik}) \tag{3.10.25a}$$

$$C_{ijkl}{}^{T} = \frac{1}{V}\left(\frac{\partial^2 F}{\partial e_{ij}\partial e_{kl}}\right)_T + p/2(2\delta_{ij}\delta_{kl} - \delta_{il}\delta_{jk} - \delta_{jl}\delta_{ik}), \tag{3.10.25b}$$

Calculating the second derivatives with respect to the finite Lagrangian strains η_{ij}, different equations are obtained (Wallace, 1998) for the case of hydrostatic pressure:

$$C_{ijkl}{}^{S} = \frac{1}{V}\left(\frac{\partial^2 E}{\partial \eta_{ij}\partial \eta_{kl}}\right)_S + p(\delta_{ij}\delta_{kl} - \delta_{il}\delta_{jk} - \delta_{jl}\delta_{ik}) \tag{3.10.26a}$$

$$C_{ijkl}{}^{T} = \frac{1}{V}\left(\frac{\partial^2 F}{\partial \eta_{ij}\partial \eta_{kl}}\right)_T + p(\delta_{ij}\delta_{kl} - \delta_{il}\delta_{jk} - \delta_{jl}\delta_{ik}) \tag{3.10.26a}$$

For a general stress the analogous equations are:

$$C_{ijkl}{}^{S} = \frac{1}{V}\left(\frac{\partial^2 E}{\partial \eta_{ij}\partial \eta_{kl}}\right)_S - 1/2(2\sigma_{ij}\delta_{kl} - \sigma_{ik}\delta_{jl} - \sigma_{il}\delta_{jk} - \sigma_{jl}\delta_{ik} - \sigma_{jk}\delta_{il}) \tag{3.10.27a}$$

$$C_{ijkl}{}^{T} = \frac{1}{V}\left(\frac{\partial^2 F}{\partial \eta_{ij}\partial \eta_{kl}}\right)_T - 1/2(2\sigma_{ij}\delta_{kl} - \sigma_{ik}\delta_{jl} - \sigma_{il}\delta_{jk} - \sigma_{jl}\delta_{ik} - \sigma_{jk}\delta_{il}) \tag{3.10.27b}$$

Equations (3.10.26-27) are particularly important, because many simulation packages define the elastic constants as:

$$c_{ijkl}{}^{S} = \frac{1}{V}\left(\frac{\partial^2 E}{\partial \eta_{ij}\partial \eta_{kl}}\right)_S \tag{3.10.28}$$

even at non-zero stresses. Details of such calculations will be given in Chapter 5. This definition is equivalent to the definition via stress-strain relations only at the zero stress. However, the definition based on stress-strain relations is the most useful one: it is directly related to the mechanical stability criteria, acoustic wave velocities,

and Debye temperature. Cauchy relations, originally derived with the definition via the energy density, can be elegantly formulated in this definition as well (see below). Note, however, that the elastic constants C_{ijkl}, defined from stress-strain relations, have the full Voigt symmetry only at hydrostatic pressure. It is essential to distinguish between different definitions of elastic constants and keep in mind the equations (3.10.26-27). Corrections due to temperature will be discussed in the end of this chapter.

3.11. Cauchy relations.

For crystals where all atoms occupy centrosymmetric positions, and where all interatomic interactions are central and pairwise (i.e., depend only on the distances between atoms, and not on angles), in the static limit Cauchy relations (Born & Huang, 1954; but take into account eq. 3.10.25) hold:

$$C_{23}\text{-}C_{44} = 2p \;\; ; \;\; C_{31}\text{-}C_{55} = 2p \;\; ; \;\; C_{12}\text{-}C_{66} = 2p$$
$$C_{14}\text{-}C_{56} = 0 \;\; ; \;\; C_{25}\text{-}C_{64} = 0 \;\; ; \;\; C_{36}\text{-}C_{45} = 0 \qquad (3.11.1)$$

These relations would reduce the maximum number of independent elastic constants to 15; however, these relations never hold exactly because there are always non-central and many-body contributions to crystal energy. Violations of the Cauchy relations can serve as a useful indicator of the importance of such interactions. While for many alkali halides Cauchy relations hold reasonably well, for alkali earth oxides, also considered as classical ionic solids, Cauchy relations are grossly violated. This is because the free O^{2-} ion is unstable and can exist only in the crystalline environment due to the stabilising Madelung potential created by all atoms in the crystal; the charge density around O^{2-} is thus very susceptible to the changes of structure, including strains. Consequently, interactions of the O^{2-} ion with any other ion depend on the volume of the crystal and location of all other ions; this is a major source of many-body effects in ionic solids. This point of view is strongly supported by the success of models such as PIB (Potential Induced Breathing; see Bukowinski, 1994, and references therein), where the size of the atom depends on its Madelung potential, in reproducing the observed Cauchy violations.

3.12. Mechanical stability.

One of the most common types of instabilities occuring in crystals is the so called mechanical instability, when one or more elastic constants (or their special

combinations) tend to zero. The condition of mechanical stability is the positive definiteness of the elastic constants matrix:

$$\begin{array}{|cccccc|} C_{11} & C_{12} & C_{13} & C_{14} & C_{15} & C_{16} \\ C_{21} & C_{22} & C_{23} & C_{24} & C_{25} & C_{26} \\ C_{31} & C_{32} & C_{33} & C_{34} & C_{35} & C_{36} \\ C_{41} & C_{42} & C_{43} & C_{44} & C_{45} & C_{46} \\ C_{51} & C_{52} & C_{53} & C_{54} & C_{55} & C_{56} \\ C_{61} & C_{62} & C_{63} & C_{64} & C_{65} & C_{66} \end{array}$$

This is equivalent to positiveness of all the principal minors of this matrix (principal minors are square sub-matrices symmetrical with respect to the main diagonal – they are indicated by dashed lines in the scheme above). All diagonal elastic constants C_{ii} are principal minors, and, therefore, must be positive for all stable crystals. Dynamical stability criteria were first suggested by Born and Huang (1954) and are sometimes called Born conditions. In general form they are analysed in detail in (Sirotin & Shaskolskaya, 1982; Fedorov, 1968). For crystals of different symmetries these conditions were thoroughly analysed by (Cowley, 1976; Terhune *et al.,* 1985). Mechanical stability criteria for crystals under stress must employ the C_{ij} derived from the stress-strain relations (Wang *et al.*, 1993; 1995; Karki, 1997). Violation of any of the mechanical stability conditions leads to softening of an acoustic mode in the vicinity of the Γ-point, inducing a ferroelastic phase transition.

3.13. Birch's law and effects of temperature on elastic constants.

The famous Birch's law (Poirier, 2000) states that compressional sound velocities depend only on the composition and density of the material:

$$V_P = a(\bar{M}) + b\rho, \qquad (3.13.1)$$

where $\bar{M}$ is the average atomic mass, a and b constants, ρ the density. E.g., for the mantle materials (average atomic mass between 20 and 22):

$$V_P = -1.87 + 3.05\rho \qquad (3.13.2)$$

Similar relations are true for the bulk sound velocity $V_\Phi = \sqrt{\frac{K}{\rho}}$; for mantle compositions:

$$V_\Phi = -1.75 + 2.36\rho \qquad (3.13.3)$$

Birch's law implies that for a given material at constant volume, the elastic constants are temperature-independent. This can be accepted only as a first (strictly harmonic) approximation. All the deviations from Birch's law are due to anharmonicity – we can distinguish between quasiharmonic and intrinsically anharmonic contributions. These contributions to the bulk modulus can be represented (Dorogokupets, 2000) as additive corrections to the zero-temperature result:

$$K^T(V,T) = K_{0\,K}(V) + \Delta K^T_{qha}(V,T) + \Delta K^T_a(V,T), \qquad (3.13.4)$$

$$\Delta K^T_{qha}(V,T) = p_{th,qha}(1+\gamma-q) - \gamma^2 T C_V/V, \qquad (3.13.5)$$

$$\Delta K^T_a(V,T) = p_a(1+\gamma_a-q_a)\,, \qquad (3.13.6)$$

where $p_a = \gamma_a E_a/V$ and $q_a = (\frac{\partial \ln \gamma_a}{\partial \ln V})_T$. For the adiabatic bulk modulus due to the relation (3.10.16):

$$K^S(V,T) = K_{0\,K}(V) + p_{th,qha}(1+\gamma-q) + p_a(1+\gamma_a-q_a) \qquad (3.13.7)$$

These results can be generalised for the individual elastic constants. For the stress tensor we have:

$$\sigma_{ij} = -p\delta_{ij} + C^0_{ijkl}e_{kl} - \gamma_{ij}E_{vib}/V\ , \qquad (3.13.8)$$

where the first term represents the initial hydrostatic pressure, the second term contribution from zero-temperature elastic constants and strain, the third term – thermal stress. For the isothermal elastic constants we obtain in the QHA:

$$C^T_{ijkl}(V,T) = (\partial\sigma_{ij}/\partial e_{kl})_T =$$

$$= C^0_{ijkl}(V) - 1/V^2[(\partial\gamma_{ij}/\partial e_{kl})_T E_{vib}V + (\partial E_{vib}/\partial e_{kl})_T\gamma_{ij}V - \gamma_{ij}E_{vib}(\partial V/\partial e_{kl})_T] \qquad (3.13.9)$$

Taking into account that $dV = Vde_{kl}\delta_{kl}$ and $dE_{vib} = -(\gamma_{kl}E_{vib}/V - \gamma_{kl}TC_V/V)Vde_{kl}$, we get:

$$C^T_{ijkl}(V,T) = C^0_{ijkl}(V) - \frac{\partial\gamma_{ij}}{\partial e_{kl}}E_{vib}/V + (\gamma_{kl}E_{vib}/V - \gamma_{kl}TC_V/V)\gamma_{ij} + (\gamma_{ij}E_{vib}/V)\delta_{kl} =$$

$$= C^0_{ijkl}(V) + (\gamma_{ij}E_{vib}/V)[\delta_{kl}+\gamma_{kl}-\frac{1}{\gamma_{ij}}\frac{\partial\gamma_{ij}}{\partial e_{kl}}] - \gamma_{ij}\gamma_{kl}TC_V/V \qquad (3.13.10)$$

It can be shown [*cf.* eq. (3.10.13)] that for the shear modulus the quasiharmonic temperature correction is zero for a cubic crystal and very small for other crystals. This is understandable, since there is no first-order volume change associated with shear strains. The shear modulus then takes the form:

$$G^T(V,T) = G_{0\,K}(V) + \Delta G_a(V,T)\,, \qquad (3.13.12)$$

where $\Delta G_a(V,T)$ is the intrinsic anharmonic contriution to the shear modulus. Often this correction is large.

Garber and Granato (1975), differentiating the free energy expressed as a sum of mode contributions (3.2.6) over the whole Brillouin zone:

$$F = E_{st} + \frac{1}{2}\sum_{i,\mathbf{k}} \hbar\,\omega_{i\mathbf{k}} + \sum_{i,\mathbf{k}} k_B\,T\ln[1-\exp(-\frac{\hbar\omega_{i\mathbf{k}}}{k_B T})] \quad , \qquad (3.13.13)$$

obtained the following result:

$$\frac{1}{V}(\frac{\partial^2 F}{\partial\eta_{ij}\partial\eta_{kl}})_V = \frac{1}{V}(\frac{\partial^2 E_{st}}{\partial\eta_{ij}\partial\eta_{kl}})_V + \frac{1}{V}\sum_{i,\mathbf{k}}[(\gamma_{ij}^{i\mathbf{k}}\,\gamma_{kl}^{i\mathbf{k}} - \frac{\partial\gamma_{ij}}{\partial\eta_{kl}})E_{vib,i\mathbf{k}} - \gamma_{ij}^{i\mathbf{k}}\,\gamma_{kl}^{i\mathbf{k}}\,C_{V,i\mathbf{k}}T] \quad (3.13.14)$$

The next chapter gives an introduction to phase transitions. Some of the most important theoretical results and general ideas will be presented there. Crystal thermodynamics and elasticity, considered in this chapter, are among the key areas of interest in the study of phase transitions.

Chapter 4. Phase transitions.

The study of phase transitions is of a central importance to modern crystallography, condensed matter physics and chemistry. Spectacular evolution of facts, ideas and theories, and technological applications of phase transitions during the last 50 years has made phase transitions one of the most popular topics in condensed matter physics. Much attention was recently paid to metastable phenomena, due to their practical importance and poor theoretical understanding. Phase transitions are a major factor determining the seismic structure of the Earth (see Chapter 2) and thus play a special role in geophysics. In this Chapter I give a brief review of the theory and classification of phase transitions. Various aspects of phase transitions will be seen throughout this thesis, especially in Chapter 9.

4.1. Classifications of phase transitions.

Perhaps the first sound classification of phase transitions was proposed by Ehrenfest in 1933 (for a detailed historical and scientific discussion see Jaeger, 1998). This purely thermodynamic classification distinguished between first-, second-, and higher-order phase transitions. For the *first*-order transitions the *first* derivatives of the free energy with respect to p and T (i.e., volume and entropy) are discontinuous at the transition point; for *second*-order transitions the *second* derivatives (compressibility and thermal expansion) are discontinuous, and so forth. Third- and higher-order transitions, though theoretically possible, so far have never been reported. More modern variants of the Ehrenfest classification distinguish only between 'first-order' and 'continuous' (i.e., all higher-order) transitions. In some cases, the order of the same phase transition is different at different p-T conditions. As we will see, isosymmetric transitions must be first order, but become completely continuous (infinite-order) transitions at and above the critical temperature. Some transitions change from first- to second-order; the crossover point is called the tricritical point. Among the examples of systems with tricritical crossover are NH_4Cl (Garland & Weiner, 1971), zone-centre cubic-tetragonal transition in $BaTiO_3$ perovskite, possibly the transition from calcite to metastable calcite (II) in $CaCO_3$ (see Hatch & Merrill, 1981), and, possibly, the α-β transition in quartz (SiO_2). For example, the order-disorder transition in NH_4Cl from a phase with a complete orientational disordering of the NH_4-group ($Pm\bar{3}m$) to an ordered phase ($P4\bar{3}m$) is

first-order at 1 atm and 242 K, but becomes second-order at the tricritical point, 0.15 GPa and 256 K.

Therefore, the order of the transition is not something fundamentally inherent to the transition. The Ehrenfest classification, however useful (it is still being widely used as a standard classification), attempts to describe only thermodynamics of phase transitions without linking it to any structural mechanisms or symmetry aspects of transitions. However, it is the structure and symmetry relations between the phases, which are the most fundamental invariant characteristic of any phase transition.

The first structural classification was due to Buerger (1961), who, instead of thermodynamics, used the intuitive language of structural schemes. First of all, he distinguished two main types of phase transitions – those with and without changes of the first coordination number. Each of these types was further classified into reconstructive (i.e., requiring formation/breaking of bonds), displacive, order-disorder, electronic, etc. transitions. *Displacive* phase transitions are accompanied by small atomic displacements (hence the name), which usually destroy some elements of symmetry. These displacement patterns are determined by the eigenvectors of one or more normal modes – the so-called soft modes. *Order-disorder* transitions occur between a low-temperature structurally ordered (e.g., having positional order in cation distribution and orientational order of atomic groups) and a high-temperature disordered phase. *Electronic* transitions are accompanied by a change of the electronic or magnetic structure and/or valence state of atoms in the structure; the structure type may or may not change in this process. *Reconstructive* phase transitions, by Buerger's definition, involve breaking/formation of at least some bonds. These transitions are always first order, involve a latent heat, and require an activation energy for bond breaking. In systems with typical reconstructive transitions, due to kinetics, phases can exist as metastable outside their stability fields. Order-disorder and displacive transitions can in principle be of any order. A modification of Buerger's classification was proposed by Urusov (1987).

The beauty of the Buerger classification is that, even though based on purely structural considerations, it naturally gives some insight into thermodynamics and kinetics of phase transitions. Its weakness is in the absence of a precisely formulated quantitative basis. Formation/breaking of bonds is one of the main criteria. However, there is no rigorous physical definition of a chemical bond in a many-atom system. In many practical cases it is very difficult to say whether or not two atoms in a given structure are linked by a bond or determine the coordination number of an atom in a

crystal[5]. This question is still an area of active research. In addition to this fundamental weakness, Buerger's classification does not discuss symmetry aspects of transitions.

It was first realised by L.D. Landau in 1937 (see Landau & Lifshitz, 1980) that often there are symmetry relations between the old and new phases. Landau has shown that for a second-order transition the two phases must be structurally related, and their symmetry groups must conform to certain group-subgroup relations. Symmetry plays a fundamental role in phase transitions, and better classifications must consider it; such a classification is proposed below[6]. Before considering this new classification, I describe some of the main theoretical ideas related to phase transitions.

4.2. Theoretical framework.

4.2.1. First-order phase transitions.

Equilibrium first-order phase transitions always involve activation, which substantially complicates their kinetics. The major factors determining the kinetics are defects, surface effects, and external fields. Polymorphs of Al_2SiO_5 (minerals kyanite, andalusite, and sillimanite, see Kerrick, 1990) are a classical example. All the transitions between these minerals are first-order reconstructive and require substantial activation energies to proceed; therefore, all the three minerals can coexist at not very high temperatures for millions of years in nature. A very interesting example is given by the HgI_2 polymorphs (Hostettler et al., 2001). At p<10 GPa and T<600 K, there are nine polymorphs in this system! Crystallisation from solution (which contains HgI_2 molecules) first produces a metastable yellow form, whose structure consists of linear HgI_2 molecules, and only then metastable orange (containing supertetrahedra $[Hg_4I_{10}]$) and stable red (containing HgI_4 tetrahedra) forms. Metastable yellow and orange crystals begin to transform into the red phase when touched by a needle. Defects thus introduced serve as nucleation centres of the stable phase. The orange phase is in fact represented by three distinct, but similar, structures, which can transform into one another. This system is a good example of the Ostwald rule, which states that often crystallisation produces a metastable phase, which transforms into the stable one via a sequence of metastable

[5] There have been many attempts to derive structural criteria for the determination of coordination numbers and bond graphs. One of the latest attempts was due to Bader (1990).
[6] Another classification based on symmetry was propsed by Christy (1993).

phases. At high temperatures, another yellow molecular form is stable (it can crystallise from the vapour). At 1.3 GPa a new phase is formed, where Hg atoms are five-coordinate. A somewhat similar kinetical behaviour was reported for Dimethyl 3,6-Dichloro-2,5-dihydroxyterephtalate (Richardson et al., 1990). For that compound, transformation kinetics and actual transition temperatures were found to depend on such factors as crystal size, degree of perfection, types of defects, and heating rate. Again, defects play the role of nucleation sites for the new phase.

Thermodynamics of first order transitions are based on the Clapeyron relation:

$$\mathrm{d}p/\mathrm{d}T = \Delta S/\Delta V, \qquad (4.2.1.1)$$

where ΔS and ΔV are the entropy and volume differences, respectively, between the phases. Using (4.2.1.1) one can calculate the slopes of the equilibrium lines of phase coexistence. This relation is valid only for first-order transitions, because for continuous transitions both ΔV and ΔS are equal to zero. The transition temperatures and pressures can be found from accurate atomistic (e.g., Parker & Price, 1989: magnesium silicates) or quantum-mechanical total energy calculations (e.g., Oganov & Brodholt, 2000: aluminium silicates), but there is no simple analytical theory. Only when the two phases are structurally similar can one apply approximate analytical theories, such as Landau theory (which was initially devised to study second-order phase transitions).

A relation, analogous to (4.2.1.1), for second-order transitions was derived by Ehrenfest:

$$\mathrm{d}p/\mathrm{d}T = \Delta C_\mathrm{P}/TV\Delta\alpha\,, \qquad (4.2.1.2)$$

where ΔC_P and $\Delta\alpha$ are the jumps of the heat capacity and thermal expansion at the transition. However, precise experiments, computer simulations, and accurate theories indicate a qualitatively different behaviour of the heat capacity – instead of having a finite jump, it logarithmically diverges to infinity on both sides of the transition. This ‘λ-behaviour’ invalidates the Ehrenfest relation.

4.2.2. Landau theory of first-and second-order transitions.

When the structural changes occurring upon transition are rather small, i.e. the two phases are structurally related, it is usually possible to define an order parameter (or several order parameters), whose continuous change describes all the intermediate structures on the transition pathway. The order parameter Q takes the

value, which would minimise the free energy $F(Q)$ at given p-T conditions. The simplest expression for the free energy is the Landau potential:

$$F(Q)=F_0+\frac{1}{2}\mathrm{A}(T-T_\mathrm{C})Q^2+\frac{1}{3}\mathrm{B}Q^3+\frac{1}{4}\mathrm{C}Q^4+\dots, \qquad (4.2.2.2)$$

where T_C is the critical temperature, and F_0 the free energy of the phase with Q=0 (e.g., high-temperature high-symmetry disordered phase). Landau's assumption that the second term of (4.2.2.2) is simply proportional to $(T-T_\mathrm{C})$ was analysed and justified mathematically within the mean-field approach by Sposito (1974). The entropy as a function of the order parameter is simply $S(Q) = -\partial F(Q)/\partial T = S_0 - \frac{1}{2}\mathrm{A}Q^2$. This dependence of the entropy on the order parameter is most appropriate for displacive phase transitions[7]. The internal energy is then $E(Q) = E_0 - \frac{1}{2}\mathrm{A}T_\mathrm{C}Q^2+\frac{1}{3}\mathrm{B}Q^3+\frac{1}{4}\mathrm{C}Q^4+\dots$ In the case A>0, B>0, C>0, this corresponds to a double-well potential $E(Q)$ [8]. For second-order transitions the odd-order terms in (4.2.2.2) must be zero (e.g., B=0), making the double well symmetric[9]. When B≠0, the double well is asymmetric, and the transition is first order. First-order transitions can also appear when C<0 (even if B=0), which requires a positive term $\frac{1}{6}\mathrm{D}Q^6$ to prevent the system from collapse.

Consider a second-order transition:

$$F(Q) = F_0+\frac{1}{2}\mathrm{A}(T-T_\mathrm{C})Q^2+\frac{1}{4}\mathrm{C}Q^4+\dots. \qquad (4.2.2.3)$$

One can observe that at the transition point (T=T_C, Q=0) the second derivative of F with respect to Q: $\frac{\partial^2 F(Q)}{\partial Q^2}= \mathrm{A}(T-T_\mathrm{C})+3\mathrm{C}Q^2+\dots$ changes its sign: it is negative below T_C and positive above T_C. For displacive phase transitions, where the order parameter Q corresponds to a particular atomic displacement, this second derivative corresponds to the squared frequency of a normal vibrational mode[10]. Its frequency ω is imaginary (i.e., $\frac{\partial^2 F(Q)}{\partial Q^2} \sim \omega^2$ is negative) in the high-symmetry phase below T_C,

[7] For order-disorder transitions the entropy is more accurately expressed as $S(Q)$=S_0-R[(1+Q)ln(1+Q)+(1-Q)ln(1-Q)].
[8] More than two minima can exist for higher-order polynomials (4.2.2.2).
[9] This is only one of the necessary conditions. Other conditions were formulated by Birman (1966) by using group theory. All these conditions are necessary, but not sufficient.
[10] And Q is its normal coordinate (see Chapter 5).

leading to a spontaneous distortion into a low-symmetry phase[11]. Above T_C, due to intrinsic anharmonic effects, this frequency becomes positive, stabilising the high-symmetry phase against distortions (see Dove, 1993, 1997). It is said that the low-symmetry phase is formed by condensation of a soft mode at $T=T_C$. Experiments do show that at the transition point one of the vibrational frequencies becomes practically zero for second-order transitions (e.g., in $SrTiO_3$ at 110 K – see Dove, 1993).

Transitions, where the soft mode is an optic mode associated with creation of a spontaneous electric dipole in the low-symmetry phase, are called *ferroelectric*. When the soft mode is an acoustic mode at the Brillouin zone centre, some of the elastic constants become zero at the transition point, and a spontaneous lattice strain is generated; such transitions are termed *ferroelastic* (see Salje, 1993)[12]. For *ferromagnetic* transitions a net magnetic moment is generated on transition from a high-temperature paramagnetic phase to a low-temperature ferromagnetic phase.

For first-order transitions, complete mode softening does not occur at $T=T_C$. For these transitions a hysteresis in temperature is observed, and mode softening can occur at the ends of the hysteresis region. All these features are correctly predicted by Landau theory.

The power of Landau theory comes from the fact that simple symmetry considerations allow one to find which of the coefficients B, C,… must be zero, and therefore (see below) which is the order of the transition and how many terms must be included in the Landau potential, including possible couplings to the strains (see below). Second-order phase transitions, corresponding to a symmetrical double-well potential $E(Q)$, are always characterised by group-subgroup relations: the symmetry group of one (often called 'ordered', usually low-temperature) phase is a subgroup of the symmetry group of the other ('disordered', usually high-temperature) phase. The two symmetrically equivalent minima then correspond to the same ordered phase, and can be considered as 'twin domains', related by a symmetry element present in the disordered phase, but absent in the ordered one (Fig. 4-1).

The potential (4.2.2.2) is often complicated by the coupling of the order parameter to lattice strains. In such cases the potential will be:

---

[11] This is the so-called dynamical instability. The soft wavevector **k** determines the modulation of the structure; the mode eigenvectors determine vectors of atomic displacements leading to the low-symmetry phase.

[12] This important particular case of dynamical instability is called mechanical instability (see Chapter 3).

$$F(Q)=(F_0+\frac{1}{2}\mathrm{A}(T-T_\mathrm{C})Q^2+\frac{1}{3}\mathrm{B}Q^3+\frac{1}{4}\mathrm{C}Q^4+\ldots)+$$

$$+a_1Q\varepsilon+a_2Q\varepsilon^2+a_3Q^2\varepsilon+1/2C\varepsilon^2+\ldots\ , \qquad (4.2.2.4)$$

where a_1, a_2, a_3 are coupling coefficients, and C is an elastic constant. Again, symmetry determines the lowest-order coupling possible (e.g., Dove, 1993). The summation in (4.2.2.4) includes, in principle, all coupled strains and all the corresponding elastic constants, and the resulting expression can be very complicated. Coupling of the order parameter to the strains can cause a first-order behaviour even for a symmetric $E(Q)$. In this case it is possible to determine the dependence of the elastic constants and spontaneous strains on temperature – see the detailed reviews by Carpenter et al. (1998) and Carpenter and Salje (1998, 2000) for a further discussion.

In some cases, more than one order parameter is required to describe a phase transition. Then, for the case of two order parameters, the Landau potential looks like:

$$F(Q)=F(Q_1)+F(Q_2)+\xi_1Q_1Q_2+\xi_2Q_1^2Q_2+\xi_3Q_1Q_2^2+\ldots\ , \qquad (4.2.2.5)$$

where ξ_1, ξ_2, and ξ_3 are coupling coefficients for the Q_1-Q_2 coupling. In cases where odd-order terms of the kind $\xi Q_1Q_2Q_3$ are present, the transition must be first order. For a detailed general account of Landau theory see Landau and Lifshitz (1980) and Dove (1993, 1997).

Finally, Landau theory is equally applicable to pressure-driven phase transitions. This case is very similar, e.g. the Landau potential analogous to (4.2.2.2) is:

$$G(Q)=F_0+\frac{1}{2}\mathrm{A}(P-P_\mathrm{C})Q^2+\frac{1}{3}\mathrm{B}Q^3+\frac{1}{4}\mathrm{C}Q^4+\ldots\ , \qquad (4.2.2.6)$$

implying $V(Q)=\partial G(Q)/\partial P=V_0+\frac{1}{2}\mathrm{A}Q^2$. The Helmholtz free energy is then $F(Q)=F_0-\frac{1}{2}\mathrm{A}P_\mathrm{C}Q^2+\frac{1}{3}\mathrm{B}Q^3+\frac{1}{4}\mathrm{C}Q^4+\ldots$

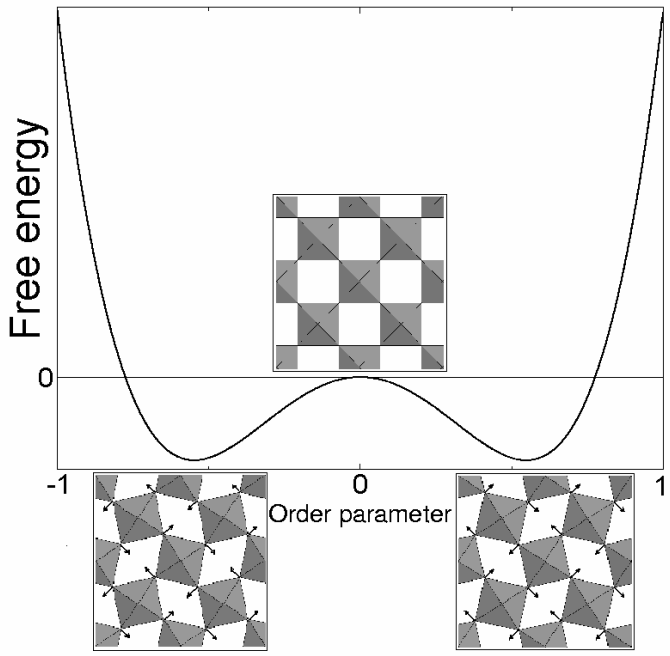

Fig. 4-1. Landau potential $F(Q)=F_0+\frac{1}{2}A(T-T_C)Q^2+\frac{1}{4}CQ^4$ at $T<T_C$, where distortions stabilise the structure. The two distorted perovskite-type structures shown on the bottom are equivalent (they are mirror reflections of each other) and differ only by the sense of the distortion; arrows show the directions of octahedral rotations away from the cubic structure. The undistorted structure is shown in the centre. At temperatures higher than T_C, the stable structure will be locally distorted, but on average will have the symmetry of the undistorted phase.

Shortcomings of Landau theory. Landau theory belongs to a class of approximate theories known as mean field theories. Mean field treatment is a common way of approximately solving complex physical problems in many areas of science (e.g., Hartree and Hartree-Fock methods for electronic structure calculations are mean field approximations). The main drawback of these methods is the neglect of short-range fluctuations (in Landau theory the local structure and fluctuations of the order parameter are neglected). In other words, Landau theory assumes that all the neighbouring unit cells have the same configuration; therefore, domain structures and fluctuations of the order parameter in space and time are not treated properly. This problem becomes severe in the vicinity of T_C (in the so called Ginzburg interval). For second-order transitions Landau theory predicts $Q\sim(T_C-T)^{1/2}$, while experiments indicate $Q\sim(T_C-T)^{1/3}$. The critical exponent of 1/3 has been many times confirmed by numerical computer simulations and could be explained only with the advent of renormalisation group theory[13]. Landau theory cannot explain the logarithmic divergence of the heat capacity near the critical point – instead, it yields

a finite jump. Finally, Landau theory does not consider quantum effects at low temperatures. As a consequence, it does not reproduce experimentally observed order parameter saturation at low temperatures; instead, it predicts a steady increase of the order parameter with decreasing temperature. However, it is generally believed that the symmetry apparatus of Landau theory is valid even where mean-field theory breaks down.

Ginzburg-Landau theory. In 1950, V.L. Ginzburg and L.D. Landau (see Landau & Lifshitz, 1980; Bowley & Sánchez, 1999) considered the case of an order parameter slowly varying in space. This leads to the simplest theory beyond the mean-field. The free energy becomes a *functional* of the order parameter, and an additional term proportional to the square of the gradient of the order parameter appears:

$$F[Q(\mathbf{r})]= \int \{f(Q(\mathbf{r})) + \frac{1}{2}\lambda[\nabla Q(\mathbf{r})]^2\}\mathrm{d}r \qquad (4.2.2.7)$$

with the stiffness parameter $\lambda>0$. E.g., for a second-order transition,

$$F[Q(\mathbf{r})]= \int \{\frac{1}{2}a(T-T_c)Q^2(\mathbf{r}) + \frac{1}{4}bQ^4(\mathbf{r}) + \frac{1}{2}\lambda[\nabla Q(\mathbf{r})]^2\}\mathrm{d}r \qquad (4.2.2.8)$$

Then, Ginzburg and Landau express the order parameter as a sum of a constant term (the average order parameter) and fluctuations, which they express as a Fourier series:

$$Q(\mathbf{r}) = \bar{Q} + \sum_{\mathbf{k}} Q_{\mathbf{k}} \mathrm{e}^{i\mathbf{kr}} \qquad (4.2.2.9)$$

Eq. (4.2.2.7) can be re-written as:

$$F[Q(\mathbf{r})] = \int \{f(\bar{Q}) + Q_1(\mathbf{r})f' + \frac{1}{2}Q_1^2(\mathbf{r})f'' + \ldots + \frac{1}{2}\lambda[\nabla Q(\mathbf{r})]^2\}\mathrm{d}r =$$

$$= V\{f(\bar{Q}) + \frac{1}{2}\sum_{\mathbf{k}} |Q_{\mathbf{k}}|^2 (f''+\lambda k^2) + \ldots\} \qquad (4.2.2.10)$$

The system is stable against all fluctuations if $f''+\lambda k^2>0$ (a more strict condition is $f''>0$) at all Q. If there is more than one minimum, $f''<0$ at some Q. By means of fluctuations, the system eventually reaches the state with the lower free energy.

Let us consider the case $f''<0$. In this case, the system is unstable against all fluctuations whose wavevectors satisfy $f''+\lambda k^2>0$. Hence, the maximum unstable wavevector is $k_c=\sqrt{\frac{|f''|}{\lambda}}$. The correlation length ξ is:

$$\xi = k_c^{-1} = \sqrt{\frac{\lambda}{|f''|}} \qquad (4.2.2.11)$$

---

[13] In fact, experiments give mean-field critical exponents far from T_C, but nearer T_C there is a crossover from the mean-field to critical behaviour, where the critical exponents depart significantly from the mean-field predictions.

Ginzburg and Landau have proposed a criterion of the validity of Landau theory. They defined the following value:

$$r(T) = \frac{f_{\mathrm{m}}\xi^3}{k_{\mathrm{B}}T} \quad , \qquad (4.2.2.12)$$

where f_{m} is the difference of energies at the energy maximum and minimum. If $r(T)>1$, fluctuations are not important, and Landau theory is valid. When $r(T)<1$, fluctuations are essential and Landau theory is invalid; this occurs in the vicinity of T_{C} (this temperature region is called Ginzburg interval). Ginzburg intervals are usually quite narrow (of the order of ~10 K).

For second-order transitions, $f_{\mathrm{m}} = \frac{a^2(T-T_c)}{4b}$ and

$$\xi = \sqrt{\frac{\lambda}{2a(T_c - T)}}, \qquad (4.2.2.13)$$

Ginzburg-Landau theory emphasises the role of critical fluctuations and defines criteria of validity of Landau theory. However, this theory is still approximate and does not reproduce experimental critical exponents, e.g. for the correlation length (4.2.2.13). Renormalisation group theory overcomes all these difficulties and serves as the modern basis of the theory of critical phenomena; applications of that theory extend well beyond the field of phase transitions and can be found in astronomy, engineering, and geology.

4.2.3. Renormalisation group theory (RGT).

This theory goes beyond the mean-field approximation and fully treats all possible fluctuations of the order parameter. Introductory texts on this theory can be found in Chandler (1987), Rao and Rao (1978), and Wilson (1983); the latter reference is the Nobel lecture of Kenneth Wilson, the main inventor of RGT. This theory is based on repeated scaling transformations of the system and its Hamiltonian, during which some degrees of freedom (e.g., some fluctuations of the order parameter) are removed. At phase transitions, the system becomes scale-invariant, and the behaviour of the system is determined by the long-wavelength fluctuations, insensitive to the details of atomic structure.

RGT explains the famous scaling hypothesis which states that ‘the correlation length, ξ, should be the longest and the only relevant length in explaining critical phenomena’ (Rao & Rao, 1978). Fluctuations with the wavelength exceeding the

correlation length are always negligible, but itself the correlation length diverges at the critical point to infinity as $|T_C - T|^{-\nu}$ (Ginzburg-Landau theory gives $\nu=1/2$ – see (4.2.2.13), but experiment indicates $\nu=2/3$). The exponent ν is not sensitive to the type of interatomic interactions, so critical phenomena in all systems (e.g., in metals, covalent, molecular, and ionic systems, solids, liquids, and gases) must be similar and all their critical exponents must be the same. The temperature dependence of ξ ($\xi \sim |T_C - T|^{-\nu}$), according to the scaling hypothesis, accounts for the major part of the temperature dependence of all properties near the critical point; 'physical quantities depend on $|T_C - T|$ only through their dependence on ξ' (Rao & Rao, 1978).

Describing the average order parameter Q near the critical point, we have $Q \sim (T_C - T)^{\beta}$, where for 3D-systems the critical exponent $\beta=1/2$ from Landau theory or 1/3 from experiment, computer simulations, and RGT. Critical exponents depend on the dimensionality of the system, and this is clearly demonstrated by RGT.

For example, in two dimensions, $\beta=1/8$, whereas Landau theory would always[14] give $\beta=1/2$. According to the other important hypothesis, understood only with the advent of RGT, the universality hypothesis, all critical phenomena can be classified by the dimensionality of the system and symmetry of the order parameter, but again not the chemical nature or structural details of the substance[15]. This means that models with simplified interactions (e.g., nearest-neighbour Ising models) still give correct critical exponents for their universality class (i.e., for all systems of the same dimensionality having order parameters of the same symmetry).

Using RGT, it can be shown that Landau theory (like any other mean-field theory) yields exact critical exponents for four- and higher-dimensional spaces; at the infinite number of dimensions all other aspects of Landau theory become exact. For lower-dimensional spaces mean-field theories become increasingly less applicable.

Finally, RGT predicts that some systems can exhibit continuous lattice melting close to the transition point. Continuous lattice melting means that on approaching the transition point, mean-square atomic displacements diverge as $\ln(T_C - T)$, but

[14] Here I consider only the second-order transitions, described by the simplest potential $F(Q)=F_0+\frac{1}{2}A(T-T_C)Q^2+\frac{1}{4}CQ^4$. When other terms are included, β changes. E.g., when DQ^6 term is added, β can take values between 0.25 and 0.5 (second order transitions), 0.25 (intermediate, or tricritical, transitions), less than 0.25 (first order transitions), or larger than 0.5 (see Redfern, 2000).

only in one direction, that crystal lattice is destroyed, and Bragg reflections disappear being replaced by broad diffuse scattering centred at the positions of Bragg peaks. After passing through the transition point, the system spontaneously recrystallises into the high-temperature phase. So far, only one example of such behaviour was found experimentally: Na_2CO_3 (Harris & Dove, 1995). The necessary condition of continuous lattice melting is that the system is 3-dimensional, and is characterised by softening of a transverse acoustic mode in a whole plane of the reciprocal space.

4.2.4. Ising spin model.

This model is widely used to describe magnetic and atomic ordering processes in materials. In this model, a spin +1 or –1 is associated with each lattice site, depending on whether the magnetic moment on the site is 'up' or 'down', or whether the atom occupying the site is of the type 'A' or 'B'.

The total energy of the system is:

$$E = E_0 - J\sum_{i,j} s_i s_j - H\sum_i s_i , \qquad (4.2.4.1)$$

where E_0 is the reference-state energy, and J the interaction parameter between the sites: if $J<0$, unlike spins prefer to group together, and there is a tendency to ordering at low temperatures; if $J>0$, unmixing will occur at low temperatures. Full disorder, although unfavourable energetically, will be stabilised by the entropy at high temperatures. An external field H leads to a preferred orientation of the spins. The Ising model can be analytically solved only in one and two (Onsager's solution) dimensions; for three dimensions it is solved numerically, usually by the Monte Carlo method. Note that the one-dimensional Ising model exhibits no phase transitions, and at all temperatures above 0 K yields the disordered state.

As noted above, the Ising model has found many applications in describing atomic and magnetic ordering in crystals. Numerical simulations based on the Monte Carlo method and Ising model yield critical exponents close to the values given by experiments and predicted by renormalisation group theory.

Ising-like models provide an interesting route for theoretical studies of polytypism and polysomatism. The crucial observation is the mathematical similarity between polytypic sequences (e.g., Fig. 4-2a-c) and one-dimensional Ising models. Layers of polytypic structures are mapped onto spin-sites of a one-dimensional Ising lattice.

---

[15] This can be understood from the fact that critical behaviour is determined by long-wavelength fluctuations; on the other hand, chemical details are only important at short wavelengths – those

Including interactions between up to three nearest layers (Price, 1983), it is possible to explain the existence of almost all the observed polytypes in spinelloid systems (Fig. 4-2d,e) just by considering the ground-state (i.e., 0 K) energy[16]. Generally, longer-period polytypes require the presence of longer-range interactions to stabilise them.

The strength of interactions decreases with distance, which explains why long-period polytypes are rarely found. Let us denote, following Price and Yeomans (1984), polytypes in a Zhdanov-like manner: e.g., the sequence …↑↑↓↓↑↑↓↓↓↑↑↓↓↑↑↓↓↓… as <2223>, or $<2^3 3>$. This symbol reads as follows: two layers 'spin-up' are followed by 2 'spin-down', then there are two 'spin-up', and three 'spin-down' layers. The stable stacking sequences are: <∞>, <1>, <2>, <3>, <12>, with marginal stability of longer-period phases along the boundary lines between these major phases.

A realistic inclusion of temperature necessitates an extension of the model beyond one dimension. The Axial Next-Nearest-Neighbour Ising (ANNNI) model (see, e.g., Price & Yeomans, 1984 and references therein) does this. The system is mapped onto a 3D-Ising lattice; each lattice site represents a finite building block of the structure. For simplicity, only the interactions between the nearest and next-nearest layers are included; within the layers, a certain degree of disorder is allowed, determined by the Ising-like interactions (4.2.4.1) with different (generally, much larger and possibly anisotropic) interaction parameters *J*. This model reproduces the stability of relatively long-period polytypes. In this model, they are stable due to a competition between the internal energy and entropy, both of which are determined by short-range interactions[17]. With increasing temperature, more longer-period polytypes acquire stability fields[18], and such phases as <23>, $<12^2>$, $<2^2 3>$, $<12^3>$, etc., appear

---

comparable to bond lengths.

[16] Finite-temperature behaviour cannot be studied with the one-dimensional Ising model: at non-zero temperatures the spin arrangement of this model becomes completely random.

[17] This is an equilibrium picture. In many cases, long-period polytypes are metastable systems, formed during crystal growth and related to dislocations and stacking faults.

[18] This implies that long-period polytypes are stabilised by the configurational entropy. This extra entropy comes from the thermal disorder within the layers. This is a very non-trivial conclusion. One must remember, however, that the ANNNI model is very crude in its way of accounting for the intralayer disorder. It also completely neglects possible lattice strains and the associated energy terms.

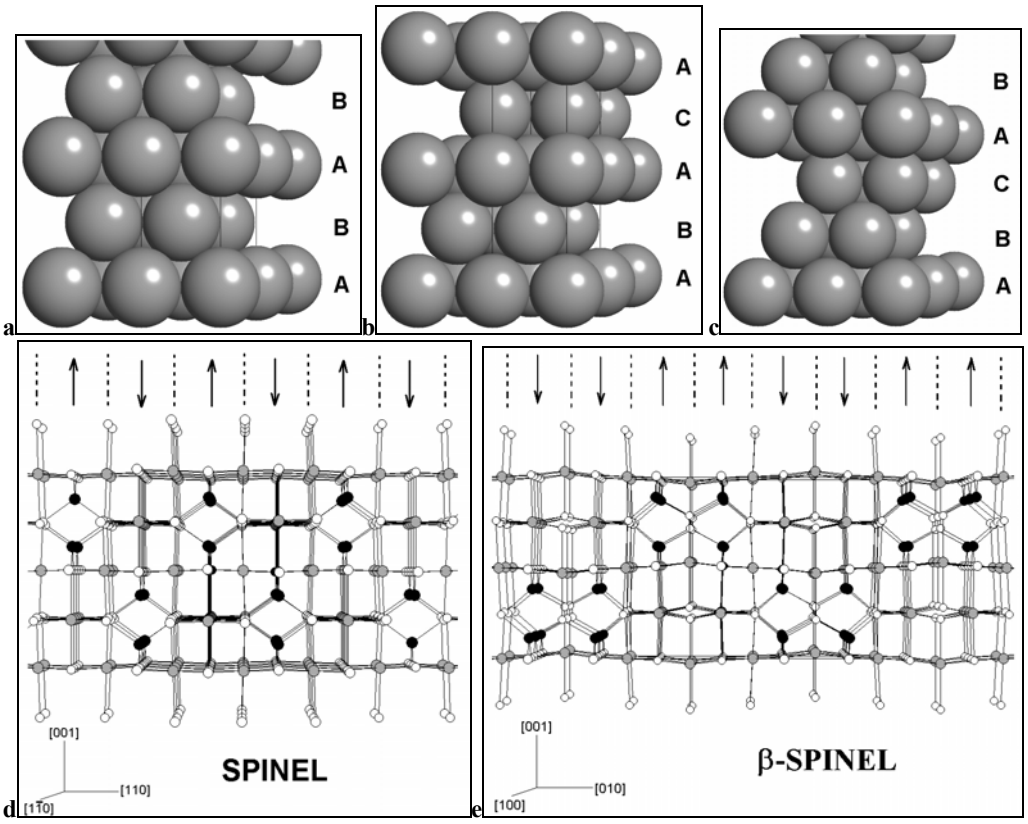

Fig. 4-2. Illustrations of polytypism. (a-c) In close-packed structures. 2-, 4-, and 3-layer close packings are shown. A,B, and C denote close-packed layers of different orentations; (d-e) spinelloid structures. Layers of different orientations are shown by 'up' and 'down' arrows highlighting the similarity with the one-dimensional Ising spin lattice. The theoretical number of possible metastable and stable polytypes is infinite. Structures based on the close packings of anions and/or cations are very common among inorganic materials. The richest example is SiC, whose structure can be described as based on a close packing of Si (or C) atoms. Dozens of polytypes of SiC are known, including some very long-period polytypes. The importance of the spinelloids is great for the Earth sciences, because of the phases of Mg_2SiO_4 – ringwoodite (spinel-like phase) and wadsleyite (β-spinel phase), which are the major constituents of the transition zone of the Earth's mantle. Intermediate polytypes can also occur in stacking faults. In diagrams d-e black circles are Si atoms (tetrahedrally coordinated), grey circles Mg atoms (octahedrally coordinated), and empty circles are O atoms.

on the phase diagram of the ANNNI model. Price et al. (1985) showed that atomistic computer simulation can be effectively used to determine the interaction parameters for the ANNNI model, and predict the possible polytypes, stacking faults, and their energetics.

The Ising model can be generalised for the case of more than two spins (see Yeomans, 1992). Such variants will be applicable to complicated ordering processes in crystal structures (e.g., ordering in multicomponent solid solutions) or polytypic (polysomatic) systems with more than two types of layers.

The conventional Ising models assume that spins can be only 'up' or 'down', and therefore these models cannot be applied to noncollinear magnetic materials. For these cases various Heisenberg models are appropriate, which take into account the

orientations of the spins. The simplest of these models is based on the following Hamiltonian:

$$E = E_0 - J\sum_{i,j} \mathbf{s_i}\mathbf{s_j} - H\sum_i s_i^z \ , \qquad (4.2.4.2)$$

involving spin vectors $\mathbf{s_i}$ and $\mathbf{s_j}$. Like the Ising model had no phase transitions for one-dimensional systems, the Heisenberg model has no phase transitions for one- and two-dimensions systems.

4.2.5. Mean-field treatment of order-disorder phenomena.

The Bragg-Williams model is the simplest mean-field approach applicable to ordering phenomena. The Helmholtz free energy of the alloy as a function of temperature and order parameter is:

$$F=E-TS=F_0-\frac{Nz}{4}JQ^2+Nk_BT\,[(1+Q)\ln(1+Q)+(1-Q)\ln(1-Q)] \ , \qquad (4.2.5.1)$$

where E_0 is the internal energy of the fully disordered state, N is the number of sites where disordering occurs, the order parameter $Q= X_{A,\alpha}-X_{A,\beta}= X_{B,\beta}-X_{B,\alpha}=2X_{A,\alpha}-1$, and the exchange energy $J=E_{AA}+E_{BB}-2E_{AB}$.

The expression (4.2.5.1) is analogous to the Landau potential (4.2.2.2), and yields the same critical exponents (e.g., $Q\sim(T_C-T)^{1/2}$ near the critical point). The Bragg-Williams model has a phase transition even in the one-dimensional case; generally, as for any mean-field model, the accuracy of predictions of the Bragg-Williams model increases with the dimensionality of the system. In three dimensions this model gives qualitatively reasonable results; however, even with accurate exchange energies J, the predicted transition temperatures are usually a few times higher than the experimental ones (Redfern, 2000).

Drawbacks of the Bragg-Williams model can be corrected by explicitly considering short-range order. In the Bethe model (see Rao & Rao, 1978), apart from the long-range order parameter Q, one or more short-range order parameters are considered. These additional parameters describe the distribution of neighbours of both kinds in the nearest proximity of each atom. Bethe and related models yield critical exponents and transition temperatures, which are much more realistic than the mean-field predictions.

4.3. New classification of phase transitions.

4.3.1. Phase transition scenarios.

All possible modifications of a given substance correspond to minima of the free energy hypersurface. The global (i.e., the deepest) minimum is related to the phase thermodynamically stable at given *p*-*T*-conditions, while local minima correspond to metastable phases. The free energy hypersurface determines the crystal structure and many of its properties; it also determines all possible transition states, phase transition paths, and activation barriers. In principle, the free energy hypersurface is a function of all coordinates of all the atoms in the system (i.e., the free energy hypersurface is infinite-dimensional for an infinite system such as an ideal crystal). In principle there can be an infinite number of local minima on this surface, corresponding to an infinite number of possible metastable phases. These phases and their properties can be simulated on the computer, but it is remarkable that only a handful of them can be experimentally synthesised and studied.

The free energy hypersurface provides the most fundamental link between crystal structure, thermodynamics, and kinetics of all processes. Although the hypersurface itself is extremely complicated, we still can fruitfully exploit its concept in studying phase transitions. Often the dimensionality of the hypersurface can be effectively reduced, and only a finite part of the degrees of freedom (e.g., only those corresponding to one unit cell or a supercell) considered. Mean-field theories such as Landau theory are based on such reductions (e.g., for a system with one order parameter, Landau theory reduces the infinite-dimensional hypersurface to a one-dimensional function! – Fig. 4-1).

At this stage we would like to include metastable phases in our considerations. Let us consider the behaviour of a phase at conditions beyond its stability field. Eventually it must transform into the state thermodynamically stable at given conditions, but at finite timescales two other scenarios are possible as well: 1) the initial phase persists as a metastable state, 2) it transforms into another metastable phase with a lower free energy, corresponding to a local minimum nearest to that of the initial phase. Numerous examples can be found for all these scenarios. Let us consider each scenario in more detail.

Transition into the stable phase. This often requires substantial structural changes and activation, in which case it can happen only at high temperatures and is catalysed by defects. If very large structural changes are required, it is likely that there will be intermediate metastable transformation products, in accordance with the famous Ostwald step transition rule. In each of these metastable states the system can stay between few picoseconds (for very shallow local minima) and indefinitely long times

(for minima with high barriers). For a transition with a complete structural change, many bonds should be broken in the activated state; as typical energies per bond in inorganic compounds are ~1eV, such activated states become accessible only at temperatures of the order of $T \sim \Delta E_a/k \sim 10{,}000$ K (!), which is well above the melting temperature of any known compound. Defects significantly lower these estimates and serve as activated centres for the nucleation of the new phase. Examples of transitions with a significant structural change include, e.g. coesite→stishovite transition in SiO_2 (Fig. 4-3). Transitions between the Al_2SiO_5 polymorphs (kyanite, andalusite, sillimanite) are other examples, though in these cases some common structural elements exist in the phases (straight chains of edge-sharing octahedral in all the Al_2SiO_5 modifications – Fig. 4-3). These transitions can occur only at elevated temperatures, being kinetically hindered at low temperatures, where metastable phases can exist indefinitely long.

The phase persists as a metastable state. Supercooled liquids (e.g., water can be supercooled) are one example. Diamond, which is metastable at ambient conditions (where graphite is stable), is another example. The three Al_2SiO_5 polymorphs can exist as metastable phases in each other's thermodynamic stability fields – this circumstance has made the experimental determination of their phase diagram very difficult! Amorphous solids are always metastable, yet can be preserved over very long timescales. The reason why these metastable phases can be retained over practically indefinite time is that their minima on the free energy hypersurface are surrounded by sufficiently high energy barriers, so that the necessary activation energy can be available only at high temperatures. At sufficiently high temperatures, therefore, metastable phases inevitably transform into other phases – either stable or metastable, but with lower free energy and higher activation barriers.

Transition into another metastable state is a very interesting possibility. Such transitions are often found in nature and technology; perhaps, the clearest example is pressure-induced amorphisation (Mishima et al., 1984). When the old phase ceases to correspond to any local free energy minimum (i.e., becomes dynamically unstable), it collapses into a nearest free energy minimum; alternatively this can happen if the temperature is high enough to enable the system to jump through the activation barrier. The new metastable state must correspond to one of the local free energy minima nearest (in configurational space) to the old one. Large leaps in the configurational space are not possible, because they would require climbing high

activation barriers and breaking too many bonds. This implies the maximum possible structural similarity between the old and new phases. In such transitions only those changes in structure (and, consequently, symmetry) are adopted, which are necessary to maintain the crystal's stability against infinitesimal (dynamical stability) and finite (stability against fluctuations) atomic displacements. In the case of pressure-induced amorphisation, preservation of the dynamical stability requires the loss of translational symmetry. Even in this extreme case the local structure retains much similarity to the structure of the original crystal, the atomic displacements being rather small. More often, crystal periodicity is at least partly preserved, and changes are rather subtle, involving group-subgroup relations between symmetries of the old and new phases. In many cases it is possible to fully preserve space group.

As we have seen, symmetry is an important parameter in Landau theory, and is a natural bridge between the structure, thermodynamics and kinetics (it determines the order of the transition and the functional form of the Landau potential and possible couplings). Symmetry changes occurring upon the transition can be used to classify phase transitions.

4.3.2. New classification.

This classification is given in Table 4-1. I divide all phase transitions into 'global' (where the new phase is always the thermodynamically stable phase – i.e., corresponds to the global free energy minimum, and there are no structural relations between the old and new phases), and 'local' (the new phase corresponds to a nearest local free energy minimum, which implies clear structural and symmetry relations between them; the new phase can be either thermodynamically stable or metastable).

Global transitions can involve any structural and symmetry changes. These transitions are always strongly first-order and reconstructive, they require substantial activation, are often catalysed by defects, and cannot proceed at low temperatures. They occur via the nucleation-and-growth mechanism, when nuclei of the new phase are precipitated near defects or surfaces.

Local transitions, on the contrary, can be second- or higher-order, as well as first-order (often the first-order component is small). They can be reconstructive as well as displacive, order-disorder, or electronic. Often there are clear orientational relations between the old and new phases – twinning and topotaxy are common phenomena here. These transitions may require no activation and, therefore, in some cases can proceed at very low (even absolute zero) temperatures. As it was already

mentioned, the new phase can be metastable. The transition path from the structure of the old phase to the new one can be described by the order parameter, specific normal mode (or modes), or ordering mechanism. According to the degree of symmetry changes, there are several possible cases (Table 4-1).

In the simplest case, there is no symmetry change upon transition. These (so-called isosymmetric) phase transitions are now being discovered experimentally in an increasing number of systems.

Next degree of symmetry change involves group-subgroup relations, while both phases are crystalline. This is the most common type of local transitions.

Further degree of symmetry change involves incommensurate modulation of the structure with partial or complete loss of translational symmetry, while preserving both short- and long-range order. Incommensurate modulation (and the corresponding loss of translational symmetry) can occur in one, two, or three dimensions.

Quasicrystals, similarly to incommensurate phases, are solids lacking crystal periodicity in one or (typically) two or three dimensions; they also have both long- and short-range order. Several types of quasicrystals are known - icosahedral quasicrystals with no lattice periodicity at all ('3D-quasicrystals'), and quasicrystals with 1-dimensional periodicity ('2D-quasicrystals') having 12-fold symmetry axes (dodecagonal quasicrystals), 5-fold and 10-fold (decagonal), and 8-fold axes (octagonal quasicrystals). The above types of quasicrystals have symmetry axes that are incompatible with translational periodicity. There can exist 1D-quasicrystals, which are simply quasiperiodic polytypes.

Further degree of symmetry breaking is present in pressure-induced amorphisation. Lattice periodicity and long-range order are destroyed in one, two, or three dimensions, while short-range order persists, guaranteeing the similarity between the local structure of the glass and structure of the original crystal. All symmetry elements are locally destroyed, but when viewed as a continuum, the amorphous phase has spherical point-group symmetry[19]. In the present context, however, it is more appropriate to classify pressure-induced amorphisation as a symmetry-lowering process, as any process involving soft modes and modulations of the structure.

One can see that this classification includes all possible cases of symmetry breaking in local phase transitions, and elegantly puts them in order from symmetry-conserving transitions to transitions with partial symmetry loss but with preservation of

[19] Pressure-induced amorphisation can produce anisotropic glasses, whose point-group symmetry is ellipsoidal (see below).

crystallinity, then to transitions with partial or complete loss of periodicity but with long-range order preserved (incommensurate transitions), and, finally, to pressure-induced amorphisation, which destroys all symmetry and long-range order, retaining only short-range order. There can be transitions between different levels of this hierarchical system – e.g., pressure-induced amorphisation of incommensurate or quasicrystalline phases. Different types of local phase transitions are considered below.

Table 4-1. Classification of phase transitions. See Fig. 4-3 for some illustrations.

I. GLOBAL TRANSITIONS.	**II. LOCAL TRANSITIONS.**
I.1. With changes of the first coodination numbers Al_2SiO_5: kyanite-andalusite-sillimanite; SiO_2: coesite-stishovite	**II.1. Isosymmetric transitions.** electronic – Ce structural – $KTiOPO_4$, PbF_2, KNO_3, sillimanite (Al_2SiO_5) structural with ordering change – NiAl, albite ($NaAlSi_3O_8$) structural & electronic – Na_3MnF_6
I.2. Without changes of the first coordination numbers SiO_2: quartz-coesite	**II.2. Group-subgroup relations.** translationengleich - α-β quartz (SiO_2) klassengleich – $P2_1/c$-$C2/c$ pyroxenes (e.g., $MgSiO_3$) general – $Pm\bar{3}m$-$Pbnm$ perovskites (e.g., $MgSiO_3$) indirect relations - rhombohedral-tetragonal $BaTiO_3$ perovskite; bcc-fcc Fe
	II.3. Incommensurate transitions 1-dimensional – sillimanite (Al_2SiO_5) 2-dimensional – quartz (SiO_2) 3-dimensional – wüstite ($Fe_{1-x}O$)
	II.4. Crystal-quasicrystal transitions
	II.5 Pressure-induced amorphisation SiO_2 (quartz, coesite), berlinite ($AlPO_4$), andalusite (Al_2SiO_5)

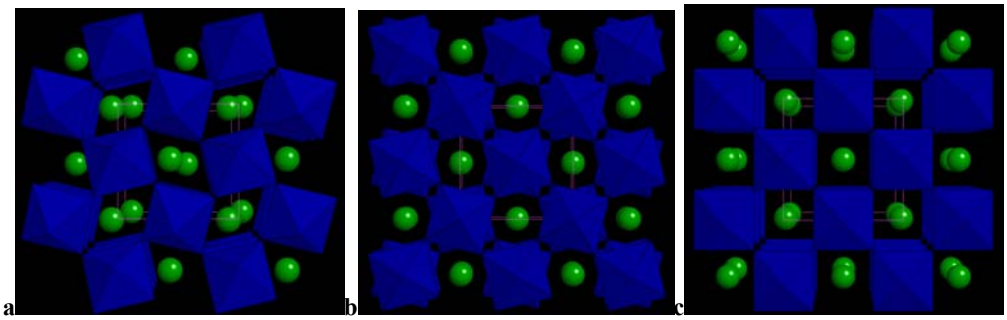

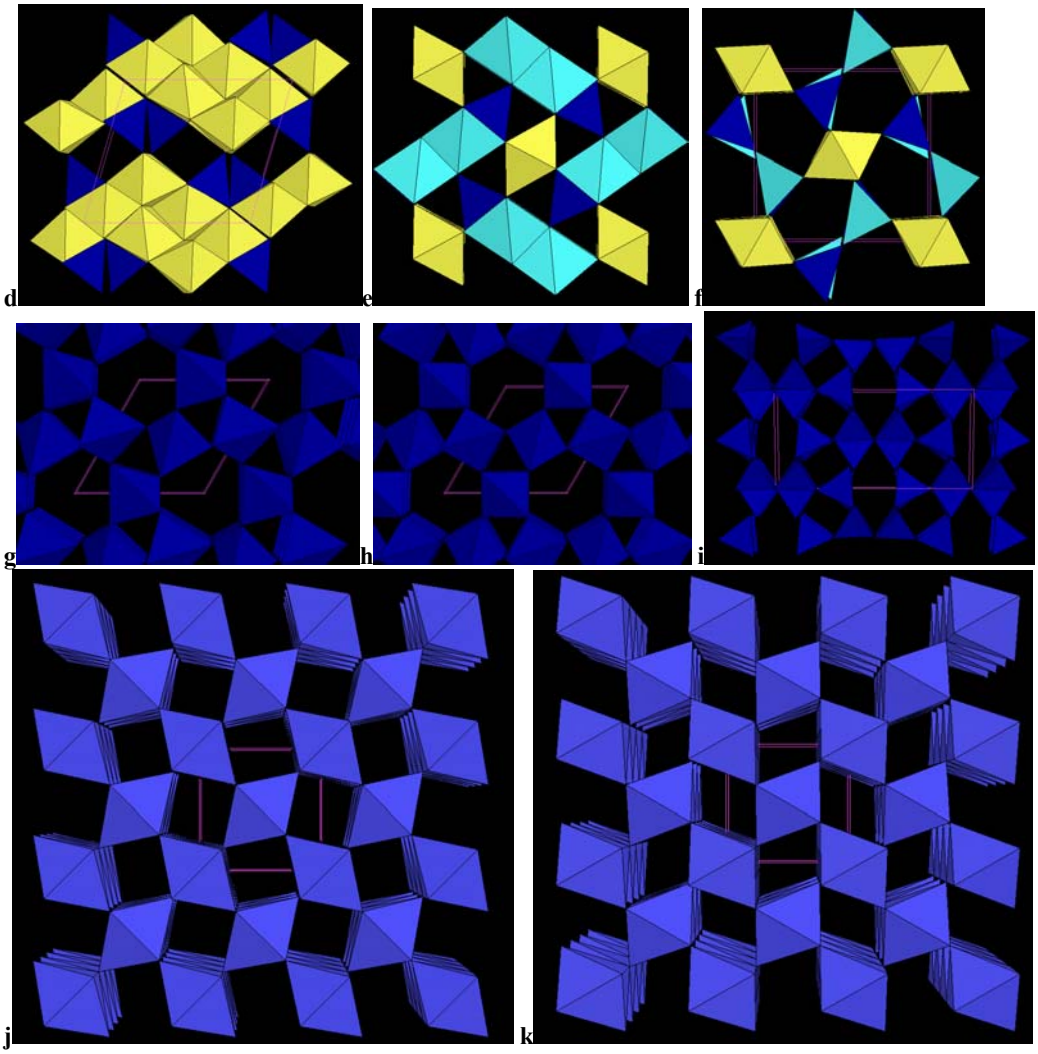

Fig. 4-3. Examples of different phase transitions. (a-c) different perovskite phases (a-*Pbnm*, b-*I*4/*mcm*, c- $Pm\bar{3}m$). Green spheres – Mg atoms. (d-f) Al_2SiO_5 polymorphs (d-kyanite, e-andalusite, f-sillimanite). Al polyhedra are shown in yellow and turquoise. (g-k) silica polymorphs (g-α-quartz, h – β-quartz, i- coesite, j- stishovite, k- $CaCl_2$-type structure, drawn with an exaggerated orthorhombic distortion). Si-polyhedra are shown in blue.

4.3.3. Phenomenology and examples of local phase transitions.

4.3.3.1. Isosymmetric transitions.

Using Landau theory, it is easy to show that isosymmetric transitions must be first-order, but can disappear (i.e. become fully continuous, infinite-order transitions) at the critical point and above it (Bruce & Cowley, 1981; Christy, 1995). There is a complete analogy here with the liquid-gas transitions (which are also isosymmetric). At supercritical temperatures there are generally rapid, but continuous changes in all properties along any *p*-*T* path going above the critical point (Angel, 1996). Second-order phase transitions must involve changes in space group symmetry. All examples known so far fully confirm these theoretical conclusions.

Another example of isosymmetric phase transition phenomena outside the realm of solids is given by the newly discovered liquid-liquid phase transitions (McMillan, 2000), which are also first order with a critical point terminating the two-phase equilibrium line. Phase transition between structurally different amorphous phases[20] of ice was observed (Mishima et al., 1985) and reported to be first order. Increasingly many crystals are now known to exhibit crystal-crystal isosymmetric phase transitions (i.e. those for which both phases have the same space group with the same number of atoms in the unit cell, with atoms occupying the same Wyckoff positions). Such transitions can be electronic (where the electronic structure changes – e.g., Ce and SmS), structural (where coordination numbers of atoms change discontinuously – e.g., $KTiOPO_4$) or intermediate (both electronic and structural changes are involved – e.g., Na_3MnF_6). Another kind of structural isosymmetric transitions associated to the change of the ordering of atoms or defects was recently predicted for the Al-rich NiAl alloy (Alavi et al., 1999) and albite $NaAlSi_3O_8$ (Oganov et al., 2001c).

Electronic transitions. Metallic Ce undergoes an isosymmetric phase transition Ce(I)-Ce(IV) (see Liu & Bassett, 1986, and references therein), presumably due to 6s-4f (or 5d) electronic transition. Both Ce(I) and Ce(IV) have the fcc structure (space group $Fm\bar{3}m$). The volume change at the transtion is very large (13%) at room temperature, but it rapidly decreases along the Ce(I)-Ce(IV) equilibrium line until it disappears at the critical point (2.15 GPa and 613 K). Corundum-type Co_2O_3 (space group $R\bar{3}c$) undergoes an isosymmetric phase transformation, accompanied by a significant volume reduction (6.4 % at zero pressure), at ~8 GPa and 1123 K (see Liu & Bassett, 1986, and references therein). This transition does not alter the structure type and is thought to be due to the high-spin - low-spin electronic transition. Another famous example of an electronic transition is SmS, which transforms from the low-pressure insulating phase to the high-pressure metallic phase; both phases have a NaCl-type structure. Fig. 4-4 explains this transition.

[20] All liquid, gaseous, and conventional amorphous phases are isosymmetric, having spherical point-group symmetry.

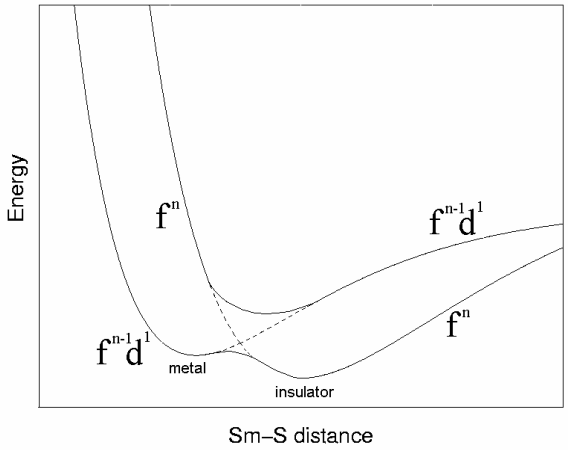

Fig. 4-4. Illustration of the isosymmetric metal-insulator transition in SmS. After Burdett (1995), with modifications. Mixing of two configurations (metallic $f^{n-1}d$ and insulating f^n) produces a double-well energy curve for the ground state, where the minimum with a smaller interatomic distance corresponds to a metal. Compression triggers the insulator-metal transition.

CsI, according to quantum-mechanical calculations (Winkler, 1997) is expected to have a weakly first-order isosymmetric (space group *Pmma*) phase change at 47 GPa.

This transition does not involve any coordination changes and was ascribed to the onset of overlap of diffuse 5p-orbitals (which are formally core orbitals) of Cs atoms with orbitals of Cs and I atoms.

Structural transitions. Structural isosymmetric crystal-crystal transitions do not involve any drastic changes in the electronic structure, but are purely atomistic. $KTiOPO_4$ (KTP) is known to undergo at 5.8 GPa a phase transition with a volume decrease of 2.7% with preservation of space group $Pna2_1$ (Alan & Nelmes, 1996). Large cages, occupied by K, lose 12% of their volume upon the transition. Glasser and Catlow (1997), using an ionic model in their static calculations, successfully reproduced isosymmetric transition in KTP and predicted such transitions in many other compounds with the KTP structure at pressures around 6 GPa. Under further compression to 25 GPa, KTP underwent another transition with a sudden decrease of volume and appearance of imaginary phonon frequencies. This behaviour was considered by Glasser and Catlow (1997) to be an artifact of the ionic model; in fact, this can also indicate the onset of pressure-induced amorphisation. KNO_3 (II) - KNO_3 (IV) phase transition, which occurs at 0.3 GPa and is accompanied by a volume decrease of 11.5%, does not alter the space group (*Pnma*) (Adams at al., 1988), but leads to drastic changes in the Raman spectra. Potassium atom coordination number changes from 9 to 11. An isosymmetric (space group *Pnam*)

phase change has been observed at 9.8 GPa for PbF_2 (Haines et al., 1998). The volume difference between the phases was estimated to be 2-3% at 1 atm. X-ray diffraction structure refinement has shown that structural topology undergoes only minor changes, and Pb atom coordination changes from 9 to 10. Compression experiments (Hugh-Jones & Angel, 1994) suggest that orthoenstatite ($MgSiO_3$) may have a weakly first-order ($\Delta V/V$=0.09%, of the order of experimental uncertainties) isosymmetric transition at 4 GPa. At this pressure sudden changes in the mechanism of compression were observed. Another possible case for isosymmetric polymorphism is anorthite $CaAl_2Si_2O_8$, where an isosymmetric $I\bar{1}$ - $I\bar{1}$ transformation was postulated in order to account for the unusually high curvature of the $P\bar{1}$ - $I\bar{1}$ equlibrium line on the phase diagram (Angel, 1996). X-ray structure determinations seem to support this hypothesis, showing significant differences in high-presure and high-temperature structures of the $I\bar{1}$-phase, and very rapid structural changes of this phase at changing p and T are probably associated with crossover above the critical point. In their molecular dynamics simulations, Badro et al. (1996) found that quartz (SiO_2) irreversibly amorphised under hydrostatic pressure of 22 GPa, but transformed into a crystalline phase with all silicon atoms in a 5-fold coordination when subjected to a uniaxial stress (20 GPa along the a and b axes and 27 GPa along the c direction). Later, Badro et al. (1997) commented that this phase is isosymmetric with quartz (space group $P3_221$). It was reproduced in *ab initio* LDA simulations; semiclassical simulations demonstrated its dynamical stability. On decompression, this phase reverted to quartz through an intermediate phase with strongly distorted SiO_4-tetrahedra, and on increasing the uniaxial stress it amorphised. The amorphous phase was structurally different from the pressure-amorphised quartz, and on decompression transformed into a defective quartz-like material at 10 GPa.

Na_3MnF_6 (space group $P2_1/n$) is an example of a phase transition with a simultaneous change in the atomic and electronic structure. At 2.2 GPa this compound undergoes a first-order isosymmetric phase transformation, which is associated with a change of orientation of the Jahn-Teller elongation of MnF_6 octahedra (Carlson et al., 1998). The transformation shows a small hysteresis of 0.5 GPa.

Anticipation of isosymmetric phase transitions, associated with a change of atomic or defect ordering. Alavi et al. (1999) have demonstrated the possibility of pressure-induced isosymmetric phase transitions in non-stoichiometric systems with different possible ways of defect ordering. They studied the non-stoichiometric alloy $Ni_{1-x}Al_{1+y}$ with excess of Al relative to Ni related either to the Ni vacancies or to the Al atoms occupying some of the Ni sites ('antisite' structure). The first structure has lower density and energy and at high pressures becomes less stable than the antisite structure. Using *ab initio* calculations, Alavi et al. (1999) have predicted the phase diagram of this alloy with a first-order isosymmetric phase transition between the defect structures, critical point behaviour, and coexistence of both defect configurations in the alloy above the critical point. My semiclassical calculations (Oganov et al. 2001c; Chapter 6) predict that triclinic ($P\bar{1}$) Na-feldspar, albite $NaAlSi_3O_8$, undergoes an isosymmetric phase transition associated with a change of the Al-Si ordering scheme, induced by non-hydrostatic stresses or high pressure. At low pressures the Al atoms predominantly occupy the T_1 tetrahedral sites, while at high pressures Al prefers the T_2 tetrahedral sites.

4.4.3.2. Transitions with group-subgroup relations.

There are several possibilities here, springing from different types of subgroups/supergroups of crystal symmetry. According to Hermann theorem (Hahn & Wondratshcek, 1994), a maximal subgroup of a space group is either *Translationengleich*[21]-type (i.e., all translations are preserved, but some of the point-group symmetry operators disappear) or *Klassengleich*[22]-type (all point-group operators are preserved, but some of the lattice translations disappear; as a consequence, a superstructure is formed). Subgroups, which are neither klassengleich, nor translationengleich, are called *general* subgroups; they involve both cell multiplication and lowering of the point-group symmetry. Examples are $\alpha \rightarrow \beta$ quartz (*translationengleich*), $P2_1/c$-$C2/c$ pyroxenes (*klassengleich*; see very interesting papers by Arlt & Angel, 2000 and Arlt et al., 1998), and $Pbnm \rightarrow Pm\bar{3}m$ transitions in perovskites (*general*).

The fourth type of transitions with group-subgroup transitions involves indirect symmetry relations between two phases via an intermediate archetypal phase of a higher symmetry, which is a supergroup for symmetries of both phases. An example is $BaTiO_3$, where the transition between the rhombohedral and tetragonal phases can be described with reference to the higher-symmetry cubic phase. Such transitions are usually weakly first-order.

Yet another possibility is that of a transition state of a lower symmetry, which is a common subgroup of the symmetries of both phases. These transitions are usually strongly first-order; often they can be described as reconstructive (see Christy, 1993). The fcc$\rightarrow$bcc transition in Fe can be described with reference to lower-symmetry tetragonal or rhombohedral configurations, whose symmetries are common subgroups of both symmetry groups of the bcc and fcc phases. Recent works of H. Sowa were dedicated to finding transition paths between simple elementary and binary structure types on the basis of symmetry. E.g., Sowa (2000 and personal communication) concluded that the transition from the sphalerite (ZnS) to the NaCl-type is most likely to proceed via an orthorhombic transition state. Catti (2001) performed accurate *ab initio* calculations for SiC and arrived at the same

[21] German word meaning 'having the same translations'; accepted as an international term (International Tables for Crystallography)
[22] German word meaning 'having the same (point-group) class'; accepted as an international term (International Tables for Crystallography)

conclusion, in conflict with the traditionally accepted rhombohedral transition state for this material.

4.4.3.3. Incommensurate transitions.

Incommensurate transitions are a topic of enormous current research. I shall not discuss these phases in detail, but refer the reader to a review (van Smaalen, 1995) and some interesting papers – on theory of incommensurate transitions in insulators (Heine & McConnell, 1981) and on unusual crystal morphology of incommensurate phases (Dam et al., 1985). Incommensurability can occur via mode softening or modulation of atomic positional occupancies, or in metals via electronic effects (e.g., Peierls transition). These are typical local transitions. They occur in a large number of compounds (e.g., $NaNO_2$) and minerals (some intermediate plagioclase feldspars, nepheline $(K,Na)AlSiO_4$, akermanite $Ca_2MgSi_2O_7$, calaverite $AuTe_2$, wüstite $Fe_{1-x}O$; there is an incommensurate phase in quartz, intermediate between α- and β-phases). Incommensurate modulation can occur in 1, 2, or 3 dimensions. An incommensurate phase is predicted for sillimanite in Chapter 9 (Oganov et al., 2001d).

4.4.3.4. Crystal-quasicrystal transitions.

The first quasicrystal ($Al_{86}Mn_{14}$) was discovered relatively recently (Shechtman et al., 1984). Now we know a large number of quasicrystals, theories of their structure and formation have been formulated, and even some computational studies performed. For a review, see Janot (1994). Quasicrystals have both short- and long-range order, but lack translational periodicity in one or (usually) more dimensions. They can have symmetry axes incompatible with translational periodicity – 5-fold axed in icosahedral quasicrystals, 5- and 10-fold axes in decagonal, 8-fold axes in octagonal, and 12-fold axes in dodecagonal quasicrystals. These 2– and 3-dimensional quasicrystals are described by 2- or 3-dimensional Penrose tilings (Fig. 4-5) with two or more types of ‘unit cells’. All quasicrystals are metallic alloys, most are metastable, but some are thermodynamically stable.

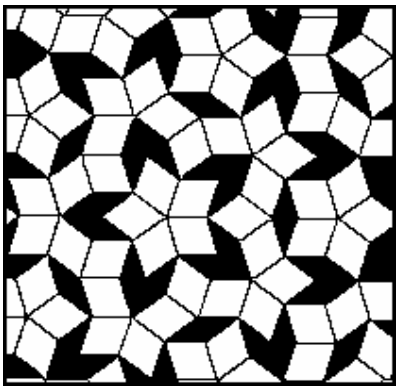

Fig. 4-5. Penrose tiling for a decagonal quasicrystal. White and black tiles are different 'unit cells' having different compositions. The ratio of white tiles to the black ones is the golden mean $\tau=(\sqrt{5}+1)/2$.

Although not known definitively, it is likely that crystal-quasicrystal transitions are local. However, an ideal crystal and ideal quasicrystal are not very likely (although can in principle) to have the same composition. Since the proportion of different tiles, or 'unit cells', in a Penrose tiling is irrational, general quasicrystal composition will be characterised by a chemical formula with irrational coefficients (see Janot, 1994). This explains both the extremely complicated chemical formulae of quasicrystals, and their occurrence exclusively among metallic alloys, where charge balance considerations are not applicable (an ionic or covalent solid cannot have an irrational chemical formula as this would break charge neutrality). Ideal stoichiometric crystals, on the other hand, must have a rational chemical formula, in accord with Dalton's law. Therefore, crystal-quasicrystal transitions are most likely to occur between disordered and non-stoichiometric states. Terminological curiosity: quasicrystals, which can be daltonides[23], do not obey Dalton's law.

[23] i.e. materials which have a constant composition, as opposed to bertollides, which are defined as non-stoichiometric compounds.

4.4.3.5. Pressure-induced amorphisation.

This phenomenon was first discovered in 1984 in experiments on compression of ice (Mishima et al., 1984), which, compressed to 1 GPa at 77 K, did not transform to the modification stable at these conditions (ice VI), but was found to amorphise. Since 1984, large efforts were made to understand the physics of this unusual type of phase transformations, but many questions remain open. Here I give only a brief overview; for detailed reviews see excellent papers (Sharma & Sikka, 1996; Richet & Gillet, 1997).

A great number of crystals undergoing pressure-induced amorphisation is known[24], as well as a few substances undergoing an opposite phenomenon – pressure-release amorphisation (for extensive reviews, see Sharma & Sikka, 1996; Richet & Gillet, 1997). In the latter phenomenon, high-pressure phases, when decompressed to pressures well below their stability fields, become dynamically unstable and amorphise[25].

Pressure-induced amorphisation is always a metastable first order transition. It requires that the amorphous phase be denser than the original crystalline phase. This means that crystals with open structures should be easier to amorphise in contrast to close packed ones.

Structural relationships between melting-and-cooling-produced amorphous phases and pressure-induced ones are still widely discussed. A similar, also widely discussed, question is about the degree of similarity of the processes of melting and amorphisation under pressure. It is often stated that pressure-induced amorphisation occurs on the metastable extension of the melting curve, in cases where the melting temperature decreases with pressure. This idea has received experimental support for several systems (see Richet & Gillet, 1997; Mishima, 1996; Hemley et al., 1988), but its generality is questionable, because melts and pressure-amorphised glasses can be structurally very different. For ice, the two amorphous phases (one produced by cooling water, the other - by pressurising ice) are separated by a first-order phase transition (Mishima et al., 1985), which indicates clear structural differences. Pressure-induced amorphisation occurs in the limit of dynamical stability of the crystal. In melting, the temperature of the onset of a mechanical instability gives an

[24] Quartz SiO_2, coesite SiO_2, berlinite $AlPO_4$, GeO_2, zeolites scolecite $Ca_8Al_{16}Si_{24}O_{80}*24H_2O$ and mesolite $Na_{16}Ca_{16}Al_{48}Si_{72}O_{240}*64H_2O$, anorthite $CaAl_2Si_2O_8$, forsterite Mg_2SiO_4, fayalite Fe_2SiO_4, wollastonite $CaSiO_3$, enstatite $MgSiO_3$, muscovite $KAl_3Si_3O_{10}(OH)_2$, serpentine $Mg_3Si_2O_5(OH)_4$, portlandite $Ca(OH)_2$ are just a few examples.

upper bound of the true thermodynamic melting temperature: solids cannot be overheated to higher temperatures. This temperature can be used as a first approximation to the true melting temperature (e.g., MD simulations of Vočadlo & Price, 1996; Chaplot et al., 1998, and comment by Belonoshko, 2001).

Behaviour of pressure-induced amorphous phases on decompression can be very different: some compounds (e.g., $Ca(OH)_2$) recrystallise into a fine-grained aggregates, others (e.g., SiO_2, ice) remain amorphous. Berlinite ($AlPO_4$) is known for exhibiting the so called "memory glass effect": the amorphous phase, appearing under compression of a single crystal of berlinite under 18 GPa, on decompression to 5 GPa turns back to the single crystal with the same crystallographic orientation (Kruger & Jeanloz, 1990). Brillouin spectroscopy (Polian et al., 1993) confirmed this effect, with a hysteresis loop between 7 and 15 GPa. The amorphous phase turned out to be elastically anisotropic. MD calculatons (Tse & Klug, 1992) successfully reproduced the memory glass effect, with considerable short-range order and long-range disorder. Gillet et al. (1995) suggested that the 'memory glass effect' was an experimental artifact. According to these authors, berlinite transformed into an intermediate strongly disordered crystalline phase at 15 GPa, and the true amorphisation occurred at higher pressures and was irreversible[26].

Elastic anisotropy was also found in pressure-amorphised quartz by Brillouin spectroscopy (McNeil & Grimsditch, 1991) and MD simulations (Tse & Klug, 1993). The latter study found no structural relationships between pressure-amorphised quartz and silica glass.

Mechanisms driving pressure-induced amorphisation are still not quite clear. The necessary conditions are: 1) Higher density of the amorphous phase compared to the crystalline one. Usually it means that coordinaton numbers increase on amorphisation; 2) Presence of soft modes in the crystalline phase. Softening of a vibrational mode at a single point of the Brillouin zone should drive a transition to a crystalline (if the soft wavevector is rational) or incommensurate (if the wavevector is irrational) phase. Only simultaneous or nearly simultaneous softening of a phonon branch at a range of **k**-vectors (e.g., along a special direction of the Brillouin zone) can produce an amorphous phase (Keskar et al., 1994; Binggeli et al., 1994; Hemmati et al., 1996). Any atomic displacement, expressible as a combination of

[25] This happens to the perovskite-structured modification of $CaSiO_3$, one of the main minerals of the Earth's lower mantle, which at ambient conditions turns to a glass within a few hours.

soft modes, lowers the energy; the multitude of possible combinations gives rise to the disorder. However, a large degree of order should remain: because the displacements are expected to be small and because only displacements related to the softening phonon branch are allowed to freeze in. Simultaneous softening of a phonon branch along a direction in the Brillouin zone implies weak dispersion of this branch, which is most naturally achieved when the unit cell is large. Indeed, crystals with complicated structures and large unit cells are more prone to pressure-induced amorphisation.

4.4. Discussion of the new classification.

The classification presented above is based on symmetry and naturally incorporates the old notions of first-order and continuous, reconstructive, displacive, order-disorder, and electronic phase transitions. Its principles are very simple, but like any classification it is not perfect. The weak point is in the distinction between local and global transitions. Such a distinction is rigorously made only by considering the free energy hypersurfaces, but in practice we make it by saying that the structures are 'related' or 'unrelated'.

Continuous paths (i.e. some structural relation) can in principle be constructed between any two structures, however different[27]. However, for strongly reconstructive (global) transitions none of these paths will be followed because of the high energy barriers required. A useful criterion of locality of a transition is given by the comparison of the shapes and parameters of the supercells and looking at the structures along possible transition paths. Yet, the transition between andalusite and sillimanite (Al_2SiO_5), here considered as global, would emerge close to local transitions. On the other hand, some transitions considered as local (especially among the indirect group-subgroup transitions) involve large atomic displacements. Examples are given by polytypic and order-disorder transformations, both of which are kinetically hindered at low temperatures.

Forces in crystals obey the space group symmetry, and will tend to preserve it. Most phase transitions, however, change crystal symmetry, usually by a group-subgroup scheme. Isosymmetric transitions remain a rare, but fundamentally important phenomenon. The present classification emphasises the fundamental role

---

[26] This seems to be a general conclusion. However, memory glass effect has also been reported for other systems, e.g. the equimolar solid solution $Ca(NO_3)_2$:$NaNO_3$ (Winters et al., 1992).

of isosymmetric polymorphism and pressure-induced amorphisation as the two extreme cases of symmetry changes.

Ostwald rule can now be formulated in new terms: 'Global phase transformations tend to occur via a sequence of local metastable transitions'. Theoretically, for any compound there can be an infinite number of metastable structures, corresponding to local minima of the free energy hypersurface. However, only a handful of these possibilities can practically be synthesised. One expects that phases, most likely to appear as metastable in synthesis, must either be stable at some *p*-*T* conditions, or be related to one of the stable phases by a local phase transition. In other words, there must be structural and symmetry relation between the possible metastable phases and the stable phases. Locality, as a major principle governing the selection of possible metastable phases, should be important for planned synthesis of technologically important metastable compounds.

[27] The simplest way to do this is to consider for both structures supercells with the same number of atoms. An infinite number of continuous transition paths between these supercells can be constructed.

Chapter 5. Simulation methods.

In this chapter I shall give an account of some of the most important advances of modern theoretical physics and their use in state-of-the-art computer simulation of condensed matter. At times this account will be only glancing; for more details there exist a number of excellent reviews and original papers. General references include several books (Born & Huang, 1954; Urusov, 1975; Catlow & Mackrodt, 1982; Allen & Tildesley, 1987; Urusov & Dubrovisky, 1989; Tossell & Vaughan, 1992; Dove, 1993; Sutton, 1993; Thijssen, 1999) and review articles (Catti, 1986; Catlow & Price, 1990; Catlow et al., 1993, 1994; Gavezzotti, 1994; Bukowinski, 1994; Cohen, 1994, 1999; Hemley & Cohen, 1996; Gale, 1996; Stixrude et al., 1998; Kohn, 1999a,b). Computer simulations represent one of the fastest-growing areas of physics, and new methods and significant developments appear continually.

First I consider the current state and predictive power of theoretical crystal chemistry. The I proceed with formulating the general quantum-mechanical problem and the Born-Oppenheimer principle, which will be followed by a discussion of quantum-mechanical methods. Both advances and problems of state-of-the-art quantum-mechanical computational methods will be discussed, as well as future areas of their development. Then, I discuss interatomic interactions and their analytical representation, with the advantages and deficiencies of this approach. The chapter finishes with a description of dynamical simulations via lattice dynamics and molecular dynamics methods.

5.1. An essay on the state of the art of predictive crystal chemistry.

The main task of any theoretical science is the explanation of known and the prediction of unknown facts. For crystal chemistry this is the task of predicting structure, properties, and stability fields of all possible modifications for a given compound. The last 20 years have seen an enormous progress towards this goal, yet we are still far from it. Nearly all modern methods start with a given topology of the crystal structure, which is then refined to the theoretically optimal structure. Knowing just the structural topology, for most compounds it is possible to accurately predict many properties and behaviour at high temperatures/pressure (Catlow & Mackrodt, 1982; Catti, 1986; Urusov & Dubrovinsky, 1989; Catlow & Price, 1990; Burnham, 1990; Silvi, 1991; Dovesi et al., 1992; Catlow et al., 1993; Catlow et al.,

1994; Bukowinski, 1994); if there are several candidate phases with known topologies, it is possible to construct a theoretical phase diagram. Prediction of the topology itself (i.e., the structure type) is possible in some cases (Burdett, 1988; Urusov et al., 1990), but successes here are rather modest.

5.1.1. Modern theoretical and predictive crystal chemistry.

Concepts and rules of crystal chemistry, largely empirical, allow one to obtain the simplest qualitative and semiquantitative predictions for the structure of materials. They are also essential for the understanding of crystal structures, their stability, and properties. The most important ones include the concept of atomic and orbital electronegativities (e.g., Pauling, 1960; Urusov, 1975; 1987; Allen, 1989; Baekelandt et al., 1991), Pauling's rules for ionic and covalent crystals (Pauling, 1960), systems of atomic and ionic radii (see Urusov, 1987), concept of close packing (Belov, 1947); the notion of the valence electron concentration for metals and alloys (e.g., Urusov, 1987); for covalent crystals – Grimm-Sommerfeld and Hume-Rothery rules, and Parthé rules (Parthé, 1996; Urusov, 1987). Burdett and McLarnan (1984) showed why Pauling's rules work and, furthermore, why they are applicable not only to ionic crystals (as originally formulated by Pauling), but also to crystals with a significant covalent component of bonding (e.g., silicates). Brown's extension of the second Pauling's rule (Brown, 1992) appears to be applicable to all chemical systems. A justification of this universality was given by Urusov (1995). Topological analysis of the electron density due to Bader (Bader, 1990) also justifies Brown's rule (see, e.g., Tsirelson, 1993). The topological analysis itself is a significant advance in theory – it defines a scheme of partitioning of the space into atomic regions, justifies the additivity of atomic properties, and allows one to define atomic charges, volumes, etc.

An example of an old elegant idea, evolving until today, is the VSEPR (Valence Shell Electron Pair Repulsion) model. Pseudopotential radii (Zunger, 1980) brought a new systematics of atomic properties relevant to chemical bonding, being simultaneously a measure of the atomic size (e.g., atomic radii – Ganguly, 1993) and an inverse measure of the electronegativity (Zunger, 1980). It was shown that at least for binary systems each structure type occupies a separate domain on the 2D-map whose axes are linear combinations of the orbital pseudopotential radii of the atoms. Each chemical composition falls in one of these domains, giving the most likely structure. These predictions are remarkably successful at least for binary compounds

(Zunger, 1980; Burdett, 1988; Ych at al., 1992). Compositions likely to produce quasicrystals were predicted using this method as well (Villars et al., 1986).

Since the 1960-s it has become possible to study both experimentally and theoretically electron density distribution in crystals (Coppens, 1992, 1997; Tsirelson, 1993; Tsirelson et al., 1986), accurate thermal motion parameters (Tsirelson, 1993), and study crystals at the temperatures and pressures of the Earth's interior. One of the greatest advances in theory was the ability to extend quantum-mechanical calculations to crystals, and to perform such calculations at arbitrary temperatures and pressures for relatively large systems (routinely up to ~100 atoms; in some studies up to ~30,000 atoms!). Less expensive (by ~10^3 times), but more restricted in accuracy, semiclassical simulations based on analytical representations of interatomic interactions can be used to study very large systems (up to millions of atoms). The semiclassical approach, due to its low computational cost, is suitable for systematic searches of possible structure types for a given compound. Such studies, based on either genetic algorithms (Bush et al., 1995; Gallagher et al., 1991), or simulated annealing (Pannetier et al., 1990), or other methods, show a great promise.

In the rest of this chapter, I will describe the foundations and some technical details of both quantum-mechanical and semiclassical simulations. First, I will outline the general problem, then describe methods for calculating the internal energy (static calculations), and then describe dynamical simulations.

5.2. Formulation of the general problem and the Born-Oppenheimer principle.

In the thermodynamic limit, any system attains the state with the lowest Gibbs free energy G at given p-T conditions:

$$G(p,T)\rightarrow\min \qquad (5.2.1)$$

All equilibrium structural and electronic parameters can be determined by minimising $G = E + pV - TS$. Many ground-state properties can then be obtained by differentiating G, e.g. with respect to the structural parameters. This general task is very difficult, and is solved in several steps, by making several consequtive approximations.

The first step is to decouple the electronic and structural (nuclear) degrees of freedom. In all practical calculations (and in experimental studies of structure and electron density) the adiabatic Born-Oppenheimer principle is assumed to hold. This principle states that, since masses of atomic nuclei are much (thousands of times)

larger than masses of electrons, atomic motion will be much slower than electronic. As a consequence, electrons will almost instantaneously relax to the ground state every time an atom displaces. This allows one to decouple the electronic and atomic degrees of freedom, and consider the quantum-mechanical problem in the framework of fixed nuclei, whose positions determine the ground-state electronic wavefunction. This is an approximation: in reality it will always take some finite time for the electrons to adjust to changing nuclear positions; however, this approximation is extremely accurate (it may possibly break down only for the lightest elements). It allows one to define the (adiabatic) energy hypersurface in terms of only atomic degrees of freedom: each structural configuration has a unique and definite value of the energy. Problems with the adiabatic principle occur when there are two or more electronic states which have the same symmetry and are very close in energy for a given structural configuration: this would result in mixing of the ground and excited states. For metals and semiconductors at finite temperatures, the excited states will be partly occupied according to the Fermi-Dirac statistics, giving some electronic contribution to the entropy and free energy. In insulators, this contribution will be negligible up to very high temperatures (well above 10,000 K).

The next step in solving this problem is to define the internal energy hypersurface. At each configuration, the internal energy can be calculated either by solving the electronic Schrödinger equation, or by using semiclassical parameterised models of interatomic interactions. Minimising the internal energy E is equivalent to the free energy minimisation at p=0 and T=0 K. Knowing the internal energy hypersurface, we can always calculate the entropy S and minimise the free energy G. Ideally, one would solve the nuclear Schrödinger equation and find all energy levels in the system, with which one can next calculate the partition function, eq. (3.1.1), and all the thermodynamic properties including the free energy, eq. (3.1.2)). Solving the Schrödinger equation for an arbitrary multi-dimensional energy hypersurface is exceedingly difficult, and two common ways of solving this problem are: 1) to use the classical approximation for nuclear motion (as in molecular dynamics and Monte Carlo simulations; this approach is valid at high temperatures) and 2) to solve the Schrödinger equation assuming that the system is harmonic (this approach is used in lattice dynamics simulations and is valid at relatively low temperatures). First, I will discuss the methods of calculating the energy, and then describe lattice dynamics and molecular dynamics simulations, which take temperature into account.

5.3. Methods of calculating the internal energy.

The total energy of an electron-nuclear system and all its energy levels can be calculated by solving the Schrödinger equation:

$$\hat{\mathbf{H}}\psi = E\psi \qquad (5.3.1)$$

where $\hat{\mathbf{H}}$ is the Hamiltonian operator of the system. Here I consider only the non-relativistic theory, sufficient when atoms lighter than krypton are treated[28]. Writing $\hat{\mathbf{H}}$ more explicitly, in atomic units[29] we have:

$$[\sum_{i=1}^{N}(-1/2\,\nabla_i^2) + \sum_{i=1}^{N} v_{\text{e-n}}(\mathbf{r}_i) + \sum_{i=1}^{N}\frac{1}{|\mathbf{r}_i - \mathbf{r}_j|}]\psi = E\psi \quad , \qquad (5.3.2)$$

where N is the number of electrons. The first term in (5.3.2) is the kinetic energy operator and the following terms are the electron-nuclear and electron-electron potential energy operators, respectively; E is the electronic energy (to find the total energy, one needs to add to it the nuclear-nuclear interaction energy). Schematically, we can write (5.3.2) as follows:

$$(-1/2\,\nabla^2 + v_{\text{e-n}} + v_{\text{e-e}})\psi = E\psi \qquad (5.3.3)$$

---

[28] Relativistic effects appear when electrons are moving at speeds comparable to the speed of light. This situation occurs only in heavy atoms, where the inner electrons move in a very strong nuclear potential. Two main manifestations of relativity in the electronic structure are scalar relativistic effects (shrinking of the innermost atomic orbitals, which also affects the potential acting on the valence electrons) and spin-orbit interaction. To see how scalar relativistic effects occur (Pisani, 1996), note that the average velocity of a 1s electron in atomic units is Z (nuclear charge), and the speed of light is 137.036 a.u. For Hg (Z=80) the relativistic mass of a 1s electron is 1.23 times its rest mass. This corresponds to a ~23% shrinking of the 1s-orbital in Hg, since the Bohr radius ($a_0=\hbar^2/me^2$) is inversely proportional to the mass of the electron. Shrunk core orbitals more effectively screen the outer orbitals; due to orthogonality with the innermost electrons, valence s- and p-electrons become contracted and stabilised relative to the non-relativistic case, whereas valence d- and f-electrons become more expanded, destabilised, and thus more chemically active. Spin-orbit interaction becomes important in heavier atoms (roughly after Xe); in solids it can remove degeneracies of electron levels at high-symmetry points of the reciprocal space (Aschcroft & Mermin, 1976). Spin-orbit interaction adds a term, proportional to the dot-product of the electron spin moment and the vector product of its velocity and the electric field, to the potential acting on the electron. For a fully relativistic treatment, one must solve the Dirac (rather than Schrödinger) equation. For a detailed review of relativistic effects in chemistry and the existing relativistic computational methods, see Pyykko (1988).

[29] In atomic units, $\hbar = m_e = e^2 = 4\pi\varepsilon_0 = 1$. The units of length and energy in this system are Bohr radius a_0=0.529 Å and Hartree (equal to minus twice the energy of the hydrogen atom): 1 Ha=27.2116 eV. Atomic units are used in all quantum-mechanical equations in this chapter.

The Hamiltonian is in principle very simple, having only Coulombic interactions. The main problem in solving (5.3.2) is that the wavefunction is a function of $3N$ electronic coordinates (where N is the number of electrons) – for many-electron systems it is exceedingly complicated! Different quantum-mechanical methods choose different ways of approximating the Hamiltonian and representing the wavefunction (in such radical density-functional approaches as Thomas-Fermi model, the wavefunction does not appear at all!). All modern computational methods are based on approximate one-electron theories, reducing (5.3.3) to a set of similar coupled equations for separate one-electron orbitals. Apart from making the wavefunction tractable, one-electron theories gain another advantage: they yield one-electron energy spectra, which enable understanding of chemical bonding and give a first approximation to the excitation spectra. In many respects, one-electron theories (e.g., Kohn-Sham density functional theory) can be exact.

Before moving on to approximate one-electron theories, I mention a few important exact results. The first result relates to the existence of a cusp of the electron density at nuclear positions, with the average derivative of the density at the nucleus ($r=r_0$):

$$\frac{\partial \bar{\rho}(r_0)}{\partial r_0} = -2Z\bar{\rho}(r_0) \quad , \tag{5.3.4}$$

where Z is the nuclear charge. Far from the nucleus, the electron density of an atom falls off exponentially, and the exponent is related to the ionisation potential I:

$$\rho(r) \sim \exp[-2(2I)^{1/2}r] \tag{5.3.5}$$

This relation is also true for molecules (Parr & Yang, 1989).

Electrons, as quantum particles, are never at rest – even at $T = 0$ K they have a large zero-point energy with a large kinetic component. For Coulombic systems (like atoms, molecules, crystals) the virial theorem (Landau & Lifshitz, 2001a) states that the total electronic energy is equal to minus the kinetic energy of the electrons and to one half of the potential energy of the electrons:

$$E = -\langle E_{\text{kin}}\rangle = \tfrac{1}{2}\langle E_{\text{pot}}\rangle \tag{5.3.6}$$

The virial theorem is exact only for an exact wavefunction.

If E is a function of some parameter q, then its derivative is:

$$\mathrm{d}E/\mathrm{d}q = \langle\psi|\frac{\mathrm{dH}}{\mathrm{d}q}|\psi\rangle + \frac{\mathrm{d}}{\mathrm{d}q}\langle\psi|\hat{\mathbf{H}}|\psi\rangle \tag{5.3.7}$$

The most important applications of (5.3.7) are the calculation of forces (in which case q is an atomic coordinate) and stresses, which are used for geometry optimisation in quantum-mechanical calculations. For an exact wavefunction, the second term in (5.3.7) is zero, and

$$dE/dq = \langle\psi| \frac{dH}{dq} |\psi\rangle \qquad (5.3.8)$$

Eq. (5.3.8) is known as the Hellmann-Feynman theorem. A consequence of this theorem is that forces acting on nuclei can be calculated from a purely classical electrostatic expression, involving nuclear positions and the electron density distribution. When the wavefunction is not exact (e.g., due to basis set incompleteness), the second term in (5.3.7) is not zero and must be taken into account. This term (taken with a minus sign) is known as the Pulay force (or Pulay stress).

5.3.1. Hartree method.

This method was widely used for atoms before the 1960-s. The only reason to consider it now is that it was the starting point of the Hartree-Fock and Kohn-Sham methods.

For the electron-electron potential, D.R. Hartree wrote simply:

$$v_H(\mathbf{r}) = \int \frac{\rho(\mathbf{r}')}{|\mathbf{r}-\mathbf{r}'|} d\mathbf{r}' \quad , \qquad (5.3.1.1)$$

i.e. he included only the classical Coulombic energy of an inhomogeneous electron gas. The corresponding energy (known as the Hartree energy E_H) is:

$$E_H = \tfrac{1}{2}\int \rho(\mathbf{r})\, v_H(\mathbf{r}) d\mathbf{r} = \tfrac{1}{2}\int \rho(\mathbf{r}) d\mathbf{r} \int \frac{\rho(\mathbf{r}')}{|\mathbf{r}-\mathbf{r}'|} d\mathbf{r}' \quad , \qquad (5.3.1.2)$$

The wavefunction was cast in the independent-particle approximation:

$$\psi = \phi_1\phi_2\phi_3\ldots\phi_n = \Pi\phi_i \qquad (5.3.1.3)$$

This representation of the wavefunction is inconsistent with the Pauli principle (which states that a fermion wavefunction must be antisymmetric with respect to particle interchange). The Schrödinger equation is transformed into a set of one-electron equations:

$$\varepsilon_i\phi_i(\mathbf{r}) = \{-1/2\,\nabla^2 + v_{e\text{-}n}(\mathbf{r}) + \int \frac{\rho(\mathbf{r}')}{|\mathbf{r}-\mathbf{r}'|} d\mathbf{r}'\}\phi_i(\mathbf{r}) \quad , \qquad (5.3.1.4)$$

The total electronic kinetic energy is simply the sum of the one-electron terms:

$$T_s = \sum_{i,\mathbf{k}} \left\langle \phi_{i\mathbf{k}} \mid -\frac{1}{2}\nabla^2 \mid \phi_{i\mathbf{k}} \right\rangle \qquad (5.3.1.5)$$

Surprisingly, the Hartree method gives many reasonable results. It correctly gives the shell structure of atoms, and the electron density distribution is quantitatively quite accurate too (most errors are at large distances from the nucleus). All this is due to the success of the independent-particle approximation to the kinetic energy (5.3.1.5): the Thomas-Fermi method (see below), which differs only in that it uses the electron-gas expression for the kinetic energy, fails to reproduce the shell structure of atoms.

The main drawback is the complete neglect of electronic exchange and correlation. Within the Hartree approximation, the electrons interact electrostatically with the average total electron density distribution. The calculated energy includes the spurious interaction of each electron with itself – the self-interaction error. The simplest way to remedy this error is to subtract, for each orbital, its contribution from the total electrostatic potential, and thus determine the electrostatic potential created by all other electrons and acting on the given orbital. This leads to an important general conclusion that the potential energy operator acts differently on different electronic orbitals, or, in other words, is orbital-dependent. In the Hartree method, electronic orbitals are uncorrelated, i.e. the probability of simultaneously finding electrons 1 and 2 in points $\mathbf{r}_1$ and $\mathbf{r}_2$, respectively, is:

$$P(\mathbf{r}_1,\mathbf{r}_2) = |\phi_1(\mathbf{r}_1)|^2 |\phi_2(\mathbf{r}_2)|^2 \qquad (5.3.1.4)$$

This means that there will be a finite probability P for the two electrons to be at the same point at the same time. This is clearly wrong as the electrostatic repulsion of the electrons will keep them apart. This repulsion necessarily introduces some interelectronic correlations, lowering the interelectronic electrostatic energy relative to the Hartree energy (5.3.1.1). To include (at least partly) these correlations, one could modify the wavefunction (5.3.1.2), taking into account the Pauli principle. This is done in the Hartree-Fock method.

5.3.2. Hartree-Fock method.

This method is used in many practical calculations until today. It is based on the Hartree method, which was improved by V.A. Fock, who took into account electron exchange energy and antisymmetry of the wavefunction.

The Hartree-Fock equations take the form:

$$\hat{\mathbf{f}}\,\phi_i(\mathbf{r}) = \varepsilon_i\phi_i(\mathbf{r}) \ , \qquad (5.3.2.1)$$

where ϕ_i are one-electron wavefunctions, ε_i are the Hartree-Fock eigenvalues (in the approximation known as the Koopmans' theorem, Hartree-Fock eigenvalues are equal to the minus orbital ionisation energies. This approximation, assuming that no relaxation of the electronic structure takes place on ionisation, works reasonably well).

The operator $\hat{\mathbf{f}}$ is known as the Fock operator; writing it explicitly, (5.3.2.1) takes the form:

$$\varepsilon_i\phi_i(\mathbf{r}) = \{-1/2\nabla^2 + v_{e\text{-}n}(\mathbf{r}) + \int \frac{\rho(\mathbf{r}')}{|\mathbf{r}-\mathbf{r}'|}\,d\mathbf{r}'\}\phi_i(\mathbf{r}) - \sum_j \delta_{\sigma i,\sigma j}\int d\mathbf{r}' \frac{\phi_j^*(\mathbf{r}')\phi_i(\mathbf{r}')}{|\mathbf{r}-\mathbf{r}'|}\,\phi_j(\mathbf{r}), \qquad (5.3.2.2)$$

where the third term is the Hartree potential, and the fourth term is the (exact) exchange potential. The exchange contribution improves agreement with experiment and completely cancels the self-interaction error. The exchange potential is non-local since it is determined by the wavefunction in all points of space; the exchange operator acts differently on different orbitals. Its non-locality renders the Hartree-Fock (HF) method computationally very expensive. The main effects of exchange are: 1. Hund's rule for atoms (e.g., each degenerate energy level is filled so as to create the maximum number of unpaired electrons with the same spin), 2. Electron pairing in covalent bonds, 3. Stabilisation of the ferromagnetic state in solids containing atoms with unpaired electrons.

The HF wavefunction of an N-electron system is a single Slater determinant composed of one-electron wavefunctions:

$$\psi_{HF} = \frac{1}{\sqrt{N!}}\begin{vmatrix} \phi_1(\mathbf{r}_1,\sigma_1) & \phi_1(\mathbf{r}_2,\sigma_2) & \ldots & \phi_1(\mathbf{r}_N,\sigma_N) \\ \phi_2(\mathbf{r}_1,\sigma_1) & \phi_2(\mathbf{r}_2,\sigma_2) & \ldots & \phi_2(\mathbf{r}_N,\sigma_N) \\ \ldots & \ldots & \ldots & \ldots \\ \phi_N(\mathbf{r}_1,\sigma_1) & \phi_N(\mathbf{r}_2,\sigma_2) & \ldots & \phi_N(\mathbf{r}_N,\sigma_N) \end{vmatrix} \ , \qquad (5.3.2.3)$$

where $\phi_i(\mathbf{r}_i,\sigma_i)$ denote spin-orbitals (represented as products of spatial orbitals and spin wavefunctions), σ_i – spins. Swapping particles means swapping columns of the determinant (5.3.2.3), which automatically changes the sign of the wavefunction in agreement with the Pauli principle. A single determinant is the simplest form for an antisymmetric wavefunction, and the HF method generates the best (i.e., the lowest-energy) single-determinantal wavefunction.

The probability of finding two electrons with spins σ_1 and σ_2 simultaneously at points r_1 and r_2, respectively, is (Thijssen, 1999):

$P(\mathbf{r}_1\sigma_1,\mathbf{r}_2\sigma_2)=$

$$=\frac{1}{N(N-1)}\sum_{k,l}[\,|\phi_k(\mathbf{r}_1,\sigma_1)|^2|\phi_l(\mathbf{r}_2,\sigma_2)|^2 - \phi_k^*(\mathbf{r}_1,\sigma_1)\phi_k(\mathbf{r}_2,\sigma_2)\phi_l^*(\mathbf{r}_2,\sigma_2)\phi_l(\mathbf{r}_1,\sigma_1)] \quad (5.3.2.4)$$

Using eq. (5.3.2.4), it can be shown (Thijssen, 1999) that for electrons having opposite spins, the second term vanishes, and the probability is the same as in Hartree method (eq. (5.3.1.4))– uncorrelated. When electrons have the same spin, the probability according to eq. (5.3.2.4) is drastically different from the uncorrelated value (5.3.1.4) – e.g., two such electrons cannot be found at the same point of space simultaneously (P=0). Effectively, there is an exchange hole around each electron, where electrons having the same spin have a reduced probability to enter. In reality, each electron also carries with it a correlation hole, but correlation effects are neglected in the HF approach.

For atoms and molecules, HF calculations have become a rather successful routine. Almost all HF studies of crystals have been performed with the CRYSTAL (Dovesi et al., 1996) code implementing non-relativistic HF theory for periodic structures (crystals, polymers, surfaces). A number of impressive studies have been performed for minerals – e.g., $MgSiO_3$ ilmenite (Nada et al., 1992) and perovskite (D'Arco et al., 1993b, 1994), sellaite MgF_2 (Catti et al., 1991), SiO_2 polymorphs – quartz, cristobalite, trydimite (Silvi et al., 1991; Silvi, 1991; Nada et al., 1990), stishovite and hypothetical high-pressure SiO_2 phases (Nada et al., 1990; Sherman, 1992), spinel-like Mg_2SiO_4 (Silvi, 1991), periclase MgO (Silvi, 1991), corundum Al_2O_3 (Salasco et al., 1991; Silvi, 1991), kaolinite $Al_2[Si_2O_5](OH)_4$ (Hess, Saunders, 1992), Si-mordenite $Si_{48}O_{96}$ (White & Hess, 1993), lizardite $Mg_3[Si_2O_5](OH)_4$ (Smrcok & Benco, 1996), brucite $Mg(OH)_2$ (D'Arco et al., 1993a), pyrope $Mg_3Al_2[SiO_4]_3$ (D'Arco et al., 1996), and many others. Preliminary results exist for the Al_2SiO_5 phases - andalusite and sillimanite (Silvi, 1991). A very interesting review of HF method and its applications to crystals is given in Dovesi et al. (1992).

The HF method is very accurate in predicting atomic energies and total energies of molecules and solids, and often gives accurate electron densities. However, binding energies in molecules and solids are always severely underestimated, typically by 20-40% (Dovesi et al., 1992; Dovesi, 1996). This is due to the correlation error, which is not completely cancelled when calculating energy

differences for processes involving breaking of electron pairs. Applying an *a posteriori* correction based on application of a correlation density functional to the HF electron density, allows one to recover typically ~80% of the correlation energy (Dovesi, 1996). This *a posteriori* correction method often improves the HF results and appears to give good predictions of chemical reaction energies (Catti et al., 1994; D'Arco et al., 1996); atomisation energies obtained using this approach are ~5-10% underestimated.

HF eigenvalues give a reasonable approximation to the experimental ionisation potentials and electron affinities of atoms and ions, but turn out to be very poor in modelling band gaps and optical excitation spectra in solids due to the correlation error and errors associated with the approximation of the Koopmans' theorem in condenced matter (Pisani, 1996).

Neglect of correlation deteriorates the predicted structures (bonds are usually ~1-3% too long; for the compounds of the 5^{th} period elements they are ~10% too long! – Aprá et al., 1991) and leads to a ~10% overestimation of the vibrational frequencies. The importance of correlation is higher for heavy elements and their compounds. Van der Waals forces, coming purely from correlation, are neglected in the HF approximation.

Electron correlation is fundamental for the metallic state, for which HF method fails completely (Pisani, 1996). E.g., the simplest metal – homogeneous electron gas – is predicted by HF method to have a zero density of states at the Fermi level, i.e. to be an insulator.

By definition, the difference between the HF energy and the exact non-relativistic energy is called the correlation energy. This is confusing since the HF wavefunction is already correlated – see (5.3.2.4). From now and on I shall mention correlation only in the meaning just introduced, and differentiate between exchange (included in HF method) and correlation effects (neglected in HF method). There are two main types of correlation effects: 1. 'Dynamical' correlation – in their instantaneous positions, electrons correlate their movement so as to avoid each other, irrespective of their spins. Van der Waals forces (coming from 'instantaneous dipoles' on atoms) are one of the manifestations of this effect, 2. Non-dynamical (or 'left-right') correlation – effect responsible for localisation of the exchange-correlation hole in molecules and solids (see below).

The significance of electron correlation indicates the need to go beyond the HF theory. For atoms and molecules, configuration interaction (CI) methods are very

popular. A single Slater determinant (5.3.2.3) cannot describe a many-electron wavefunction completely, but Slater determinants composed of one-electron spin-orbitals form a complete basis set for any antisymmetric wavefunction (Thijssen, 1999). This means that all correlation effects can be taken into account in the CI methods, which represent the many-electron wavefunction as a linear combination of determinants with variationally determined coefficients. Each of the determinants is obtained from the HF ground state by excitation. The first determinant is the ground-state HF wavefunction, the second one is the first excited state, etc. The excited wavefunctions are found from the ground-state HF spectrum – usually without optimising the excited state wavefunctions. When such optimisation is performed, the convergence of results with the number of configurations significantly increases; this is the so-called multi-configuration self-consistent field (MCSCF) method. The computational cost of CI calculations is enormous even for small systems and quickly grows with the number of electrons N (as $\sim N^{6\text{-}7}$); this is why only the lowest excited states are usually taken into account. Approximate CI calculations have a serious drawback – they are not size-consistent (i.e., the energy of a system with n infinitely separated atoms is not equal to n times the energy of one isolated atom). Full CI calculation (which is size-consistent) encounters an exponential growth with N of the number of determinants that need to be included, and can be done only for very small molecules. None of the CI methods can be applied to condensed matter. Other methods incorporating correlation exist for solids; among these, quantum Monte Carlo methods promise a great future (see Foulkes et al., 2001). Perturbation theory can also be used to study correlation effects. Currently, the most popular methods are based on density functional theory (DFT).

5.3.3. Density functional theory (DFT) – introduction.

Hohenberg-Kohn theorems. DFT is a revolutionary theory in quantum mechanics: it formulates quantum mechanics in terms of the observable and tractable electron density instead of the extremely complicated and unobservable wavefunction. Currently DFT is the main method used in quantum-mechanical studies of solids; it competes with CI methods in molecules. The most impressive achievements of computational mineral physics are associated with DFT.

Pre-DFT works include important developments in 1927 by L.H. Thomas and E. Fermi, and the Xα-method proposed by J.C. Slater in 1951. The rigorous foundation

of DFT, however, was laid in the work of Hohenberg and Kohn (1964) and their followers, who formulated and proved two remarkable theorems:

Theorem 1. The electron density $\rho(\mathbf{r})$ determines (within an additive constant) the external potential, i.e. the potential due to the nuclei.

Theorem 2. In the ground state the total energy of a system is variational with respect to the electron density, i.e. the exact $\rho(\mathbf{r})$ provides the minimum possible energy for the ground state.

The $\rho(\mathbf{r})$ determines the total number of electrons and the external potential, which implies that the whole Hamiltonian in (5.3.2) and, consequently, the total energy and wavefunction can all be in principle determined from the electron density alone. The first Hohenberg-Kohn theorem shows that there exists a universal total energy functional $E[\rho]$, and that all ground-state properties are completely determined by the electron density. The first theorem applies to the ground and excited states alike; the variational principle of the second theorem is applicable only to the ground state and, as shown by Gunnarsson and Lundqvist, also to the lowest-energy excited states of a given symmetry (see Jones & Gunnarsson, 1989).

The total electronic energy can be written as:

$$E[\rho] = \mathrm{T}[\rho] + E_{\text{e-n}}[\rho] + E_{\text{e-e}}[\rho] = \mathrm{T}[\rho] + \int d\mathbf{r}\, \rho(\mathbf{r}) v_{\text{e-n}}(\mathbf{r}) + E_{\text{e-e}}[\rho] \quad , \qquad (5.3.3.1)$$

where $\mathrm{T}[\rho]$ is the kinetic energy functional and $v_{\text{e-n}}(\mathbf{r})$ is the potential due to the nuclei. The problem is that the exact functional $E[\rho]$ is unknown and is likely to be exceedingly complicated, because it must be non-local.

The Thomas-Fermi model is the lowest-order approximation to $E[\rho]$. The kinetic energy functional in this model is based on the homogeneous electron gas expression:

$$\mathrm{T}^{\mathrm{TF}}[\rho] = {}^{3}/_{10}(3\pi^2)^{2/3} \int \mathrm{d}r\, \rho^{5/3} \qquad (5.3.3.2)$$

and the electron-electron interactions are approximated by the Hartree expression (5.3.1.1-2). The Thomas-Fermi-Dirac model also includes approximate exchange energy:

$$E_{\mathrm{x}}[\rho] = \int \mathrm{d}r\, \rho(\mathbf{r}) e_{\mathrm{x}}(\rho(\mathbf{r})) = -\frac{3}{4\pi}(3\pi^2)^{1/3} \int \mathrm{d}r\, \rho^{4/3} \quad , \qquad (5.3.3.3)$$

where $e_{\mathrm{x}}(\rho(\mathbf{r}))$ is the exchange energy of a homogeneous electron gas per 1 electron.

The errors in the kinetic energy associated with these approximations are too large for these approximations to be useful; e.g., the shell structure of atoms cannot be

accounted for[30]. By the Teller theorem, no binding is permitted for molecules and solids in the Thomas-Fermi (and Thomas-Fermi-Dirac) models. Introduction of the density gradients in the energy expression does permit some binding, but the inclusion of successively higher-order gradients of the density is not a way to eventually obtain an accurate representation of the kinetic and other energy terms: the sixth-order gradient expansion of the kinetic energy diverges for atoms, and no further expansion can be constructed (Parr & Yang, 1989). In a way, Hohenberg-Kohn theorems provide an exactification of Thomas-Fermi theory (Kohn, 1999a), but only in principle, because known approximate kinetic energy functionals fail to give reasonable results.

Kohn-Sham method. Kohn and Sham (1965) devised a method, which enables accurate practical calculations. As Kohn (1999a) described it, this method is a formal exactification of the Hartree method. It starts with a system of non-interacting electrons having the same electron density as the real system of interacting electrons. We introduce a wavefunction[31] and calculate the kinetic energy T_s of this fictitious non-interacting system as a sum over all occupied orbitals:

$$T_s = \sum_{i,\mathbf{k}} \left\langle \phi_{i\mathbf{k}} \mid -\frac{1}{2}\nabla^2 \mid \phi_{i\mathbf{k}} \right\rangle \qquad (5.3.3.4)$$

T_s is a much better estimate of the kinetic energy than (5.3.3.2), as we know from the experience with the Hartree method (Kohn, 1999a)[32]. We also know that it gives a lower bound to the true kinetic energy (Parr & Yang, 1989):

$$T_s[\rho] \le T[\rho] \qquad (5.3.3.5)$$

The aim of the Kohn-Sham method is to overcome the difficulty in constructing a density functional for the kinetic energy; the price to be paid for that is the introduction of orbitals[33].

The total electronic energy is:

$$E[\rho] = T_s[\rho] + \int d\mathbf{r}\, \rho(\mathbf{r}) v_{e\text{-}n}(\mathbf{r}) + \tfrac{1}{2} \int d\mathbf{r}\, \rho(\mathbf{r}) v_H(\mathbf{r}) + E_{xc}[\rho]\,, \qquad (5.3.3.6)$$

---

[30] Thomas-Fermi model also incorrectly results in the ionisation potentials and atomic sizes equal for all elements, i.e. it does not reflect the Periodic Law (Landau & Lifshitz, 2001b).

[31] Which in Kohn-Sham theory is but an auxiliary construction with no real physical meaning other than a tool to calculate the kinetic energy with a reasonable accuracy.

[32] Still, there are some errors in the kinetic energy. In DFT, these errors are included in the exchange-correlation term.

[33] Note that in Thomas-Fermi and related models there was no wavefunction and no orbitals at all.

i.e. it is a sum of the non-interacting kinetic energy, energy of electrons due to the interaction with the nuclei, Hartree energy, and exchange-correlation energy. All the contributions in (5.3.3.6) are known exactly, apart from the exchange-correlation energy functional $E_{xc}[\rho]$, which has to be somehow approximated. By definition (5.3.3.6), the difference between T_s and the exact kinetic energy T is included in the exchange-correlation energy. Because of that, the virial theorem (5.3.6) does not hold in the Kohn-Sham DFT – even if the exact functional were known (Parr & Yang, 1989).

The formidable many-body problem (5.3.1) was reduced by Kohn and Sham (1965) to a set of coupled one-electron equations mathematically similar to (but simpler than) the Hartree-Fock equations:

$$\{-1/2\nabla^2 + v_{e\text{-}n}(\mathbf{r}) + v_H[\rho(\mathbf{r})] + v_{xc}[\rho(\mathbf{r})]\}\phi_i(\mathbf{r}) = \varepsilon_i\phi(\mathbf{r}) \qquad (5.3.3.7)$$

The exchange-correlation potential $v_{xc}(\mathbf{r})$ is defined as:

$$v_{xc}(\mathbf{r}) = \frac{\delta E_{xc}[\rho(\mathbf{r})]}{\delta\rho(\mathbf{r})} \qquad (5.3.3.8)$$

The orbitals $\phi_i(\mathbf{r})$ and eigenvalues ε_i are physically meaningless here – the meaningful quantities are the total energy and the total electron density:

$$\rho(\mathbf{r}) = \sum_i \phi_i^2(\mathbf{r}) \qquad (5.3.3.9)$$

<u>*Kohn-Sham orbitals.*</u> Although the Kohn-Sham orbitals were introduced only as a means to get the kinetic energy, and these orbitals do not have any strict physical meaning, in all practical calculations an Aufbau principle is assumed to hold, where only the lowest-energy orbitals are occupied (Parr & Yang, 1989). Kohn-Sham orbitals (and densities of states) are often used in chemical studies; Baerends & Gritsenko (1997) advocated their use on general grounds, and Stowasser and Hoffmann (1999) have demonstrated on several cases that these orbitals are similar in shape and energy to the more meaningful Hartree-Fock and orbitals of the extended Hückel method. A few exact results exist; among them is the Janak theorem (Parr & Yang, 1989), which states that the eigenvalues are the derivatives of the total energy with respect to the orbital occupancies:

$$\left(\frac{\partial E}{\partial n_i}\right) = \varepsilon_i \qquad (5.3.3.10)$$

This contrasts with the Koopmans' theorem in Hartree-Fock theory. Only for the highest occupied orbital, as it has been proved (see Jones & Gunnarsson, 1989), is

the eigenvalue equal to minus the ionisation potential of the system. However, this result, proved in the exact DFT, does not hold for DFT with approximate functionals.

For band gaps E_g in solids, an interesting result exists (Jones & Gunnarsson, 1989):

$$E_g = \Delta\varepsilon + \Delta \,, \tag{5.3.3.11}$$

where $\Delta\varepsilon$ is the eigenvalue gap, and Δ is a correction arising from exchange-correlation effects. This correction is present even in the case of the exact exchange-correlation functional, but it is not well known how large it is. In the extreme case of Mott insulators, when the eigenvalue gaps are very small (or zero), it probably is of the order of the band gap itself, up to several eV. Such approximate exchange-correlation functionals as LDA or GGA usually give eigenvalue gaps smaller than experimental band gaps by ~30-50%; it is unclear whether it is mainly due to large Δ or true errors of the functionals.

The sum of the occupied eigenvalues:

$$\Sigma\varepsilon_i = T_s[\rho] + \int d\mathbf{r}\, \rho(\mathbf{r}) v_{eff}(\mathbf{r}) =$$

$$= T_s[\rho] + \int d\mathbf{r}\, \rho(\mathbf{r}) v_{e\text{-}n}(\mathbf{r}) + \int d\mathbf{r}\, \rho(\mathbf{r}) v_{xc}(\mathbf{r}) + 2E_H[\rho] \tag{5.3.3.12}$$

is related to the total electronic energy:

$$E[\rho] = \Sigma\varepsilon_i - E_H[\rho] - \int d\mathbf{r}\, \rho(\mathbf{r}) v_{xc}(\mathbf{r}) + E_{xc}[\rho] \,, \tag{5.3.3.13}$$

Exchange-correlation hole. The DFT exchange-correlation energy includes a term corresponding to exchange (like in Hartree-Fock theory), terms corresponding to correlation, and the difference between the kinetic energy of the real system of interacting electrons and the kinetic energy of a model non-interacting system having the same electron density. Let us consider the physics of exchange-correlation in some detail.

The exchange-correlation energy is defined as:

$$E_{xc}[\rho] = \tfrac{1}{2} \int d\mathbf{r} \int \frac{\rho(\mathbf{r}) \rho_{xc}(\mathbf{r}, \mathbf{r}')}{|\mathbf{r} - \mathbf{r}'|} d\mathbf{r}' \,, \tag{5.3.3.14}$$

i.e. it is just the classical electrostatic energy of interaction between an electron and its exchange-correlation hole $\rho_{xc}(\mathbf{r},\mathbf{r}')$. If the reference electron is sitting at the point $\mathbf{r}$, the exchange-correlation hole $\rho_{xc}(\mathbf{r},\mathbf{r}')$ shows how much the probability of finding an electron at the point $\mathbf{r}'$ is decreased (compared to the time-averaged electron density $\rho(\mathbf{r}')$. A number of simple rules exist.

The exchange-correlation hole can never exceed (by the absolute value) the charge density available at the point $\mathbf{r}'$:

$$-\rho_{xc}(\mathbf{r},\mathbf{r}') \leq \rho(\mathbf{r}') \qquad (5.3.3.15)$$

The $\rho_{xc}(\mathbf{r},\mathbf{r}')$ can be split into the exchange hole $\rho_x(\mathbf{r},\mathbf{r}')$ and correlation hole $\rho_c(\mathbf{r},\mathbf{r}')$:

$$\rho_{xc}(\mathbf{r},\mathbf{r}') = \rho_x(\mathbf{r},\mathbf{r}') + \rho_c(\mathbf{r},\mathbf{r}') , \qquad (5.3.3.16)$$

and the following important properties can be formulated:

$$\int d\mathbf{r}' \rho_{xc}(\mathbf{r},\mathbf{r}') = \int d\mathbf{r}\, \rho_x(\mathbf{r},\mathbf{r}') = -1 \quad \text{(exchange hole sum rule)} \qquad (5.3.3.17)$$

$$\rho_x(\mathbf{r},\mathbf{r}') \leq 0 \quad \text{(non-positiveness of the exchange hole)} \qquad (5.3.3.18)$$

$$\int d\mathbf{r}' \rho_{xc}(\mathbf{r},\mathbf{r}') = 0 \quad \text{(correlation hole sum rule)} \qquad (5.3.3.19)$$

While the exchange hole is always non-positive, the correlation hole is positive in some places and negative in others, integrating in total to zero. The effect of correlation is to make the exchange-correlation hole deeper and shorter-ranged, with a negative on-top correlation hole:

$$\rho_c(\mathbf{r},\mathbf{r}) \leq 0 \qquad (5.3.3.20)$$

The on-top exchange hole is determined by the spin densities $\rho\uparrow(\mathbf{r})$ and $\rho\downarrow(\mathbf{r})$ (Perdew & Kurth, 1998):

$$\rho_x(\mathbf{r},\mathbf{r}) = -[\rho^2\uparrow(\mathbf{r}) + \rho^2\downarrow(\mathbf{r})]/\rho(\mathbf{r}) \qquad (5.3.3.21)$$

In molecules and solids, both exchange and correlation holes can be strongly delocalised over many centres, but their sum – the exchange-correlation hole – is always well localised (largely, within a typical atomic volume – see Fig. 5-1). The exchange-correlation hole can be positive, unlike the exchange hole, eq. (5.3.3.18). The important property of 'short-sightedness' of electrons is one of the main justifications of the local density approximation (LDA). The long-ranged part of the correlation, which exactly cancels the long-range part of the exchange, is called 'right-left' correlation. As is clear from the present discussion and as was elucidated by J. Slater in 1950s, LDA and other local approximations (e.g., GGA) automatically include 'right-left' correlation by using a localised exchange-correlation hole.

The so-called pair correlation function $h_{xc}(\mathbf{r},\mathbf{r}')$ can be introduced (Parr & Yang, 1989):

$$\rho_{xc}(\mathbf{r},\mathbf{r}') = h_{xc}(\mathbf{r},\mathbf{r}')\rho(\mathbf{r}') \qquad (5.3.3.22)$$

The probability of finding an electron at $\mathbf{r}'$, when the reference electron is at $\mathbf{r}$, is:

$$\rho(\mathbf{r},\mathbf{r}') = \rho(\mathbf{r}') + \rho_{xc}(\mathbf{r},\mathbf{r}') = [h_{xc}(\mathbf{r},\mathbf{r}') + 1]\rho(\mathbf{r}') , \qquad (5.3.3.23)$$

where for a homogeneous electron gas $g(|\mathbf{r}'-\mathbf{r}|) = [h_{xc}(\mathbf{r},\mathbf{r}') + 1]$ is called the radial distribution function. This function, obtained in the HF approximation for the three-dimensional homogeneous electron gas, is given in Fig. 5-2. It is easy to see that for like-spin electrons Hartree-Fock approximation introduces no correlation, as was stated before, in eq. (5.3.2.4).

More accurate quantum Monte Carlo results (Ortiz & Ballone, 1994) for the radial distribution function are given in Fig. 5-3.

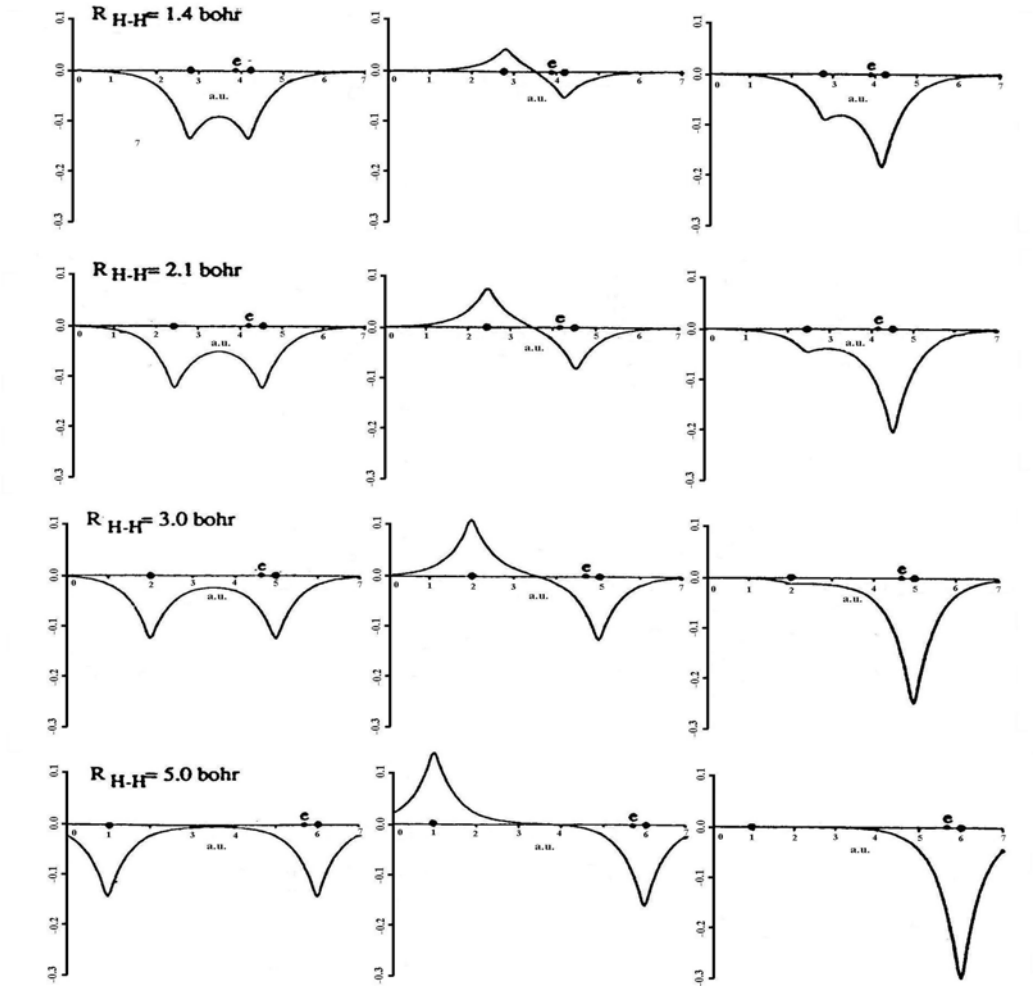

Fig. 5-1. Exchange, correlation, and total exchange-correlation holes in H_2 molecule. After Baerends & Gritsenko (1997). The nuclei are shown by black solid circles. The reference electron is located 0.3 bohr to the left of the right nucleus.

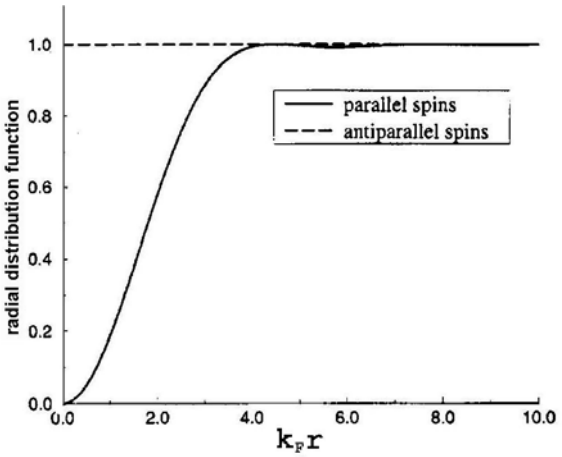

Fig. 5-2. Radial distribution function for a homogeneous three-dimensional electron gas: Hartree-Fock approximation. After Foulkes et al. (2001). For a homogeneous electron gas, the pair correlation function depends only on the interelectronic distance r and the Fermi wavevector $k_F = (3\pi^2\rho)^{1/3}$.

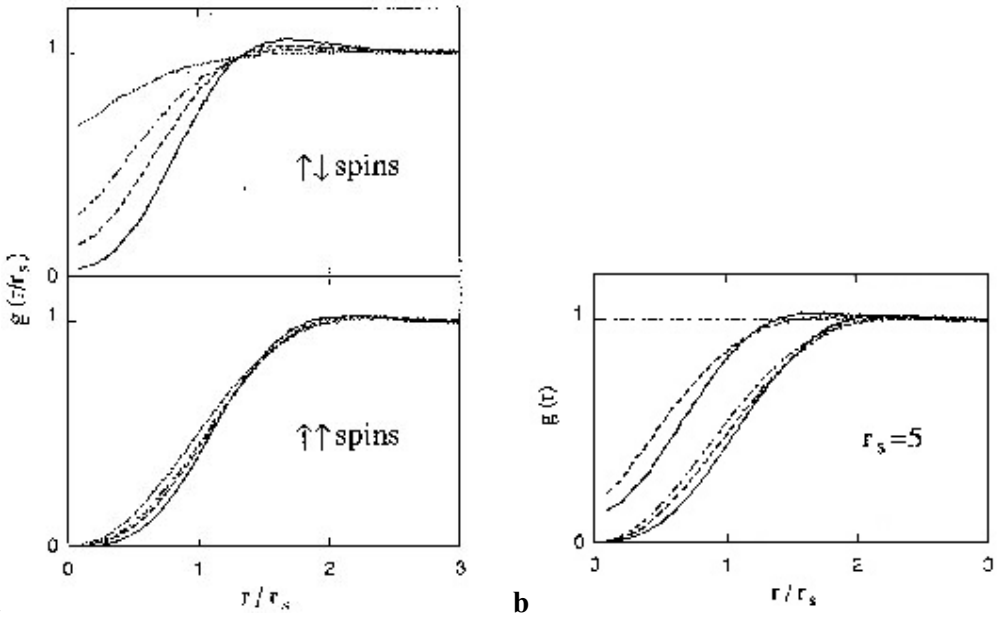

Fig. 5-3. Results of Ortiz and Ballone (1994) for a homogeneous spin-unpolarised electron gas. (a) Diffusion Monte Carlo results for r_S = 1 (dotted line), r_S = 3 (dash-dotted line), r_S = 5 (dashed line), r_S = 10 (solid line). (b) Spin-parallel (lower three curves) and antiparallel (upper curves) pair correlation functions for r_S = 5 calculated in the Hartree-Fock (dash-dotted lines), variational Monte Carlo (dashed line), diffusion Monte Carlo (solid line) methods. The Wigner-Seitz radius is defined as $r_S = (^4/_3\pi\rho)^{-1/3}$.

Formal properties of the exchange-correlation functional. Now let us consider the exchange-correlation functional. Even though the exact functional is unknown, a number of its important formal properties are known (Perdew & Kurth, 1998). These properties are essential in the derivation of good approximate functionals.

First of all, the exchange energy is negative and correlation energy is non-positive:

$$E_x[\rho] < 0 \qquad (5.3.3.24)$$

$$E_c[\rho] \leq 0 \qquad (5.3.3.25)$$

Second, exact exchange completely corrects the self-interaction error. For any one-electron system, exchange potential cancels the Hartree potential:

$$v_x(\mathbf{r})|_{N=1} = - v_H(\mathbf{r}) \qquad (5.3.3.26)$$

and there is no correlation in a one-electron system:

$$v_c(\mathbf{r})|_{N=1} = 0 \qquad (5.3.3.27)$$

Several exact uniform scaling properties are known. In such scaling, we replace all the coordinates $\mathbf{r}$ with scaled coordinates $\gamma\mathbf{r}$. The density scales as:

$$\rho_\gamma(\mathbf{r}) = \gamma^3\rho(\mathbf{r}) \qquad (5.3.3.28)$$

For the Hartree energy $[E_H[\rho] = \frac{1}{2}\int d\mathbf{r}\ \rho(\mathbf{r})v_H(\mathbf{r})]$ the scaling is:

$$E_H[\rho_\gamma] = \gamma E_H[\rho] \qquad (5.3.3.29)$$

The kinetic energy of a non-interacting system scales as:

$$T[\rho_\gamma] = \gamma^2 T[\rho]\ , \qquad (5.3.3.30)$$

and the scaling relation for the exchange energy is

$$E_x[\rho_\gamma] = \gamma E_x[\rho] \qquad (5.3.3.31)$$

For the correlation energy, there exist the following scaling inequalities:

$$E_c[\rho_\gamma] > \gamma E_c[\rho] \qquad (\gamma > 1)$$

$$E_c[\rho_\gamma] < \gamma E_c[\rho] \qquad (\gamma < 1) \qquad (5.3.3.32)$$

A number of inequalities play an important role in DFT. The Lieb-Thirring hypothesis states that the kinetic energy of a non-interacting system is greater than or equal to the Thomas-Fermi esimate:

$$T_s[\rho] \geq T^{TF}[\rho] = {}^3/_{10}(3\pi^2)^{2/3}\int d\mathbf{r}\ \rho^{5/3} \qquad (5.3.3.33)$$

Of special importance is the Lieb-Oxford bound for the exchange-correlation energy:

$$|E_{xc}[\rho]| \leq 2.273|E_{x,LDA}[\rho]| = 2.273\,\frac{3}{4\pi}(3\pi^2)^{1/3}\int d\mathbf{r}\ \rho^{4/3} \qquad (5.3.3.34)$$

We also know the exact spin scaling relations for the exchange energy:

$$E_x[\rho\uparrow,\rho\downarrow] = \tfrac{1}{2}E_x[2\rho\uparrow,0] + \tfrac{1}{2}E_x[0,2\rho\downarrow] \qquad (5.3.3.35)$$

and for the non-interacting kinetic energy:

$$T_S[\rho\uparrow,\rho\downarrow] = \tfrac{1}{2}T_S[2\rho\uparrow,0] + \tfrac{1}{2}T_S[0,2\rho\downarrow] \qquad (5.3.3.36)$$

These relations play the central role in DFT for spin-polarised systems. Unfortunately, there is no simple spin scaling relation for the correlation energy.

Other notations are useful, e.g. the spin density:

$$\rho_{spin}(\mathbf{r}) = \rho\uparrow(\mathbf{r}) - \rho\downarrow(\mathbf{r}) \qquad (5.3.3.37)$$

and dimensionless spin polarisation ranging between 0 and 1:

$$\xi(\mathbf{r}) = |\rho\uparrow(\mathbf{r}) - \rho\downarrow(\mathbf{r})|/[\rho\uparrow(\mathbf{r}) + \rho\downarrow(\mathbf{r})] \qquad (5.3.3.38)$$

It is possible to extend DFT to treat non-collinear magnetism (see Hobbs et al., 2000 for a practical implementation).

As it was noted before, in exact DFT the highest-occupied eigenvalue is equal to minus the ionisation potential of the system; it must change discontinuously at an integer number Z of electrons:

$$\varepsilon_{HO} = \left(\frac{\partial E}{\partial n_{HO}}\right) = -I \quad (Z\text{-}1 < N < Z)$$
$$-A \quad (Z < N < Z\text{+}1) \quad , \qquad (5.3.3.39)$$

where I and A are the ionisation potential and electron affinity of the Z-electron system (e.g., atom). The exchange-correlation potential has the following asymptotical behaviour at $r\to\infty$:

$$v_{xc}(\mathbf{r}) \to -\frac{1}{|\mathbf{r}|} + I + \varepsilon_{HO} \quad , \qquad (5.3.3.40)$$

which reduces to $-\frac{1}{|\mathbf{r}|}$ for the exact functional. In approximate DFT the derivative discontinuity (5.3.3.39) cannot be reproduced; instead, we approximately get

$$\varepsilon_{HO} \approx -(I+A)/2 \quad , \qquad (5.3.3.41)$$

which confers the meaning of minus the Mulliken electronegativity on the highest-occupied eigenvalue ε_{HO}. Consequently, for the eigenvalue gap in (5.3.3.8) we have:

$$\Delta\varepsilon = (I - A_2)/2 \, , \qquad (5.3.3.42)$$

where A_2 is the affinity for the second electron, and the band gap is:

$$E_g = I - A \, , \qquad (5.3.3.43)$$

which gives the exchange-correlation correction Δ in (5.3.3.8):

$$\Delta = (I - 2A + A_2)/2 \qquad (5.3.3.44)$$

5.3.4. Density functional theory (DFT) – approximate functionals.

In this section I shall expose some of the theory behind the most popular approximate DFT methods. The performance of these methods is illustrated by the

comparison between different methods and experiment, demonstrated in Tables 5-1 to 5-5.

Local density approximation (LDA). LDA is the simplest approximation to $E_{xc}[\rho]$; although the local expression (5.3.3.2) for the kinetic energy is very poor for atoms, local exchange-correlation is rather accurate. In LDA, the kinetic energy is calculated from orbitals using (5.3.3.4), rather that from the electron-gas formula (5.3.3.2).

The exchange-correlation energy is calculated as:

$$E_{xc}[\rho] = \int d\mathbf{r}\, \rho(\mathbf{r}) e_{xc}(\rho(\mathbf{r})) \quad , \tag{5.3.4.1}$$

where the exchange energy density of a homogeneous electron gas is known exactly from (5.3.3.3):

$$e_x(\rho) = -\frac{3}{4\pi}(3\pi^2)^{1/3}\rho^{1/3} = -\frac{3}{4\pi}(9\pi/4)^{1/3} r_s^{-1} \ , \tag{5.3.4.2}$$

and the correlation energy density is known very accurately from quantum Monte Carlo simulations of Ceperley and Alder (1980) and Ortiz and Ballone (1994). An analytical representation satisfying the exactly known high- and low-density analytical limits and fitting the numerical quantum Monte Carlo results for the spin-unpolarised case, is (Perdew & Zunger, 1981):

$$e_c(\rho) = 0.0311 \ln r_s - 0.048 + 0.0020 r_s \ln r_s - 0.0116 r_s \quad (r_s < 1),$$

$$e_c(\rho) = -0.1423/(1 + 1.0529\sqrt{r_s} + 0.3334 r_s) \quad (r_s > 1) \tag{5.3.4.3}$$

Fig. 5-4 shows different contributions to the total energy of the homogeneous electron gas and clearly indicates the importance of the correlation contribution.

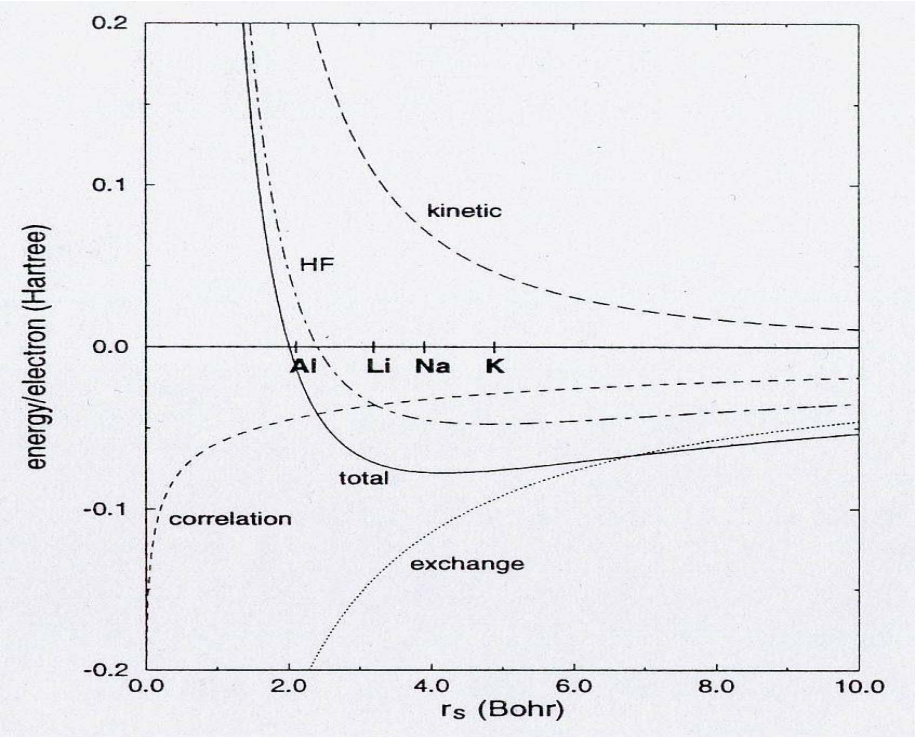

Fig. 5-4. Energy contributions for the homogeneous electron gas (per 1 electron). Average r_s values of the valence electrons of several metals are shown. After Pisani (1996).

Perdew and Wang (1992) expressed the correlation energy of the homogeneous electron gas more accurately by a single analytical formula, which also satisfies the high- and low-density limits and quantum Monte Carlo data:

$$e_c(\rho) = -2c_0(1+\alpha_1 r_s)\ln[1+\frac{1}{2c_0(\beta_1 r_s^{1/2} + \beta_2 r_s + \beta_3 r_s^{3/2} + \beta_4 r_s^2)}] \ , \qquad (5.3.4.4)$$

where c_0=0.031091 and c_1=0.046644, $\beta_1 = \frac{1}{2c_0}\exp(-\frac{c_1}{2c_0})$=7.5957, α_1=0.21370, $\beta_2 = 2c_0\beta_1^2$= 3.5876, β_3=1.6382, and β_4=0.49294 for the spin-unpolarised (ξ=0) electron gas. For a fully spin-polarised case (ξ=1) c_0=0.015545 and c_1=0.025599, α_1=0.20548, β_3=3.3662, and β_4=0.62517.

The LDA generalised for spin-polarised systems is called LSDA (local spin density approximation). For the exchange energy we have a simple exact spin scaling relation (5.3.3.35), which implies:

$$e_x(\rho\uparrow,\rho\downarrow) = e_x(\rho)\frac{(1+\xi)^{4/3} + (1-\xi)^{4/3}}{2} \qquad (5.3.4.5)$$

The most popular spin-interpolation formula used for the correlation energy is that due to Vosko et al. (1980):

$$e_c(\rho\uparrow,\rho\downarrow) = e_c(\rho) + \alpha_c(\rho)\frac{f(\xi)}{f''(\xi)}(1-\xi^4) + [e_c(\rho,0) - e_c(\rho)]f(\xi)\xi^4 \quad , \qquad (5.3.4.6)$$

where $f(\xi)=\frac{(1+\xi)^{4/3}+(1-\xi)^{4/3}-2}{2^{4/3}-2}$, and $-\alpha_c(\rho)$ can be accurately represented by a function of the type (5.3.4.4) with c_0=0.016887, c_1=0.035475, α_1=0.11125, β_3=0.88026, β_4=0.49671.

LDA leads to significant errors in exchange (about -5%) and correlation (about +100%), but these largely cancel each other, explaining the successes of the LDA. This approximation does not give accurate exchange-correlation holes for atoms, but gives reasonable spherical averages for these holes – luckily, it is only the spherically-symmetric part of the multipole expansion that is important. In addition, and perhaps most importantly, LDA exactly satisfies all the sum rules (5.3.3.17) and (5.3.3.19) that are true for the exact functional. The self-interaction error is largely cancelled by the exchange-correlation potential; e.g., in the H atom ~95% of this error is cancelled at the LSDA level of theory (Thijssen, 1999). However, this error becomes important for highly localised electronic states (such as d-states in transition metal atoms). Perdew and Zunger (1981) devised a simple method to incorporate the self-interaction correction in the LDA approach (LDA+SIC). LDA+SIC offers a significant improvement for atomic energies, but is difficult to apply to crystals, where the electronic orbitals are usually represented by delocalised Bloch functions, whose self-interaction is zero[34].

The shortcomings of the LDA include the following: 1.Underestimation of the energies of isolated atoms – LDA treats well the valence electrons, but significantly underbinds the core electrons, 2. Overbinding (by ~20%) in molecules and crystals, 3. Bond lengths are usually ~1% too short, 4. Reaction barriers are usually too low compared to experiment, 5. Large errors for weakly bonded systems (e.g., hydrogen bonds), 6. van der Waals bonding cannot be treated correctly within the LDA, 7. Sometimes the energy differences between polymorphs are inaccurate (e.g., for quartz-stishovite the huge energy difference of ~0.5 eV is not reproduced: even the sign is wrong!), 8. Often a wrong ground state is predicted (e.g., paramagnetic fcc instead of ferromagnetic bcc for Fe), 9. Serious errors for many Mott insulators (often magnetic moments are underestimated or low-spin states are predicted to be

[34] In such cases, it is necessary to select and localise some orbitals (e.g., d- and f-orbitals of transition metal ions) – see Szotek & Temmerman (1993) for details and application to transition metal oxides.

more stable, LDA fails to properly split the d-levels of transition metal ions and predicts no band gap[35]), 10. In many cases, the dissociation products are not neutral atoms, but atoms with non-physical fractional charges (due to the self-interaction error - see a very interesting paper by Becke (2000)).

These serious shortcomings inspire further developments of functionals. The impressive successes of the LDA suggest it as a reference point in these developments.

Table 5-1. Total energies of atoms (in a.u.): comparison of experiment with several approximate methods. Data were taken from Perdew & Zunger (1981), Parr & Yang (1989), Lee & Martin (1997).

Atom	HF	LSDA	LSDA+SIC	GGA (PW91)	Exp.
H	-0.500	-0.479	-0.500	-0.500	-0.500
He	-2.86	-2.835	-2.918	-2.900	-2.904
Ne	-128.55	-128.228	-129.268	-128.947	-128.937
Ar	-526.82	-525.938	-528.289	-527.539	-527.60

Generalised gradient approximation (GGA). The most obvious way to construct an improved functional is to expand the exchange-correlation energy in powers of the density gradients. This approximation, called GEA (Gradient Expansion Approximation), exact for an electron gas with a slowly varying density, turns out to be worse than the LDA for atoms. The main reason of this is that GEA does not satisfy the sum rules (5.3.3.17) and (5.3.3.19). The short-range part of the exchange-correlation hole is improved over the LDA, but the long-range part is worsened and has spurious undamped oscillations, due to which GEA does not satisfy the sum rules and exchange hole sometimes becomes positive. It is possible to construct a very accurate functional by setting the exchange-correlation hole to zero everywhere the GEA exchange hole is positive and everywhere beyond a certain cut-off radius, chosen so as to enforce the sum rules.

Table 5-2. Exchange-correlation energies of atoms (in a.u.): comparison of LDA, GGA (PW91), and exact values. Data were taken from Parr & Yang (1989) and Perdew & Kurth (1998). In this table, GGA is represented by the PBE functional, numerically very similar to the PW91 functional, used in Table 5-1.

Atom	HF	LSDA	GGA	Exact

[35] This is artificially corrected by the LDA+U method, which enforces splitting of the d-levels.

			(PBE)	
H	-0.31	-0.29	-0.31	-0.31
He	-1.03	-1.00	-1.06	-1.09
Li	-1.78	-1.69	-1.81	-1.83
Ne	-12.11	-11.78	-12.42	-12.50

GGA is constructed in such a way as to preserve all the correct features of the LDA and add some more. There are several popular GGA functionals, the best of which seem to be the PW91 functional (Wang & Perdew, 1991) and a very similar functional PBE (Perdew et al., 1996) – below I will mainly describe their features. Good GGA exchange-correlation functionals satisfy several conditions:

- Reduce to GEA for slowly varying densities.
- Reduce to LDA for the homogeneous electron gas.
- Satisfy sum rules (5.3.3.17) and (5.3.3.19).
- Satisfy conditions (5.3.3.15,18,20).
- Have proper scaling (5.3.3.31,32).
- Have proper spin scaling (5.3.3.35).
- Obey the Lieb-Oxford bound (5.3.3.34).

GGA exchange is defined as:

$$E_x[\rho,\nabla\rho] = \int d\mathbf{r}\, F_x(s)\rho(\mathbf{r})e_x(\rho(\mathbf{r})) \ , \qquad (5.3.4.7)$$

where $e_x(\rho(\mathbf{r}))$ is the exchange energy of the homogeneous electron gas per 1 electron (given by (5.3.5.1)), and the exchange enhancement factor $F_x(s)$ is a function of the reduced density gradient s:

$$s = \frac{|\nabla\rho|}{2(3\pi)^{1/3}\rho^{4/3}(\mathbf{r})} = \frac{|\nabla\rho|}{2k_F\rho(\mathbf{r})} \qquad (5.3.4.8)$$

Set in this form, GGA exchange automatically has the correct scaling behaviour (5.3.3.31). For the total exchange-correlation functional the definition is:

$$E_{xc}[\rho,\nabla\rho] = \int d\mathbf{r}\, F_{xc}(\rho,s)\rho(\mathbf{r})e_x(\rho(\mathbf{r})) \ ^{36} \ , \qquad (5.3.4.9)$$

where the enhancement factor $F_{xc}(\rho,s)$ now depends on both the density and its reduced gradient. No GGA functional is expected to be accurate for $s>>1$; happily,

[36] For spin-polarised cases, $E_{xc}[\rho,\xi,\nabla\rho] = \int dr\, F_{xc}(\rho,\xi,s)\rho(r)e_x(\rho(r))$.

only the range $0<s<3$ is important in atoms, molecules, and solids. Values of $s>3$ correspond to atomic tails and are unimportant (Perdew & Kurth, 1998).

The Lieb-Oxford bound (5.3.4.34) can be rewritten in terms of $F_{xc}(\rho,s)$:

$$F_{xc}(\rho,s) \le 2.273 \qquad (5.3.4.10)$$

A summary of several functionals in terms of their enhancement factors is given in Fig. 5-5.

GGA significantly improves the description of atomic core electrons and to some extent the valence electrons as well. Total energies are much better than in LSDA and even better than in HF. LSDA overbinding is corrected by the GGA. Energy differences and especially reaction barriers are often significantly improved, as well as the description of magnetic systems. Exchange energies of atoms are reproduced with a typical error of only 0.5%; the typical error for the correlaton energy is 5% (Perdew & Kurth, 1998). GGA exchange-correlation cannot be formally self-interaction-free; however, for the H atom, the self-interaction error is practically completely cancelled within the GGA. GGA, like LSDA, cannot reproduce the derivative discontinuity (5.3.3.39) on passing an integer number of electrons and does not have the correct (5.3.3.40) long-range behaviour.

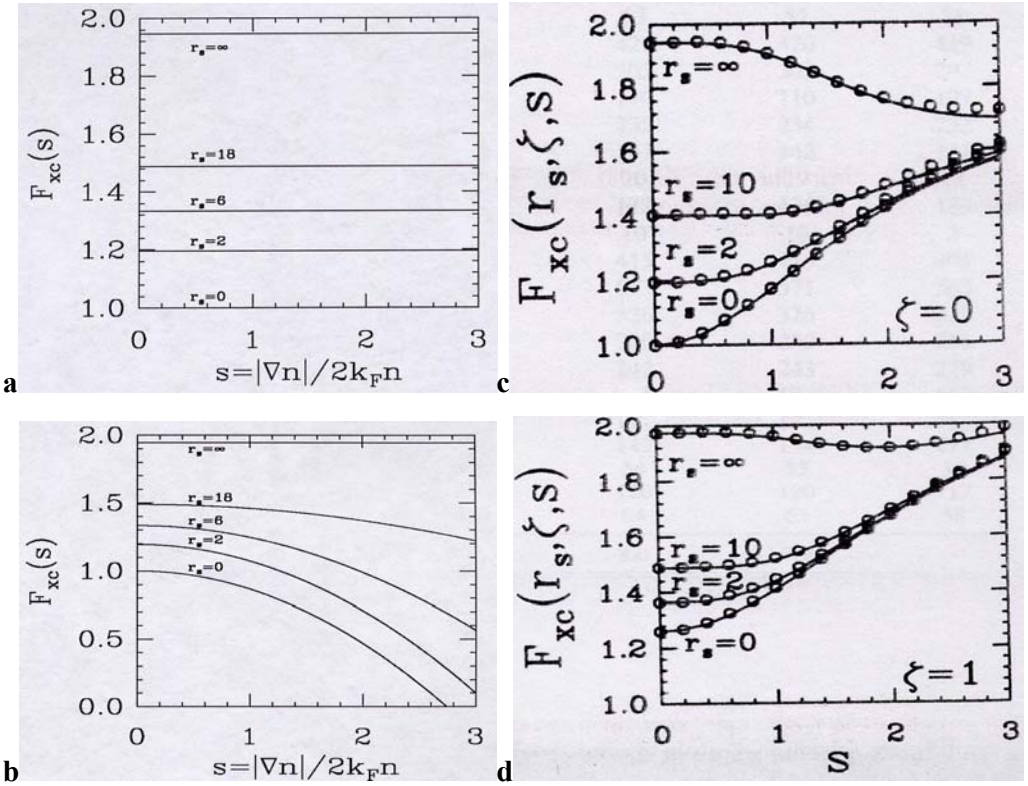

Fig. 5-5. Exchange-correlation enhancement factors. a)LDA, b)GEA, c-d)GGA – PW91 (circles) and PBE (solid lines). Figures a-b (after Perdew & Burke, 1996) refer to the spin-

unpolarised cases; figures c and d (after Perdew et al., 1996) refer to the unpolarised and fully polarised cases, respectively.

Some of the failings of the GGA include: 1. Bond lengths are usually overestimated by ~1%, 2. Like in the LSDA, but less often, electronic ground states of atoms, molecules, and solids can sometimes be incorrect. 3. Sometimes the energy differences are incorrect. GGA is particularly inaccurate for the heavy transition metals (e.g., Au). For bond lengths the GGA 'overcorrects' the LDA.

It can be demonstrated (Zupan et al., 1998; Perdew & Kurth, 1998) that gradient correction would favour a process, for which:

$$\frac{d < s >}{< s >} \geq \frac{d < r_s >}{2 < r_s >} \quad , \qquad (5.3.4.11)$$

where r_s and s are the Wigner-Seitz radius (see caption to Fig. 5-3 and eq. (5.3.4.2)) and the reduced density gradient (see eq. (5.3.4.8)), respectively.

In a process towards a less dense structure (e.g., atomisation, bond stretching) $d\langle r_s\rangle > 0$ and often (but not always) $d\langle s\rangle > 0$. This suggests that the total effect of the gradient corrections should be small – hence many of the successes of the LSDA. However, usually the left-hand side of (5.3.4.11) is larger than the right, explaining why gradient corrections usually lead to longer bond lengths and more open structures.

Table 5-3. Comparison of HF, LDA and GGA for solids. Data are compiled from Lee & Martin (1997), Lichanot (2000), Dovesi (1996), Zupan et al. (1998). HF+c means Hartree-Fock calculation with an *a posteriori* estimate of the correlation energy by a density functional.

Property	**HF (HF+c)**	**LSDA**	**PW91 (PBE)**	**Experiment**
Periclase MgO [GGA = PW86]				
a_0**, Å**	4.191	4.160	4.244	4.20
E_a**, eV**	-7.32 (-9.69)	-	-	-10.28
K**, GPa**	186	198	157	167
Ferromagnetic bcc-Fe				
V_0**, Å^3**	-	10.44	(11.34)	11.77
K**, GPa**	-	260	(200)	172
K**'**	-	4.6	(4.5)	5.0
Diamond C				
a_0**, Å**	3.58	3.53	3.57 (3.57)	3.567
E_a**, eV**	-5.2 (-7.4)	-8.87	-7.72 (-7.72)	-7.55

***K*, GPa**	471	455	438 (439)	442

Table 5-4. Comparison between LSDA, LDA+U, GGA, and experiment for antiferromagnetic FeO. Data are taken from Isaak et al. (1993), Cohen et al. (1997), Fang et al. (1999), Gramsch et al. (2001).

	LSDA	LDA+U	GGA	Experiment
V_0, Å^3	141.5	161.2	165.8, 156.8, 157.1	162.82
***K*, GPa**	173	186	178, 180, 158	142-180
K'	4.3	3.43	4.2, 3.55, 3.05	4.9
μ_{Fe}	3.4	3.4	-, 3.46, 3.5	4.2

Notes: 1. The ground state of FeO at 0 K is rhombohedral antiferromagnetic; however, the Neél temperature of FeO (198 K) is below room temperature and most experiments refer to the spin-disordered cubic phase. This is a different phase, whose properties are, however, similar. 2. The LSDA entry for the volume is ambiguous: Isaak et al. (1993) give only the lattice parameter, which they seem to define as the cubic root of the volume of the rhombohedrally distorted cell. 3. Experimental magnetic moments of Fe atoms have a large orbital component, which is not included in usual calculations. For the spin magnetic moments agreement between theory and experiment is good.

Meta-GGA. The next step after GGA is to include the Laplacian of the electron density $\nabla^2\rho$. The inclusion of this variable is very promising, since the Laplacian of the density proved to be very important in the Bader analysis of chemical bonding (Bader, 1990; Coppens, 1997; Tsirelson, 1993). Quantum Monte Carlo simulations (Nekovee et al., 2001) demonstrated that often GGA would worsen the LDA exchange-correlation hole. They also showed that inclusion of the Laplacian of the density is essential in reasonable modelling of the exact hole. There have been several attempts to construct meta-GGA functionals. E.g., Perdew et al. (1999) have constructed a meta-GGA functional including the Laplacian of the density and the kinetic energy density, which is defined as:

$$\tau(\mathbf{r}) = \tfrac{1}{2}\Sigma\nabla^2\phi_i(\mathbf{r}) \qquad (5.3.4.12)$$

Table 5-5. Atomisation energies (in eV) of several molecules: experiment versus theory. Experimental values include a correction for zero-point vibrational energy. All calculations are spin-polarised. (Taken from Perdew et al., 1996; meta-GGA results: from Perdew et al., 1999). Meta-GGA calculations used GGA electron densities.

Molecule	HF	LSDA	GGA (PBE)	GGA (PW91)	Meta-GGA	Experiment
H_2	3.64	4.90	4.55	4.55	4.97	4.73
OH	2.95	5.38	4.77	4.77	4.67	4.64
H_2O	6.72	11.58	10.15	10.19	9.98	10.06
HF	4.21	7.03	6.16	6.20	6.01	6.11
Li_2	0.09	1.00	0.82	0.87	0.98	1.04

N_2	4.99	11.58	10.54	10.49	9.94	9.93
O_2	1.43	7.59	6.24	6.20	5.70	5.25
F_2	-1.60	3.34	2.30	2.34	1.87	1.69
CH_4	14.22	20.03	18.21	18.26	18.26	18.17
C_2H_4	18.56	27.45	24.76	24.85	24.35	24.41

Becke (2000) showed that $\tau(\mathbf{r})$ is a useful indicator of delocalisation of the exchange hole. Conventional functionals fail for systems with significantly delocalised exchange holes (such as stretched H_2^+) because of the large self-interaction error – see Zhang & Yang (1998). Including $\tau(\mathbf{r})$ it is possible to accurately model the exchange energy of systems with highly delocalised exchange holes – e.g., Becke (2000). $\tau(\mathbf{r})$ can even be used to recognise the regions of such delocalisation (as regions where $\tau(\mathbf{r}) >> {}^3/_{10}(3\pi^2)^{2/3}\rho^{5/3}$). Becke (2000) has constructed a meta-GGA exchange functional, which very accurately simulated the exact exchange. Perdew et al. (1999) have constructed a meta-GGA functional, which has two fitted parameters. Among its good properties are self-interaction-free correlation and reduction to LDA for the uniform electron gas. The performance of this meta-GGA for atomisation energies is significantly better than GGA, but bond lengths (and lattice parameters) seem to be slightly worse. There are other meta-GGA functionals and much ongoing work on the derivation and testing of meta-GGAs.

Hybrid functionals. Adding local (LDA or GGA) correlation to the exact (HF) exchange turns out to give worse results than pure GGA exchange-correlation. Nevertheless, as emphasised in A.D. Becke's seminal paper (Becke, 1993), exact exchange is important in constructing accurate functionals. Becke proposed a hybrid functional, whose exchange part is a mixture of local and exact exchange and whose correlation part is a local functional, schematically:

$$E_{xc} = E_{xc}^{local} + a_{mix}(E_x^{exact} - E_x^{local}) \quad , \qquad (5.3.4.13)$$

where a_{mix} is a fitted parameter equal to 0.20. Hybrid functionals generally are highly accurate in predicting structures and atomisation energies, as well as total energies of atoms. There are a host of hybrid functionals, the most popular of which is called B3LYP.

Van der Waals bonding. One of the most difficult problems for quantum-mechanical simulations has been to reproduce van der Waals bonding. Originating from dynamical correlation, van der Waals forces are by definition absent in the

Hartree-Fock theory. Even at the DFT level, there are problems as these long-range forces cannot be adequately reproduced by any of the local functionals. LDA is too crude for correlation generally; GGA (PBE functional) can give some dispersion forces and even give reasonable bond lengths for noble-gas dimers. However, due to its local nature, GGA gives an exponential, rather than R^{-6} dependence for the van der Waals energy. Kohn et al. (1998) have proposed a practical recipe in order to get accurate dispersion forces and their long-range behaviour within the DFT framework.

5.3.5. Technical details of *ab initio* simulations.

Brillouin zone sampling. An infinite crystal contains an infinite number of electrons. Exploiting translational symmetry of crystals and introducing the reciprocal lattice, it is possible to consider only the number of electrons contained within one unit cell. However, the HF or Kohn-Sham equations must be solved for each point of the first Brilluoin zone. The wavevector **k** becomes a new quantum number.

By Bloch theorem, an *i*-th crystal orbital with the wavevector **k** can be written as:

$$\phi_{i\mathbf{k}}(\mathbf{r}) = e^{i\mathbf{kr}} w_{\mathbf{k}}(\mathbf{r}) = e^{i\mathbf{kr}} \sum_{\mathbf{K}} C_{\mathbf{k}+\mathbf{K}}\, e^{i\mathbf{Kr}} \quad , \qquad (5.3.5.1)$$

i.e. is a product of a periodic function $w_{\mathbf{k}}(\mathbf{r})$ and a plane wave. In the last equality of (5.3.5.1) the periodic function $w_{\mathbf{k}}(\mathbf{r})$ is expressed as a Fourier series with coefficients $C_{\mathbf{k}+\mathbf{K}}$ (**K** is a reciprocal lattice vector). All the *i*-th orbitals with different **k**-vectors form a band, in which the orbital energy generally depends on the **k**-vector, much like phonon frequencies depend on it. In the exact solution one has to solve the one-electron equations at every **k**-point and perform integration over the Brillouin zone. In practice, only a finite set of **k**-points can be used, and it is important to achieve convergence with as small a number of **k**-points as possible. Generally, for metals one needs many more **k**-points than for insulators or semiconductors. Smaller unit cells also require more **k**-points to be included. Monkhorst and Pack (1976) suggested a recipe, which has become the most commonly used one. They defined a uniform set of special **k**-points as:

$$\mathbf{k} = u_p\mathbf{b_1} + u_r\mathbf{b_2} + u_s\mathbf{b_3} \quad , \qquad (5.3.5.2)$$

where $\mathbf{b_1}$, $\mathbf{b_2}$, and $\mathbf{b_3}$ are the reciprocal lattice vectors and u_p, u_r, u_s are numbers from the sequence:

$$u_r = (2r-q-1)/2q \qquad (r=1,2,3,\ldots q) \qquad (5.3.5.3)$$

The total number of *k*-points is q^3, but due to symmetry the number of independent **k**-points can be much smaller.

Basis sets. Here I shall consider only the traditional atomic-orbital and plane wave basis sets. There exist other possibilities, e.g. hybrid basis sets of the LAPW method.

In the LCAO (Linear Combination of Atomic Orbitals) scheme one defines atom-centred orbitals as a product of the angular (Y_{lm}) and radial ($\chi(r)$) parts:

$$\phi_i(\mathbf{r}) = Y_{lm}\chi(|\mathbf{r}|) \quad , \tag{5.3.5.4}$$

where the radial part is a linear combination of either Slater-type functions:

$$\chi(|\mathbf{r}|) = r^m e^{-\xi r} \tag{5.3.5.5}$$

or Gaussian-type functions:

$$\chi(|\mathbf{r}|) = e^{-\alpha r^2} \quad , \tag{5.3.5.6}$$

where m, ξ, and α are parameters. Slater orbitals are more accurate and require fewer functions in an accurate representation of orbitals. However, they are much more computationally expensive, and Gaussian functions are usually preferred.

From atomic orbitals we form a set of Bloch functions, whose linear combinations give the crystal orbitals. In practice, LCAO basis sets almost always suffer from incompleteness. In molecules and crystals, parameters (e.g., exponents) of the orbitals (5.3.5.5) and (5.3.5.6) depend on the atomic positions, but are only optimised for one structure. Dependence of the basis set on atomic positions implies the presence of Pulay forces, which must be evaluated when optimising crystal structures. Although very economical for insulators, LCAO basis needs very many Gaussian functions for studies of metals. LCAO basis also suffers from the basis set superposition error. It is also difficult to systematically increase the basis set expressed in local orbitals.

Plane wave basis set is the most natural and general basis set for crystals, following directly from the Bloch theorem. A single plane wave is:

$$\phi^{PW}_{\mathbf{k}+\mathbf{K}}(\mathbf{r}) = e^{i(\mathbf{k}+\mathbf{K})\mathbf{r}} \tag{5.3.5.7}$$

This basis set is complete and very convenient for many applications. Its main shortcoming is that a huge number of plane waves are needed to describe rapidly changing wavefunctions in solids. E.g., for the valence electrons in Al, an estimated 10^6 plane waves are needed to reproduce oscillations of the valence electron wavefunction in the core region. For the core electrons this problem is even much more serious – because the core electron wavefunctions are more rapidly changing and there is a cusp in the density (eq. 5.3.4) at the nucleus. There are several ways to

overcome this problem – e.g., the LAPW method, PAW (Projector Augmented-Wave) method, linear muffin-tin method, and the pseudopotential method, which I shall describe below. For details of all these methods see Singh (1994), Blöchl (1994), Thijssen (1999).

By construction, plane wave basis set can be used only in conjunction with periodic boundary conditions. Atoms, molecules, and surfaces can be treated in an approximate fashion by using sufficiently large unit cells preventing significant interaction between their periodic images. A very large number of plane waves is required to treat such systems.

Pseudopotentials. The main ideas of the pseudopotential approach are: 1) to exclude chemically inactive core electrons from explicit consideration and 2) to replace (within the sphere of the radius r_c) the true Coulombic potential due to the core by a smoother effective potential acting on the valence electrons. In this approach, we use the frozen core approximation, which usually works well. Where this is not the case, it is always possible to use 'small core' pseudopotentials with some of the core orbitals treated as valence orbitals.

Outside the 'core' radius r_c the potential and the wavefunction are correct. Within the core region the wavefunction is different from the exact one in that it is nodeless and is smoother (Fig. 5-6 and Fig. 5-7). Nodes and oscillations of the exact valence functions in the core region are due to the orthonormality constraints[37].

The definition of a pseudopotential is inherently non-unique: it depends on r_c and other technical details. Larger r_c result in smoother potentials, which allow a smaller number of plane waves to be used, but degrade the accuracy. In molecular and solid-state calculations particular care must be taken to avoid large overlaps of the core

[37] Valence orbitals must be orthogonal to the core electrons. If they have a different angular momentum, orthogonality is achieved automatically due to their angular parts; orbitals with the same angular momentum must be orthogonal due to the sign-changing radial part of the wavefunction. This implies that if orbitals of a given angular momentum appear only in the valence shell, there will be no radial orthogonality with the core, no radial nodes, and these valence electrons will better penetrate the core and experience very strong potentials. As a consequence, for elements where this occurs (1st row elements, 3d- and 4f-elements) pseudopotentials must be very hard. The way out was found in the formulation of ultrasoft pseudopotentials (Vanderbilt, 1990).

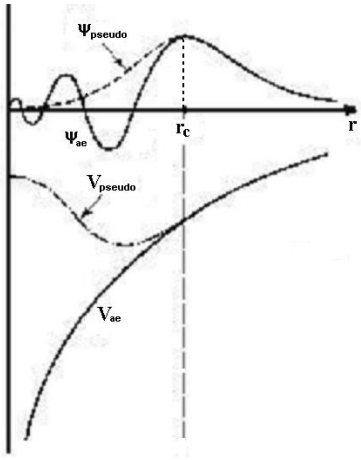

Fig. 5-6. Construction of a pseudopotential. Beyond r_c the wavefunction and potential match the true all-electron ones (with modifications after Payne et al., 1992).

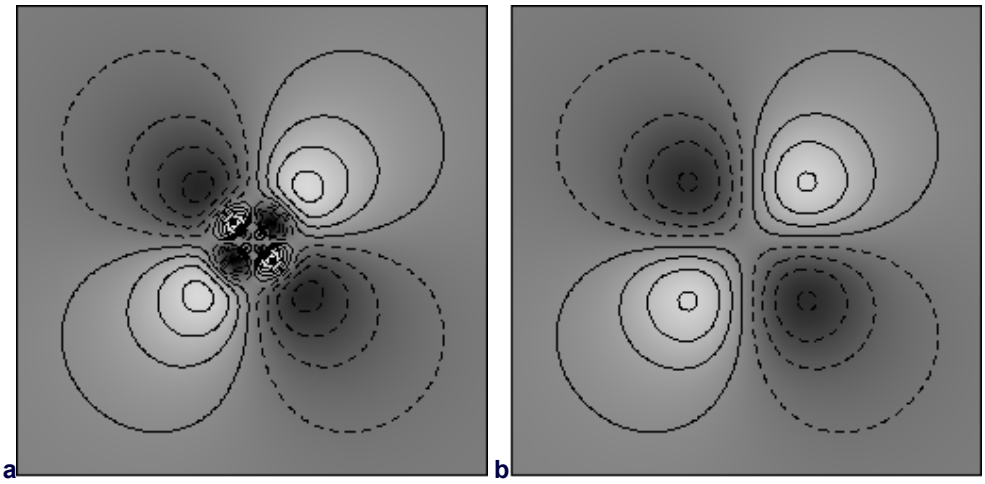

Fig. 5-7. All-electron (a) and pseudowavefunction (b) of a 5d-orbital in Au. Solid contours – positive, dashed contours – negative wavefinction (taken from A. Rappe's web-page at: http://www.sas.upenn.edu/chem/faculty/rappe/rappe.html).

regions. At r_c not only the wavefunction, but also its first derivative are exact, therefore small overlaps are not critical. Pseudopotentials are constructed so as to match the all-electron eigenvalues in as many different atomic configurations as possible, to ensure transferability of the pseudopotential to chemically different systems.

Usually, pseudopotentials are generated under a constraint of norm-conservation:

$$\sum_i \int_0^{r_c} |\phi_i^{ps}(\mathbf{r})|^2 \, d\mathbf{r} = \sum_i \int_0^{r_c} |\phi_i^{ae}(\mathbf{r})|^2 \, d\mathbf{r} \quad , \qquad (5.3.5.8)$$

i.e. the pseudowavefunction gives the correct (equal to the all-electron result) number of valence electrons within the core region. These pseudopotentials are called hard, or norm-conserving. It is possible to use much softer pseudopotentials

(called ultrasoft, or non-normconserving) by relaxing the norm-conservation condition (Vanderbilt, 1990). This allows one to use relatively large r_c and reduce the number of plane waves by a factor of ~2 without any loss in accuracy. In Vanderbilt pseudopotentials, one has to add the so called 'augmentation charge' (which is the strongly atom-localised part of the valence electron density) to $\sum_i |\phi_i^{ps}(\mathbf{r})|^2$ in order to obtain the charge density within the core spheres. Ultrasoft pseudopotentials are almost indispensable in simulations of compounds of 'hard' elements – such as O and other 1st row elements, Fe and other 3d-elements, and rare earths.

Milman and co-workers (2000) have presented an analysis of the performance of plane wave pseudopotential calculations for compounds of almost all elements. Comparison of the performance of pseudopotential and all-electron methods was made in many works, e.g. Holzwarth et al. (1997). The general conclusion is that pseudopotential calculations are very accurate, except in cases where core polarisation effects are significant (e.g., Ca atom in CaF_2). Another source of errors of pseudopotential calculations is significant overlap of the valence and core orbitals for some elements (e.g., Na). In such cases, non-linear core corrections (Louie et al., 1982) significantly improve pseudopotentials. It is important that the same functional is used in generating the pseudopotential and in performing solid-state calculations (Fuchs et al., 1998); this point, not taken into account by many researchers, was always kept in my works, all of which used the PW91 functional for both solid-state calculations and pseudopotential generation.

In conjunction with pseudopotentials, plane wave basis sets become extremely useful. Using ultrasoft pseudopotentials, it is possible to give a satisfactory description of solids by using typically a basis set of ~100 plane waves per atom. Only the plane waves with the lowest kinetic energy need to be included. The number of plane waves is controlled by the kinetic energy cut-off parameter E_{cut}; only plane waves with the kinetic energy below E_{cut} are included:

$$\frac{1}{2}|\mathbf{k}+\mathbf{K}|^2 \le E_{cut} \quad \text{(in atomic units)} \tag{5.3.5.9}$$

The number of plane waves is roughly proportional to the volume of the unit cell and depends on the cut-off as $E_{cut}^{3/2}$; an approximate estimate of the number of plane waves:

$$N_c = \frac{V}{6\pi^2}(2E_{cut})^{3/2} \tag{5.3.5.10}$$

differs only slightly from the actual number N_a. It must be always checked that E_{cut} is high enough for good convergence of results.

A plane wave basis set does not depend on atomic positions; therefore, there are no Pulay forces. However, this basis does depend on the volume when a finite number of plane waves are included[38]. This is the origin of the so-called Pulay stress. This stress is always negative, i.e. tends to compress the structure. It is nearly isotropic, has zero shear components and is roughly independent of volume:

$$\sigma_p = \frac{2}{3V}\frac{\partial E}{\partial \ln E_{cut}} \quad , \tag{5.3.5.11}$$

Pulay stress affects mainly the pressure, which can be easily corrected by shifting the calculated values by a constant:

$$p(V) = p_N(V) + \sigma_p \quad , \tag{5.3.5.12}$$

where p_N is the pressure calculated at the constant number of plane waves. The origin of the Pulay stress is in the basis set incompleteness due to the presence of only a finite number of plane waves. A related correction to the total energy (Francis & Payne, 1990) is:

$$E_{tot} = E_{tot}(N) - \frac{2}{3}\frac{\partial E}{\partial \ln E_{cut}} \ln \frac{N_a}{N_c} \tag{5.3.5.13}$$

Increasing the basis set, it is possible to reduce the Pulay stress and errors in the total energy to arbitrarily small values; all my calculations have negligible Pulay stresses and very small total energy errors avoiding the use of the approximate equations (5.3.5.11-13). For more details of the plane wave pseudopotential method see Singh (1994) and Payne et al. (1992).

Fig. 5-8 presents valence electron distributions calculated using this method. Analysis of the charge and spin densities is a powerful tool for investigation of chemical bonding and interatomic interactions in crystals (Coppens, 1992, 1997; Tsirelson, 1986, 1993). Figure 5-8 already gives some indication of the ionicity of bonds and degree of charge transfer. More quantitative information can be obtained by integration of the charge density within a sphere and comparison of results obtained for different systems. This is shown in Fig. 5-9.

Existing programs for crystals. A number of codes based on DFT exist for crystals. Plane-wave pseudopotential codes include VASP, CPMD, CASTEP, CETEP, PWSCF, DoD-Planewave, ABINIT. WIEN is an all-electron code based on

[38] There are even discontinuities in the basis set related to volume change during structural optimisation. Such effects are significantly reduced when working with large sets of plane waves.

the linearised augmented plane wave method (see Singh, 1994). SIESTA uses localised basis sets in conjunction with pseudopotentials. All the mentioned programs are based on DFT; CRYSTAL is a unique program employing the Hartree-Fock method, but also having DFT options and hybrid functionals. All these codes develop quickly; frequent updates and documentation can be found on their

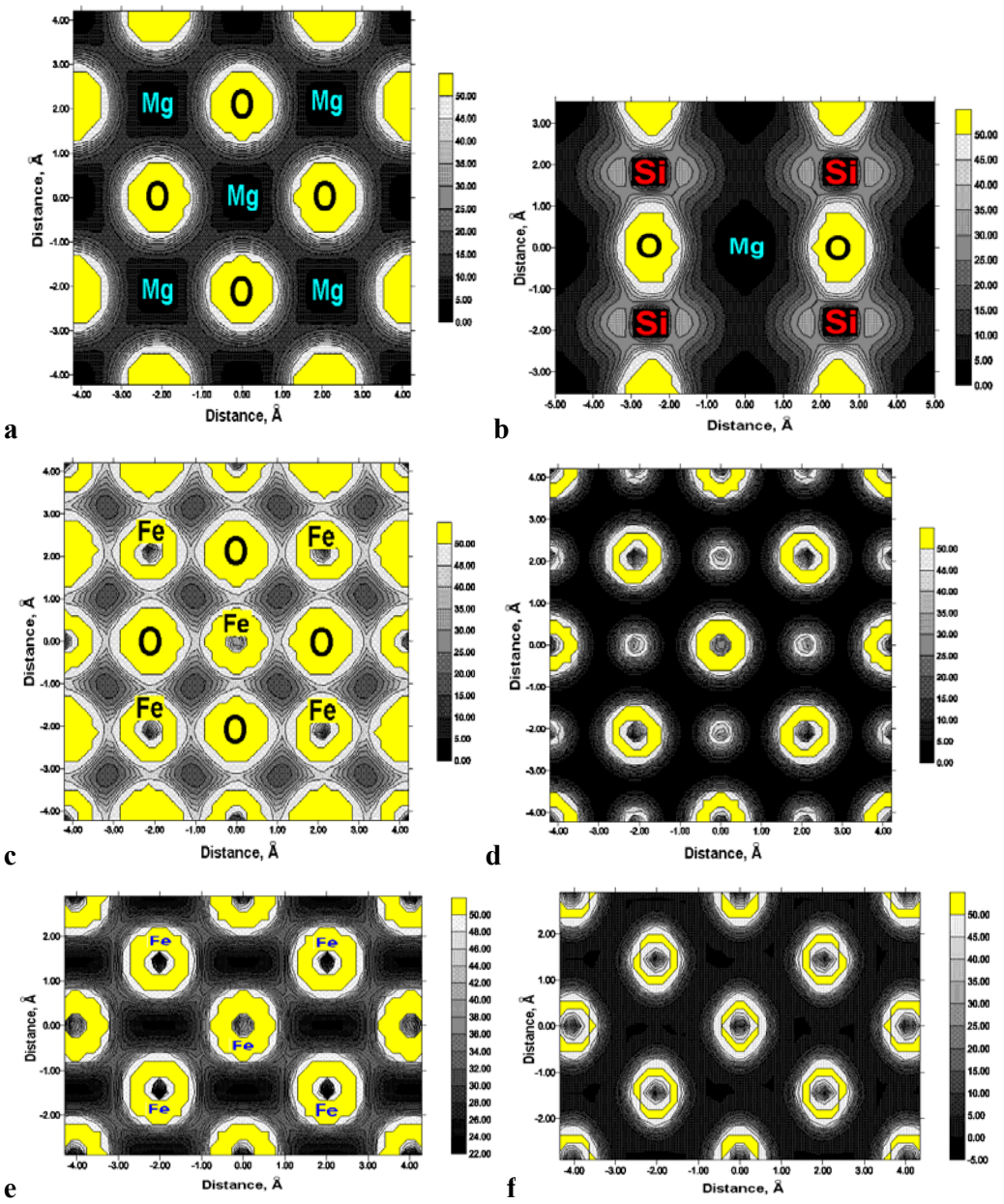

Fig. 5-8. Theoretical valence electron distributions in minerals. (a) MgO ([100] plane), (b) cubic $MgSiO_3$ perovskite ([110] plane), (c) ferromagnetic FeO ([100] plane), (d) spin density in ferromagnetic FeO ([100] plane), (e) ferromagnetic bcc-Fe ([110] plane), (f) spin density in ferromagnetic bcc-Fe ([110] plane). The density units shown in figures are 0.01 e/Å^3. Contours with density >0.5 e/ Å^3 (yellow regions) are not shown. MgO: most valence electrons are localised on O atoms, leaving Mg almost completely ionised. $MgSiO_3$: Mg atoms are almost fully ionised, but there is a significant electron density on Si atoms, indicating partial covalency of the Si-O bonds. FeO: Note 'bridges' of charge density between Fe and O atoms, indicative of some covalency. Also note a significant spin density on the O atoms. Fe: Electron density is high everywhere, explaining the

metallic conductivity of iron. In the ferromagnetic phase, the spin density is localised on the atoms and is positive everywhere, perhaps except for small interstitial regions where it is slightly negative. Calculations were performed using GGA-PW91 and VASP. Lev00 code (Kantorovich, 1996-2001) was used in constructing these images. Experimental structures were used for MgO (a_0 = 4.211 Å) and Fe (a_0 = 2.866 Å) and theoretical structure (a_0=3.527 Å) was used for the cubic $MgSiO_3$ perovskite. For FeO calculations, a_0 = 4.211 Å was used for comparison with MgO.

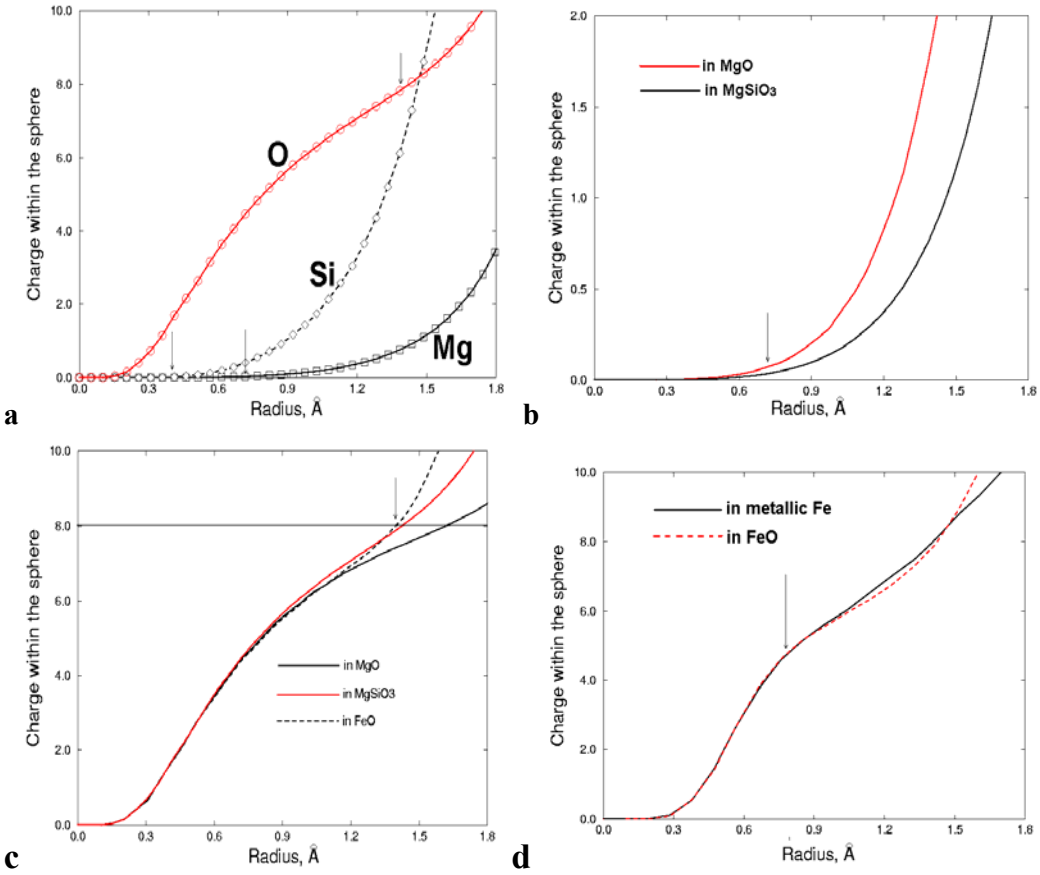

Fig. 5-9. Amount of charge inside atomic spheres in mineral structures. (a) in $MgSiO_3$ perovskite, (b) Mg in MgO and $MgSiO_3$ perovskite, (c) O in MgO, $MgSiO_3$, and FeO, (d) Fe in FeO and metallic Fe. Arrows show the ionic radii (0.72 Å for Mg^{2+} and 1.40 Å for O^{2-}, 0.40 Å for Si^{4+}, and 0.78 Å for the high-spin Fe^{2+}). Integrating charge within the spheres with these radii gives the atomic charges of Mg (+1.94 in MgO, +1.96 in $MgSiO_3$), Si (+3.98), Fe (+3.27 in FeO and Fe), and O (–1.4 in MgO, -1.88 in $MgSiO_3$, -2.00 in FeO). These figures, based on the same calculations as Fig. 5-8, show that: 1) atoms have nearly formal charges within the ionic radius spheres, 2) the sum of thus determined charges is not zero, because of the interstitial regions, 3) there is a striking difference between charge distributions around Mg in MgO and $MgSiO_3$ and a striking similarity between charge distributions around the Fe atom in both Fe metal and FeO. The latter lends some support to the model of a metal as a system of ionic cores immersed in the sea of the free electrons; FeO is an ionic compound. The horizontal line in (c) indicates the full ionic charge. These images were created using the Lev00 code (Kantorovich, 1996-2001).

web-pages, which can be accessed from my home page http://slamdunk.geol.ucl.ac.uk/~artem/7.html).

VASP (Vienna *Ab initio* Simulation Package: Kresse & Furthmüller, 1996a,b) code is the main tool used in my work. It is based on DFT within the plane wave pseudopotentials method, and has both static and molecular dynamics regimes. There are numerous options of static structural relaxation in VASP, the most robust of

which is the conjugate gradients method (see Payne et al., 1992). For studies of metals, a number of 'smearing' methods are available, in which an electronic temperature is specified and the electronic entropy is computed from the density of states. Molecular dynamics can be performed with VASP only in the *NVE* and *NVT* ensembles. Equations of motion are solved using the Verlet algorithm; the constant-temperature molecular dynamics is based on the method of Nosé (1984). The program uses pseudopotentials of several types (including the ultrasoft ones), very efficient matrix diagonalisation and charge density mixing algorithms; it is very effectively parallelised, and can be used to study relatively large systems. Pseudopotentials are generated by a scalar relativistic code; a library of pseudopotentials for all elements is available.

5.3.6. Semiclassical simulations.

These are based on the methods developed by M. Born and co-workers (Born & Huang, 1954). Computationallly much less expensive than *ab initio* calculations, semiclassical simulations allow very large and complex systems, defects, and dynamics to be studied.

Any potential energy hypersurface in principle can be represented analytically. Knowing the whole potential energy surface, one can calculate the equilibrium structure, its dynamics, all responses to the temperature and stress (e.g., elastic constants, thermal expansion), defect properties, diffusion coefficients, vibrational spectra, thermodynamic properties, melting curves, etc. See (Catlow et al., 1994) for a good review. The only class of phenomena that cannot be calculated even in principle is the electronic properties (e.g., magnetic structures, excitation energies), which are entirely in the domain of *ab initio* methods. The Kohn anomalies in phonon dispersion curves of metals also cannot be reproduced by semiclassical methods. Generally, there are practical difficulties for metals, compounds with electronic effects (e.g., Jahn-Teller effect, lone electron pairs)[39] and difficulties in situations where the bonds form, break, or significantly change.

On electron gas methods. There is a large group of methods intermediate between purely quantum-mechanical and semiclassical. Electron gas models represent the

[39] Certain electronic effects – e.g., Jahn-Teller distortion and lone electron pair effects – are not normally studied with interatomic potentials. However, in principle such possibility does exist when it is not the electrons themselves, but their effects on the atoms that are of interest. For example, Nikiforov & Shashkin (1995) devised an accurate model with many-body forces to study Jahn-Teller distortions; Dubrovinsky et al. (1994) studied paratellurite TeO_2 and effects of the lone electron pair on its structure using atomistic simulations.

total electron density as a superposition of ionic (e.g., HF) densities, and the total energy is determined as a local functional of the electron density, using the Thomas-Fermi approximation for the kinetic energy. Depending on the details of the ionic electron densities used, and account of the effects of ion contraction/expansion in the crystal field, a host of electron-gas methods can be distinguihed (see Bukowinski, 1994; Lacks & Gordon, 1995). Some of these implicitly include many-body interactions. One of such methods, MVIB (Modified Variational Induced Breathing), in complete agreement with experiment predicted the transition from stishovite to the $CaCl_2$–type phase at high pressures; at pressures over 1.7 Mbar SiO_2 was predicted to be stable in a monoclinically ($P2_1/c$) distorted pyrite-type phase (see Bukowinski, 1994).

Many-body interactions. The most important contribution to the cohesion energy of a crystal comes from pairwise interactions, however, many-body interactions are always present and turn out to be essential in metals, very important in covalent solids, and significant in ionic crystals (where they are ~10% of the binding energy). For example, the explanation of the correct phase stability (B1-B2 transition) of alkali halides and noble gases (fcc *vs* hcp) requires at least three-body terms in the potential[40] (Jansen & Lombardi, 1965).

The static lattice energy of a crystal is given as a sum of interactions:

$$E_{\text{latt}} = \sum_{i>j} U_{ij} + \sum_{i>j>k} U_{ijk} + \ldots \,, \qquad (5.3.6.1)$$

where U_{ij} are pair potentials, and U_{ijk} – three-body potentials; more complex (e.g., four-body, five-body, etc.) many-body potentials are also present in the sum (5.3.6.1). For an infinite system, one has an infinite number of many-body terms of up to the infinite order. Unfortunately, the convergence of the sum (5.3.6.1) is often very poor and some energy terms are non-additive (e.g., strictly speaking, dispersion interactions are non-additive). Often, many-body terms are not considered explicitly – some of their effects being included in the effective pair potentials. Since many-body interactions depend on the structure, such effective potentials will in general not be tranferable. Moreover, even for the same crystal at different conditions different effective potentials should ideally be used. When the structural changes are large (e.g., changes of the first coordination number), transferred potentials become unreliable in predicting structural energy differences.

[40] For noble gases it is also important to include zero-point energy.

Potential parameterisations. Parameterisation of the potential is done using either experimental properties or quantum-mechanical calculations. In the first case only a very small region of the potential energy surface is effectively taken into account. Therefore, such potentials can become invalid at different pressures or temperatures, or when studying, for example diffusion - generally, when different parts of the potential energy hypersurface are explored, or properties not used in the fitting procedure. It is always a challenge to develop reliable potentials, suitable for extrapolations and transferable to other compounds.

In practice, even simple interatomic potentials in most situations work well for ionic (Burnham, 1990) and molecular (Kitaigorodsky, 1971) solids and liquids. Bond lengths are routinely given within ~3%, vibrational frequencies and elastic constants within ~30%, and accurate predictions of the defect (Mackrodt, 1982) and surface energies (Mackrodt, 1988) and dielectric constants are often obtained. Entropies and heat capacities can be routinely calculated within several percent of their experimental values. Of course, care must be taken in choosing the potential model. Related problems will be discussed in Chapter 10 (see Oganov et al., 2000).

Potentials in metals are very complicated and have long-range oscialltions; Sutton (1993) described their derivation and Burdett (1995) applied them to some interesting structural problems. Below I consider in some detail conventional potential models applied to essentially ionic crystals.

Potentials in ionic crystals. The most important and universal effects in ionic crystals are: 1) long-range Coulombic interactions, 2) short-range atomic repulsion due to the overlap of closed-shell ions and Pauli principle, 3) van der Waals attraction. These effects are best described by the potential:

$$U_{ij}(R_{ij}) = \frac{z_i\, z_j}{R_{ij}} + b_{ij}\exp\left(-\frac{R_{ij}}{\rho_{ij}}\right) - \frac{c_{ij}}{R_{ij}^6}, \qquad (5.3.6.2)$$

where parameters b_{ij}, ρ_{ij}, and c_{ij} are constants for a given pair of atoms. The first term in (5.3.6.2) is the Coulombic energy, the second is Born-Mayer repulsion due to orbital overlap, and the third term is the van der Waals attraction energy due to the interactions of the instantaneous dipoles on atoms. Their parameters are usually found by fitting to experimental data (Lewis, 1985; Lewis & Catlow, 1985; Sanders et al., 1984; Bush et al., 1994; Gale, 1996), using non-empirical electron gas methods (Burnham, 1990), or by fitting to quantum-mechanical potential surfaces of crystals (Gale et al., 1992) or clusters (Catlow, 1977; Tsuneyuki et al., 1989). The GULP code (Gale, 1997) incorporates the best available fitting procedures (Gale, 1996).

There are some correlation problems in fitting these parameters – e.g., parameters b_{ij} and ρ_{ij} are heavily correlated. The best solution of the correlation problem is to fix some of the parameters by approximate theoretical equations.

The exponential asymptotic long-range behaviour of the electron density of atoms (eq. (5.3.5)) justifies the exponential form of the repulsion potential; in fact, it can be shown (Urusov, 1975, 1995; Urusov & Dubrovinsky, 1989) from (5.3.5) that

$$\rho_{ij} = \frac{1.85}{\sqrt{I_i} + \sqrt{I_j}} \ , \qquad (5.3.6.3)$$

if ionisation potentials are measured in electron-volts and ρ_{ij} is in Ångstroms. This physical determination of the repulsion exponents ρ_{ij} ensures the best transferability of the potential and removes the problem of correlation between b_{ij} and ρ_{ij}. The b_{ij} parameters have to be fitted; for better transferability, a correction is sometimes (Lewis, 1985; Lewis & Catlow, 1985; Urusov et al., 1998) introduced in b_{ij} to account for different coordination numbers of cations.

The van der Waals interaction is in fact only the leading term in the multipole expansion:

$$U_{ij}^{disp}(R_{ij}) = -\frac{c_{ij}}{R_{ij}^6} - \frac{d_{ij}}{R_{ij}^8} - \frac{e_{ij}}{R_{ij}^{10}} - \dots \ , \qquad (5.3.6.4)$$

which also includes dipole-quadrupole, quadrupole-quadrupole and higher-order terms. All these interactions are due to dynamical electron correlation; usually only the van der Waals term is significant. The parameter c_{ij} can be determined either by fitting or by using approximate formulas, e.g. London or Slater-Kirkwood formulas (Kitaigorodsky, 1971). The simpler London formula is more popular:

$$c_{ij} = \frac{3}{2} \alpha_i \alpha_j \frac{I_i + I_j}{I_i I_j} \ , \qquad (5.3.6.5)$$

where α_i and α_j are polarisabilities of the i-th and j-th ions (atoms), and I_i and I_j are their first ionisation potentials. The van der Waals interactions are significant only between large and polarisable atoms and ions. Different estimates of c_{ij} are typically different by ~20% (Born & Huang, 1954).

Dipole polarisation is impossible when an atom occupies a position without any degrees of freedom, but is always important in lattice dynamics. It is also one of the main factors stabilising ternary and more complex compounds (Urusov, 1993). This effect can be accounted for by the shell model (Dick & Overhauser, 1958), in which a polarisable ion is represented as a system of a ‘core’ (which contains all the mass

of the atom) and a massless shell, which are coupled and held together by a harmonic spring:

$$U_s = k_s\,(\Delta r)^2\,, \qquad (5.3.6.6)$$

where Δr is the core-shell distance and k_s is the force constant. The sum of the core (Q) and shell (q) charges must equal the total ionic charge: $q+Q=z$. There is a useful relation with the ionic polarisability α_i:

$$\alpha_i = \frac{q^2}{k_s} \qquad (5.3.6.7)$$

Inclusion of the shell model is necessary for the calculation of the dielectric constants (especially at high frequencies) and improves the description of the structure and elastic properties. In the shell model, the electrostatic interaction between the core and its shell is ignored; shells serve as centres of application of all non-coulombic forces.

It is often important to include angular many-body interactions, especially when strong partially covalent bonds are present. Concentration of valence electrons on bonds leads to a strong repulsion between bonding electron pairs and enhances the tendence of atoms to regular coordination. This is one of many examples of the VSEPR effects. This effect can be described (Kitaigorodky, 1971) by a simple three-body potential with the force constant k_b :

$$U_{ijk} = k_b\,(\varphi-\varphi_0)^2\,, \qquad (5.3.6.8)$$

where φ_0 is the valence angle between bonds ij and ik in a regular polyhedron (in a tetrahedron $\varphi_0 = 109{,}47^0$), and φ is the corresponding real valence angle. Calculations (Sanders et al., 1984; Price & Parker, 1984) demonstrated the importance of the three-body interactions (5.3.6.8) in modelling structure and elastic constants of silicates.

Schröder (1966) proposed a breathing shell model, in which an account is taken of the ionic compressibility; compression of the ions changes the repulsion potential. This model is particularly successful at modelling lattice dynamics and was recently revived by Matsui (1998). Results for NaI (Fig. 5-10) clearly demonstrate the advantages of the simple shell model and breathing shell model over rigid-ion models.

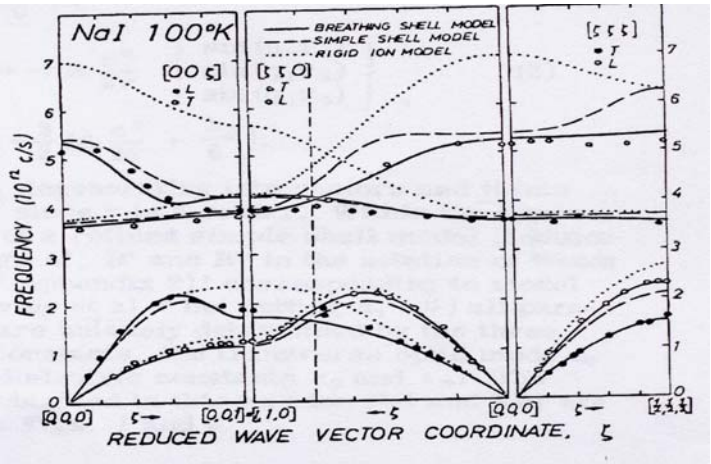

Fig. 5-10. Phonon dispersion curves of NaI calculated with the rigid-ion, simple shell, and breathing shell models. After Schröder (1966). Symbols – experimental data.

Charge-optimised potentials. There is no rigorous definition of the atomic charges in crystals and molecules, but a host of methods resulting in different estimates instead – e.g., from the electron density distribution (Bader, Hirshfeld, multipole charges), from spectroscopy, from dielectric constants (Szigeti method), from band gaps (Phillips method), from the calculated wavefunction (Mulliken, Löwdin charges), from density functional perturbation theory (Baroni et al., 2001), or from the Mortier electronegativity equalisation (see Parr & Yang, 1989). It emerges that fully ionic charges overestimate the magnitude of electrostatic potential in the interatomic space (e.g., White & Hess, 1993).

In the ionic model, charges in (5.3.6.2) are fixed at their formal values. Often this is not satisfactory, and atomic charges are fitted either to properties (especially useful here are the elastic constants and vibrational frequencies) or to quantum-mechanical results.

A different approach was taken by Urusov, who suggested determining the atomic charges from an energy minimisation procedure, together with structural parameters. The quantity under minimisation is the atomisation energy E_a, related to the lattice energy (Urusov & Dubrovinsky, 1989) for a fixed structural configuration:

$$E_a(z_1, z_2,..., z_i, ...) = E_{latt}(z_1, z_2,..., z_i, ...) + \sum_i \Delta E_i(z_i)\,, \qquad (5.3.6.9)$$

where $\Delta E_i(z_i)$ is the atomic charge transfer energy (equal to the ionisation potential for z=1 and electron affinity for z=-1). The lattice energy now includes a covalent contribution, modelled by a Morse function. There are two major difficulties in using (5.3.7.9): first, the charge-interpolation form for the lattice energy is unknown, second, the charge transfer energy is unknown as a function of charge. For both

problems approximate solutions have been found (Urusov, Eremin, Oganov, 1999), but this approach remains open to further improvements. Another weakness is a large number of fitted parameters. Nevertheless, some results of this method are quite encouraging - for example, for potential high-pressure phases of silica. A fluorite-like phase was found to be unstable, spontaneously distorting into lower-symmetry phases. For the octahedral phases the following results were obtained (Oganov, 1997):

	z_{Si}	E_a (eV)	V_m (cm^3/mole)	K_V (GPa)	G_V (GPa)
Stishovite	+2.04	-18.62	13.94	368	218
α-PbO_2 phase	+2.04	-18.53	13.80	361	207
SiO_2 -brookite	+1.96	-18.47	14.38	311	175
SiO_2 -anatase	+1.92	-18.38	15.11	276	137

Stishovite is the most stable of these phases, followed by the α-PbO_2-like phase, which is also slightly denser. A rough estimate of the transition pressure from stishovite to the α-PbO_2-like phase ($p=\Delta E/\Delta V$) gives 62 GPa (not considering the intermediate $CaCl_2$-like phase), while accurate *ab initio* calculations (Karki et al., 1997) give ~80 GPa; experimental results are controversial. The anatase and brookite phases are higher in energy, less dense, and cannot be stable. The energy increases with increasing number of shared edges, in accordance with the 3rd Pauling's rule. The atomic charges are large, but much lower than in the ionic model. We see that the highest charges occur where (as in stishovite and the α-PbO_2–like phase) the number of shared polyhedral edges is minimal (two); SiO_6-octahedra have three shared edges in brookite and four in anatase. Generally, charges on atoms should depend not only on the first coordination sphere, but also on the number of neighbours in the second coordination sphere. Note also that for these polymorphs there is a large difference in the elastic properties and molar volumes, which are strongly dependent on the number of shared polyhedral edges.

Ewald summation. In the potential (5.3.6.2), the first term (Coulombic) is extremely long-ranged and there is a problem in its summation over the infinite lattice. The last two terms (known as the Buckingham potential) are short-ranged and can be easily summed in the real space. There are several methods of summation of long-ranged electrostatic interactions – the real-space method of Evjen, reciprocal-space summation of Berthaut, and the most popular method due to Ewald (see Allen & Tildesley, 1987), which splits the ill-convergent sum into real-space and

reciprocal-space sums, whose convergence is good. Ewald summation is also an ingredient of all periodic *ab initio* codes.

The derivation of the Ewald method follows two stages. First, we add to the atomic point charges some atom-centred neutralising spherical charge distributions, with the equal and opposite amount of charge. These distributions are usually takes as Gaussians:

$$\rho = \frac{z_i \kappa}{\pi^{3/2}} e^{-\kappa^2 r^2} \quad , \qquad (5.3.6.10)$$

where κ is a parameter chosen to ensure good convergence. The neutralising Gaussian distributions screen Coulombic interactions and make them short-ranged and summable in the real space. Then, we add the same Gaussians, but now of the same sign as the original charges. Their interactions can be summed in the reciprocal space and transformed back into the real space. Spurious self-interaction, present in this sum, must then be subtracted. Finally, the so-called surface term (non-vanishing only in polar structures) is subtracted, giving the final result:

$$E_{\text{coulombic}} = \frac{1}{2}\sum_{i=1}^{N}\sum_{j=1}^{N}[\sum_{|\mathbf{n}|=0}^{\infty} z_i z_j \frac{\text{erfc}(\kappa |\mathbf{r}_{ij}+\mathbf{n}|)}{|\mathbf{r}_{ij}+\mathbf{n}|} + \frac{1}{\pi L^3}\sum_{\mathbf{K}\neq 0} z_i z_j \frac{4\pi^2}{|\mathbf{K}|^2}\exp^{-\frac{|\mathbf{K}|^2}{4\kappa^2}}\cos(\mathbf{K}\mathbf{r}_{ij})] -$$

$$- \frac{\kappa}{\pi^{1/2}}\sum_{i=1}^{N} z_i^2 + \frac{2\pi}{3L^3}|\sum_{i=1}^{N} z_i \mathbf{r}_i|^2 \quad , \qquad (5.3.6.11)$$

where erfc(x) is the complementary error function: $\text{erfc}(x) = \frac{2}{\pi^{1/2}}\int_x^{\infty} e^{-t^2} dt$. In the sum (5.3.6.11) indices i and j denote atoms, **n** – lattice vectors, and **K** – reciprocal lattice vectors.

<u>*Calculation of properties.*</u> With a given potential model and having a rough starting structural model, it is easy to find the minimum energy structure – by using the steepest descent, conjugate gradients, or damped molecular dynamics algorithms.

Near the equilibrium we can expand the energy as:

$$E = E_0 + \tfrac{1}{2}\mathbf{u}^{\mathrm{T}}\mathbf{W}_{uu}\mathbf{u} + \mathbf{u}^{\mathrm{T}}\mathbf{W}_{ue}\mathbf{e} + \tfrac{1}{2}\mathbf{e}^{\mathrm{T}}\mathbf{W}_{ee}\mathbf{e} \quad , \qquad (5.3.6.12)$$

where E_0 is the equilibrium energy, $\mathbf{u} = (u_x(1), u_y(1), u_z(1), u_x(2), \ldots, u_z(n))$ is a $1*3n$ matrix of atomic positions, $\mathbf{u}^{\mathrm{T}}$ its transpose, and **e** is a 3*3 strain matrix. $\mathbf{W}_{uu}$, $\mathbf{W}_{ue}$, and $\mathbf{W}_{ee}$ are the second derivative matrices defined as:

$$\mathbf{W}_{uu} = \frac{\partial^2 E}{\partial u_\alpha(i)\partial u_{\alpha'}(j)} \; ; \; \mathbf{W}_{ue} = \frac{\partial^2 E}{\partial u_\alpha(j)\partial e_{\alpha'}} \; ; \; \mathbf{W}_{ee} = \frac{\partial^2 E}{\partial e_\alpha \partial e_{\alpha'}} \qquad (5.3.6.13)$$

At the equilibrium

$$\frac{\partial E}{\partial \mathbf{u}} = 0 = \mathbf{W}_{uu}\mathbf{u} + \mathbf{W}_{ue}\mathbf{e} \qquad (5.3.6.14)$$

or

$$\mathbf{u} = -\mathbf{W}^{-1}{}_{uu}\mathbf{W}_{ue}\mathbf{e} \qquad (5.3.6.15)$$

With (5.3.6.12) our expansion (5.3.6.10) becomes

$$E = E_0 + \tfrac{1}{2}\mathbf{e}^T[\mathbf{W}_{\varepsilon\varepsilon} - \mathbf{W}_{eu}\mathbf{W}^{-1}{}_{uu}\mathbf{W}_{ue}]\mathbf{e} \ , \qquad (5.3.6.16)$$

from which we obtain the elastic constants tensor:

$$\{\mathbf{c}_{ij}\} = \frac{1}{V}[\mathbf{W}_{\varepsilon\varepsilon} - \mathbf{W}_{eu}\mathbf{W}^{-1}{}_{uu}\mathbf{W}_{ue}] \qquad (5.3.6.17)$$

The last term in this equation represents the effect of internal strains on the elastic constants. For more details and theory behind calculations of dielectric and piezoelectric constants, see Catlow & Mackrodt (1982) and Dove (2002).

5.4. Lattice dynamics (LD).

Let us assume that ionic displacements are small enough for the interatomic interactions to be harmonic, find the harmonic interatomic force constants as second derivatives of the energy, and solve a system of Newtonian equations of motion (derivation based on quantum mechanics leads to identical results). The solutions of these equations are normal modes – independent harmonic oscillators involving collective motions of atoms. For a crystal, we must take into account periodic boundary conditions, which leads to $3n$ (n is the number of atoms in the unit cell) equations of motion at each **k**-vector and $3n$ normal modes for each **k**-vector. There is much resemblance in this procedure with the solution of one-electron equations of quantum mechanics. For each normal mode, the solution gives the frequency and the pattern of atomic displacements (from which one can determine the symmetry of the vibration). Theory presented here is well described by Venkataraman et al. (1975) and Dove (1993).

To obtain vibrational frequencies, at each k-point one should solve the following determinantal equation:

$$\det||\mathrm{D(k)} - \omega^2(\mathbf{k},\nu)\delta_{\alpha\beta}\,\delta_{ij}|| = \mathbf{0} \ , \qquad \textbf{(5.4.1)}$$

where **D** is the dynamical matrix, and ω^2 are its eigenvalues. Indices α, β =1, 2, or 3 (x, y, z coordinates), and indices i and j denote different atoms within the unit cell. Solving the eigenvalue problem (5.4.1) is equivalent to the diagonalisation of the

dynamical matrix, whose dimensions are 3*n**3*n*. This leads to 3*n* solutions, denoted by index ν.

Negative ω^2 (i.e., imaginary ω) signify dynamical instability of the structure with respect to a particular atomic motion, given by the mode eigenvectors, and indicate a soft-mode driven phase transition. The soft-mode wave vector **k** determines the direction and periodicity of the modulation imposed on the parent lattice at the phase transition. The dynamical matrix **D** is defined as:

$$\mathbf{D}^{ik}_{\alpha\beta}(\mathbf{k}) = \frac{1}{(m_i m_j)^{1/2}} \sum_l \mathbf{\Phi}^{ij}_{\alpha\beta}(0,l) \exp[i\mathbf{k}(\mathbf{r}_j(l) - \mathbf{r}_i(0)] \ , \qquad (5.4.2)$$

where m_i and m_j are masses of the i-th and j-th atoms, sum over *l* is the sum over all unit cells (i.e. over the whole crystal), and $\Phi^{ij}_{\alpha\beta}(0,l)$ are force constants between the atom i in the reference cell (*l*=0) and atom *j* in the *l*-th cell, whose positions are described by vectors $\mathbf{r}_i(l)$ and $\mathbf{r}_j(0)$. The force constant matrix $\Phi^{ij}_{\alpha\beta}(l, l')$ is defined as:

$$\Phi^{ij}_{\alpha\beta}(l, l') = \frac{\partial^2 E}{\partial u^i_\alpha(l) \partial u^j_\beta(l')} \quad , \qquad (5.4.3)$$

where $u^i_\alpha(l)$ denotes a displacement of an i-th atom in the *l*-th unit cell along the α-coordinate axis. The dynamical matrix can be thought of as a Fourier transform of the force constant matrix times the $\frac{1}{(m_i m_j)^{1/2}}$ factor.

The solutions for the atomic displacements as a function of time are linear combinations of plane wave-type functions and read as:

$$\mathbf{u}_i(l,t) = \frac{1}{(Nm_i)^{1/2}} \sum_{\mathbf{k},\nu} \mathbf{U}_i(\mathbf{k},\nu) \exp[i(\mathbf{k}\mathbf{r}_i(l) - \omega(\mathbf{k},\nu)t)] \ , \qquad (5.4.4)$$

where $\mathbf{U}_i(\mathbf{k},\nu)$ is the amplitude vector, containing information on the direction and amplitude of the displacement of all the i-th atoms under the influence of the ν-th mode at the wavevector **k**. Usually, the time dependence and the amplitude are grouped in the new quantity $Q(\mathbf{k},\nu)$ (called the normal coordinate), which leads to:

$$\mathbf{u}_i(l,t) = \frac{1}{(Nm_i)^{1/2}} \sum_{\mathbf{k},\nu} \mathbf{e}_i(\mathbf{k},\nu) \exp[i\mathbf{k}\mathbf{r}_i(l)] Q(\mathbf{k},\nu) \ , \qquad (5.4.5)$$

where the eigenvector $\mathbf{e}_i(\mathbf{k},\nu)$, parallel to $\mathbf{U}_i(\mathbf{k},\nu)$, contains only the information on the direction and symmetry of displacements. This vector is normalised:

$$\sum_{i} | \mathbf{e}_i(\mathbf{k},\nu) |^2 = 1 \qquad (5.4.6)$$

This normalisation allows one to obtain atomic projections of the total phonon density of states. For a longitudinal mode, $\mathbf{e}_i(\mathbf{k},\nu)$ is parallel to **k**; for a transverse mode $\mathbf{e}_i(\mathbf{k},\nu)$ is perpendiculr to **k**. At a given **k**, the eigenvectors belonging to different modes are orthogonal.

Normal coordinates provide an elegant way of expressing the kinetic energy of a crystal:

$$<E_{\text{kin}}> = \frac{1}{2}\sum_{\mathbf{k},\nu} \omega^2(\mathbf{k},\nu)\left\langle | Q(k,\nu)|^2 \right\rangle \qquad (5.4.7)$$

and the total harmonic energy:

$$<E> = <E_{\text{kin}}> + <E_{\text{pot}}> = \sum_{\mathbf{k},\nu} \omega^2(\mathbf{k},\nu)\left\langle | Q(k,\nu)|^2 \right\rangle \ , \qquad (5.4.8)$$

from which the normal coordinate as a function of temperature is (Dove, 1993):

$$\left\langle | Q(k,\nu)|^2 \right\rangle = \frac{\hbar}{\omega(\mathbf{k},\nu)}\left(\frac{1}{2} + \frac{1}{\exp\left(\frac{\hbar\omega(k,\nu)}{k_{\text{B}}T}\right) - 1}\right) \qquad (5.4.9)$$

In the classical limit we simply have $\left\langle | Q(k,\nu)|^2 \right\rangle = \frac{k_{\text{B}}T}{\omega^2(\mathbf{k},\nu)}$.

To find the eigenvectors as well as eigenvalues, one must solve the following equation:

$$\omega^2(\mathbf{k},\nu)\mathbf{e}(\mathbf{k},\nu) = \mathbf{D}(\mathbf{k})\,\mathbf{e}(\mathbf{k},\nu) \qquad (5.4.10)$$

All the above equations play the central role in lattice-dynamical calculations and their interpretation. The most important application of LD is the calculation of thermodynamic functions from the phonon density of states; basic theory and equations were discussed in Chapter 3.

Calculation of the free energy enables the optimisation of the structure by minimising the free energy within the quasiharmonic approximation. Usually, this is done by computing the free energy derivatives numerically, within the so-called ZSISA (Zero Static Internal Stress Approximation, in which only the unit cell parameters are determined by the free energy minimisation, while all atomic coordinates calculated by minimising the *internal* energy, rather than *free* energy) and by assuming that the thermal pressure is isotropic (or, equivalently, that the Grüneisen parameter is a simple scalar rather than a tensor).

It is possible to calculate the free energy derivatives analytically. This not only greatly increases precision, but also allows one to go beyond ZSISA and the isotropic thermal pressure approximation. The only difficulty for analytical free energy derivatives calculation is the calculation of the eigenvalue derivatives ($\partial\omega^2/\partial q$) with respect to the structural parameters q. This problem was solved by Kantorovich (1995) by means of perturbation theory; his method was recently implemented (Gale, 1998) in GULP code (Gale, 1997). Without ZSISA, dynamical instabilities appear at lower temperatures; as a rule of thumb, the quasiharmonic approximation breaks down above half the melting temperature.

LD simulations are now possible in conjunction with DFT by means of density functional perturbation theory (Baroni et al., 2001). Fig. 5-11 shows an example of such calculations.

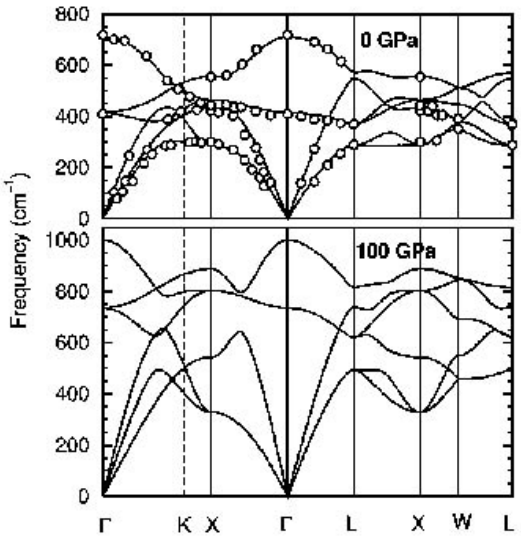

Fig. 5-11. Phonon dispersion curves of MgO at zero pressure and 100 GPa. Experiment (circles) and results of density functional perturbation theory within the LDA (after Karki et al., 2000a).

5.5. Molecular dynamics (MD).

The MD method, invented in 1950s by Alder and Wainwright, is complementary to LD. Unlike LD (which accounts for quantum effects and is based on the harmonic approximation), MD is based on the classical approximation and fully accounts for the anharmonic effects. Unlike LD, MD is applicable to fluids. LD is accurate at low temperatures, but breaks down at high temperatures; MD is exact in the high-temperature limit.

In MD, we describe a classical system by the set of positions and velocities ($\mathbf{r}_i(t)$, $\mathbf{v}_i(t)$) of all particles. For a system of n atoms there are ($3n$-3) degrees of freedom, and the classical kinetic energy is:

$$E_{\text{kin}} = \sum_i \frac{\mathrm{m}_i \mid \mathbf{v}_i \mid^2}{2} = \frac{(3n-3)k_{\text{B}}T}{2} \qquad (5.5.1)$$

The initial kinetic energy (or temperature) is specified as an input, and the initial velocities are assigned to the atoms randomly, according to the Maxwell distribution. Having initial velocities thus specified and starting from the input configuration, the system evolves with the atoms exploring trajectories, which are constructed by solving Newtonian equations of motion. During this evolution, the atoms exchange their kinetic energies, and the system equilibrates. Newton's equations of motion are conservative (i.e. there is no energy dissipation), the volume and the number of particles are conserved as well, so here we are describing the microcanonical, or *NVE*-, ensemble. Once equilibrated, the system explores all possible states having the same energy E, and for some properties the expectation values can be computed as the ensemble averages. One can introduce the instantaneous values of properties; for example, the instantaneous values of the stress tensor[41] are calculated as:

$$\sigma_{\text{ij}} = -[\frac{Nk_{\text{B}}T}{V}\delta_{\text{ij}} - \frac{1}{V}\frac{\partial E_{\text{pot}}}{\partial e_{\text{ij}}}] \quad , \qquad (5.5.2)$$

while for the instantaneous pressure we have the virial expression:

$$p = \frac{Nk_{\text{B}}T}{V}\delta_{\text{ij}} - \frac{1}{3V}\sum_{\text{i}} \mathbf{F}_{\text{i}}\mathbf{r}_{\text{i}} \qquad (5.5.3)$$

Technical notes: 1. Trajectories can be calculated only by using a finite timestep Δt (rather than infinitesimal dt). The most reliable algorithm for integrating the equations of motion is the Verlet leapfrog algorithm:

$$\mathbf{r}_{\text{i}}(t+\Delta t) = 2\mathbf{r}_{\text{i}}(t) - \mathbf{r}_{\text{i}}(t-\Delta t) \frac{\mathbf{F}_i(t)}{\mathrm{m}_i}(\Delta t)^2 \quad , \qquad (5.5.4)$$

where $\mathbf{F}_{\text{i}}(t)$ is the force acting on the i-th atom. The error in the positions is of the order $(\Delta t)^4$. Δt must be sufficiently small (typically ~1 fs).

2. For simulating bulk materials, a large supercell should be used in conjunction with periodic boundary conditions. The larger the system size, the more phonons are

[41] Note the convention that stress tensor is positive when directed outwards, i.e. pressure and stress have opposite signs. This is responsible for the minus sign in (5.5.2). Most simulation packages do not take this minus sign into account.

included and the better description of long-wavelength fluctuations. Large supercell size allows for more couplings between phonons with different **k**-vectors and therefore improves the description of anharmonicity. The effect of the system size must be always checked. For Lennard-Jones systems, the largest systems studied include millions of atoms, with *ab initio* MD the current limit is ~100-200 atoms in the supercell.

3. To explore all possible states, simulations should run infinitely long. Usually, good statistical averages can be collected over a reasonable time, ~ 1-10 ps after equilibration.

It is possible to extend MD to other ensembles – *NVT*, *NPT*, etc. In the *NVT*-ensemble, it is possible to keep the temperature constant by simple rescaling of velocities, but this would not result in correct canonical distributions. The most popular correct way is to use extended Lagrangian formulations.

The Lagrangian function defined (Landau & Lifshitz, 2001a) as:

$$L = E_{\text{kin}}(\mathbf{v}) - E_{\text{pot}}(\mathbf{r}) = \sum_{\text{i}} \frac{\text{m}_\text{i} \mid \mathbf{v}_\text{i} \mid^2}{2} - E_{\text{pot}}(\mathbf{r}) \qquad (5.5.5)$$

leads to the following equation of motion:

$$\frac{d}{dt}\left(\frac{\partial L}{d\text{v}_\text{i}}\right) = \left(\frac{\partial L}{dr_\text{i}}\right) \qquad (5.5.6)$$

from which Newton's equations of motion ($\text{m}_\text{i}\partial\text{v}_\text{i}/\partial t = -\partial E_{\text{pot}}(\mathbf{r})/\partial\text{r}_\text{i} = \mathbf{F}_\text{i}$) follow. The total energy is a constant of motion, i.e. is time-independent.

In the constant-temperature method of Nosé (1984), the Lagrangian (5.5.5) is augmented by two other terms:

$$L = \sum_{\text{i}} \frac{\text{m}_\text{i} \mid \mathbf{v}_\text{i} \mid^2}{2} - E_{\text{pot}}(\mathbf{r}) + \tfrac{1}{2}\text{Q}\dot{s}^2 - (\text{f}+1)k_\text{B}T_0\ln s\,, \qquad (5.5.7)$$

where s is the new dynamical variable, and Q is the associated mass parameter. T_0 is the externally set temperature, and f is the number of degrees of freedom in the system. This Lagrangian leads to conservation of the temperature, which fluctuates around T_0. The most important constant of motion is the Hamiltonian - the sum of the real energy and the fictitious Nosé terms. New equations of motion, with modified forces, are obtained:

$$\text{m}_\text{i}\ddot{\mathbf{r}}_\text{i} = \frac{1}{s^2}\mathbf{F}_\text{i} - \frac{2}{s}\dot{s}\,\text{p}_\text{i} \qquad (5.5.8)$$

$$Q\ddot{s} = \sum_i m_i s |\dot{r}_i|^2 - \frac{(f+1)k_B T_0}{s} \qquad (5.5.9)$$

The choice of the mass parameter Q does not affect the canonical averages in principle, but in order to approach these averages in reasonably short time, it is better to choose Q so that the period of oscillation of the temperature (or s) is similar to the average period of atomic vibrations. The period of oscillations of s is:

$$t_0 = 2\pi\left(\frac{Q<s>^2}{2fk_B T_0}\right)^{1/2} \approx 2\pi\left(\frac{Q}{2fk_B T_0}\right)^{1/2} \qquad (5.5.10)$$

In a similar way, Parrinello and Rahman (1981) devised a constant-pressure method. They added into the Lagrangian an extra potential term (pV) and kinetic term ($\frac{1}{2}Q\sum_\alpha\sum_\beta \dot{\mathbf{H}}_{\alpha\beta}^2$, where $\mathbf{H}_{\alpha\beta}$ is the matrix of lattice vectors).

Car and Parrinello (1985) applied the same trick to construct the first scheme of *ab initio* MD simulations, where both atomic coordinates and electronic coordinates (plane wave coefficients $C_{\mathbf{k}+\mathbf{K}}$) evolve simultaneously with time. The Car-Parrinello method is discussed in detail by Remler & Madden (1990). More modern versions of *ab initio* MD are based on the determination of the ground state at each atomic configuration ('Born-Oppenheimer dynamics'); this method, implemented in VASP and used in my works, is more stable and controllable and is much more suitable for metals. Some of the significant advances in the Earth (de Wijs et al., 1998; Alfé et al., 1999; Oganov et al., 2001b) and planetary (Ancilotto et al., 1997; Cavazzoni et al., 1999) sciences have been obtained with *ab initio* MD simulations. This is the method of choice for accurate simulations of high-temperature phenomena that are significantly anharmonic, such as melting (Sugino & Car, 1995; Alfé et al., 1999), ionic conductivity, displacive phase transitions, thermal expansion (Buda et al., 1990) and elastic properties.

Most properties can be obtained from MD in one of the three ways: 1) by calculating time averages directly, 2) by extracting properties from fluctuations, 3) from correlation functions. The first method is self-evident; I shall discuss briefly the latter two. The main sublety is that different formulas are needed for different ensembles.

Fluctuations provide a convenient route to calculate numerous response properties (heat capacity, elastic constants, Grüneisen parameter, etc.). Generally, one can write:

$$\frac{\mathrm{d}S}{k_\mathrm{B}} = \frac{\mathrm{d}E}{k_\mathrm{B}T} + \xi \mathrm{d}\mathrm{X} \quad , \tag{5.5.11}$$

where X is some extensive variable, and ξ is the associated intensive variable (divided by $k_\mathrm{B}T$). A general equation for fluctuations is then (Chandler, 1987):

$$-\left(\frac{\partial < \mathrm{X} >}{\partial \xi} \right) = <(\Delta \mathrm{X})^2> \tag{5.5.12}$$

Let us consider some particular equations for different ensembles (Allen & Tildesley, 1987). In the *NVT*-ensemble one has:

$$<(\Delta E)^2>_\mathrm{NVT} = k_\mathrm{B}\mathrm{T}^2\mathrm{C}_\mathrm{V} \tag{5.5.13}$$

$$<\Delta E_\mathrm{pot}\Delta W>_\mathrm{NVT} = k_\mathrm{B}\mathrm{T}^2[\mathrm{V}(\frac{\partial p}{\partial T})_\mathrm{V} - \mathrm{N}k_\mathrm{B}) \quad , \tag{5.5.14}$$

where the virial $W = \frac{1}{3}\sum_i \mathbf{F}_i\mathbf{r}_i$.

$$<\Delta E_\mathrm{pot}\Delta p>_\mathrm{NVT} = k_\mathrm{B}\mathrm{T}^2[(\frac{\partial p}{\partial T})_\mathrm{V} - k_\mathrm{B}/V] \quad , \tag{5.5.15}$$

In the *NVE*-ensemble:

$$<(\Delta E_\mathrm{pot})^2>_\mathrm{NVE} = <(\Delta E_\mathrm{kin})^2>_\mathrm{NVE} = \frac{3}{2}Nk_\mathrm{B}^2T^2(1-\frac{3Nk_\mathrm{B}}{2C_\mathrm{V}}) \tag{5.5.16}$$

$$<\Delta p\Delta \mathrm{E}_\mathrm{pot}>_\mathrm{NVE} = <\Delta p\Delta \mathrm{E}_\mathrm{kin}>_\mathrm{NVE} = \frac{1}{V}Nk_\mathrm{B}^2T^2[1-\frac{3V}{2C_\mathrm{V}}(\frac{\partial p}{\partial T})_V] \tag{5.5.17}$$

In the *NPT*-ensemble:

$$<(\Delta V)^2>_\mathrm{NPT} = \frac{V\mathrm{k}_\mathrm{B}T}{K_\mathrm{T}} \tag{5.5.18}$$

$$<\{\Delta(E+pV)\}^2>_\mathrm{NPT} = k_\mathrm{B}T^2C_\mathrm{p} \tag{5.5.19}$$

$$<\Delta V\Delta(E+pV)>_\mathrm{NPT} = k_\mathrm{B}T^2V\alpha_\mathrm{p} \tag{5.5.20}$$

Parrinello and Rahman (1982) have derived equations for the determination of all elastic constants from the strain fluctuations in the *NPT*-ensemble:

$$<\Delta e_\mathrm{ij}\Delta e_\mathrm{kl}>_\mathrm{NPT} = \frac{k_\mathrm{B}T}{V}S_{ijkl}^T \tag{5.5.21}$$

For more extended treatments of fluctuations, see Landau and Lifshitz (1980), Allen and Tildesley (1987), Chandler (1987), Dove (1988), Cheung (1977). Landau and Lifshitz (1980) derived general theory of fluctuations from the equilibrium ensemble distribution functions.

Correlation functions are a very important tool for studying transport properties (e.g., viscosity) and power spectra, the most important of which, the phonon density

of states, is considered below. The velocity autocorrelation function for an i-th atom is defined as:

$$C_i(t) = \frac{< \mathbf{v}_i(0)\mathbf{v}_i(t) >}{<| \mathbf{v}_i(0) |^2>} = \frac{(\lim \tau \to \infty)\frac{1}{\tau}\int_0^{\tau} \mathbf{v}_i(t')\mathbf{v}_i(t'+t)\mathrm{d}t'}{< \mathbf{v}_i^2 >} \qquad (5.5.22)$$

The phonon density of states is just a Fourier transform of the mass-weighted sum of atomic velocity autocorrelation functions (Dove, 1993):

$$g(\omega) \sim \frac{1}{T}\int [\sum_i m_i C_i(t)]\cos(\omega t)\mathrm{d}t \qquad (5.5.23)$$

The free energy, unlike many of its derivatives, is not an ensemble average and cannot be determined from MD directly; sophisticated indirect methods exist, such as thermodynamic integration (see Allen & Tildesley, 1987; Sugino & Car, 1995).

Standard MD uses classical approimation and therefore cannot be applied at low temperatures, where quantum effects are essential[42]. Quantum effects can be incorporated by 1) path integral MD (see Allen & Tildesley, 1987), 2) by using the phonon density of states g(ω) calculated from the velocity autocorrelation function and applying harmonic formulas of Chapter 3, 3) by applying quantum corrections as discussed by Matsui (1989). The quantum correction for the Helmholtz free energy per atom in the lowest order is (Landau & Lifshitz, 1980):

$$\Delta F = F(\text{quantum}) - F(\text{classical}) = \frac{\hbar^2}{24 k_B T} < \sum_i \frac{\nabla_i^2 E_{\text{pot}}}{m_i} > \ , \qquad (5.5.24)$$

where ∇_i^2 is the Laplacian with respect to the coordinates of the i-th atom. Higher-order ($\hbar^3$ and higher) corrections are needed only at temperatures below ~$\theta_D/2$. Quantum corrections to other properties can be worked out by differentiating (5.5.24) – see Matsui (1989). Good general reviews of MD can be found in Allen and Tildesley (1987) and Dove (1988).

The following chapters will present results of computer simulations of several important systems, with important mineralogical and geophysical implications.

---

[42] Some properties (e.g., mode-average Grüneisen parameter) can be derived from classical MD at any temperatures, but there will be many fundamental errors in other properties (heat capacity, thermal expansion) at low temperatures in addition to difficulties in equilibrating the system at low temperatures, where vibrations are nearly harmonic and there is practically no energy transfer between phonon modes. This is to be contrasted with the case of high temperatures, where MD is exact in all respects.

Chapter 6. Antiordering in albite ($NaAlSi_3O_8$).

This chapter will present a theoretical study of the anomalous antiordering in albite recently found experimentally (Organova et al., 1999). The results are from Oganov et al. (2001c), one of my earlier studies, actually performed in 1998. The study is performed using crystal-chemical analysis supported by ionic shell model calculations and preliminary Hartree-Fock calculations.

The antiordering phenomenon, i.e. preferential occupation of the T_{2o} positions by the Al atoms, was found in the albite component of the two-phase feldspar from the Pektusan volcano (Russian Far East). Ionic shell model calculations reproduce the normal stability of the T_{1o} ordering, but show that the antiordered structure has a lower energy at the experimental lattice parameters corresponding to the antiordered sample. Simulations and crystal-chemical analysis conclude that antiordering can take place as a result of a special strain (compression along *c* and/or stretching along *b*). Such a deformation (stretching along *b*) does indeed occur in albite at the coherent intergrowth boundaries $(\bar{6}01)$ with K-feldspar in the spinodal decomposition structures from Pektusan volcano. K-feldspar lamellae experience an opposite strain and show no change of the ordering scheme. Calculations also indicate that the antiordered structure might become thermodynamically stable at pressures of the order of a few GPa, corresponding to the deep lithosphere. The predicted transition from the normal to the antiordered structure is isosymmetric. Both ionic model calculations and preliminary Hartree-Fock simulations indicate a correlation between the type of Al-Si ordering and the position of Na atoms in the structure.

6.1. Introduction.

Crystal structures of alkali feldspars ($MAlSi_3O_8$) consist of the aluminosilicate framework, whose cavities are occupied by large alkali atoms M = K and Na (Fig. 6-1a). Si and Al are distributed over 2 crystallographically independent positions (T_1 and T_2) in the monoclinic disordered structure ($C2/m$) or over 4 positions (T_{1o} , T_{1m},

T_{2o}, and T_2) in the ordered triclinic $C\bar{1}$ structure. There are 5 oxygen positions (O_{A1}, O_{A2}, O_B, O_C, and O_D) in the monoclinic and 8 in the triclinic structure.

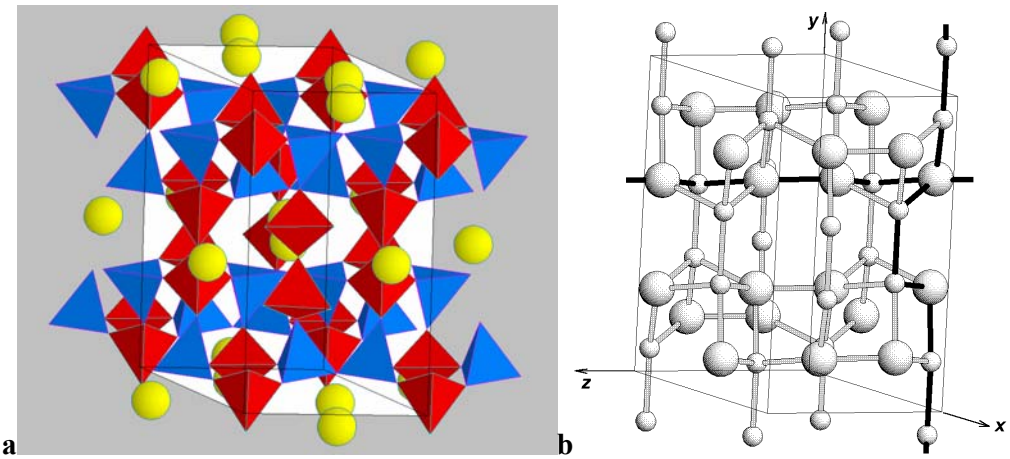

Fig. 6-1. Feldspar structure. (a) General view. *Yellow spheres* – alkali atoms in the cavities of the tetrahedral framework. *Blue* and *red* – T_1- and T_2-tetrahedra, respectively. (b) Detailed scheme of the framework. Spheres denote centres of the aluminosilicate tetrahedra. Large spheres: T_1-, small spheres: T_2-tetrahedra. Tetrahedral chains running along the *b* axis (1 period = $4T_2+2T_1$) and *c* axis (1 period = $2T_1+1T_2$) are highlighted.

All structural studies have shown that Al preferentially occupies the T_1 position in monoclinic (T_{1o} in triclinic) alkali feldpars. At low temperatures, alkali feldspar solid solutions exsolve into K- and Na-components, but some limited mutual solubility is always present.

Recently, an anomalous sample of two-phase feldspar from the Russian Far East was found and studied (Organova et al., 1999). The sample was found by V.V. Nasedkin near the Pektusan volcano. The sample crystallised at the depth of 5-6 km at temperatures of ~1173-1273 K and pressures of ~0.3 GPa. This material was later brought to the surface as a result of an explosive eruption. The sample was studied by single crystal structural refinement, electron microprobe analysis, and high-resolution electron microscopy. The latter method showed that the sample is a product of spinodal decomposition with alternating lamellae of K- and Na-components with the intergrowth boundary $(\bar{6}01)$. The average thickness of the K-lamellae is 40 Å; Na-lamellae are 120 Å thick. Structural refinements showed two anomalies. First, both phases had a monoclinic shape of the unit cell. Second, Al was found to concentrate in the T_{2o}, rather than T_{1o}, positions. Results of structural refinements of both phases for the space group $C\bar{1}$ are given in Table 6-1.

The stability of the T_{1o}-ordered phase was reproduced by computer simulation studies (Post & Burnham, 1987; Purton & Catlow, 1990; Kenny et al., 2000); however, the energy advantage over the T_{2o}-variant is rather small.

Table 6-1. Refined atomic positions in the two feldspar phases from Pektusan volcano (Organova et al., 1999). Space group $C\bar{1}$ was assumed in the refinement procedure, occupancies of the split alkali metal positions are given.

	K-phase	Na-phase
Lattice parameters		
a_0, Å	8.544(2)	8.126(1)
b_0, Å	12.998(4)	12.996(3)
c_0, Å	7.181(2)	7.164(2)
β, °	116.16(2)	116.65(2)
V_0, Å^3	715.7(7)	676.2(5)
Atomic coordinates		
M1	(0.2873; 0.0036; 0.1336)	(0.2600; 0.023; 0.156)
M2	(0.2801; -0.0086; 0.1451)	(0.2760; -0.023; 0.131)
$\mathbf{T_{1o}}$	(0.0096; 0.1834; 0.2237)	(0.0080; 0.174; 0.227)
$\mathbf{T_{1m}}$	(-0.0092; 0.1837; -0.2234)	(-0.0066; 0.177; -0.225)
$\mathbf{T_{2o}}$	(0.7064; 0.1179; 0.3433)	(0.6880; 0.118; 0.341)
$\mathbf{T_{2m}}$	(0.7064; -0.1176; 0.3436)	(0.6883; -0.115; 0.341)
$\mathbf{O_{A1}}$	(0.0005; 0.1440; -0.0001)	(0.0009; 0.132; 0.003)
$\mathbf{O_{A2}}$	(0.6310; -0.0002; 0.2835)	(0.5944; -0.008; 0.285)
$\mathbf{O_{Bo}}$	(0.1732; -0.1446; -0.2255)	(0.1843; -0.138; -0.213)
$\mathbf{O_{Bm}}$	(0.1720; 0.1448; -0.2270)	(0.1820; 0.132; -0.232)
$\mathbf{O_{Co}}$	(0.0328; 0.3092; 0.2567)	(0.0133; 0.300; 0.248)
$\mathbf{O_{Cm}}$	(-0.0329; 0.3095; -0.2565)	(-0.0176; 0.293; -0.245)
$\mathbf{O_{Do}}$	(0.1818; 0.1253; 0.4049)	(0.1971; 0.1237; 0.408)
$\mathbf{O_{Dm}}$	(0.1813; -0.1257; 0.4043)	(0.1944; -0.118; 0.407)
Occupancies of the M-positions		
M1	0.49	0.46
M2	0.49	0.52

6.2. Computer simulations.

It is well known (Burnham, 1990) that the ionic shell model is very successful at describing structures of silicates. This model also successfully reproduces the elasticity of crystal structures and their components – bonds and polyhedra. This is particularly important in the present case, where the unit cells of feldspar minerals are deformed (unit cell of albite is expanded by 1.51%, that of K-feldspar – compressed by 0.95%) because of the fine intergrowth along coherent phase boundaries.

The simplest setting of the problem includes the consideration of only the two limiting cases: 1) fully ordered with Al in T_{1o} ($MAl^{T1o}Si^{T1m}$ $(Si^{T2})_2O_8$), and 2) antiordered ($MAl^{T2o}Si^{T2m}(Si^{T1})_2O_8$) phases. Calculations were performed using the METAPOCS code (Parker, 1983) adapted to IBM PC (Urusov et al., 1994). I also performed calculations on the fully disordered phases (high albite and sanidine) using the virtual crystal formulation of Winkler et al. (1991).

The potential model used in the calculations included pairwise interactions (5.3.6.2), shell model (5.3.6.6), and three-body angle-bending potentials (5.3.6.8). There exist good sets of potential parameters for Si-O, Al-O, O-Si-O, O-O interactions and for the shell model of O^{2-}; I used parameters from (Catlow, 1977; James, 1979; Sanders et al., 1984). On the contrary, there are no well-established potential parameters for K-O and Na-O interactions. Therefore, it is preferable to use several models for these interactions and trust only those results, which are similar in different models. I used three different potentials for the Na-O and K-O interactions: potential calculated by the modified electron gas method (MEG) (Post & Burnham, 1986), empirical potential (EP), obtained by simultaneous fitting to a large number of structures (Bush et al., 1994), and my own potential (AP), which was derived *a priori*, using equation (5.3.6.3) and tables of ionic radii. Potential parameters are given in Table 6-2; AP- and MEG-potentials for Na-O are compared in Fig. 6-2. All potentials lead to reasonable predictions of the structures and properties; the best structural predictions are given by the MEG model. For high-symmetry solutions Born stability criteria were checked using the calculated elastic constants. These indicated a triclinic distortion of the disordered albite structure (see below).

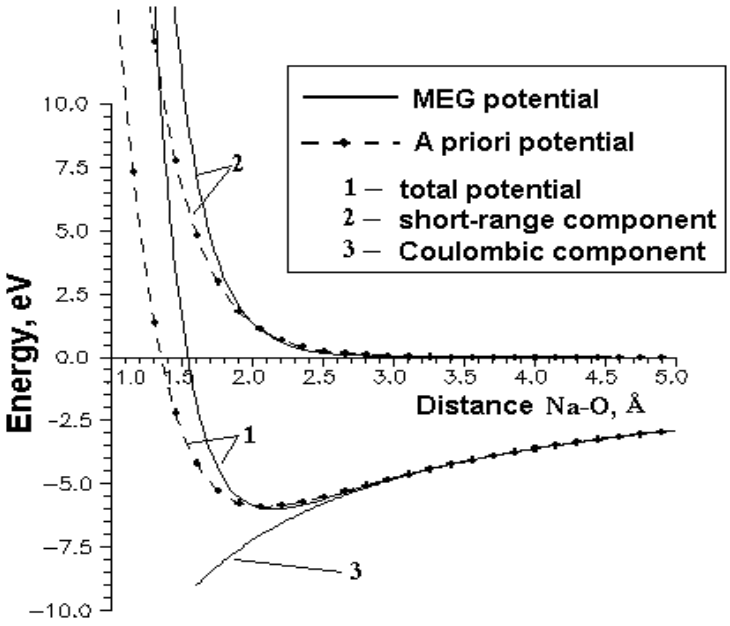

Fig. 6-2. Na-O potential: MEG and AP models.

Table 6-2. Parameters of the ionic shell model for (Na,K)$AlSi_3O_8$.
(Z_{Si} =+4.00 ; Z_{Al} =+3.00; Z_O =-2.00).

Pair potentials			
Interaction	b_{ij}, **eV**	ρ_{ij}, **Å**	c_{ij}, **eV* Å^6**
O-O	22764.3	0.1490	27.88
Al^{IV}-O	1460.3	0.29912	0
Si^{IV}-O	1283.9	0.3205	10.66
Na-O (MEG)	5836.814	0.2387	0
Na-O (EP)	1271.504	0.3000	0
Na-O (AP)	864.0	0.3110	0
K-O (MEG)	65269.710	0.2134	0
K-O (EP)	3587.500	0.3000	0
K-O (AP)	1789.3	0.3200	0
Shell parameters (only for O^{2-})			
k_s (O)=74.9204 eV*Å^{-2}. q(shell) = -2.84819. Q(core) = +0.84819			
Three-body potentials (only for tetrahedral coordination; φ_0 = 109.47°)			
k_b (O-Al-O)= k_b (O-Si-O)=2.09724 eV/rad^2			

6.3. Results.

Simulations correctly reproduce crystal structures of feldspars; some results are given in Tables 6-3 to 6-6 (compare with experimantal data from Table 6-1). Space group $C2/m$ is correctly given for the fully disordered K-feldspar (sanidine). For high albite, in accordance with experiment, the $C2/m$ solution is mechanically unstable (condition $C_{44}>0$ is violated) in the MEG- and AP-models, and the space group is lowered to $C\bar{1}$. This symmetry lowering is accompanied by the collapse of the aluminosilicate framework around the Na^+, which is too small to support large cavities of the undistorted framework. EP-potential, overestimating the Na-O repulsion and, as a consequence, the effective size of Na^+ ions, does not give this symmetry lowering. In the case of sanidine with a larger K^+, the monoclinic structure is stable in all the three models.

Let us first consider albite. All the three models show that the T_{2o}-structure has a higher energy and a higher density than the T_{1o}-structure and therefore should become thermodynamically stable at high pressures; estimates based on $p_{tr}=\Delta E/\Delta V$ are 0.3 GPa, 5.0 GPa, and 11 GPa for the MEG-, AP-, and EP-models, respectively. Therefore, it is possible that this transition takes place in the deep parts of the lithosphere, at pressures of a few GPa. Since both ordering schemes (T_{1o} and T_{2o}) result in the same symmetry ($C\bar{1}$), the transition should be isosymmetric; it must be first-order, but will become fully continuous above the critical temperature (which in this case is the temperature of Al-Si disordering).

All the three models show the following trends for the lattice parameters: increase of a_0 (by 0.7%) and c_0 (by 0.8%) in the sequence $T_{2o}\rightarrow$disordered$\rightarrow T_{1o}$ and increase of b_0 by 1% in the opposite sequence $T_{1o}\rightarrow$disordered$\rightarrow T_{2o}$. The clear dependence of the b_0 and c_0 parameters on the degree of ordering is well known from experiment and was used (Stewart & Wright, 1974) as a basis of an X-ray diffraction method of determination of the degree of ordering of feldspars.

Table 6-3 shows a significant difference in the coordinates of the Na atom in the T_{1o}- and T_{2o}-structures (the difference in the z coordinate reaches 0.052). This corresponds well to the experimentally observed 'splitting' of the Na position in partially ordered albites. The splitting of other atomic positions is much smaller.

Table 6-3. Albite: results for the EP and AP models of Na-O interactions. T_{1o}, T_{2o}, and fully disordered variants are considered. Lattice energies are given per formula unit.

Parameter	EP model			AP model		
	Al(T_{1o})	Al(T_{2o})	Disord.	Al(T_{1o})	Al(T_{2o})	Disord.
a_0, Å	8.40	8.36	8.39	8.35	8.30	8.34
b_0, Å	12.89	13.06	13.01	12.85	13.04	12.97
c_0, Å	7.17	7.10	7.15	7.15	7.08	7.13
α, °	92.7	89.0	90	93.5	88.2	88.0
β, °	116.2	116.3	116.4	116.3	116.4	116.5
γ, °	87.9	90.1	90	88.0	90.0	89.8
V_0, Å^3	695.3	694.3	698.3	687.1	685.7	689.9
Space group	$C\bar{1}$	$C\bar{1}$	$C2/m$	$C\bar{1}$	$C\bar{1}$	$C\bar{1}$
$E_{latt.}$, eV	-481.726	-481.709	-476.446	-481.771	-481.760	-476.487

Table 6-4. Crystal structure of albite: MEG model for Na-O interactions.

	Al(T_{1o})	Al(T_{2o})	Disordered
Lattice parameters			
a_0, Å	8.24	8.16	8.22
b_0, Å	12.82	12.96	12.95
c_0, Å	7.11	7.04	7.07
α, °	93.1	92.4	85.9
β, °	117.2	117.2	117.0
γ, °	92.3	90.3	89.9
V_0, Å^3	665.6	661.6	661.7
	Space group $C\bar{1}$		Space group $C\bar{1}$
Atomic coordinates (Z=4)			
Na	(.277; .030; .100)	(.268; -.003; .152)	(.273; -.011; .133)
T_{1o}	(.008; .160; .220)	(.013; .169; .217)	(.0003; .183; .226)
T_{1m}	(.000; -.188; .218)	(.002; -.176; .225)	(.007; -.162; .212)
T_{2m}	(.688; -.124; .339)	(.681; -.116; .340)	(.689; -.110; .313)
T_{2o}	(.690; .109; .322)	(.687; .115; .319)	(.684; .122; .349)
O_{A1}	(.009; .130; .002)	(.020; .134; -.004)	(-.006; .129; .018)
O_{A2}	(.596; -.014; .272)	(.583; -.009; .270)	(.590; .008; .275)
O_{Bo}	(.197; .154; -.221)	(.181; .150; -.242)	(.183; .107; -.188)
O_{Bm}	(.181; -.108; -.201)	(.170; -.109; -.198)	(.186; -.154; -.238)
O_{Co}	(.024; .286; .282)	(.025; .293; .266)	(.020; .311; .206)
O_{Cm}	(-.019; .324; -.206)	(-.014; .308; -.212)	(-.020; .288; -.277)
O_{Do}	(.185; .112; .403)	(.200; .120; .400)	(.182; .134; .433)
O_{Dm}	(.190; -.135; .435)	(.183; -.123; .408)	(.192; -.109; .389)
Lattice energies			
$E_{latt.}$, eV	-482.269	-482.267	-477.030

Table 6-5. K-feldspar: results for the EP and AP models of K-O interactions. Lattice energies are given per formula unit.

Parameter	EP model			AP model		
	Al(T_{1o})	Al(T_{2o})	Disord.	Al(T_{1o})	Al(T_{2o})	Disord.
a_0, Å	9.00	8.96	8.98	8.94	8.91	8.92
b_0, Å	12.92	13.11	13.03	12.93	13.12	13.04
c_0, Å	7.26	7.18	7.23	7.25	7.17	7.22
α, °	90.6	89.9	90	90.7	89.8	90
β, °	115.9	115.8	115.8	115.9	115.8	115.8
γ, °	88.1	90.4	90	88.0	90.3	90
V_0, Å^3	758.0	759.4	760.7	753.1	754.3	755.7
Space group	$C\bar{1}$	$C\bar{1}$	$C2/m$	$C\bar{1}$	$C\bar{1}$	$C2/m$
$E_{latt.}$, eV	-480.932	-480.926	-475.675	-480.953	-480.942	-475.691

Table 6-6. Crystal structure of K-feldspar: MEG model for K-O interactions.

	Al(T_{1o})	Al(T_{2o})	Disordered
	Lattice parameters		
a_0, Å	8.59	8.57	8.58
b_0, Å	12.93	3.09	13.03
c_0, Å	7.18	7.11	7.15
α, °	90.7	89.8	90
β, °	116.1	116.1	116.1
γ, °	87.8	90.5	90
V_0, Å^3	715.53	716.66	718.35
	Atomic coordinates		
K	(.282; -.008; .142)	(.283; -.002; .139)	(.282; 0; .140)
T_{1o}	(.008; .186; .215)	(.013; .181; .224)	(.008; .183; .222)
T_{1m}	(.007; -.179; .231)	(.006; -.185; .221)	(.008; -.183; .222)
T_{2m}	(.705; -.116; .350)	(.708; -.118; .340)	(.709; -.118; .342)
T_{2o}	(.713; .119; .337)	(.709; .117; .342)	(.709; .118; .342)
O_{A1}	(.002; .142; -.018)	(.016; .145; .008)	(0; .143; 0)
O_{A2}	(.636; .005; .284)	(.632; -.007; .281)	(.633; 0; .283)
O_{Bo}	(.172; .145; -.236)	(.172; .146; -.226)	(.172; .145; -.223)
O_{Bm}	(.179; -.145; -.214)	(.163; -.145; -.217)	(.172; -.145; -.223)
O_{Co}	(.036; .318; .252)	(.044; .304; .260)	(.037; .308; .256)
O_{Cm}	(-.044; .304; -.269)	(-.027; .306; -.246)	(-.037; .308; -.256)
O_{Do}	(.189; .124; .406)	(.180; .127; .408)	(.178; .126; .405)
O_{Dm}	(.170; -.124; .414)	(.171; -.127; .390)	(.178; -.126; .405)
	Lattice energies		
$E_{latt.}$, eV	-481.744	-481.714	-476.467

Results for K-feldspar (Tables 6-5 and 6-6) show that T_{1o}-structure is again the most stable one. However, all the three models indicate that the T_{1o}-structure also has the highest density and will be stable also at high pressures, unlike albite. Parameter a_0 is practically independent of the degree of ordering (its changes are within 0.03 Å). Like for albite, all the three models show an increase of b_0 by 1.4% in the sequence T_{1o}→disordered→T_{2o} and decrease of c_0 by 1.1% in the same sequence.

Splitting of the K position in K-feldspars is quite small; deviations of the angles α and β from 90° are also much smaller that in albite. All these findings are in complete agreement with experiment.

6.4. Nature of the antiordering.

As described above, all the potential models in agreement with experiment show that for both alkali feldspars the normal T_{1o}-ordering is energetically preferred. Antiordering can occur in albite at high hydrostatic pressures (perhaps, a few GPa), because the antiordered structure is slightly denser. However, for the sample from the Pektusan volcano another mechanism is more likely.

The energy differences between the T_{1o}- and T_{2o}-structures (per 1 Al atom) are reported in Table 6-7. These differences are very small[43]. When lattice parameters are fixed at the experimental values for the sample from Pektusan (Table 6-1), all the three models show that the antiordered T_{2o}-structure is energetically favourable for albite, but not for K-feldspar. This supports the experimental evidence of antiordering and suggests that it can be a quasi-equilibrium effect[44] related to the deformation of the structure.

Table 6-7. Energetic preference of the T_{1o} –ordering (per 1 formula unit, in kJ/mol).

Potential	Albite		K-feldspar	
	(*p*=const)	(*V*=const)	(*p*=const)	(*V*=const)
MEG	0.2	-3.0	2.9	0.6
EP	1.7	-0.8	0.7	1.8
AP	1.1	-1.8	1.1	1.2

One of the features of the feldspar structure (Fig. 6-1) is its significant anisotropy. The b_0 parameter is mainly determined by the size of the T_2-tetrahedra ($4T_2$- and $2T_1$-tetrahedra per 1 b_0 period); the opposite is true for the c_0 period ($2T_1$- and $1T_2$-tetrahedron per period). Compression along *c* will result in concentration of smaller

[43] In agreement with LDA-calculations of Kenny et al. (2000), who found the energy difference of only 3 kJ/mol between the T_{1o}- and T_{2o}-albite.

[44] More precisely, this should be described as a forced equilibrium phenomenon. Forced equilibrium is an equilibrium in the presence of additional factors, such as elastic strains on phase boundaries (Urusov et al., 1997). Exsolution of the alkali feldspar solid solution creates these strains on the intergrowth planes. These strains, as shown here, determine the subsequent process of Al-Si ordering. We know only one sample with antiordered albite; all other samples from the same location are normally ordered. A remarkable feature of our sample is a practically complete exsolution into practically pure Na- and K-feldspars. Such complete exsolution could not be an equilibrium process.

Si atoms in T_1 positions and outflow of Al into T_2, with antiordering as the end result (if compression is large enough). Analogously, stretching along *b* will result in antiordering. The opposite result (i.e. enhancement of the tendency to normal ordering) would be created by compression along *b* and/or stretcing along *c* axis.

There must be good matching of the lattice parameters of the two phases at the coherent intergrowth boundaries. As a result, the unit cell of albite is expanded, and that of K-feldspar – compressed relative to unstrained samples. In our sample, the largest stretching is along *b* and much smaller – along *c*. This is consistent with the fact that the intergrowth plane is $(\bar{6}01)$; *b* axis lies in this plane, explaining why the largest deformation is along this axis. Stretching along *b* axis should lead to antiordering; this was observed in the sample from the Pektusan volcano. In K-feldspar the deformation is opposite, and there is no change in the ordering scheme.

6.5. Hartree-Fock calculations: correlation of Na position and Al-Si ordering in albite.

Some preliminary Hartree-Fock calculations have been performed with the CRYSTAL95 code (Dovesi et al., 1996). In these calculations, performed on a Pentium II PC, I used a minimal basis set STO-3G and fixed experimental geometry from Table 6-1, with all Al in the T_{2o} positions and all Na either in the M1 (column 'Na1' in Table 6-8) or in the M2 (column 'Na2') positions. 2*2*2-mesh (4 unique points), used for the Brillouin zone sampling, leads to a very good convergence of all calculated properties. Recommended (Dovesi et al., 1996) integration tolerances were used for bielectronic integrals: ITOL1, ITOL2, ITOL3, ITOL4 and ITOL5 were equal to 10^{-6}, 10^{-6}, 10^{-6}, 10^{-6} and 10^{-12}, respectively.

Table 6-8 shows the Mulliken charges of atoms and total energies of the 'Na1' and 'Na2' structures. One can see that with T_{2o}–ordering Na atoms strongly prefer the M2 position (by 0.20 eV/(atom Na) or 19.4 kJ/mol). This is in agreement with the ionic shell model, which showed (Table 6-4) that the position of the Na atom depends on the type of ordering. Indeed, in our antiordered sample Na occupies M2 position more (Table 6-4). The ratio of the site occupancies Na1/Na2 should be directly related to the type and degree of ordering.

Table 6-8. Mulliken charges and total energy of albite from Hartree-Fock calculations (STO-3G basis).

Position	Na1	Na2

Na	+0.75	+0.74
T_{1o} (Si)	+1.28	+1.29
T_{1m} (Si)	+1.28	+1.28
T_{2m} (Si)	+1.17	+1.18
T_{2o} (Al)	+1.34	+1.34
O_{A1}	-0.70	-0.70
O_{A2}	-0.74	-0.74
O_{Bo}	-0.74	-0.74
O_{Bm}	-0.74	-0.75
O_{Co}	-0.67	-0.69
O_{Cm}	-0.77	-0.76
O_{Do}	-0.72	-0.72
O_{Dm}	-0.74	-0.74
Total energies (per 1 formula unit)		
***$E_{total.}$*, eV**	-50266.3717	-50266.5733

As Table 6-8 also shows, the position of Na does not affect the atomic charges (including the charge of Na itself). This suggests that the main effects of the Na^+ ions in the structure can be represented by the strong Coulombic interaction with the $\{AlSi_3O_8\}^{-1}$ framework and a small perturbation of the framework by orbital overlap. The calculated atomic charges are large, but much smaller than the formal ionic values. Partly this is due to the use of a minimal basis set (which usually underestimates Mulliken charges), partly due to a non-uniqueness of the definition of the atomic charge, and partly due to the real partial covalency of the chemical bonds in crystals. The ionic model is just a first approximation, but a very effective and well established one for silicate minerals. Chapter 7 (and later, Chapter 9) will present a good example of successes and failures of this model.

Chapter 7. Ionic modelling of Al_2SiO_5 polymorphs.

This chapter is rather introductory – it presents an overview of the mineralogy of the Al_2SiO_5 polymorphs and their study with simple semiclassical simulations based on the ionic shell model. This will be followed by the application of much more powerful techniques to the same minerals in Chapters 8 and 9. The results presented in this chapter are from my MSc thesis (Oganov, 1997) and an early paper (Urusov et al., 1998); only a few selected results from these works are presented here. These results were obtained using the METAPOCS code (Parker, 1983) in a version adapted to IBM PC (Urusov et al., 1994). Note that different results are sometimes obtained with the more modern GULP code, but the difference is insignificant.

7.1. Introduction.

Crystal structures of the Al_2SiO_5 polymorphs (kyanite, andlausite, sillimanite) were first solved in 1928-1929 and refined many times since, by neutron and, mainly, X-ray diffraction. High-temperature (Winter & Ghose, 1979) and high-pressure (Ralph et al., 1984; Yang et al., 1997a,b; Comodi et al., 1997) studies have been performed. A comprehensive review (Kerrick, 1990) exists on these minerals.

Kyanite is triclinic ($P\bar{1}$), andalusite and sillimanite are orthorhombic (*Pnnm* and *Pbnm*, respectively). Their structures are depicted in Fig.4-3. In these structures, Si is tetrahedrally coordinate. In all these structures, half of the Al positions are octahedrally coordinated, whereas the other half is either tetrahedrally (sillimanite), again octahedrally (kyanite) or fivefold coordinate (andalusite). It is possible to consider sillimanite as a band aluminosilicate with the band polyanions $[AlSiO_5]^{3-}$ running along the *c* axis. All the three minerals have chains of edge-sharing Al-octahedra along the *c* axis. These chains make andalusite and sillimanite highly anisotropic minerals. Anisotropy is pronounced in their thermal expansion (Winter, Ghose, 1979), linear compressibilities and elastic constants (Vaughan & Weidner, 1978). The dense structure of kyanite is based on the cubic close packing of the oxygens; electron microscopy revealed a polytype with a 4-layer packing (Grobety & Veblen, 1995).

Only kyanite satisfies the II Pauling's rule (local charge balance), which explains why kyanite is the lowest-energy phase. On the other hand, the kyanite structure has the largest number of shared polyhedral edges, which should destabilise it by the III Pauling's rule. In fact, the least stable structure (sillimanite) has the lowest number of shared polyhedral edges. However, that the energy differences between these phases are very small.

Sillimanite is structurally close to incommensurately modulated mullite ($\sim 3Al_2O_3*2SiO_2$), which is formed as a product of incongruent melting of sillimanite. Kyanite is structurally related to staurolite $Fe_2Al_9Si_4O_{22}(OH)_2$, whose structure contains kyanite layers alternating with layers of the composition AlOOH*2FeO; this explains the frequent intergrowth of the two minerals.

Vaughan and Weidner (1978) have measured the elastic constants of andalusite and sillimanite and related them to the crystal structures. Combination of accurate IR- and Raman spectra with model forcefields has lead to first lattice-dynamical models and phonon spectra of andalusite (Iishi et al., 1979; Salje & Werneke, 1982a,b) and sillimanite (Salje & Werneke, 1982a,b). Winkler and Buehrer (1990) and Rao et al. (1999) have successfully used semiclassical simulations to study the lattice dynamics of the Al_2SiO_5 polymorphs.

All Al_2SiO_5 polymorphs melt incongruently into mullite and SiO_2 melt: sillimanite at 1545°C, andalusite at 1400°C, and kyanite at 1510°C; metastable congruent melting of sillimanite occurs at 1816°C. Due to incongruent melting, these minerals are never found in magmatic rocks, but are typical metamorphic minerals. Their phase diagram, very important in the context of metamorphic petrology, has attracted much attention over the last 50 years (see, e.g., Zen, 1969; Kerrick, 1990; Hemingway et al., 1991; Olbricht et al., 1994).

For a long time, the determination of the phase diagram of Al_2SiO_5 posed a problem, due to the very small energy differences between the polymorphs. Now the problem seems to have been solved (Olbricht et al., 1994). It is interesting to note that transition metal impurities can significantly alter the stability fields of these minerals (Cr enhances the stability of kyanite, Mn stabilises andalusite). Salje (1986) experimentally demonstrated that fibrolite (fine-grained highly defective sillimanite) has a significantly higher heat capacity than sillimanite, and the grain size affects the phase diagram. Combination of neutron diffraction and NMR (Stebbins et al., 1993) showed that fibrolite has a complete Al-Si order, but there is a significant disorder in

the relative location of the fully ordered [$AlSiO_5$] bands along the *c* axis. Full Al-Si disorder in sillimanite is expected to occur at ~1700-1800 °C (Holland & Carpenter, 1986), well above the incongruent melting temperature. Thermodynamic functions have been measured many times; they have been tabulated by Robie and Hemingway (1995).

7.2. Mineralogy of Al in the lower mantle.

Although Al is expected to be one of the most abundant elements in the Earth's lower mantle (Table 2-1), not much is known about its mineralogy in that region. The mineralogy of Al is of particular interest, since if Al does not form a separate phase, it must be predominantly contained in (Mg,Fe)SiO_3-perovskite. It has been shown that if this is the case, it would radically change Fe/Mg-partitioning and phase equilibria (Wood and Rubie, 1996) between perovskite and magnesiowüstite, leading to significant enrichment of perovskite in Fe (especially in the form of Fe^{3+}) (McCammon, 1997), and that would change dramatically many physical and chemical properties (e.g. electrical conductivity, thermodynamic, rheological and diffusional properties) of perovskite. These changes could strongly affect the current geophysical and geochemical models of the mantle.

Based on the high-pressure experiments on pyrolitic material at 1800-1900 K and 23-28 GPa, Irifune (1994) has concluded that $MgSiO_3$-perovskite should be the main host of Al in the lower mantle, being able to accommodate all Al present in the lower mantle. This closely corresponds to results of Liu (1977), who showed that up to 25 mol.% of Al_2O_3 can be present in $MgSiO_3$-based perovskite solid solution. However, many other experimental studies (Madon et al., 1989; Irifune et al., 1991; Ahmed-Zaid & Madon, 1991, 1995) reveal high-pressure aluminous phases that have been proposed to be the main hosts of Al in the lower mantle. In the earlier work, Irifune et al. (1991) proposed a high-pressure form of $MgAl_2O_4$ with the $CaFe_2O_4$ structure as the main Al-phase in the lower mantle; recently, Funamori et al. (1998) synthesised an even denser phase with the $CaTi_2O_4$ structure, stable at higher pressures. Another candidate is a high-pressure modification of (Ca,Mg)$Al_2Si_2O_8$ with a hollandite-like structure (Madon et al. 1989).

Most attention has been paid to a possible high-pressure phase of Al_2SiO_5. Birle and Ehlers (1969) have studied a high-pressure phase transition of Al_2GeO_5 at 3.5 GPa and concluded that such a transition could occur in Al_2SiO_5 at 15 GPa. Powder

diffraction data on this phase did not allow the authors to identify the crystal structure of this new phase, although many of the diffraction lines can be indexed assuming the pseudobrookite structure (Oganov, 1997). At the same time Ringwood and Reid (1969) showed that Al_2GeO_5 decomposes to Al_2O_3 + GeO_2 at high pressures and Liu (1974) found that a similar decomposition of kyanite into corundum (Al_2O_3) + stishovite (SiO_2) at pressures 14-16 GPa and temperatures 1300-1700 K.

However, in the more recent experiments of Ahmed-Zaid and Madon (1991, 1995), a high-pressure form of Al_2SiO_5 with the V_3O_5-type structure was found at 40-70 GPa and 2500 K. Lattice parameters were measured for this phase and, on the basis of these values and the composition, it was found found that at the atmospheric pressure the V_3O_5-type phase of Al_2SiO_5 is 4.5% denser than the isochemical mixture of corundum and stishovite. The fact that this phase was formed as a high-pressure product in all studied samples of kyanite (Al_2SiO_5), anorthite ($CaAl_2Si_2O_8$), grossular ($Ca_3Al_2Si_3O_{12}$) and pyrope ($Mg_3Al_2Si_3O_{12}$), supported the idea that this phase might be the main host of Al in the lower mantle, comprising up to 5% of its volume. This is similar to the proportion of $CaSiO_3$-perovskite and exceeds the volume of the Earth's crust by about 3 times! (This volume is sufficient to comprise a 125-km thick layer at depth of 2000 km or a 60-km thick layer at the surface of the Earth). More recent experiments on kyanite (Al_2SiO_5) (Gautron et al. 1997; Schmidt et al. 1997), however, have shown that this phase is not formed; instead, kyanite (Al_2SiO_5) transforms into a mixture of corundum (Al_2O_3) + stishovite (SiO_2) at 25-75 GPa and T<1900 K according to Gautron et al. (1997) and at 14-17 GPa and 1300-2300 K according to Schmidt et al. (1997) and in close correspondence to earlier estimates (Liu, 1974).

In addition to the known Al_2SiO_5 polymorphs, here I consider two hypothetical phases with the V_3O_5-like and pseudobrookite structures. The latter structure deserves attention because it is thermodynamically stable for many ternary transition-metal oxides (e.g., pseudobrookite Fe_2TiO_5, armalcolite $Ti_2(Fe,Mg)O_5$, karrooite Ti_2MgO_5, anosovite Ti_3O_5, tieilite Al_2TiO_5, Ti_2CoO_5, Ga_2TiO_5, Fe_2ZrO_5, Sc_2TiO_5) and, presumably, was observed in high-pressure experiments on Al_2GeO_5.

7.3. Simulation results.

The ionic shell model included pairwise interactions (5.3.6.2), shell model (5.3.6.6), and three-body angle-bending potentials (5.3.6.8). The parameters are

given in Table 7-1. Most of them were taken from other works (Catlow, 1977; Sanders et al., 1984; Lewis & Catlow, 1985); Different repulsion parameters b_{ij} were adopted for different coordinations – for Al-O repulsion by using coordination number corrections described by Lewis and Catlow (1985), for Si^{VI}-O repulsion by fitting the energy difference quartz-stishovite to experimental values (Holm et al., 1967).

Table 7-1. Parameters of the ionic shell model for Al_2SiO_5.
(Z_{Si} =+4.00 ; Z_{Al} =+3.00; Z_O =-2.00).

Pair potentials			
Interaction	**b_{ij}, eV**	**ρ_{ij}, Å**	**c_{ij}, eV* Å^6**
O-O	22764.3	0.1490	27.88
Al^{VI}-O	1474.4	0.3006	0
Al^{V}-O	1390.3	-//-	0
Al^{IV}-O	1334.3	-//-	0
Si^{IV}-O	1283.9	0.3205	10.66
Si^{VI}-O	1318.45	-//-	-//-
Shell parameters (only for O^{2-})			
k_s (O)=74.9204 eV*Å^{-2}. q(shell) = -2.84819. Q(core) = +0.84819			
Three-body potentials (only for tetrahedral coordination; φ_0 = 109.47°)			
k_b (O-Al-O)= k_b (O-Si-O)=2.09724 eV/rad^2			

Before our work (Urusov et al., 1998), the most successful simulation study of these minerals was that by Winkler et al. (1991). We used a very similar potential model; the main difference was in the shell model parameters and in the absence of an *ad hoc* three-body potential with φ_0(O-Al-O)=95° for the five-coordinated Al polyhedron in andalusite in our work.

In our calculations (as well as in most of the previous ones) the largest deviations from experiment were for sillimanite (Table 7-2). The maximum error in lattice parameters is 4.5% (for a_0); unit cell volume is almost 4% wrong. These large errors are probably due to the largest overestimate of the ionicity and Coulombic interactions for this mineral. This leads to an overestimation of the cation-cation electrostatic repulsion and stretching of the structure (by almost 2.5%) along the *c* axis, where the Al-Al separation is minimal in the sillimanite structure. Second coordination effects account for a large part of the failings of structural predictions of the ionic model. In andalusite, the ionic model underestimates the length of the short O-O edge shared between the five-coordinate Al-polyhedra (2.0 Å instead of the

experimental 2.3 Å). This is again due to the overestimated Al-Al repulsion, a consequence of which is shortening of common polyhedral edges and faces.

Table 7-2. Crystal structure of sillimanite.

	Ionic shell model						Experiment (Winter & Ghose, 1979)		
	Winkler et al. (1991)			This work					
a_0, Å	7.271			7.153			7.4883		
b_0, Å	7.514			7.540			7.6808		
c_0, Å	5.862			5.919			5.7774		
V_0, Å^3	320.3			319.2			332.29		
Atomic coordinates									
	x	y	z	x	y	z	x	y	z
Al1	0	0	0	0	0	0	0	0	0
Al2	0.137	0.344	1/4	0.137	0.342	¼	0.1417	0.3449	¼
Si	0.153	0.333	1/4	0.151	0.336	¾	0.1533	0.3402	¾
O_a	0.366	0.401	3/4	0.370	0.402	¾	0.3605	0.4094	¾
O_b	0.357	0.437	1/4	0.357	0.436	¼	0.3569	0.4341	¼
O_c	0.473	0.000	3/4	0.475	0.004	¾	0.4763	0.0015	3/4
O_d	0.125	0.218	0.513	0.123	0.223	0.512	0.1252	0.2230	0.5145

Elastic constants have been measured only for andalusite and sillimanite; for these minerals the ionic model gives a fairly good agreement with measured values (Table 7-3). Simulations correctly describe elastic anisotropy ($C_{33}>C_{11}$, C_{22}), give realistic shear moduli (errors ~4%), but overestimate the bulk modulus by ~30%. These results are quite typical of the ionic model applied to silicates. The dielectric properties (both static and high-frequency ones) are lower than experiment by ~30%.

In the ionic model kyanite is much less stable than andalusite and sillimanite[45]. This is probably due to the large number of shared polyhedral edges in the structure of kyanite (*cf*. III Pauling's rule). Winkler et al. (1991) stated that the ionic model is too crude for prediction of the phase diagram of Al_2SiO_5. Generally, one cannot expect reliable energy differences from this model in cases where there are large structural changes between phases.

Table 7-3. Elastic properties of andalusite and sillimanite: experiment (Vaughan & Weidner, 1978) and ionic model.

	Sillimanite			Andalusite		
	Winkler et al. (1991)	This work	Experiment	Winkler et al. (1991)	This work	Experiment

[45] Their energies relative to kyanite are –0.93 eV and –0.88 eV, respectively. Experiment (Olbricht et al., 1994) gives 0.04 eV and 0.08 eV, respectively.

Elastic constants (in GPa)						
C_{11}	285	208	287.3	264	261	233.4
C_{22}	277	278	231.9	254	361	289.0
C_{33}	539	569	388.4	438	429	380.1
C_{44}	130	135	122.4	85	83	99.5
C_{55}	89	97	80.7	81	93	87.8
C_{66}	85	57	89.3	120	107	112.3
C_{12}	-	138	94.7	-	128	81.4
C_{13}	-	138	83.4	-	171	116.2
C_{23}	-	179	158.6	-	155	97.7
Voigt bulk and shear moduli (in GPa)						
K_V	-	218	175.1	-	217	165.9
G_V	-	98	95.1	-	97	100.4

Table 7-4 shows the results for the hypothetical phases. Both of them are much less compressible than the real phases and higher in energy. The pseudobrookite phase is unlikely to be stable at high pressures, because it is less dense than kyanite. The V_3O_5–like phase spontaneously distorts in the ionic model and transforms into another structure type. The resulting crystal structure has very high static dielectric constants. These distortions are an artifact of the ionic model; partly covalent models (Oganov, 1997; Oganov et al., 1997) and *ab initio* simulations (Oganov & Brodholt, 2000) do not find them.

A general conclusion is that the ionic shell model is in many cases semi-quantitatively correct in predicting structures, elastic, and dielectric properties of silicate minerals. It can also be useful in simulating lattice dynamics and defects. It is generally not reliable in predictions of the energy differences between structurally very different phases. Caution must be always paid, because structural predictions can sometimes be qualitatively wrong. In 'good' cases the model leads to results semiquantitatively similar to those of high-quality *ab initio* simulations (see Oganov et al., 2001d and Chapter 9).

In the next chapter the performance of *ab initio* GGA simulations will be analysed. These highly accurate simulations have helped us to resolve the long-standing problem of high-pressure stability of the Al_2SiO_5 polymorphs.

Table 7-4. Ionic model predictions for the hypothetical high-pressure phases of Al_2SiO_5.

	"V_3O_5-like" phase	**Pseudobrookite-like phase**
Lattice parameters		
a_0**, Å**	9.764	3.419
b_0**, Å**	4.508	9.390

c_0, Å	9.671			9.222		
β, °	142.19			(90)		
V_0, Å^3	260.97			296.05		
Atomic coordinates						
	Space group* C*2/c			Space group *Cmcm*		
	x	y	z	x	y	z
Al	0.089	0.725	0.166	0	0.139	0.570
Si	¼	¼	½	0	0.167	¼
O_a	0.200	0.501	0.109	0	0.741	¼
O_b	0.133	0.000	0.513	0	0.046	0.116
O_c	0	0.447	¼	0	0.288	0.090
Voigt bulk and shear moduli (GPa)						
K_V	343			322		
G_V	152			129		

Chapter 8. High-pressure stability of Al_2SiO_5 and mineralogy of aluminium in the Earth's lower mantle: *ab initio* calculations.

As shown in the previous chapter, the ionic model is not accurate enough to be used for calculating phase diagrams. Modern DFT can be used for such calculations. In this chapter I show how DFT simulations have resolved the long-standing problem of the high-pressure stability of the Al_2SiO_5 polymorphs discussed in the previous chapter. The results presented here are from the paper by Oganov and Brodholt (2000).

Ab initio GGA-DFT calculations have been performed using plane wave pseudopotential method. Polymorphs of Al_2SiO_5 (kyanite, andalusite, sillimanite, and hypothetical V_3O_5-like and pseudobrookite-like phases – see Fig. 8-1), SiO_2 (stishovite, quartz) and Al_2O_3 (corundum) have been considered. Good agreement of crystal structures, bulk moduli, atomisation energies and the phase diagram of Al_2SiO_5 with experimental data was found. Strong disagreement between the calculated lattice parameters and density of V_3O_5-like phase of Al_2SiO_5 and the experimental values (Ahmed-Zaid & Madon, 1991) suggests that the phase studied in the latter work is not a V_3O_5-structured phase of Al_2SiO_5. In addition, we found that Al_2SiO_5 breaks down into the mixture of oxides at 11 GPa (at T=O K), in excellent agreement with experimental estimates (9.5-15 GPa). The instability of Al_2SiO_5 phases with octahedrally coordinated Si to decomposition was explained on the basis of Pauling's second rule.

8.1. Computational methodology.

The calculations were performed with the VASP code (Kresse & Furthmuller, 1996a,b) and were based on DFT within the generalised gradient approximation (PW91-GGA functional: Wang & Perdew (1991)). Valence electron wavefunctions were expanded in plane-wave basis set and all core electrons replaced by effective core pseudopotentials. All adopted pseudopotentials are non-local: norm-conserving

pseudopotentials (Rappe et al., 1990) with partial core corrections (Louie et al., 1982) for Al and Si; non-normconserving (ultrasoft) pseudopotentials (Vanderbilt, 1990) for O. Core region cutoffs are 0.96 Å for Al (valence configuration $3s^2 3p^1 3d^0$), 0.95 Å for Si (valence configuration $3s^2 3p^2 3d^0$), and 0.82 Å for O (valence configuration $2s^2 2p^4 3d^0$). All these pseudopotentials are supplied with the VASP package.

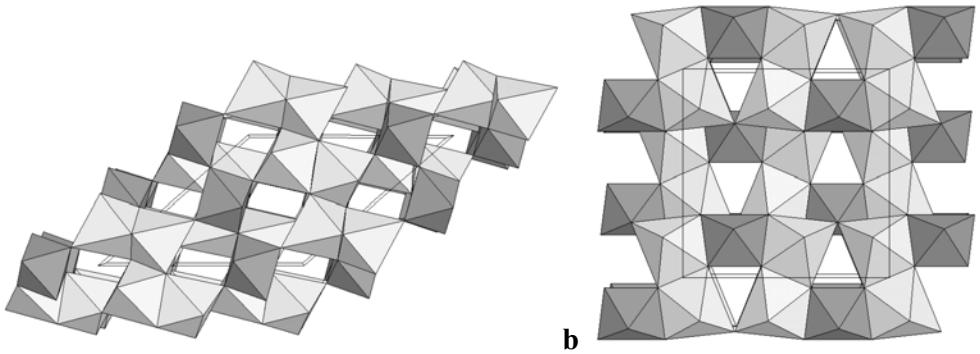

a **b**

Fig. 8-1. Theoretically calculated crystal structures of the hypothetical high-pressure phases of Al_2SiO_5. Si-polyhedra are grey, Al-polyhedra are light grey.

(a) V_3O_5-like structure. This structure is based on the hexagonal close packing of oxygen atoms. Remarkable pairs of face-sharing octahedra tend to be occupied by Al rather than Si in order to reduce the cation-cation electrostatic repulsion (3rd and 4th Pauling's rules); this leads to the cation ordering shown here and space group C2/c.

(b) Pseudobrookite-like structure. This structure is not close packed, but contains only fragments ("islands") of close packing. Therefore, its density cannot be very high: it should be close to the density of the high-pressure Al_2SiO_5-melt. Interestingly, due to its topology, this structure in principle cannot be built from ideal Al-octahedra.

The Al_2SiO_5-polymorphs are known to have very small energy differences (~0.04 eV per formula unit at ambient conditions); the resulting kinetic problems precluded precise experimental determination of the phase diagram of Al_2SiO_5 for a long time (Zen, 1969; Kerrick, 1990). Therefore, care must be taken in order to reproduce these small effects correctly and reliably.

A plane-wave cut-off energy of 800 eV proved to be very reliable (convergence to within $6*10^{-4}$ eV/atom) and computationally acceptable; this was used throughout all calculations. For Brillouin-zone sampling I used Monkhorst-Pack (1976) meshes: 4*4*4 for corundum (10 symmetrically unique points) and stishovite (6 unique points), 3*3*3 for quartz (7 unique points), and 2*2*2 for all the Al_2SiO_5 phases (4 unique points for kyanite, 3 for V_3O_5-like phase, 2 for pseudobrookite-like phase, and 1 unique point for andalusite and sillimanite). Increasing these numbers did not

lead to the total energy changes exceeding 0.01 eV per formula unit. The number of plane waves included in the calculation is roughly proportional to the unit cell volume, and for the most difficult cases - kyanite, andalusite, and sillimanite at equilibrium volumes, it was 15450, 17990, and 17430 plane waves per **k**-point, respectively. These demanding calculations were performed on 64 nodes of a CRAY T3E supercomputer at Edinburgh Parallel Computer Centre.

The present calculations are static, performed with full symmetry-preserving relaxation of the lattice parameters and ionic positions. The energy minimisation procedure is iterative and proceeds until self-consistency within a prescribed tolerance (10^{-3}eV for ionic and 10^{-4}eV for electronic relaxation). Stresses and forces on atoms, used for structure relaxation, are calculated from the charge density using the Hellmann-Feynman theorem. An efficient constant-volume energy minimisation technique was used, which in VASP optimises all lattice parameters and ionic coordinates within the specified volume constraint. This technique reduces to minimum the effects of basis set incompleteness. Stresses and forces are more sensitive to errors due to incomplete convergence (of the wavefunction and of the atomic positions) than the energy: these errors, causing only second-order errors in the energy, lead to first-order errors in the stresses and forces. For quartz, which has an open structure with extremely flexible Si-O-Si tetrahedral linkages, errors due to incomplete convergence of atomic coordinates proved to be significant. Therefore, it may be more reasonable to obtain pressure indirectly as $p = -(\frac{dE}{dV})$, with $E(V)$-functions fitted as 3rd or 4th-order polynomials. These analytical $E(V)$-curves, together with the original $E(V)$-datapoints, calculated by VASP, are shown on Fig. 8-2. The maximum difference found between the polynomial expansion and VASP points is only 0.005 eV for all minerals considered. Typical differences for pressure are within 1-2 kbar; only for quartz they were larger by an order of magnitude. In all cases, the total energies were converged to within 0.02 eV per formula unit.

In order to obtain atomisation energies, I performed special calculations on atoms in their spin-polarised ground states using the same pseudopotentials, plane wave cutoff, and exchange-correlation functionals as before and large (15 Å side) primitive cubic unit cells. These calculations proved to be very demanding, since the basis set included over 173,000 plane waves. The atomic ground states were reproduced correctly. The atomic energies are converged to better than 0.01 eV/atom with respect to the unit cell size. Zero-point vibrational energies were estimated by lattice

dynamics simulations using the GULP code (Gale, 1997) and ionic shell model of Chapter 7. In these calculations, the dynamical matrix was diagonaled at 1000 reducible points of the Brillouin zone after complete structural relaxation.

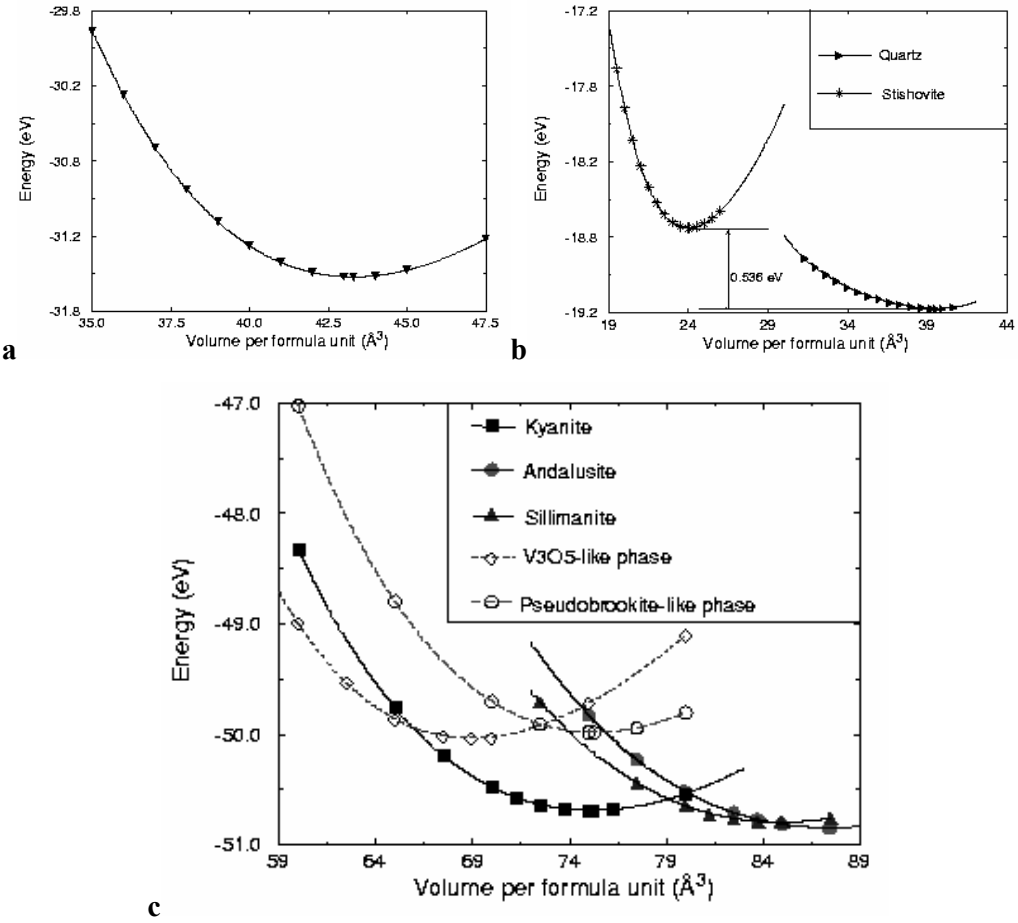

Fig. 8-2. Calculated E(V) curves. (a) Corundum, (b) Quartz and stishovite, (c) Al_2SiO_5 polymorphs. Symbols indicate results of individual calculations, and lines are polynomial fits (solid lines – for real phases, broken – for the hypothetical ones).

8.2. Results.

Comparison between the calculated and experimental values of the equilibrium unit cell parameters and volumes, atomisation energies, bulk moduli, K_0, and their pressure derivatives K' (obtained by fitting the Vinet EOS) is given in Table 8-1 together with theoretical data on the hypothetical phases of Al_2SiO_5. Atomic fractional coordinates are typically reproduced to within 0.001. Theoretical predictions of atomisation energies are very good (underestimation by only about 1.1% (0.07 eV/atom) and 2.7% (0.17 eV/atom) without and with the zero-point energy correction, respectively). Theory overestimates the unit cell parameters and

volumes by a few percent; this noticeable error is typical for the GGA. Equations of state of these minerals are shown in Fig. 8-3.

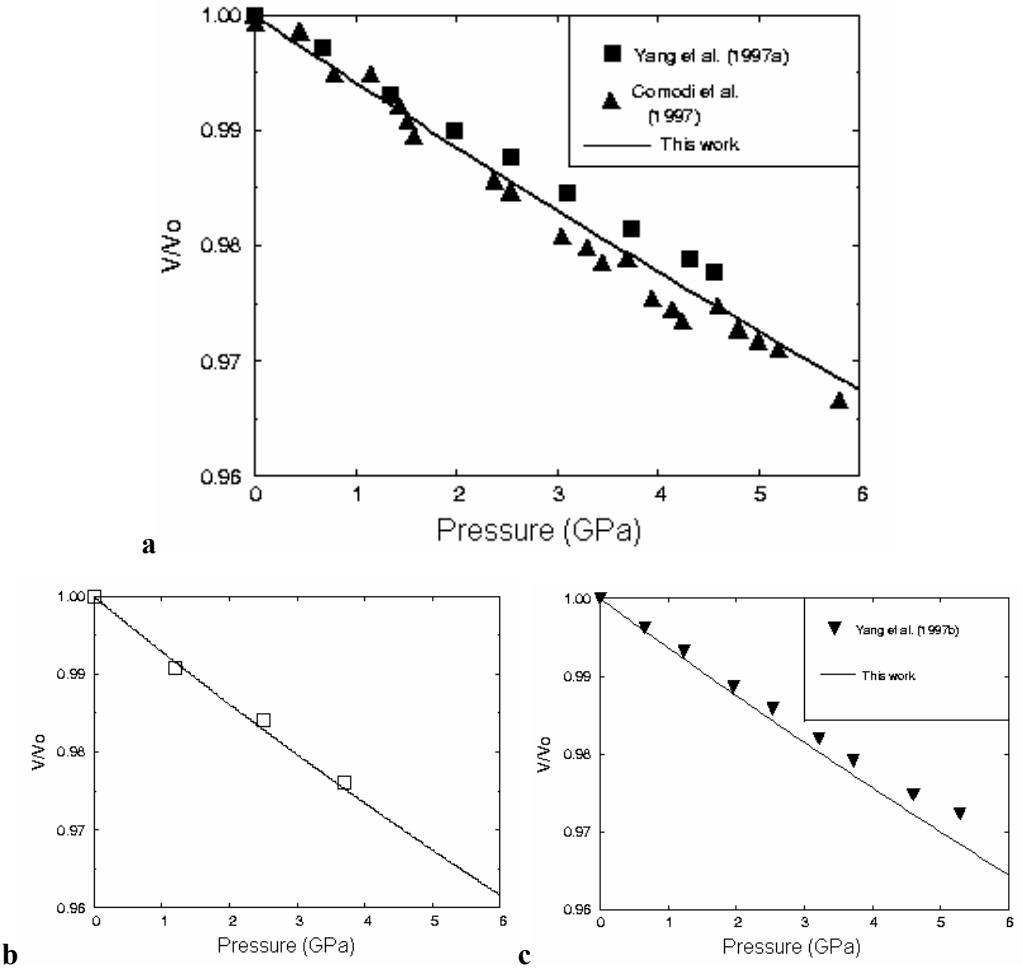

Fig. 8-3. p(V)-equations of state of Al_2SiO_5 polymoprhs. (a) Kyanite ; (b) Andalusite. Empty squares - experimental data of Ralph et al. (1984) corrected by Yang et al. (1997b); (c) Sillimanite. Solid lines – theoretical results (present work).

Density differences between the phases are reproduced very accurately. The energy differences are more interesting (Table 8-2): it is interesting to observe that in absolutely all cases the lower-density phases (on the left hand sides of the reactions in Table 8-2) are overstabilised by the GGA relative to the experiment. The forces, responsible for the overexpansion of structures in GGA, are also responsible for the overstabilisation of polymorphs with more open structures. Recent all-electron study (Zupan et al., 1998) showed stabilisation of lower-density phases in the GGA with respect to the local spin density approximation (LSDA). It was concluded that both this effect and overexpansion of crystal structures in GGA are due to stabilisation of more inhomogeneous electron density distributions, characteristic of less dense

structures, by gradient corrections (see equation (5.3.4.11) and discussion there). Results of all-electron calculations of Zupan et al. (1998) on quartz and stishovite (structural parameters, K_0 and K') are in excellent agreement with our pseudopotential study, highlighting very high quality of the pseudopotentials used in our work.

As a consequence of the above discussed GGA error, in our calculations (as well as in subsequent GGA calculations of Iglesias et al. (2001), but in contrast to experiment) kyanite is not the thermodynamically stable phase at p=0 and T=0 K. The application of pressure corrects this situation, increasing the relative stability of the denser polymorphs. As a result, the phase diagram of Al_2SiO_5 (Fig. 8-4) is reproduced very well, all the calculated transition pressures being only ~2 GPa higher than the corresponding experimental values.

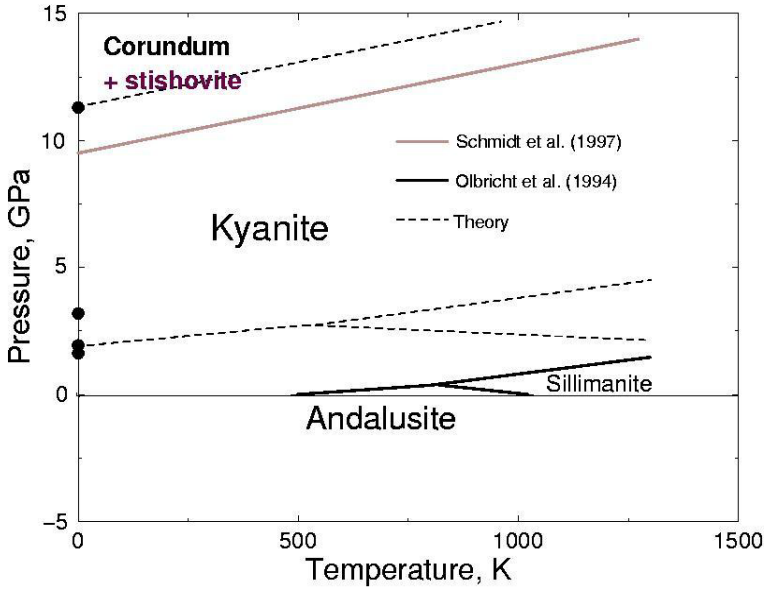

Figure 8-4. Phase diagram of Al_2SiO_5. Solid lines – experimental data, filled circles – calculated transition pressures at T= 0 K, dashed lines were drawn through these points with experimental p(T)-slopes of equilibria kyanite-(corundum+stishovite), kyanite-andalusite, and kyanite-sillimanite. These data are suffiient to determine the p(T)-slope of andalusite-sillimanite equilibrium.

Enthalpy *vs* pressure curves $H(p)$ are represented in Fig. 8-5. From Fig. 8-2 and Fig. 8-5 it is obvious that the pseudobrookite structure cannot be thermodynamically stable for Al_2SiO_5 and becomes increasingly less stable at high pressures. It can also be seen that kyanite, which in GGA simulations becomes the most stable phase at 1.9 GPa, transforms into the mixture of corundum and stishovite at 11 GPa (compare

with 9.5 GPa extrapolated to T=0 K from experimental data of Schmidt et al. (1997) or 15 GPa from earlier estimates of Liu (1974)).

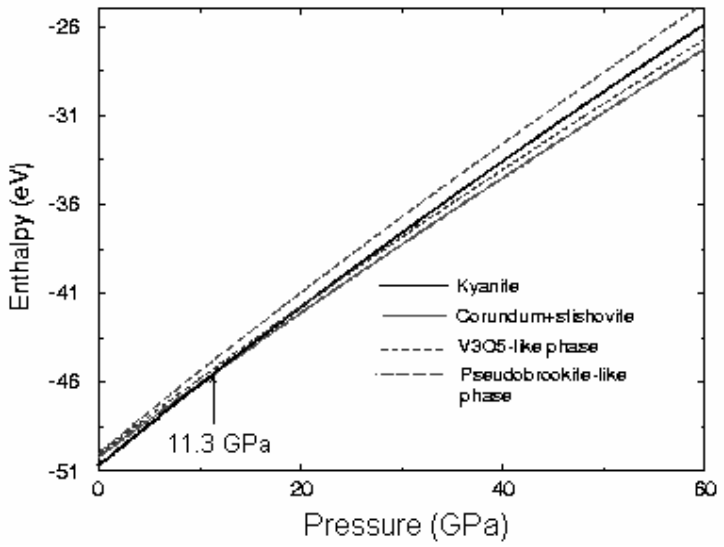

Fig. 8-5. Calculated enthalpy vs. pressure curves for kyanite and high-pressure candidate phases. Pressure of kyanite→(corundum+stishovite) transformation is indicated by an arrow.

V_3O_5-like structure becomes more favourable than kyanite at 21 GPa, but is less stable than the Al_2O_3+SiO_2 (corundum+stishovite) mixture at all pressures between 0 and 150 GPa. Vibrational entropy cannot stabilise this phase, since the enthalpy of its decomposition is very large (-0.47 to -0.61 eV at 40 to 70 GPa and -0.83 eV at 150 GPa). The maximum configurational entropy, assuming complete Al-Si disordering in octahedral sites, $\Delta S_{conf}^{\max} = -3R[\frac{1}{3}\ln(\frac{1}{3})+\frac{2}{3}\ln(\frac{2}{3})]$=15.87 J/(mole*K), can make the disordered V_3O_5-like phase stable to decomposition only at the temperatures higher than T=2900 at 40 GPa or above 5000 K at 150 GPa (i.e. above the mantle solidus of Zerr et al. (1998)). Since Al-Si disordering is associated with local charge imbalance, it would significantly increase the enthalpy of this phase, shifting its stability field towards even higher temperatures, not available in the Earth's mantle.

While stability considerations still leave some possibility for the V_3O_5-like phase to be stable at very high temperatures, consideration of the lattice parameters and density indicates that this phase has never been synthesised. We predict that V_3O_5-like phase should be 2.3% less dense than the corundum+stishovite mixture, in contradiction to results of Ahmed-Zaid and Madon (1991), who found that their phase (indentified as the V_3O_5-structured phase of Al_2SiO_5) was 4.5% denser than

the oxide mixture. The difference in the unit cell volume of the V_3O_5-like phase between our calculations and results of Ahmed-Zaid and Madon (1991) is 11%, which is well beyond the errors of the calculation. Lattice parameters, obtained in the latter experiment, differ strikingly from ours (Table 8-1); however, care must be taken since for monoclinic crystals (e.g., V_3O_5) three alternative settings of the coordinate system - "cell choices" (International Tables for Crystallography, 1994)) - are possible. Simple matrix transformations allow one to change the cell choice. All these cell choices are listed in Table 8-1. Cell choice 2 resembles results of Ahmed-Zaid and Madon (1991) (a_0 = 8.478 Å, b_0 = 4.471 Å, c_0 = 6.782 Å, β = 104.25°; V_0 = 249.08 Å^3) more than the others, however, the differences, especially in the a_0-parameter, are irreconciliable. Therefore, the phase synthesised by Ahmed-Zaid and Madon (1991) is unlikely to be a V_3O_5-like polymorph of Al_2SiO_5.

I have also studied a variant of the V_3O_5-like structure with the space group *P*2/*c*, differing in the distribution of Al and Si in octahedral sites. This structure, due to the lower symmetry, has four (rather than two) non-equivalent cationic positions. This variant can be produced from the *C*2/*c*–variant by exchanging positions of Si and one half of Al atoms. This structure is much higher in energy than the *C*2/*c*-variant (ΔE=0.23 eV per formula unit) and somewhat less dense (ΔV=0.30 cm^3/mole). Therefore, it should not be expected as a candidate high-pressure phase. Its equilibrium lattice parameters are in a similarly striking disagreement with data of Ahmed-Zaid and Madon (1991). The large value of ΔE=0.23 eV shows that the energy cost of Al-Si disordering in this structure is high.

Based on the data from the paper by Ahmed-Zaid and Madon (1991) and on the present results, we doubt that the Ahmed-Zaid and Madon's phase is at all a polymorph of Al_2SiO_5. A possibility, more consistent with the experimental unit cell volume, is $Al_8Si_3O_8$ (isochemical mixture of corundum and stishovite at ambient pressure would have the molecular volume of 239.6 Å^3). It should be possible to determine, which structure and composition match the experimental lattice parameters, using the newly developed genetic algorithms technique (Bush et al., 1995).

8.3. Discussion.

Using *ab initio* calculations, we have demonstrated that kyanite, V_3O_5–like and pseudobrookite-like phases of Al_2SiO_5 are unstable with respect to decomposition

into simple oxides, corundum (Al_2O_3) and stishovite (SiO_2). It was recently discovered that both corundum and stishovite are not the most stable phases of the corresponding oxides at high pressures and should undergo phase transitions. Corundum transforms into a phase with the Rh_2O_3(II)-type structure at 80-100 GPa (experiment: Funamori & Jeanloz, 1997; theory: Marton & Cohen, 1994; Duan et al., 1998), and stishovite transforms into a phase with the $CaCl_2$-type structure at *ca* 50 GPa (experiment: Kingma et al., 1995; theory: Karki et al., 1997); there are also theoretical predictions of further phase transitions for both minerals at higher pressures. All these phase transitions occur at much higher pressures than the decomposition of kyanite into corundum and stishovite (11 GPa) and, therefore, do not change the calculated phase diagram, but only enhance our conclusion at very high pressures, where even more stable oxide phases appear.

The results, concerning the hypothetical phases, can be rationalised in terms of classical crystal chemistry. It turns out that the V_3O_5–like phase does not satisfy Pauling's second rule (sum of the electrostatic bond valences on the anion should be equal to the anion's valence). It is easy to check that this rule cannot be satisfied by any composite phase in the Al_2O_3-SiO_2 system with octahedrally coordinated Al and Si. As has been shown by Brown (1992), structures that do not satisfy the second Pauling's rule must undergo distortions, quantified by the modified Pauling's rule, proposed by Brown (1992). Apart from such electronic effects as Jahn-Teller effect, these distortions are usually destabilising. The distortion also results in an increase of the average bond lengths (the "distortion theorem" (Brown, 1992) implied by Brown's rule), which may decrease the density of the structure. In contrast to V_3O_5–like and pseudobrookite-like phases, corundum and stishovite satisfy Pauling's rule exactly. This partly explains the higher energy and lower density of the hypothetical Al_2SiO_5-phases with respect to the mixture of corundum and stishovite.

Table 8-1. Phases in Al_2O_3-SiO_2 system: theoretical results and experimental data.

A. Simple Oxides.

Property	**VASP**	**Experiment**
Corundum (space group $R\bar{3}c$; Z=6[a]).		
$a_0 = b_0$, Å	4.811	4.7570[b]
c_0, Å	13.072	12.9877[b]
V_0, Å^3	259.77	254.52[b]
Al (x, y, z)	(0, 0, 0.3521)	(0, 0, 0.35220)[b]
O (x, y, z)	(0.3062, 0, ¼)	(0.30627, 0, ¼)[b]
K_0, GPa	233	254.4[c]; 258[d]
K'	3.99	4.275[c]; 4.88[d]
$E_{atom.}$, eV	-31.518 (-31.04) [e]	-31.73[f]
Stishovite (space group $P4_2/mnm$; Z=2)		
$a_0 = b_0$, Å	4.229	4.1801[g]
c_0, Å	2.687	2.6678[g]
V_0, Å^3	48.04	46.615[g]
Si (x, y, z)	(0, 0, 0)	(0, 0, 0)[g]
O (x, y, z)	(0.3071, 0.3071, 0)	(0.3067, 0.3067, 0)[g]
K_0, GPa	265	306[g]; 313[h]
K'	4.88	2.8[g]; 6[h]
$E_{atom.}$, eV	-18.687 (-18.40) [e]	-19.08[i]
Quartz (space group $P3_221$; Z=3)		
$a_0 = b_0$, Å	4.994	4.91239[j]
c_0, Å	5.498	5.40385[j]
V_0, Å^3	118.76	112.933[j]
Si (x, y, z)	(0.5257, 0, 2/3)	(0.5299, 0, 2/3)[j]
O (x, y, z)	(0.5846, 0.7399, 0.7921)	(0.5861, 0.7326, 0.7856)[j]
K_0, GPa	44.3	37.12[k]
K'	3.20	5.99[k]
$E_{atom.}$, eV	-19.224 (-18.92) [e]	-19.467 [f]

B. Known Al_2SiO_5 polymorphs.

Property	**VASP**	**Experiment**
Kyanite (space group $P\bar{1}$; *Z*=4).		
a_0 **, Å**	7.185	7.1262[l]
b_0**, Å**	7.916	7.8520[l]
c_0**, Å**	5.613	5.5724[l]
α**, °**	89.9	89.99[l]
β**, °**	101.1	101.11[l]
γ**, °**	106.0	106.03[l]
V_0**, Å^3**	300.64	293.60[l]
Al1 (x, y, z)	(0.3247, 0.7039, 0.4581)	(0.3254, 0.7040, 0.4582)[l]
Al2 (x, y, z)	(0.2966, 0.6986, 0.9502)	(0.2974, 0.6989, 0.9505)[l]
Al3 (x, y, z)	(0.0994, 0.3864, 0.6407)	(0.0998, 0.3862, 0.6403)[l]
Al4 (x, y, z)	(0.1116, 0.9170, 0.1645)	(0.1120, 0.9175, 0.1649)[l]
Si1 (x, y, z)	(0.2961, 0.0650, 0.7066)	(0.2962, 0.0649, 0.7066)[l]
Si2 (x, y, z)	(0.2909, 0.3315, 0.1896)	(0.2910, 0.3317, 0.1892)[l]
O_a (x, y, z)	(0.1105, 0.1461, 0.1284)	(0.1095, 0.1468, 0.1288)[l]
O_b (x, y, z)	(0.1230, 0.6858, 0.1816)	(0.1230, 0.6856, 0.1812)[l]
O_c (x, y, z)	(0.2735, 0.4550, 0.9556)	(0.2747, 0.4545, 0.9547)[l]
O_d (x, y, z)	(0.2816, 0.9341, 0.9338)	(0.2831, 0.9354, 0.9353)[l]
O_e (x, y, z)	(0.1218, 0.6300, 0.6389)	(0.1219, 0.6307, 0.6389)[l]
O_f (x, y, z)	(0.2810, 0.4447, 0.4289)	(0.2822, 0.4453, 0.4288)[l]
O_g (x, y, z)	(0.2901, 0.9465, 0.4658)	(0.2915, 0.9467, 0.4659)[l]
O_h (x, y, z)	(0.5018, 0.2770, 0.2449)	(0.5008, 0.2749, 0.2440)[l]
O_k (x, y, z)	(0.1091, 0.1532, 0.6682)	(0.1084, 0.1520, 0.6669)[l]
O_m (x, y, z)	(0.5024, 0.2298, 0.7560)	(0.5015, 0.2312, 0.7553)[l]
K_0**, GPa**	172	156[m] ; 193[n]
K'	4.01	5.6[m] ; [4][n]
$E_{atom.}$**, eV**	-50.692 (-49.91) [e]	-51.27 [f]
Andalusite (space group *Pnnm* ; *Z*=4)		
a_0 **, Å**	7.860	7.7980[l]
b_0**, Å**	7.956	7.9031[l]
c_0**, Å**	5.592	5.5566[l]
V_0**, Å^3**	349.68	342.45[l]
Al1 (x, y, z)	(0, 0, 0.2419)	(0, 0, 0.2419)[l]
Al2 (x, y, z)	(0.3709, 0.1389, ½)	(0.3705, 0.1391, ½)[l]
Si (x, y, z)	(0.2458, 0.2522, 0)	(0.2460, 0.2520, 0)[l]
O_a (x, y, z)	(0.4243, 0.3627, ½)	(0.4233, 0.3629, ½)[l]
O_b (x, y, z)	(0.4238, 0.3640, 0)	(0.4246, 0.3629, 0)[l]
O_c (x, y, z)	(0.1025, 0.4006, 0)	(0.1030, 0.4003, 0)[l]
O_d (x, y, z)	(0.2311, 0.1341, 0.2401)	(0.2305, 0.1339, 0.2394)[l]
K_0**, GPa**	142	135[o] ; 151[p]
K'	4.18	[4] [o] ; [4] [p]
$E_{atom.}$**, eV**	-50.844 (-50.07) [e]	-51.23 [f]

Sillimanite (space group *Pbnm* ; *Z*=4)		
a_0, Å	7.555	7.4883[l]
b_0, Å	7.756	7.6808[l]
c_0, Å	5.795	5.7774[l]
V_0, Å^3	339.57	332.29[l]
Al1 (x, y, z)	(0, 0, 0)	(0, 0, 0)
Al2 (x, y, z)	(0.1429, 0.3464, ¼)	(0.1417, 0.3449, ¼)[l]
Si (x, y, z)	(0.1530, 0.3413, 3/4)	(0.1533, 0.3402, ¾)[l]
O_a (x, y, z)	(0.3594, 0.4110, 3/4)	(0.3605, 0.4094, ¾)[l]
O_b (x, y, z)	(0.3571, 0.4342, ¼)	(0.3569, 0.4341, ¼)[l]
O_c (x, y, z)	(0.4776, 0.0020, 3/4)	(0.4763, 0.0015, ¾)[l]
O_d (x, y, z)	(0.1253, 0.2239, 0.5135)	(0.1252, 0.2230, 0.5145)[l]
K_0, GPa	159	171[p]
K'	2.70	[4][p]
$E_{atom.}$, eV	-50.795 (-50.01) [e]	-51.19 [f]

C. Hypothetical polymorphs of Al_2SiO_5.

Property	Pair potentials[r]	VASP
Pseudobrookite-like phase (space group *Cmcm* ; *Z*=4).		
a_0 , Å	3.498	3.552
b_0, Å	9.228	9.261
c_0, Å	9.168	9.158
V_0, Å^3	295.91	301.26
Al (x, y, z)	(0, 0.139, 0.566)	(0, 0.135, 0.567)
Si (x, y, z)	(0, 0.182, ¼)	(0, 0.184, ¼)
O_a (x, y, z)	(0, 0.736, ¼)	(0, 0.740, ¼)
O_b (x, y, z)	(0, 0.051, 0.120)	(0, 0.055, 0.118)
O_c (x, y, z)	(0, 0.301, 0.087)	(0, 0.313, 0.090)
$E_{atom.}$, eV	-49.62	-49.982(-49.23) [e]
K_0, GPa	260.0 (Voigt)	218.41
K'	-	3.545
V_3O_5-like phase (space group *C2/c* ; *Z*=4).		
a_0 , Å	9.623	9.474
b_0, Å	4.648	4.705
c_0, Å	9.328	9.312
β_0, °	138.76	137.98
V_0, A^3	269.50	275.68
Al (x, y, z)	(0.148, 0.752, 0.263)	(0.156, 0.760, 0.273)
Si (x, y, z)	(¼,¼, ½)	(¼, ¼, ½)
O_a (x, y, z)	(0.220, 0.608, 0.147)	(0.217, 0.608, 0.147)
O_b (x, y, z)	(0.126, 0.924, 0.451)	(0.121, 0.924, 0.452)
O_c (x, y, z)	(0, 0.432, ¼)	(0, 0.439, ¼)

$E_{atom.}$, eV	-49.99	-50.038
K_0, GPa	288.0 (Voigt)	227
K'	-	4.08

Lattice parameters for different cell choices (VASP results)

	Cell choice 1	**Cell choice 2**	Cell choice 3
a_0, Å	9.474	9.312	6.676
b_0, Å	4.705	4.705	4.705
c_0, Å	9.312	6.676	9.474
β_0, °	137.98	109.51	112.11

a – Z is the number of formula units in the unit cell.
b – Kirfel and Eichhorn (1990).
c – d'Amour et al. (1978).
d – Dubrovinsky et al. (1998).
e – Numbers in parentheses include the zero-point energy correction. In the ionic model, the V_3O_5-like phase spontaneously transformed into another structure, obstructing estimation of the zero-point energy correction for this phase.
f – Recalculated from (Olbricht et al. 1994).
g – Ross et al. (1990).
h – Sugiyama et al. (1987).
i – estimated from the data (Olbricht et al. 1994) on quartz and the most recent data on ΔH of quartz-stishovite transformation (0.384 eV) (Akaogi et al. 1995).
j – Will et al. (1988).
k – Angel et al. (1997).
l – Winter and Ghose (1979).
m – Comodi et al. (1997).
n – Yang et al. (1997a). K' fixed equal 4.
o – Ralph et al. (1984). K' fixed equal 4.
p – Yang et al. (1997b). K' fixed equal 4.
r – Charge-variational potentials from (Oganov, 1997; Urusov et al., 1999).

Table 8-2. The energy and volume effects of mineral transformations at zero pressure: theory and experiment.

Reaction	**ΔE, eV**		**ΔV_m, cm^3/mole**	
	VASP	*Exp.*	VASP	*Exp.*
Andalusite→Sillimanite	0.05 (0.06) [a]	0.04	-1.5	-1.5
Andalusite→Kyanite	0.15 (0.16) [a]	-0.04	-7.4	-7.4
Quartz→Stishovite	0.54 (0.51) [a]	0.38[b]; 0.51[c]	-9.4	-8.6
Andalusite→Corundum+Quartz	0.10 (0.11) [a]	0.03	-2.7	-3.3
Kyanite→Corundum+Stishovite	0.49 (0.46) [a]	0.46	-4.7	-4.6

a – Numbers in parentheses include the zero-point energy correction, which proved to be small enough for the energy differences and was neglected in all our further calculations.
b – Akaogi et al. (1995).
c – Holm et al. (1967).

On the other hand, it is well known that the formation of complex oxides and silicates from the constituent oxides is favoured when cations differ significantly in the electronegativities (Urusov, 1993) and ionic radii (e.g., $MgO+SiO_2 \rightarrow MgSiO_3$ due to significant differences in the electronegativities and ionic radii of Mg and Si). In other terms, the formation of the complex compounds is strongly favoured if the constituent components have different acid-base properties and can play different crystal-chemical roles. At high pressures, both Si^{4+} and Al^{3+} adopt octahedral coordination and cannot play significantly different structural roles anymore. As a result, pure Al-silicates are likely to break down, as in the case considered here. In contrast, aluminosilicates of large and electropositive cations (Ca, Mg, Na, K), e.g. the hollandite-like phase of $(Ca,Mg)Al_2Si_2O_8$, or the high-pressure modifications of $MgAl_2O_4$, could be stable in the lower mantle and be major hosts of Al in the lower mantle, unless Al prefers to form $(Mg,Fe)(Si,Al)O_3$-perovskite solid solutions[46].

In the next chapter I discuss the compression behaviour of the Al_2SiO_5 polymorphs simulated by *ab initio* and semiclassical methods. Their anomalous behaviour at high pressures gives much insight into the nature of pressure-induced phase transitions and metastability.

[46] Note, however, that both arguments (Pauling's second rule and acid-base properties of cations) are purely energetical and do not apply to the entropy. Although the octahedral Al-silicates are unfavoured energetically, they may be stabilised by the configurational entropy of Al-Si disorder at high temperatures. In the particular case of the V_3O_5–like modification of Al_2SiO_5 we have shown that the lower mantle temperatures are insufficient to stabilise it. One can expect that Al-Si disordering in $(Mg,Fe)(Si,Al)O_3$-perovskite, where Al is a minor element, would produce a greater net entropical effect than in any phase with both Al and Si as major components.

Chapter 9. Metastable Al_2SiO_5 polymorphs.

The previous chapter demonstrated the high accuracy and reliability of DFT simulations. These simulations showed that all Al_2SiO_5 polymorphs become thermodynamically unstable with respect to decomposition into the mixture of constituent oxides above 11 GPa. Here I investigate the compression behaviour of the Al_2SiO_5 polymorphs in the pressure regime where they are metastable. Static DFT simulations are used in parallel with lattice dynamics simulations based on the ionic shell model. The results presented here are from the paper by Oganov et al. (2001d).

I predict a series of metastable phase transitions occurring in low-pressure Al_2SiO_5 polymorphs (andalusite and sillimanite); similar results were obtained using DFT simulations and semiclassical calculations using the ionic shell model. Soft lattice modes as well as related structural changes are analysed. For sillimanite, I predict an isosymmetric phase transition at *ca* 35 GPa; an incommensurately modulated form of sillimanite can also be obtained at low temperatures and high pressures. The high-pressure isosymmetric phase contains five-coordinate Si and Al atoms. The origin of this peculiar fivefold coordination is discussed in detail. Andalusite was found to transform into an amorphous phase at ~50 GPa. This study provides insight into the nature of metastable modifications of crystal structures and the ways in which they are formed. Present results indicate the existence of a critical bonding distance, above which interatomic contacts cannot be considered as bonds. The critical distance for the Si-O bonds is 2.25 Å.

9.1. Introduction.

Metastability phenomena play an important role in many natural and technological processes. Metastable phases are often obtained in synthesis and as products of phase transformations. Recent discoveries, *e.g.* of pressure-induced amorphisation by Mishima *et al.* (1984) and the memory glass effect by Kruger and Jeanloz (1990), have boosted interest in metastability phenomena. It is possible, for instance, that ice comets to a large extent are made of amorphous ice phases, formed at high pressure and low temperatures. Another example is provided by isosymmetric

phase transitions, which can lead to both stable (*e.g.*, $KTiOPO_4$, see Alan & Nelmes, 1996) and metastable (*e.g.*, SiO_2, Badro *et al.,* 1996) phases. This type of phase transitions, until recently thought to be very unusual, is now being found in an increasing number of systems.

Here I discuss state-of-the-art theoretical simulations of metastable phases in the Al_2SiO_5 system. A variety of metastable phases predicted here make Al_2SiO_5 an ideal subject for studies of metastable phenomena.

Both experiments (Schmidt et al., 1997) and theory (Oganov & Brodholt, 2000) indicate that above ~10 GPa Al_2SiO_5 phases become thermodynamically unstable and decompose into the mixture of oxides, Al_2O_3+SiO_2. However, as metastable phases they can exist up to much higher pressures. Kyanite, whose dense structure is based upon cubic closest packing of oxygen atoms, can persist as a metastable phase up to at least 80 GPa; the same is true for the hypothetical dense pseudobrookite-like and V_3O_5-like phases of Al_2SiO_5 (Oganov & Brodholt, 2000). Using *ab initio* simulations, I have found that the low-density phases, andalusite and sillimanite, spontaneously undergo extremely interesting phase transitions in the region 35-55 GPa. These transitions will be considered below.

9.2. Computational methodology.

Two distinct computer simulation methods were employed: 1) first principles pseudopotential calculations and 2) semiclassical calculations, based on empirically derived interatomic potentials. Quantum-mechanical calculations are very accurate and reliable, but computationally expensive. Their results comprise the main quantitative basis for discussion of structural and thermodynamic aspects of the phase transitions. More approximate semi-classical calculations, which are very cheap in terms of CPU time (about 10^3 times faster than the first principles calculations), can be used efficiently for dynamical as well as for static calculations. This technique is employed here for studying dynamical properties at a qualitative level.

Theoretically, a structure can be metastable at given conditions if there are no net forces acting on atoms at rest, and there are no soft modes. As present calculations show, andalusite and sillimanite can persist as metastable phases up to ~35-55 GPa; at these pressures they cease to be in the local energy minima (soft modes appear), and spontaneously transform into other metastable phases.

First-principles calculations were performed on the Cray T3E supercomputers at Edinburgh Parallel Computer Centre and Manchester Computer Centre. The computational method was described in Chapter 8. The main difference is that the present calculations were performed using the constant-pressure enthalpy minimisation algorithm. This was done iteratively until self-consistency to within 10^{-3} eV for ionic and 10^{-4} eV for electronic relaxation was achieved.

Semiclassical calculations were performed with the GULP package. Lattice dynamics is a key point in theory of phase transitions. Unfortunately, non-empirical calculations are currently computationally too demanding to be routinely used for lattice dynamics, especially in the case of low-symmetry ionic crystals with large unit cells.

The performance of the ionic shell model was analysed in Chapter 7. This model is known to have serious drawbacks, but at the same time in a large number of cases, including the Al_2SiO_5 polymorphs (Winkler & Buehrer, 1990; Rao et al., 1999), proved to be sufficiently good at describing lattice dynamics of silicate minerals (Burnham, 1990). In my calculations the Buckingham potentials were summed over all interatomic pairs with distances below 10 Å; three-body potentials were calculated only between strong bonds (shorter than 1.8 Å for Si-O and 1.9 Å for Al-O bonds). Three-body terms are important for tetrahedrally coordinated silicates. For consistency I use the same 'tetrahedral' three-body terms even for non-tetrahedral high-pressure structures, even though this can lead to some ambiguity.

9.3. Accuracy of simulations.

It is known that semiclassical calculations are unreliable in predicting phase transformation enthalpies, when large structural changes are involved, *e.g.* for transitions between kyantite, andalusite, and sillimanite (Winkler *et al.,* 1991; Urusov et al., 1998). *Ab initio* GGA calculations, on the other hand, successfully reproduce the phase diagram (Fig. 8-4) of the Al_2SiO_5 system (Oganov & Brodholt, 2000). However, both methods give a very similar qualitative picture of the metastable and largely structure-conserving pressure-induced phase transitions in andalusite and sillimanite. Only the transition pressures predicted by semiclassical calculations are ~2 times lower than the GGA values. Although the GGA usually results in a shifted pressure scale (Oganov *et al.,* 2001a) and often overestimates

phase transition pressures (for a discussion, see Oganov & Brodholt, 2000; Zupan *et al.*, 1998), the errors are usually within a few GPa. In the following discussion I use only the GGA pressures.

9.4. Phase transitions in sillimanite.

The change of structure occurring upon compression above 33.5 GPa, can be seen in Fig. 9-1. Both low- and high-pressure phases have the same symmetry, *Pnma*, and similar structures; the Al1 positions are octahedrally coordinated in both structures. The difference is that in the high-pressure meta-sillimanite phase all Si atoms and half of the Al atoms (Al2 positions) are in the five-fold coordination instead of the tetrahedral coordination they adopt in sillimanite. This is achieved by pulling the oxygen atoms, initially nonbonded to Si and Al2, inside the first coordination spheres of Si and Al2. Increase of coordination numbers, as usual, is correlated with the increase of density upon the transition. Structural parameters of the meta-sillimanite phase are given in Table 9-1.

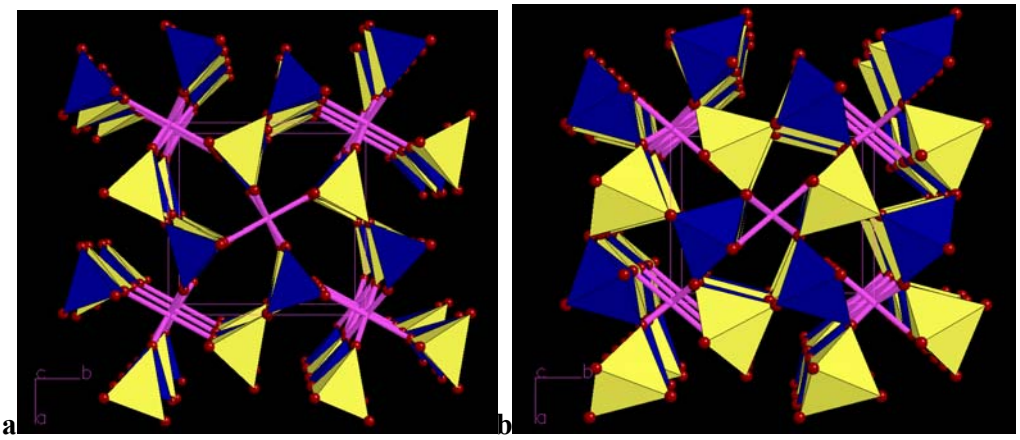

Fig. 9-1. Crystal structures of (a) sillimanite and (b) meta-sillimanite. *Blue* Si polyhedra, yellow Al2 polyhedra; purple sticks – octahedral Al1-O bonds, small red spheres – O atoms. Unit cell contours and orientation (in *Pbnm* setting) are also shown.

Table 9-1. Crystal structure and equation of state of the meta-sillimanite phase.

Property	GULP (30 GPa)	VASP (50 GPa)
Unit cell parameters and volume		
a_0 , Å	5.891	6.178
b_0, Å	7.443	7.135
c_0, Å	6.044	5.773
V_0, Å^3	265.00	254.49
Atomic coordinates (space group P*bnm*)		
Al1 (x, y, z)	(0, 0, 0)	(0, 0, 0)
Al2 (x, y, z)	(0.1189, 0.3126, ¼)	(0.1151, 0.3047, ¼)
Si (x, y, z)	(0.1215, 0.3064, ¾)	(0.1249, 0.2915, ¾)
O_a (x, y, z)	(0.3939, 0.3755, ¾)	(0.3829, 0.3721, ¾)
O_b (x, y, z)	(0.4002, 0.3793, ¼)	(0.3892, 0.3747, ¼)
O_c (x, y, z)	(0.5089, -0.0139, ¾)	(0.4987, -0.0167, ¾)
O_d (x, y, z)	(0.1605, 0.2079, 0.5071)	(0.1843, 0.1853, 0.5060)
***E*(*V*) equation of state (BM3 fit, VASP data)**		
$E_{atom.}$, eV	-49.861	
V_0, Å^3	325.68	
K_0, GPa	112.50	
K'	4.73	

Pentacoordinate silicon was discovered in an inorganic compound ($K_2Si_4O_9$ glass) only recently (Stebbins & McMillan, 1989) using NMR spectroscopy; the first structural characterisation of 5-coordinate Si was first obtained for $CaSi_2O_5$ (Angel *et al.,* 1996), almost simultaneously with a theoretical prediction of a metastable SiO_2 phase with five-coordinate silicon atoms (Badro *et al.,* 1996). Using quantum-mechanical simulations, Warren *et al.* (1999) considered the pressure-induced transition between the phases of $CaSi_2O_5$ containing Si in octahedral and fivefold coordination. Another case of this exotic coordination of Si was found in a recent experimental study (Alberti *et al.*, 1999) of temperature-induced dehydration of zeolite mineral brewsterite ($(Sr,Ba)Al_2Si_6O_{16}*5H_2O$). Molecular dynamics simulations of $MgSiO_3$ (Chaplot & Choudhury, 2000) enstatite have indicated a phase containing fivefold-coordinate Si roughly at the pressure-temperature conditions of the Earth's mantle transition zone. This phase is almost certainly metastable, and appears as an intermediate step in the pressure-induced transformation from enstatite (Si in the tetrahedral coordination) to $MgSiO_3$ perovskite (Si in the octahedral coordination). My work (Oganov et al., 2001d) reported on the next example of this unusual coordination. The interest in pentacoordinate silicon is mainly prompted by its anticipated importance for the transport properties in the Earth's mantle (see Angel *et al.,* 1996 and references therein), because the fivefold coordination, intermediate between the tetrahedral and octahedral coordinations, is likely to appear in fluids, especially at pressures

corresponding to the change of the coordination number of Si in mantle minerals (8-30 GPa), and can serve as a convenient transition state in mass transport.

In Table 9-2 and Fig. 9-2 I analyse the geometry of the SiO_5 polyhedra found in these calculations. Comparison with two other studies (Angel *et al.,* 1996; Badro *et al.,* 1996) indicates similarities with results of Badro *et al.* (1996), who also found one Si-O bond to be noticeably longer than the others, and the overall geometry of the polyhedron intermediate between a trigonal bipyramid and a square pyramid, rather than a square pyramid found by Angel *et al.* (1996) in $CaSi_2O_5$. The difference is easy to explain by the genesis of these polyhedra. In the low-pressure titanite-like $CaSi_2O_5$ studied by Angel *et al.* (1996) the SiO_5 polyhedra were formed by removing one oxygen atom from SiO_6 octahedra of the high-pressure phase, naturally producing a square pyramid. In SiO_2 (Badro *et al.,* 1996) and Al_2SiO_5 (this work) SiO_5 polyhedra are formed by adding one oxygen atom to SiO_4 tetrahedra, and this results in a trigonal bipyramid. The two types of polyhedra, however, can be converted to one another by small displacements of oxygen atoms known as the Berry pseudorotation.

Table 9-2. Geometry of the SiO_5 polyhedra[a]. Distances are given in Å, bond angles in °.

Parameter	Meta-sillimanite (GULP, 30 GPa)	Meta-sillimanite (VASP, 50 GPa)	Meta-quartz (SiO_2)
Si-O1	1.685	1.695	1.728
Si-O2	1.901	1.878	1.869
Si-O3	1.543	1.567	1.617
Si-O4,5	1.657 (x2)	1.641 (x2)	1.674; 1.626[b]
O1-Si-O2	151.1	160.7	168.2
O1-Si-O3	102.1	99.3	93.7
O1-Si-O4,5	90.2	86.9	95.9
O2-Si-O3	106.8	100.0	87.6
O2-Si-O4,5	76.9	83.2	76.3; 94.6[b]
O3-Si-O4,5	116.9	120.8	142.4; 106.1[b]
O4-Si-O5	124.7	118.3	108.9

a – LDA results on meta-quartz from Badro *et al.* (1996) at 16 GPa. The meta-quartz phase is a metastable phase isosymmetric with quartz and succeeding it at high non-hydrostatic pressures. The polyhedron described by Badro *et al.* (1996) is very similar to ours.

b – In our polyhedron the O4 and O5 vertices are symmetrically equivalent, but in the polyhedron of Badro *et al.* (1996) they are different. Two entries relate to the two symmetrically distinct parameters of the polyhedron of Badro *et al.* (1996).

In Fig. 9-3 one can see how Al-O and Si-O distances evolve with pressure: when initially non-bonding 'fifth' Al-O or Si-O contact reaches some threshold distance, a bond is formed. The bond formation changes the topology of crystal structure and the force balance in it, making it collapse into the higher-density phase. On

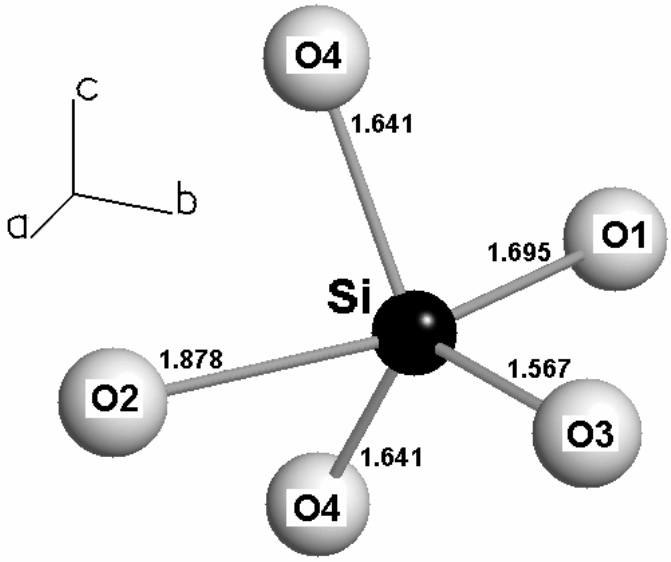

Fig. 9-2. Geometry of the SiO_5 polyhedra in the meta-sillimanite structure (VASP results at 50 GPa). Crystallographic types of oxygen atoms and their distances to the Si atom are indicated. This polyhedron can be described either as a distorted trigonal bipyramid (with apical O4 atoms) or a distorted square pyramid (apical O3 atom). Orientation with respect to the unit cell (*Pbnm*) axes is indicated.

decompression, the exactly opposite situation occurs: when a bond becomes too long, it ceases to be a bond, and the non-bonded atom is expelled from the coordination sphere. In other words, the formation of the new bond or destruction of an old one is the cause of the phase transition. The critical interatomic distances, which I find to be 2.25 ± 0.17 Å and 2.05 ± 0.04 Å for Si-O and Al-O bonds, respectively, can be used as a criterion of bonding in oxygen compounds of Al and Si, and are potentially important in structural studies of glasses and transition states in these systems. It is interesting, that purely ionic shell model calculations reproduce these critical lengths remarkably well: 2.27 ± 0.15 Å for Si-O and 2.01 ± 0.02 Å for Al-O bonds. Therefore, the nature of the critical bonding distances in Al_2SiO_5 is not related to the changes in electronic structure, which are not accounted for by the simple ionic shell model. Bond valences, calculated using parameters of Brown & Altermatt (1985), are 0.18 and 0.34 valence units, respectively (for the ionic model, 0.17 and 0.34, respectively). The Al-O critical bond length (2.05 ± 0.04 Å) seems too small; a better value (~2.4 Å) would result if we take the structure before the onset of the incommensurate modulation (see below) occurring in sillimanite in the region of the anomalous softening of the structure in the hysteresis region. It is possible that this incommensurate modulation and

softening reflect the steric strain associated with the formation of the new Al-O bonds.

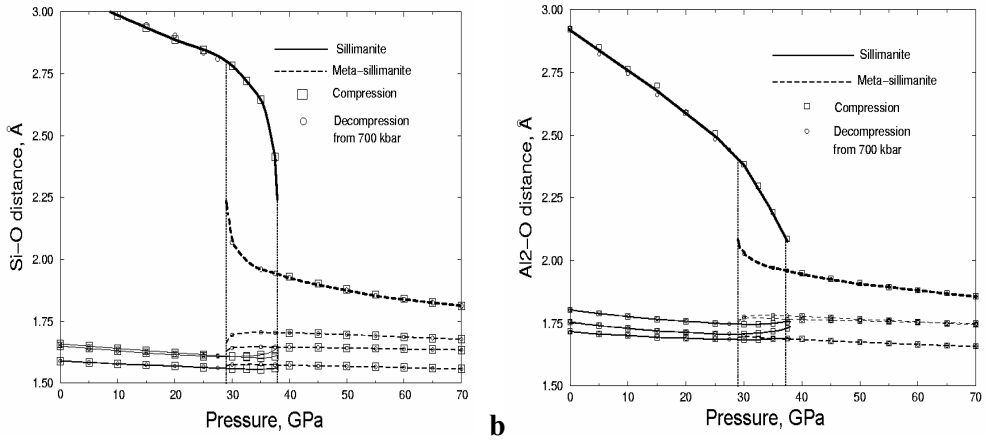

Fig. 9-3. Evolution of Si-O (a) and Al-O (b) distances in sillimanite. Vertical lines show the hysteresis loop.

Pressure-induced variation of the unit cell parameters and volume is shown in Fig. 9-4. Several features deserve a special notice. This phase transition, with the equilibrium transition pressure of 33.5 GPa, is reversible, and in Fig 9-4 I show results, obtained on decompression as well as on compression. The transition is first order with a marked volume discontinuity and strong hysteresis (which is a necessary feature of all reversible first-order transitions). This agrees with the conclusion of Bruce & Cowley (1981) and Christy (1995), that isosymmetric phase transitions must be first order, but can disappear (i.e., become fully continuous) at temperatures above the critical point. Lattice parameters and volume have normal pressure dependence outside the hysteresis region. Inside that region one can observe anomalously large fall of the volume and *a*-parameter with increasing pressure, and non-monotonic variation of the *c*-parameter, which increases with pressure near the transition. Parameter *b* is affected only slightly by the phase transformation. The negative linear compressibility along the *c* axis, which I have found in sillimanite and its high-pressure isosymmetric successor in the transition region, is a very interesting phenomenon. Bulk compressibility cannot be negative, as this is forbidden by mechanical stability criteria. Linear compressibility, however, can be negative in some directions for non-cubic crystals. In our case it is associated with an

incipient phase transition and formation/breaking of new bonds in the structure[47]. This isosymmetric transition is ferroelastic, because it is associated (as shown by GULP calculations) with a complete softening of the C_{11} elastic constant. This correlates with the collapse of the *a* axis, associated with the formation of new Si-O and Al-O bonds directed largely along the *a* direction.

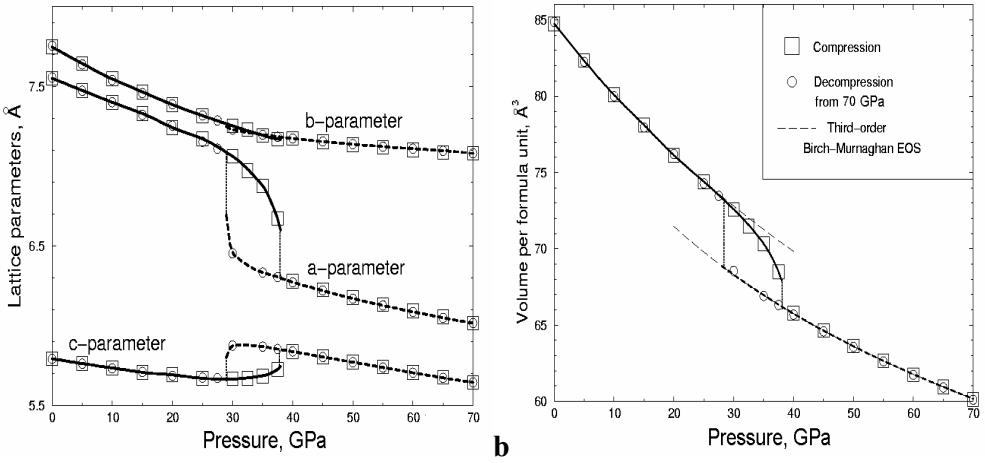

Fig. 9-4. Pressure evolution of (a) lattice parameters and (b) volume of sillimanite. Hysteresis loop is very pronounced.

Variation of the lattice parameters in the vicinity of the transition suggests that structures of the both phases 'prepare' for the transition, i.e. their lattice parameters tend to merge towards the transition. It is well known (Sirotin & Shaskolskaya, 1975) that for structural transitions with symmetry breaking, structure of the low-symmetry phase becomes increasingly more similar to the high-symmetry structure, whereas the latter shows no indication of approaching the low-symmetry structure. As our example suggests, in cases when symmetry of the phases is identical, both structures show a tendency to approach each other in the vicinity of the transition.

Using semi-classical simulations, I considered dynamical stability criteria (Fig. 9-5). At ambient pressure, sillimanite is dynamically stable, in agreement with experiment. The high-pressure isosymmetric phase is also dynamically stable. However, *ca* 1 GPa below the high-pressure transition sillimanite acquires a minor

[47] In $Pb_3(PO_4)_2$ negative linear compressibility was found along the c direction of the monoclinic cell (Angel, 2000); it was tentatively ascribed to the stereochemical activity of lone electron pair of Pb^{2+} (R.J. Angel, private communication).

dynamical instability, which would lead to an incommensurate modulation with **k**≈(0.47,0,0) (Fig. 9-5b). The imaginary frequencies are very small, suggesting that the modulation may be anharmonically suppressed even at not very high temperatures, and the isosymmetric phase transition would occur bypassing the incommensurate phase.

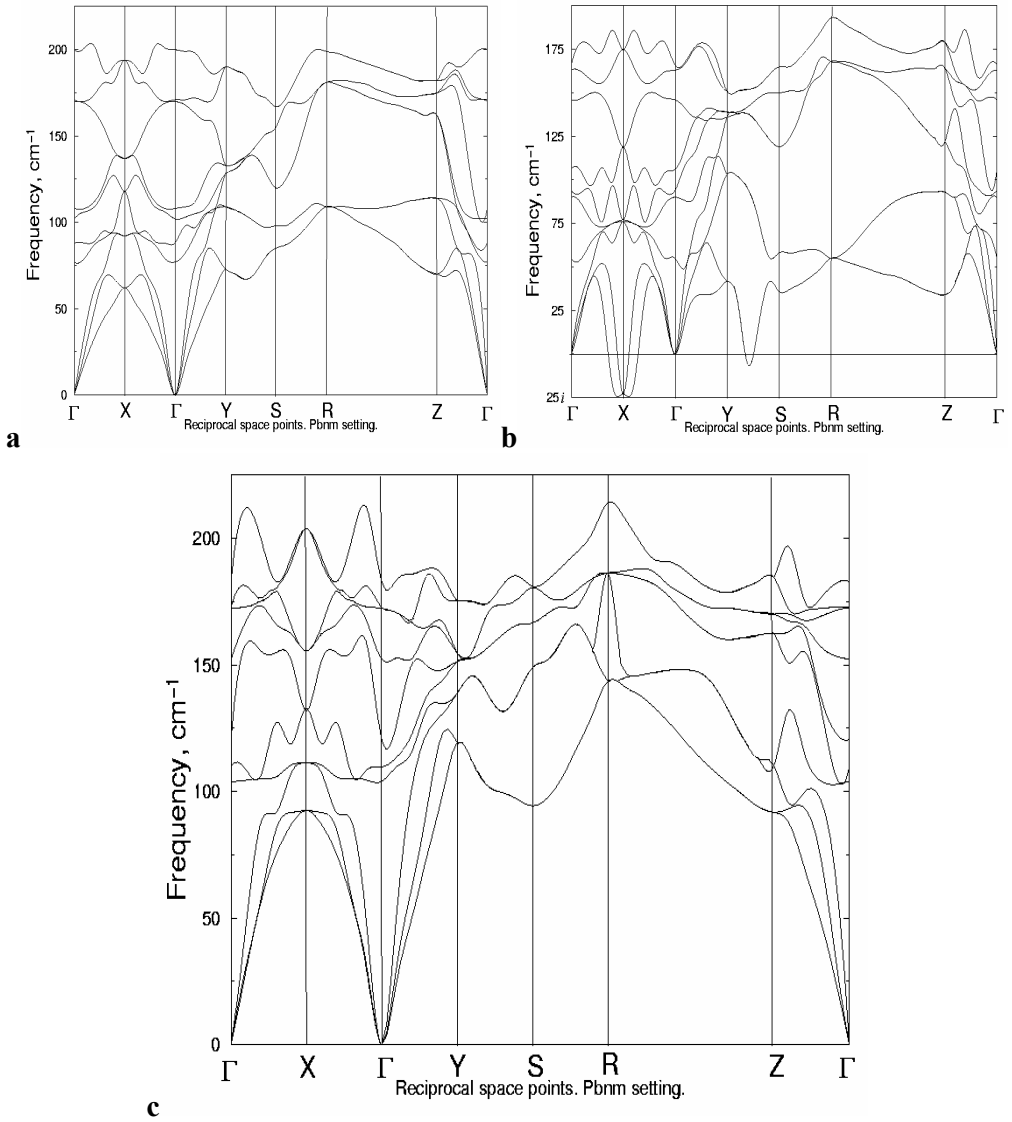

Fig. 9-5. Phonon dispersion curves of sillimanite under pressure. (a) Sillimanite at room pressure, (b) sillimanite near the transition to the isosymmetric phase, (b)isosymmetric phase. Only several lowest-frequency phonon branches are shown. *Pbnm* setting is used in the notation of reciprocal space points.

Several spot-checks were performed using both VASP and GULP, in order to make sure that the input structure did not bias the results. These spot-checks started with a slightly deformed (by 0.01-0.02 Å and 1-2º) unit cell and displaced atoms (by 0.01-0.02 Å) picked at random, followed by static constant-pressure relaxation of the structure. For the high-pressure meta-sillimanite modification the original structure

was always recovered in VASP calculations even at pressures as high as 70 GPa. At the same time, ~10 GPa after the formation of the isosymmetric phase, GULP calculations show soft modes and difficulties in optimising the structure and removing the introduced strains; however, this is due to the inadequacy of the three-body potentials, which becomes critical at these high pressures as all the five Si-O (and Al-O) bonds become strong (i.e., shorter than 1.8 and 1.9 Å for Si-O and Al-O bonds, respectively).

9.5. Phase transitions in andalusite.

Andalusite appears to be metastable in a much broader pressure range, up to 52 GPa. Crystal structures of andalusite and the meta-andalusite phase succeeding it are shown in Fig. 9-6. Equations of state and pressure evolution of lattice parameters are shown in Fig. 9-7, which shows an extremely large hysteresis region, in the range 17-52 GPa. The meta-andalusite phase, however, is dynamically unstable at all pressures. The character of the dynamical instability (Fig. 9-8), involving softening of almost a whole transverse acoustic branch along some directions, suggests amorphisation of this structure (Binggeli *et al.,* 1994; Keskar *et al.,* 1994). The appearance of an isosymmetric phase in this case is, therefore, nothing more than an artifact of periodic boundary conditions. In this unstable phase all Al atoms are octahedrally coordinated, while in andalusite the Al2 positions are penta-coordinate; Si atoms are in the tetrahedral coordination in both structures. In order to make sure that amorphisation does happen, I performed several static spot-checks using the method described in the previous section. The fact that the structure of the high-pressure successor of andalusite was not recovered is a clear evidence of its instability. The resulting structure drastically differs from the original structure in the unit cell volume and shape. GULP calculations still find some soft modes for this structure, suggesting that larger supercells are necessary to describe relaxation of this amorphous structure correctly.

The pressure evolution of lattice parameters (Fig. 9-7) and interatomic distances show no ‘preparation’ for the transition of the kind encountered in sillimanite. Instead, the transition is abrupt, apparently caused by cooperative rather than local effects driving the crystal to a dynamical instability. Although crystal structures of

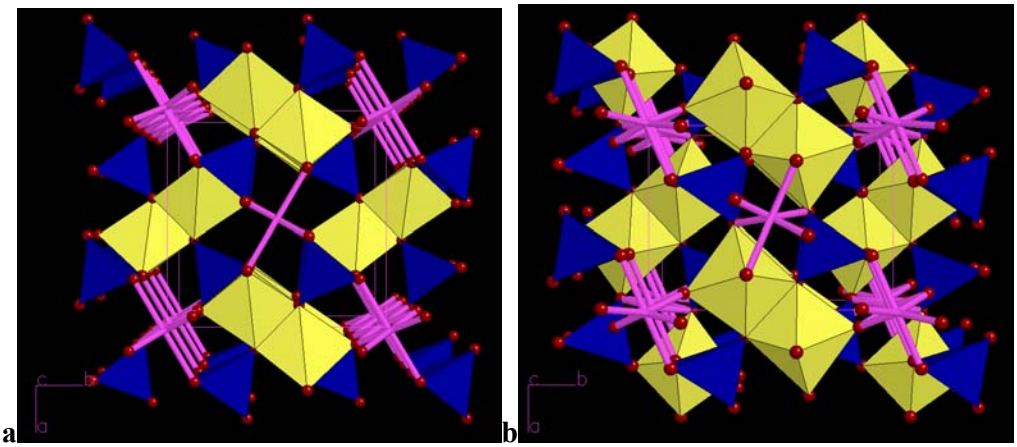

Fig. 9-6. Crystal structures of (a) andalusite and (b) high-pressure isosymmetric dynamically unstable phase. Instead of the latter phase, an amorphous solid is predicted to occur at high pressures. *Blue* Si polyhedra, *yellow* Al2 polyhedra; *purple sticks* Al1-O bonds, *small red spheres* O atoms.. Unit cell contours are also shown.

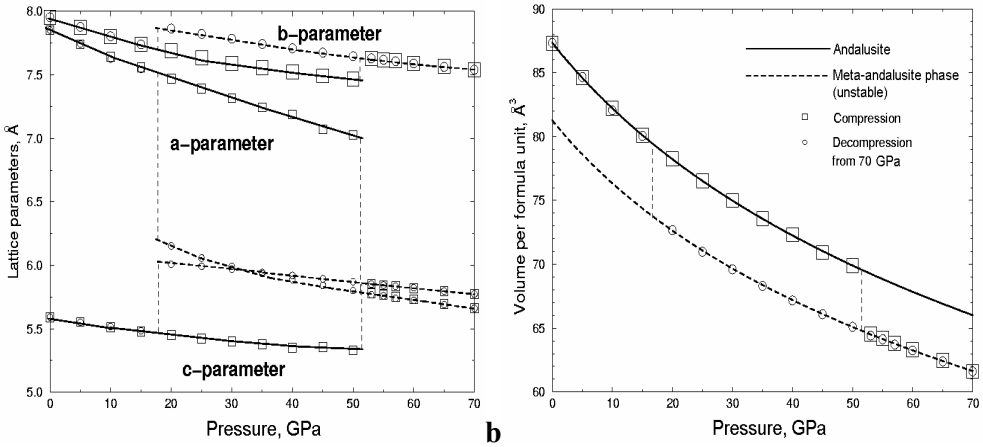

Fig. 9-7. Pressure evolution of (a) lattice parameters and (b) volume of andalusite. *Dotted lines* show the hysteresis loop. *Squares* - results on compression, *circles* - results on decompression from 70 GPa.

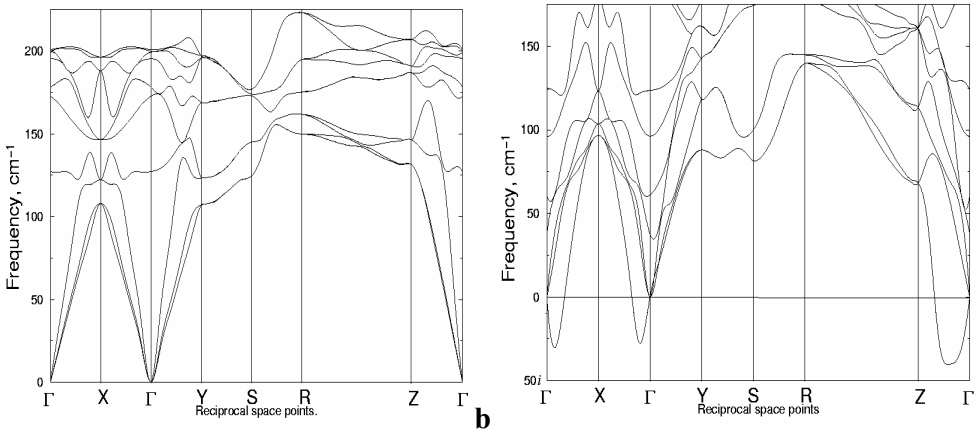

Fig. 9-8. Phonon dispersion curves of (a) andalusite at room pressure and (b) of the high-pressure dynamically unstable post-andalusite phase. Figure (b) shows that pressure-induced amorphisation should occur along the *c* and, possibly, *a* axes. Only several lowest-frequency phonon branches are shown.

andalusite and sillimanite are quite similar, the drastic difference between their high-pressure behaviour springs from the difference in the degree of flexibility of the structural motif, which is rather supple in sillimanite and rigid in andalusite. Due to this factor andalusite can stay metastable up to much higher pressures than sillimanite, and this transformation is not associated with the critical bond mechanism discussed in the previous section.

9-6. Discussion and conclusions.

Using *ab initio* simulations, I have predicted a number of metastable modifications of Al_2SiO_5. Sillimanite undergoes an isosymmetric phase transition at 33.5-38 GPa, preceded by an incommensurate transition at low temperatures. Andalusite transforms into an amorphous phase at 34-51 GPa. I have analysed geometry of the SiO_5 polyhedra found in the high-pressure meta-sillimanite phase. These polyhedra can be described as intermediate between trigonal bipyramids and square pyramids, just as those studied by Badro *et al.* (1996) in a metastable isosymmetric phase formed from quartz (SiO_2). Trigonal bipyramids are more likely to be formed by an addition of an oxygen atom to an SiO_4 tetrahedron on increasing pressure, while square pyramids are more relevant for the case of removal of one oxygen atom from an SiO_6 octahedron on decreasing pressure (Fig. 9-9). Apart from direct results on the given system, this study provides several general conclusions.

First, I have proposed the existence of a critical bonding distance R_{CR}, and transferability of the R_{CR} values between different crystals. This concept naturally explains the metastable phase transitions in sillimanite and should be able to explain a number of other displacive phase transitions. Knowing the R_{CR} it becomes easy to determine unambiguously the coordination numbers of atoms, which is often difficult, *e.g.* for ionic crystals with large cations. Therefore the R_{CR} criterion, if robust enough, should bring more order into structural chemistry of such compounds. The fact that R_{CR} values given by quantum-mechanical calculations and simple interatomic potentials, are identical, implies that R_{CR} is not sensitive to the details of electronic structure and their changes.

Second, one can generally expect that for crystals with complicated low-symmetry structures and many degrees of freedom metastable pressure-induced phase transitions should be very common. In such systems relaxation of internal degrees of freedom under pressure would easily lead to situations where initially non-bonded atoms approach each other closely enough ($R<R_{CR}$) to form a new bond,

which automatically triggers a phase transition. There are several systems in which such transitions are very likely – titanite-like $CaSi_2O_5$, SiO_2 (quartz and coesite), feldspars, zeolites, berlinite $AlPO_4$.

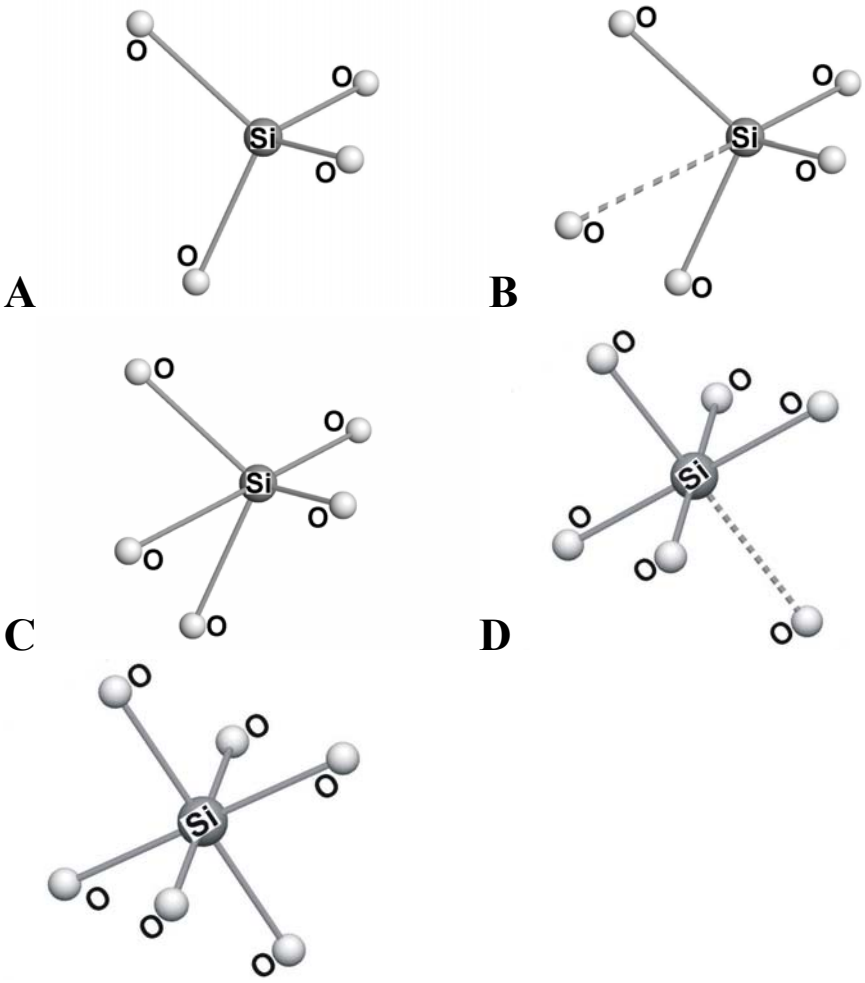

Fig. 9-9. Genesis of the fivefold coordination of silicon. Tetrahedral Si (A) can capture a neighbouring O atom (B), becoming fivefold-coordinate (C). The coordination polyhedron is intermediate between trigonal bipyramid and square pyramid (cf. Fig. 3), into which it can easily transform by Berry pseudorotation (C→D). Capturing another O atom, a square bipyramid becomes an octahedron (D, E). The reverse transformation path is equally possible. In this study we see stages A-C; Angel *et al.* (1996) and Warren *et al.* (1999) observed stages D-E in $CaSi_2O_5$.

As structures tend to accommodate minimum changes necessary to maintain stability, symmetry will be preserved whenever possible. The predicted transitions are certainly local in the terminology of Chapter 4, but the cases of sillimanite and andalusite are opposite extremes in the sense that the high-pressure transition in sillimanite preserves all symmetry, while the transition in andalusite completely destroys crystal symmetry.

Chapter 10. Thermoelasticity and phase transitions of $MgSiO_3$ perovskite.

$MgSiO_3$ perovskite is the most abundant mineral in the Earth's lower mantle and in the Earth generally. The experimental information on many of its properties is discrepant; some of the properties (e.g., elastic constants at high pressures and temperatures) have not been measured at all. *Ab initio* simulations can resolve the existing controversies and often give reliable predictions of the properties that cannot currently be studied in the laboratory. Such simulations have been performed; their results have significantly extended the current understanding of the Earth's mantle. The results presented in this chapter have been published in three papers (Oganov et al., 2000; Oganov et al., 2001a,b). In the following discussion, I shall highlight such issues relevant to the mantle as its composition, temperature distribution, mantle convection, nature of the electrical conductivity of the lower mantle, and the possibility of partial melting of the mantle.

10.1. Introduction.

It is established, by the analysis of phase diagrams (Ringwood, 1991) and mantle inclusions in diamonds (Harte et al., 1999), that $MgSiO_3$ perovskite[48] (*Mg-pv*) is the main mineral of the Earth's lower mantle (at least 60 vol.%) and the most abundant mineral in the Earth. Yet, there are major controversies in the experimental information on many of its important properties.

The EOS of this phase at simultaneously high pressures and temperatures of the lower mantle (pressure between 24 and 136 GPa, temperature *ca* 2000-3000 K) is crucial for interpreting seismological data and constructing reliable chemical, mineralogical, and thermal models of the lower mantle. Yet, accurate experimental

[48] Of course, not pure. In the lower mantle, it is generally expected to have the composition close to $(Mg_{0.9}Fe_{0.1})SiO_3$, probably with a few percent Al_2O_3. The effects of the moderate Fe content, while potentially important for certain properties (e.g., shear modulus), are expected to be negligible for others, especially for the thermal expansion, bulk modulus, and p-T-derivatives of the elastic moduli and seismic wave velocities. For this reason, most experimental and theoretical studies concentrate on the pure *Mg-pv*. Recent *ab initio* study by Brodholt (2000) showed that Al impurities would significantly affect the EOS of *Mg-pv* only below ~30 GPa.

EOS of *Mg-pv* is available only at 298 K (e.g., Knittle & Jeanloz 1987; Fiquet et al. 2000). Accurate experimental measurement of the temperature effects still poses a problem – e.g., there is a sharp conflict between different experimental data on thermal expansion coefficient of *Mg-pv*. At the same time, thermal expansion of *Mg-pv*, crucial for models of the lower mantle composition and dynamics, is poorly known even at the ambient conditions (for a discussion see Anderson et al., 1995; Ringwood, 1991). For the Grüneisen parameter γ_0, the reported values at ambient conditions are scattered between 1.2 and 2.0, and its volume dependence parameter, $q=\partial\ln\gamma/\partial\ln V$, is uncertain roughly between 1 and 2.5. The difficulties in obtaining accurate thermoelastic parameters of this mineral from experiment were discussed in detail by Shim and Duffy (2000).

The highest experimentally reached hydrostatic pressure in experiments at the lower mantle temperatures is 94 GPa (Fiquet et al., 2000), which is still well below the core-mantle boundary pressure of 136 GPa. Moreover, experiments at such high pressures and high temperatures can presently be performed only in laser-heated diamond anvil cells with very large uncertainties in temperature. To reproduce the extreme conditions of the lower mantle remains a major challenge for both theoreticians working at the *ab initio* level and experimentalists.

The elastic constants have been studied experimentally only at ambient conditions (Yeganeh-Haeri, 1994). One needs to know these constants at the lower mantle pressures and temperatures in order to be able to interpret seismic tomography maps in terms of the temperature distribution (see Oganov et al., 2001b and below).

These and other issues can now be addressed with accurate *ab initio* simulations. A breakthrough in theoretical simulations was marked by the works of Stixrude and Cohen (1993) and Wentzcovitch et al. (1993), who demonstrated the feasibility and enormous potential of quantum-mechanical simulations based on density functional theory. In parallel with these studies, D'Arco et al. (1993) performed successful Hartree-Fock simulations of this mineral. A number of important contributions have been made since (D'Arco et al., 1994; Wentzcovitch et al., 1995, 1998; Karki et al., 1997, 2000, 2001; Warren et al., 1998; Brodholt, 2000; Oganov et al., 2000, 2001a,b).

10.2. Computational methodology.

Ab initio. All my *ab initio* simulations of *Mg-pv* (Oganov et al., 2001a,b and this work) are based on DFT and use the PW91 GGA (Wang & Perdew, 1991; see Chapter 5). Plane wave pseudopotential methodology as implemented in the VASP code (Kresse & Furthmüller, 1996a,b) is used. I use very accurate non-local pseudopotentials for all atoms; for O atoms an ultrasoft pseudopotential (Vanderbilt, 1990) was used[49]. The ground state was found by solving the Kohn-Sham equations self-consistently to within $5*10^{-10}$ eV/atom; static structure was optimised to within $5*10^{-10}$ eV/atom using the conjugate gradients method. For the Brillouin zone sampling I used 2*2*2 meshes for the orthorhombic (space group *Pbnm*) and tetragonal *I*4/*mcm*-phases (each having 20 atoms in the conventional unit cell) and 4*4*4 mesh for the cubic ($Pm\bar{3}m$) phase. This proved to be sufficient for an accurate determination of the equations of state, elastic constants, and the enthalpy differences.

The use of an ultrasoft pseudopotential for oxygen allowed me to use a relatively small basis set with the plane-wave cut-off energy of 500 eV without any loss of accuracy and perfect convergence of all properties with respect to the basis set size (the Pulay stress was only 0.05 GPa and was neglected). This significantly reduced the computational cost of the simulations, allowing me to perform the largest-scale *ab initio* molecular dynamics simulations of this mineral up-to-date (Oganov et al., 2001a,b) and address such challenging issues as elasticity at high pressures and temperatures of the lower mantle (Oganov et al., 2001b). Such issues cannot presently be addressed by experiments.

Our work (Oganov et al., 2001b) has reported, to the best of our knowledge, the first finite-temperature calculations of the elastic constants of any material using *ab initio* molecular dynamics (MD). These dynamical simulations were performed in the constant-temperature (*NVT*) ensemble (Nosé, 1984) with an 80-atom supercell (2*a**2*b**1*c Pbnm*-supercell), Γ-point for the Brillouin-zone sampling, and a timestep of 1 fs; for each configuration the ground state was found self-consistently to within $6.25*10^{-8}$ eV/atom. The dynamical simulations were run for at least 0.8 ps after equilibration. The thermostat mass parameter was optimised so as to produce

[49] The pseudopotentials for Mg and Si are norm-conserving (Rappe et al., 1990) with partial core corrections (Louie et al., 1982). The core radii are 1.06 Å for Mg (valence configuration $3s^2 3p^0 3d^0$), 0.95 Å for Si ($3s^2 3p^2 3d^0$), and 0.82 Å for O ($2s^2 2p^4 3d^0$).

temperature oscillations with a period of atomic vibrations. Our *ab initio* MD runs, although relatively short, proved to be sufficient for obtaining well-converged statistical averages for the stress tensor. All calculations were performed on the CRAY T3E supercomputer at Manchester Computer Centre.

The elastic constants were calculated, following Karki (1997) and the theory outlined in Chapter 3, from the non-linear stress-strain relations using simulations at a series of small strains (0, 1%, 2%, and 3%) and fitting the stress-strain functions with 2nd order polynomials. It is essential to consider the non-linear elastic effects in such calculations. In my *ab initio* MD simulations, I used +2% and –2% strains; the use of two independent MD calculations, apart from accounting for the non-linear effects, significantly increased the statistical significance of the results.

Most of the previous workers (Wentzcovitch et al., 1993, 1995; Karki et al., 1997, 2000, 2001; Warren et al., 1998) utilised the local density approximation (LDA) of density functional theory and hard pseudopotentials; Stixrude and Cohen (1993) used LDA in conjunction with all-electron LAPW method. D'Arco et al. (1993, 1994) used Hartree-Fock method. Currently, GGA is the state-of the art in quantum-mechanical computational studies, but an encouraging circumstance is that results of the GGA, LDA, and Hartree-Fock calculations are in a good semiquantitative agreement with each other for *Mg-pv*, as well as for many other ionic systems. Results of different *ab initio* methods are compared in Table 10-1. HF calculations are very accurate in describing its crystal structure, but not elasticity or binding energy. LDA and GGA are capable of giving high accuracy for the prediction of the crystal structure as well as its response to pressure and temperature.

The GGA systematically overestimates bond lengths and unit cell parameters by ~1-2%. This causes significant errors in the EOS. In a recent comparative study (Favot & Dal Corso, 1999) of the GGA- and LDA- phonon dispersion curves in several compounds it was suggested that the gradient corrections to the LDA act as a negative pressure. Usually, GGA overcorrects the LDA, resulting in overexpansion of crystal structures and lowering of the vibrational frequencies and elastic moduli[50]. An important observation is that this error can be largely ascribed to an error in the

[50] The nature of this effect was discussed in Chapter 5. In most cases, GGA overexpands crystal structures because the gradient corrections favour more inhomogeneous electron density distribution achieved in more open structures. Patton et al. (1997) arrived at the same conclusion. Oganov and Brodholt (2000) suggested that for the same reason lower-density phases are often more energetically favourable in the GGA than in the LDA or in experiment.

pressure: GGA can be imagined to contain some spurious pressure, which shifts the whole pressure scale by a constant[51], while leaving all properties as a function of volume unchanged. Indeed, for *Mg-pv*, GGA calculations (see Table 10-1 and below) at the experimental unit cell volume at ambient conditions (162.40 $Å^3$) give all the elastic constants coinciding with the experimental values within the experimental errors. In these calculations, all the lattice parameters and atomic positions were fully relaxed under the only constraint of a fixed unit cell volume. The GGA volume dependences of the elastic constants are in excellent agreement with independent LDA simulations of Karki et al. (1997) (see Fig. 10-1).

The systematic error of the GGA can be systematically corrected by shifting the GGA pressures by a constant, effectively recovering the experimental unit cell volume at ambient conditions (see Oganov et al., 2001a). A similar procedure was used by Vanderbilt (1998) in his LDA studies of phased transitions in perovskites. This simple procedure, although not fully *ab initio*, is useful because it allows one to obtain very accurate results for the elastic constants and EOS of *Mg-pv* and gives confidence in the simulated thermal properties.

The pressure correction is easy to work out. Writing the corrected pressure as follows:

$$p_{total}^{true}(V,T) = p_{st}^{GGA}(V) + p_{\text{th}}(V,T) + \Delta p \quad , \qquad (10.2.1)$$

for the volume corresponding to the ambient conditions (where $p_{total}^{true} = 0$) we have the pressure correction:

$$\Delta p = -p_{st}^{GGA}(V_0) - p_{\text{th}}(V_0,T) \qquad (10.2.2)$$

The first term is just minus the GGA static pressure at the experimental volume (-8.5 GPa) and the second term is minus the thermal pressure at this volume and 298 K (-3.58 GPa). The second term was evaluated using the Grüneisen parameter from *ab initio* MD simulations (see below). Pressure-corrected GGA turns out to be far more accurate than any other *ab intio* method in Table 10-1. In what follows, pressure correction was not applied only in the calculations of the relative stability of different

Table 10-1. *Ab initio* simulations of $MgSiO_3$ perovskite. HF results are from D'Arco et al. (1993, 1994); GGA results are from Oganov et al. (2001a). 'GGA+p' means pressure-corrected GGA.

Propert	HF	LDA	GGA	GGA+p	Exp.

[51] Note that a constant pressure correction is equivalent to adding an energy term linear in volume. At each volume, this leaves unchanged all properties that are second or higher derivatives of the energy.

y		a	b	c			
V_0, Å^3	162.12	157.50	162.47	157.87	168.04	162.40	162.45
a_0, Å	4.786	4.711	4.7891	4.7272	4.8337	4.7765	4.7747
b_0, Å	4.913	4.880	4.9219	4.8889	4.9830	4.9333	4.9319
c_0, Å	6.896	6.851	6.8925	6.8311	6.9767	6.8919	6.8987
Mg x	0.5112	0.5174	0.5129	0.5160	0.5148	0.5154	0.5143
y	0.5476	0.5614	0.5521	0.5576	0.5552	0.5570	0.5556
z	¼	¼	¼	¼	¼	¼	¼
Si (x; y; z)	(0; ½; 0)	(0; ½; 0)	(0; ½; 0)	(0; ½; 0)	(0; ½; 0)	(0; ½; 0)	(0; ½; 0)
O_1 x	0.0999	0.1128	0.0980	0.1044	0.1018	0.1030	0.1037
y	0.4643	0.4608	0.4686	0.4654	0.4664	0.4666	0.4655
z	¼	¼	¼	¼	¼	¼	¼
O_2 x	0.1980	0.1928	0.1983	0.1969	0.1983	0.1972	0.1974
y	0.2029	0.1995	0.2033	0.2015	0.2031	0.2019	0.2011
z	0.5522	0.5582	0.5507	0.5539	0.5527	0.5530	0.5538
C_{11}, GPa	-	496	487	499	444	493	482
C_{22}	-	560	524	561	489	546	537
C_{33}	-	504	456	466	408	470	485
C_{12}	-	132	128	123	110	142	144
C_{13}	-	136	144	137	126	146	147
C_{23}	-	156	156	142	136	160	146
C_{44}	-	151	203	217	194	212	204
C_{55}	-	198	186	186	172	186	186
C_{66}	-	171	145	160	131	149	147
K_V, GPa	-	267.6	258.1	258.8	231.7	267.2	264.2
K_R	309	266.5	257.5	257.8	230.9	266.2	263.7
K_{VRH}	-	267.1	257.8	258.3	231.3	266.7	264.0
G_V, GPa	-	179.7	176.1	187.6	164.0	180.1	178.5
G_R	-	177.8	173.3	185.1	160.5	177.4	176.2
G_{VRH}	-	178.7	174.7	186.3	162.3	178.7	177.4
C_L, m/s	-	10926	10935	10953	10620	11091	11042
C_T	-	6498	6524	6641	6395	6598	6574
θ_D, K	-	1077	1069	1097	1036	1082	1078

a – Wentzcovitch et al. (1995)

b – Karki et al. (1997); Karki (1997)

c – This work. The same computational parameters were used as in the GGA simulations. All pseudopotentials used in LDA-simulations were generated within the LDA. LDA-pseudopotential for Si was of the same type as the one used in GGA-simulations, with the same valence configuration, core radius, and also with partial core corrections. LDA-pseudopotential for Mg was ultrasoft with valence configuration $2p^6 3s^2 3d^0$, core radius 1.06 Å, and partial core corrections. Pseudopotential for O was ultrasoft with valence configuration $2s^2 2p^4 3d^0$ and core radius 1.01 Å. The results are much closer to those of Wentzcovitch et al. (1995) than to those of Karki et al. (1997).

d – Crystal structure from (Ross & Hazen, 1989). Elastic constants and related properties from (Yeganeh-Haeri, 1994) or calculated using data of Yeganeh-Haeri (1994).

perovskite polymorphs. The large energy differences obtained in such calculations should be sufficiently accurate, especially because the (already small) energy terms related to the pressure correction largely cancel in calculations of the energy differences.

Most of the previous calculations were static, i.e. done at 0 K without zero-point vibrations. Wentzcovitch et al. (1993, 1995) used the MD method, but only at 0 K, simply as a means of structural optimisation. Warren et al. (1998) were the first to apply finite-temperature *ab initio* molecular dynamics, but at that time it was possible only for a small number of atoms in the cell (20 atoms) with short simulation times and other restrictions, which obstructed many possible applications.

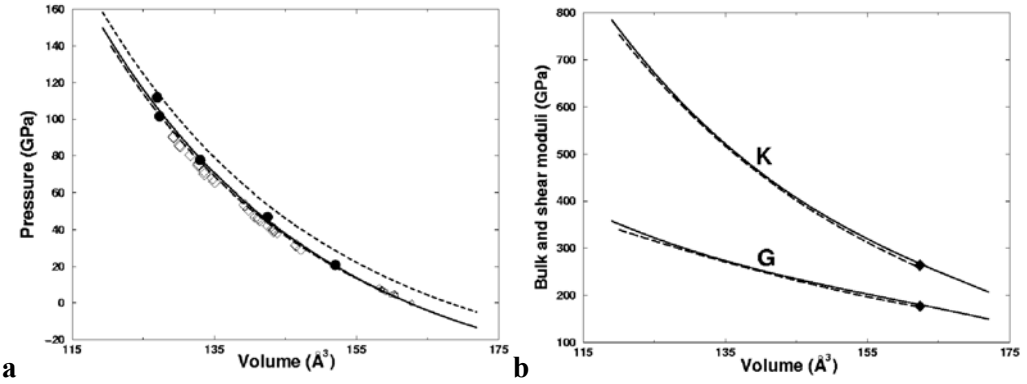

Fig. 10-1. Equation of state of orthorhombic $MgSiO_3$ perovskite from DFT calculations and experiment. (a) EOS at 298 K. *Lower dashed line* athermal LDA (B. Karki, personal communication, 1997), *upper dashed line* athermal GGA, *solid line* GGA shifted in pressure, effectively at 298 K. Experiments at 298 K: *small circles* (Yagi et al., 1982), *large solid cirles* (Knittle & Jeanloz, 1987), *diamonds* (Fiquet e al., 2000). (b) Bulk and shear moduli as a function of volume. *Solid lines* GGA (this study); *dashed lines* LDA (Karki, 1997), *diamonds* experimental data (Yeganeh-Haeri, 1994).

It has been shown (Matsui et al., 1994, Oganov et al., 2000, see below) that at mantle temperatures (roughly 1500-4000 K) MD is the most suitable method. At such high temperatures the quasiharmonic approximation starts to break down, whereas MD is exact in the high-temperature limit. Nevertheless, detailed and insightful lattice-dynamical calculations of Karki et al. (2000b, 2001) are very useful and should be compared with the *ab initio* MD simulations.

In this study used semiclassical methods in parallel with quantum-mechanical simulations. Less expensive semiclassical simulations can be applied where *ab initio* calculations are still prohibitively expensive. Valence electron density distributions (Fig. 5-8, 5-9) support the traditional view that this mineral is essentially ionic, but with a significant covalency of the Si-O bonds.

<u>*Semiclassical.*</u> In order to perform semiclassical simulations, I chose the simplest appropriate potential form (5.3.6.2) including only pairwise interactions and rigid ions with partial charges. Although there are a number of interatomic potentials available in the literature (e.g., Lewis & Catlow, 1985; Matsui et al., 1987; Matsui,

1988; Wall, 1988; Leinenweber & Navrotski, 1988; Choudhury et al., 1988; Kubicki & Lasaga, 1991; Ghose at al., 1992; Stuart & Price, 1996), I preferred to derive my own potential.

First of all, many previous potentials were derived from fitting calculated structure and properties at T = 0 K to experimental data at 300 K. Recent developments in the GULP code (Gale, 1996, 1997, 1998), which I used in my work (Oganov et al., 2000), for the first time allowed us to include quasiharmonically all thermal and zero-point motion effects in the fitting procedure, which itself now involves complete structure optimisation for each set of trial potential parameters, making the whole procedure much more rigorous. Implementation of analytical free energy derivatives (Kantorovich, 1995; Gale, 1998) has speeded up free energy minimisation by orders of magnitude, thus enabling finite-temperature fitting even for relatively large systems.

Some previous potentials, e.g. purely ionic transferable potential models (Lewis & Catlow, 1985), are known to perform poorly for *Mg-pv*. This can clearly be improved by adopting partial ionic charges (e.g., Matsui, 1988).

Another problem is that none of the previous studies paid any attention to the severe correlation problem between the potential parameters (e.g., ρ_{ij} and b_{ij} in (5.3.6.2)) in the potential, leading to poor transferability and reliability of the potential for the prediction of properties not used in fitting. Statistical significance of the fitted potential parameters is often poor, because the number of observables used in fitting is usually comparable to the number of the fitted parameters. These problems can be solved by setting some of the parameters to values, determined by physical considerations. I fixed ρ_{ij} at the values, calculated from (5.3.6.3). This physical determination of the repulsion exponents ρ_{ij} ensures the best transferability of such a potential, and removes the problem of correlation between b_{ij} and ρ_{ij}. The O-O short-range potential ($b_{O\text{-}O}$ = 2023.8 eV, $\rho_{O\text{-}O}$ = 0.2674 Å and $c_{O\text{-}O}$ = 13.83 eV*Å^6) was taken from Gavezzotti's works (e.g., 1994), where it was extensively validated for organic compounds. Oxygen-oxygen short-range potential is very weak in most existing models, and therefore its details are not very important. I preferred Gavezzotti's potential, because it had the closest ρ_{ij} to the one given by (5.3.6.3) and a reasonable van der Waals parameter $c_{O\text{-}O}$.

I neglected weak cation-cation short-range interactions and cation-anion dispersion interactions. As a result, only 4 independent parameters had to be fitted:

atomic charges Z_{Si} and Z_{Mg} (Z_O=-1/3(Z_{Mg}+Z_{Si})), and pre-exponential repulsive parameters $b_{Mg\text{-}O}$, and $b_{Si\text{-}O}$. These parameters are virtually uncorrelated with each other and give a stable solution for the fitting problem. In this fitting procedure, I used experimental crystal structure at 1 atm and 300 K (Ross & Hazen, 1989) and full elastic constants tensor (Yeganeh-Haeri, 1994). Temperature was explicitly included via quasiharmonic LD treatment with analytical free energy derivatives. A 2*2*2 grid was used for the Brillouin zone sampling in this finite-temperature fitting.

The resulting potential parameters are: Z_{Mg} = +1.9104; Z_{Si} = +2.9043; Z_O = -1.6049; $b_{Mg\text{-}O}$ =1007.526 eV, $\rho_{Mg\text{-}O}$ = 0.2866Å; $b_{Si\text{-}O}$ = 1108.983 eV, $\rho_{Si\text{-}O}$ = 0.2827Å; $b_{O\text{-}O}$ = 2023.8 eV, $\rho_{O\text{-}O}$ = 0.2674 Å, $c_{O\text{-}O}$ = 13.83 eV*Å^6. Note that a simple crystal potential fitting procedure has given chemically reasonable atomic charges. Results obtained with this potential are given in Table 10-2. One can see that apart from describing well crystal structure and elastic properties, this potential gives very reasonable thermal expansion coefficient, which was not used in the fitting of the potential. The calculated shear modulus is underestimated; this is partly responsible for the small overestimation of the entropy (Table 10-2). The calculated heat capacity and entropy at 300 K compare well with experimental estimates and are superior to those calculated with previous potentials (Stuart & Price, 1996). Room-temperature Birch-Murnaghan EOS parameters are: K_0=266 and 269 GPa, K'= 3.9 and 4.04 in experiment (Knittle & Jeanloz, 1987) and theory (my LD calculations), respectively. These observations strongly support this simple potential, which perhaps is as good as a pairwise rigid-ion model can be.

This interatomic potential has been used (Oganov et al., 2000) in a comparative study of LD and MD simulations, as well as of the Debye model, applied to *Mg-pv*. The results of that study are presented in the next section.

10.3. Comparative study of LD, MD and Debye model applied to $MgSiO_3$ perovskite.

Debye model (DM). It has become an almost common practice (e.g., Stixrude et al., 1992; Anderson et al., 1995; Jackson & Rigden, 1996; Yagi & Funamori, 1996; Shim & Duffy, 2000; Stacey & Isaak, 2000; Hama et al., 2000) to use the Debye model (DM) in geophysical studies, in fitting the experimental thermal expansion, heat capacity data, or experimental equations of state. The DM does describe the shape of the temperature dependences of thermodynamic functions of solids, and this

is the reason why it often can be used for their fitting even without Debye theory being quantitatively accurate or even physically realistic. Anderson (1998) claimed

Table 10-2. Performance of the fitted interatomic potential: crystal structure and elastic properties of $MgSiO_3$ perovskite. Elastic properties in GPa, α in 10^{-5} K^{-1}, C_V and S are in J/(mol*K).

Property	Rigid-ion model (Oganov et al., 2000)	Experiment
a_0, Å	4.7822	4.7747
b_0, Å	4.8960	4.9319
c_0, Å	6.9322	6.8987
V_0, Å^3	162.31	162.45
Mg (x; y; z)	(0.5056; 0.5267; ¼)	(0.5143; 0.5556; ¼)
Si (x; y; z)	(0; ½; 0)	(0; ½; 0)
O_1 (x; y; z)	(0.1026; 0.4620; ¼)	(0.1037; 0.4655; ¼)
O_2 (x; y; z)	(0.1982; 0.2014; 0.5526)	(0.1974; 0.2011; 0.5538)
C_{11}	500	482
C_{22}	509	537
C_{33}	398	485
C_{12}	116	144
C_{13}	210	147
C_{23}	188	146
C_{44}	174	204
C_{55}	189	186
C_{66}	102	147
K_{VRH}	270.4	264.0
G_{VRH}	146.3	177.4
θ_D, K	984	1078
α	2.09	1.57[a]; 2.2[b]
C_V	80.88	80.6[c]
S	61.81	57.2[c]

a – Fiquet et al. (1998).

b – Ross et al. (1989). Experimental data on the volume thermal expansion coefficient of MgSiO3 perovskite are still highly uncertain. The most plausible range is 1.5-1.9*10^{-5} K^{-1} at 300 K and 1 atm.

c –C_p and S from Akaogi and Ito (1993).

that '$MgSiO_3$-perovskite is one of a small, select group of Debye-like minerals, for which thermoelastic properties and the equation of state (EOS) are calculable from acoustic data'.

In the Mie-Grüneisen formalism (see Chapter 3), all one needs to know to construct a high-temperature EOS is a reference isothermal (e.g., static) EOS and functions $C_V(V,T)$ and $\gamma(V)$. It is possible to obtain both C_V and γ using lattice-dynamical models, of which the DM is the simplest. This model has been considered in Chapter 3. Here I only need to add that in this model there is a simple quasiharmonic expression for the Grüneisen parameter:

$$\gamma = - \frac{d \ln \theta_D}{d \ln V} \quad , \qquad (10.3.1)$$

From the computational point of view this model is very tempting, since using only static EOS and elastic constants this model allows one to predict *all* thermoelastic properties at arbitrary *p-T*-conditions. Accurate *ab initio* static EOS and elastic constants of *Mg-pv* already exist in the literature (Wentzcovitch et al 1995, 1998; Karki et al. 1997; Oganov et al., 2001a).

Thoroughly reviewed and criticised as inapplicable to most minerals (Kieffer, 1979a), the DM in application to $MgSiO_3$ perovskite was rehabilitated by O.L. Anderson (1998), who has shown that it yields very accurate values of C_V at ambient pressure and T>400 K.

However, it has never been demonstrated that (10.3.1) does give accurate results. In fact, it does not, as I show below. Recently, Stacey and Isaak (2000) used acoustic Grüneisen parameters to construct EOS of the lower mantle minerals. Hama et al. (2000) used a self-consistent DM in order to obtain thermal EOS and seismic velocities of the major lower mantle minerals and construct a mineralogical and thermal model of the lower mantle. Since (10.3.1) is not accurate, such an approach is very crude.

What is a Debye-like solid? There are no strictly Debye-like solids, i.e. solids satisfying all the assumptions of Debye theory. With regards to geophysical applications, high-*p-T* EOS, elastic properties, and thermal expansion are the key quantities of interest, and therefore for a Debye-like solid the DM should closely reproduce

1. heat capacity $C_V(T)$, at least at elevated temperatures, and

2. Grüneisen parameter $\gamma(V)$.

Errors in any of these quantities will result in erroneous thermal EOS and, therefore, invalidate the model. For DM to give a reasonable $C_V(T)$, Anderson (1998) formulated the following conditions: a) no gap should be present in the phonon spectrum, b) not many modes should have frequencies above the maximum Debye frequency, $k\theta_D/\hbar$, c) phonon density of states should be close to (3.3.1) at least in the limit of small ω. One can see (Fig. 10-2) that conditions a-c are met for *Mg-pv*. This explains why Debye theory gives accurate predictions for $C_V(T)$. Nevertheless, as I show below, *Mg-pv* is not a Debye-like solid, since DM does not give accurate predictions for its $\gamma(V)$. Part of the reason is that in structures of such level of

complexity, optic modes (whose behaviour is not directly linked to the elastic constants) dominate. This and some other important conclusions have been reached by comparing the results of the self-consistent DM (based on the calculated athermal EOS and elastic constants) with more accurate LD and MD simulations based on the same model interatomic potential.

Unlike the DM, the LD and MD calculations take into account all the phonons across the Brillouin zone and not just the acoustic modes at $\mathbf{k}\rightarrow 0$, and intrinsic anharmonic effects are also accounted for by MD simulations. As we shall see, the DM does not reproduce the full-phonon calculations.

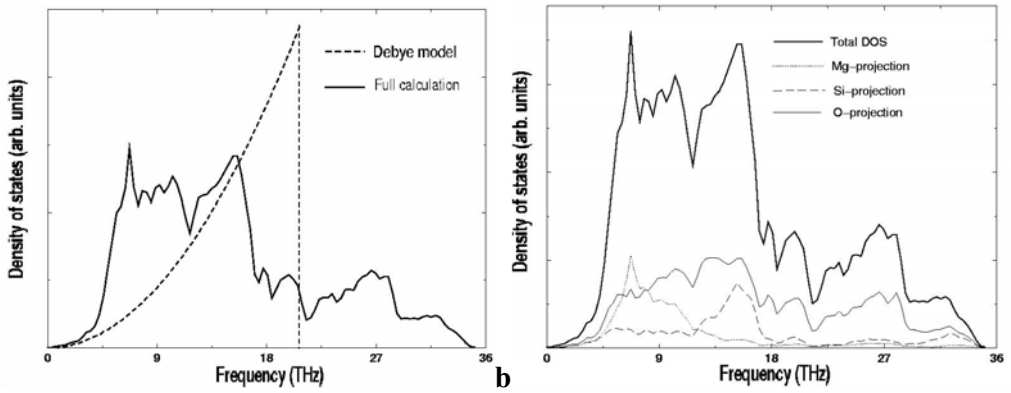

Fig. 10-2. Phonon density of states (DOS) of $MgSiO_3$ perovskite. (a) Full harmonic calculation versus the Debye model. (b) Projections of the total harmonic DOS onto atomic species. Athermal calculations at 0 GPa (V_0=160.46 Å^3). For a Debye solid, all atoms have a constant proportion of the total DOS determined by relative masses and numbers of atoms of each sort. LD-calculations show that this is far from reality: Mg-contribution clearly tends to the low-frequency part, while Si-projection leans to the high-frequency region of the DOS, as a direct result of the different bond strengths (Si-O bonds are much stiffer than Mg-O).

Computational methodology. LD calculations were performed with GULP, using analytical free energy derivatives and without the commonly used 'ZSISA' (see Chapter 5). Free energy minimisation was performed with 6*6*6 grids for the Brillouin zone integration. This grid showed very good convergence for all properties. For calculations of the density of states and its projections and heat capacity (C_V) I used even denser grids – 12*12*12 and 20*20*20, respectively.

MD calculations were performed with the Moldy code (Refson 1988-2000). The *NPT*-ensemble in conjunction with Nose-Hoover (Hoover, 1985) thermostat and Parrinello-Rahman (Parrinello & Rahman, 1981) constant-pressure algorithm was used throughout. The computational box contained 540 atoms (3*3*3 supercell), which was sufficient to obtain highly accurate results. The system was allowed to evolve for 10 ps, of which the first 5 ps were used for equilibration and not included

in the calculation of statistical averages. Timestep of 1 fs was used for integrating equations of motion.

In the high-temperature limit (closely approached at the lower mantle temperatures, roughly between 2000 K and 4000 K), where atomic motion is classical, MD (based on the classical approximation) becomes exact. Quasiharmonic LD, on the other hand, breaks down at high temperatures. Divergence of the LD and MD results at high temperatures indicates degradation of the quasiharmonic LD.

Results of semiclassical calculations. In Fig. 10-3 I compare C_V given by the DM and by the full LD treatment with the DOS integrated over a 20*20*20 Monkhorst-Pack grid. The DM is exact for the heat capacity in the low-temperature limit, although at temperatures about 100 K it already gives serious errors, which practically disappear at 500 K and above. As can be seen in Fig. 10-2, the average mode frequencies of the DM and of the full harmonic spectrum, and, consequently, their zero-point vibrational energies ($E_{zp}=3n<\frac{\hbar\omega_{ik}}{2}>$), are close. The same follows from the $C_V(T)$ plot (Fig.10-3), because $E_{zp}=\int_0^\infty (3nk_B - C_V)dT$, and areas below the $C_V(T)$ curves of the DM and full harmonic calculation are very close. According to LD and DM calculations, the classical limit is nearly reached at 1000 K and higher temperatures.

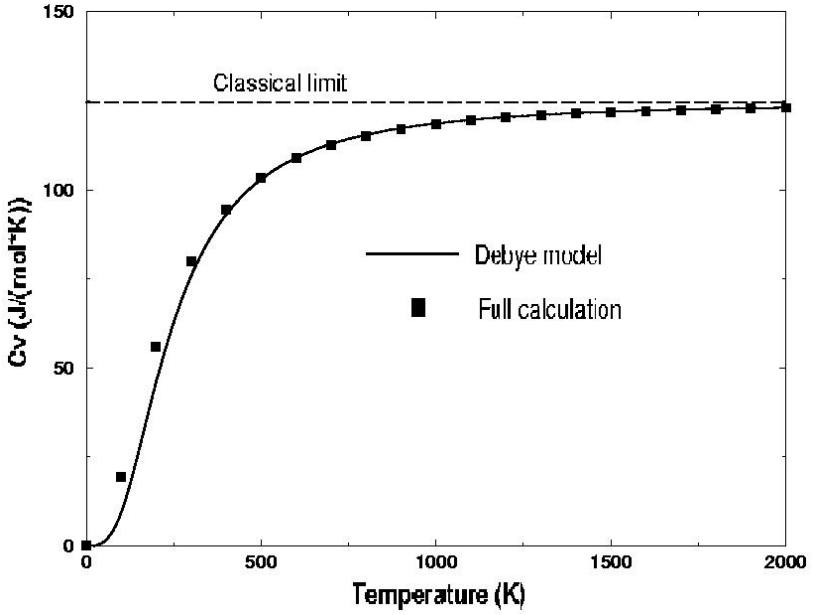

Fig. 10-3. Heat capacity C_V of $MgSiO_3$ perovskite. Filled squares - harmonic calculation, solid line - Debye model. The calculations were done at the volume corresponding to 0 GPa and athermal conditions (V_0=160.46 Å^3).

Fig. 10-4a depicts the temperature dependence of the Grüneisen parameter at 50 GPa. In LD and MD calculations the Grüneisen parameter was calculated from the thermal expansion coefficient via eq. (3.7.5)[52]. The high-temperature constant value ($<\gamma_{i\mathbf{k}}>$ - see Chapter 3) is virtually reached in LD calculations at 500 K, and a small linear increase of γ is due to the change of volume with temperature. MD, based on the classical approximation, always gives the high-temperature limit value. Below 500 K, LD gives a noticeable non-monotonic temperature variation of γ. A sudden rise and anomalously high values of γ, found in LD-calculations at T>2000 K, are artifacts of the QHA and indicate its breakdown in this temperature range, where MD is a more justified technique. DM does not reproduce neither LD nor MD results. A similar picture is observed for the thermal expansion (Fig. 10-4b).

Fig. 10-5 shows the results of full-phonon calculations of the high-temperature γ in comparison with the predictions of the DM. Results of LD-calculations differ significantly from MD-results, especially at large volumes (low pressures), in line with the earlier work by Matsui et al. (1994). This is because of the neglect of the intrinsic anharmonic effects in the QHA. Errors of the DM are typically about –30% at all volumes, and reach almost -50% at the bottom of the lower mantle. This implies an error of typically 30% in the thermal expansion coefficient.

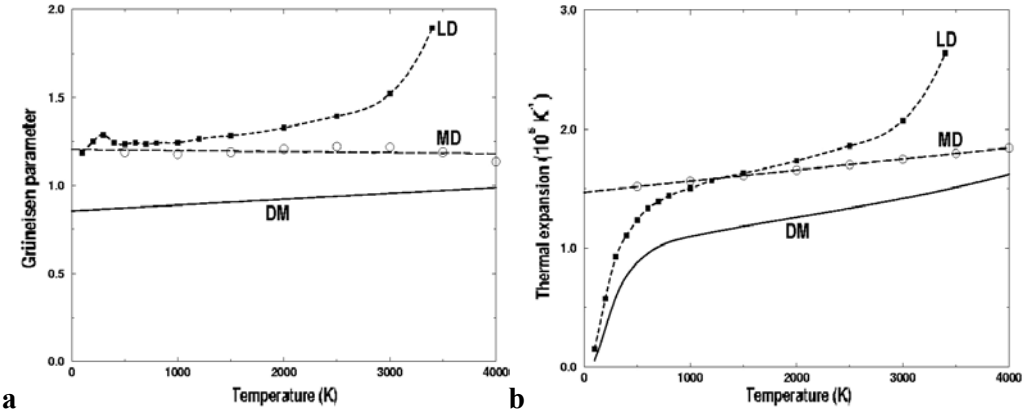

a **b**

[52] Since MD is based on the classical approximation, C_V was assumed to be equal to $(3n\text{-}3)k_B$ (per supercell containing n atoms). The anharmonic contribution, by eq. (3.6.2), is expected to be a few percent of $(3n\text{-}3)k_B$ at mantle temperatures (<4000 K).

Fig. 10-4. Grüneisen parameter (a) and thermal expansion (b) of $MgSiO_3$ perovskite at 50 GPa. Debye model – solid curves; LD – dashed lines with filled squares; MD – long-dashed lines with empty circles.

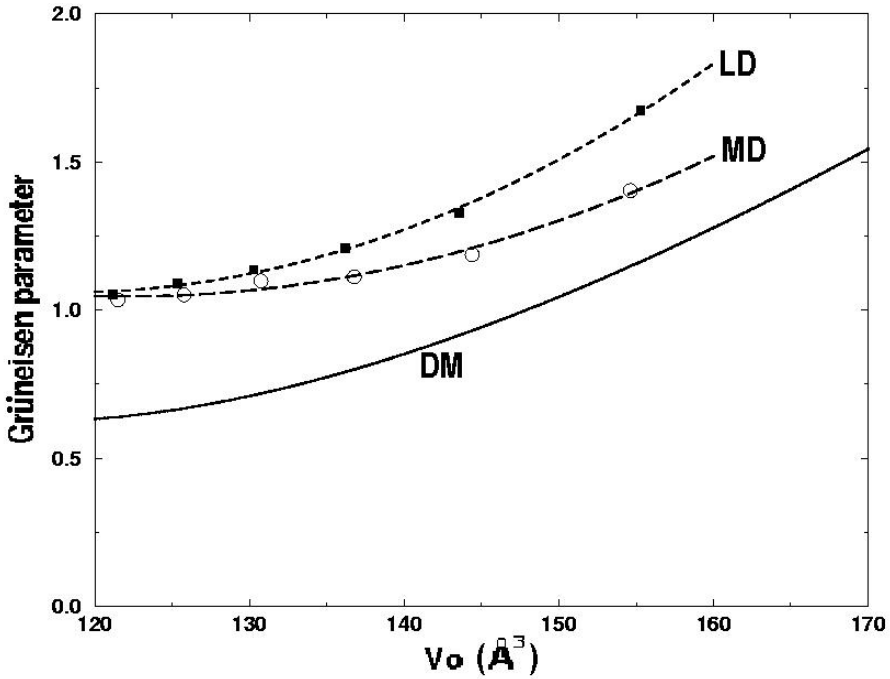

Fig. 10-5. Grüneisen parameter of $MgSiO_3$ perovskite at 1500-2500 K as a function of volume. Symbols the same as in Fig. 10-4. Average values of q=dlnγ/dln$V$ are 2.6, 1.8, and 1.2 for the DM, LD, and MD curves, respectively. Contrary to the common assumption, q is found to vary considerably with V, approaching zero at large compressions.

It is interesting to calculate the EOS with each of these methods. Vinet EOS parameters for pressures in the range 0-150 GPa at temperatures 500 K, 1500 K, 2500 K are given in Table 10-3. At 0 GPa, LD calculations give dynamical instabilities at and above 1500 K, so LD-values of the zero-pressure V_0, K_0, and K' at these temperature in Table 10-3 are merely extrapolated numbers. No such phonon catastrophes were observed in MD and DM calculations.

Table 10-3. EOS of $MgSiO_3$ perovskite from semiclassical calculations.

	T = 500 K			T = 1500 K			T = 2500 K		
	DM	**LD**	**MD**	**DM**	**LD**	**MD**	**DM**	**LD**	**MD**
V_0, Å^3	162.9	163.1	162.4	167.6	168.2	168.0	174.8	176.2	174.9
K_0, GPa	255.0	258.7	261.0	211.2	221.0	216.7	158.0	167.7	174.1
K'	4.42	4.37	4.35	4.85	4.63	4.73	5.45	5.15	5.10

Analysis of these results shows that at the lower mantle conditions the DM overestimates density of $MgSiO_3$ perovskite by ~1%. This seemingly small error would lead to the error of 3 mol.% in Fe content or ~1000 K in temperature for the perovskite lower mantle.

Comparison of the experimental $p(V)$-isotherm at 2000 K and up to 90 GPa (Fiquet et al., 1998, 2000) with the MD results shows the pressure difference up to 5 GPa, which is of the order of the experimental uncertainties. This again confirms the validity of the model potential used.

Conclusions. The results just discussed indicate that *Mg-pv* cannot be regarded as a good Debye-like solid, and its EOS cannot be accurately determined from acoustic data, contrary to the conclusion of Anderson (1998). Adiabatic thermal gradient of the lower mantle, $(\partial T/\partial P)_S=\gamma T/K_S$, cannot be constructed without accurate knowledge of the Grüneisen parameter γ. In agreement with this, Brown and Shankland (1981) on the basis of Debye theory found an adiabatic temperature increase of ~560 K across the lower mantle, while my *ab initio* adiabatic geotherm (see below) gives much higher increase of ~800 K. When deriving the temperature profile by matching PREM bulk modulus and density with the properties of plausible mineral assemblages, errors of ~30% (i.e., ~1000 K) in the temperature would arise from the use of acoustic γ.

If DM is used self-consistently (like in Hama et al. 2000), i.e. γ is related to the volume derivatives of the acoustic velocities, significant errors are expected. Likewise, it is not justified to extract γ from seismological profiles. On the other hand, it should be safe to use the DM for inverting experimental data sets (e.g., Stixrude et al., 1992; Jackson & Rigden, 1996; Yagi & Funamori, 1996; Fiquet et al., 2000; Shim & Duffy, 2000). However, in this case parameters of the model lose their original meaning and become unrelated to the acoustic velocities.

It is now clear that at mantle temperatures only MD simulations can give very accurate results. Such calculations will be discussed below, after I discuss an important issue of the stability of *Mg-pv* in the lower mantle.

10.4. Stability of $MgSiO_3$ perovskite.

If *Mg-pv* perovskite undergoes a phase transition within the lower mantle, it would have dramatic consequences, at least by creating a major seismic boundary. Indeed, there are seismic discontinuities in the lower mantle (e.g., Le Stunff et al., 1995), but all of them are rather weak and may not be global.

Two main possibilities of a phase transition have been considered – 1) temperature-induced transition to another perovskite phase and 2) breakdown of *Mg-pv* into the mixture of oxides, $MgSiO_3 \rightarrow MgO+SiO_2$. Both possibilities have been

reviewed in Chapter 2. There is almost no doubt that *Mg-pv* remains stable at mantle conditions. The main question therefore is whether it remains in the usual orthorhombic (*Pbnm*) phase or transforms into another perovskite phase at high mantle temperatures.

The *raison d'etre* of any temperature-induced transition is the higher entropy of the high-temperature phase; usually this means an increase of symmetry by means of static or dynamic disorder. The cubic ($Pm\bar{3}m$) and tetragonal ($I4/mcm$) phases have become the main (but not the only) candidates for the high-T phase. Together with *Pbnm*, these are among the phases most commonly found in analogue perovskites.

The cubic phase should be a superionic conductor of electricity (O'Keeffe & Bovin, 1979; Matsui & Price, 1991) due to the diffusion of O^{2-} ions. Indeed, geophysical observations and laboratory experiments show that the electrical conductivity of the lower mantle is unusually high, ~1-10 S/m (for an extensive discussion, see Xu et al., 2000), but cubic *Mg-pv* is not the only possible explanation.

Meade et al. (1995) observed a cubic phase preceding the breakdown of *Mg-pv* in their experiments. Likewise, Saxena et al. (1998) reported a 'pseudocubic' phase before the breakdown. As noted above, the very existence of this breakdown is highly controversial. In some (but not all) of their *in situ* diffraction experiments at 83 GPa and 1700 K, Shim et al. (2001) found a diffraction peak that could not be explained by the *Pbnm* phase, but could be indexed in any of the three space groups: $P2_1/m$, *Pmmn*, or $P4_2/nmc$. Only the latter space group is higher in symmetry than *Pbnm*.

Lufaso and Woodward (2001) have presented an interesting analysis of the symmetry statistics for perovskite structures. It follows that $P4_2/nmc$ is not a likely space group for *Mg-pv*: none of the numerous known ABX_3 perovskites have $P4_2/nmc$ symmetry; this group appears only in 1 compound with A-substitutions and the associated cation ordering. Lufaso and Woodward found the following distribution of the likely space groups: *Pbnm* (65%), $R\bar{3}c$ (13%), $Pm\bar{3}m$ (11%), $I4/mcm$ (5%), $P4/mbm$ (3%), *Imma* (3%). Low-symmetry ABX_3 perovskites (space groups $C2/m$, $P\bar{1}$, $P2_1/m$) are very unlikely – they are known for only 6 compounds (3% of the total).

The remaining experimental evidence in favour of a temperature-induced transition is indirect. Wang et al. (1990, 1992) found extensive twinning in quenched

samples of *Mg-pv* synthesised at mantle conditions (e.g., 26 GPa and 1900 K). The twinning planes found indicated that the samples could undergo the cubic→tetragonal and then tetragonal→orthorhombic transitions on quenching. By itself, the observation of twinning does not necessarily suggest the existence of such transitions at mantle temperatures, but is very important in a different way. It shows that in the mantle *Mg-pv* can be heavily twinned; the twin boundaries can strongly affect the rheological and transport properties of the lower mantle, as well as attenuation of seismic waves passing through it.

For $CaTiO_3$ perovskite, Vogt and Schmahl (1993) claimed that the orthorhombic phase transforms directly into the cubic one; Redfern (1996) found a narrow temperature interval of stability of the intermediate tetragonal phase. All these transitions are close to second order. Zhao et al. (1993) studied neighborite ($NaMgF_3$); they found only the orthorhombic→cubic transition, which they showed to be tricritical, i.e. first-order transition very close to second order[53]. All these transitions occur close to the melting point.

As suggested by the behaviour of the analogue compounds and by all semiclassical MD (e.g., Matsui & Price, 1991; Chaplot et al., 1998) and hybrid Monte Carlo (Purton et al., 1999) simulations, the *Pbnm*→$Pm\bar{3}m$ is tricritical in *Mg-pv* perovskite and occurs close to the melting curve. For strongly first-order transitions (e.g., for melting) conventional MD can give large hysteresis and overheating effects. For displacive second-order and tricritical transitions such problems do not exist, and conventional MD can be used. Matsui and Price (1991) found a hysteresis of only 100-200 K for the *Pbnm*→$Pm\bar{3}m$ transition in *Mg-pv*. Hybrid Monte Carlo simulations (Purton et al., 1999), which do not encounter problems with overheating, gave results similar to the those of the conventional MD simulations.

Large-scale semiclassical MD simulations found at most three perovskite phases: orthorhombic, tetragonal, and cubic, in the order of increasing temperature. The most accurate simulations of this kind are those of Chaplot et al. (1998), whose

---

[53] The *Pbnm*→$Pm\bar{3}m$ transition cannot be truly second-order because it involves two order parameters going to zero simultaneously. On the other hand, the $I4/mcm \rightarrow Pm\bar{3}m$ transition could be second-order.

simulations included 12,000 atoms in the supercell. These authors found that at most conditions the tetragonal phase had a negligible distortion and was practically equivalent to the cubic one[54]. They also found that the transition temperatures were significantly lowered when vacancies were introduced. Nevertheless, even when vacancies were introduced, the transition temperatures remained well above the range of mantle temperatures. Static (Stixrude & Cohen, 1993; Wentzcovitch et al., 1993, 1995; D'Arco et al., 1993, 1994; this work) and MD (Warren et al., 1998; Oganov et al., 2001a,b; this work) quantum-mechanical calculations arrive at the same conclusion, but the role of vacancies and other defects has not yet been studied using *ab initio* simulations.

At zero pressure, my GGA calculations show that the cubic and tetragonal phases are higher in energy than the orthorhombic phase by 1.21 eV (116 kJ/mol) and 0.55 eV (53 kJ/mol), respectively (Fig. 10-6). The cubic and tetragonal phases are also significantly less dense, so the very large enthalpy differences rapidly increase with pressure. This is demonstrated in Fig. 10-7, which shows the $\Delta H/k_B$. This value has the dimension of temperature and gives a rough idea of the transition temperatures. My GGA results are in excellent agreement with LDA results of Stixrude and Cohen (1993) and Wentzcovitch et al. (1993; not shown here) and HF results of D'Arco et al. (1993; not shown here). Also shown in Fig. 10-7 are the results of my semiclassical simulations based on the interatomic potentials of Oganov et al. (2000) and Matsui (1988). The agreement with *ab initio* results is very reasonable, but the transition enthalpies are systematically underestimated by both semiclassical models.

[54] Smaller-scale semiclassical MD studies of Matsui and Price (1991) and in this work were able to resolve only the cubic phase. However, this difference might also be due to the different potential parameterisations used in all these studies.

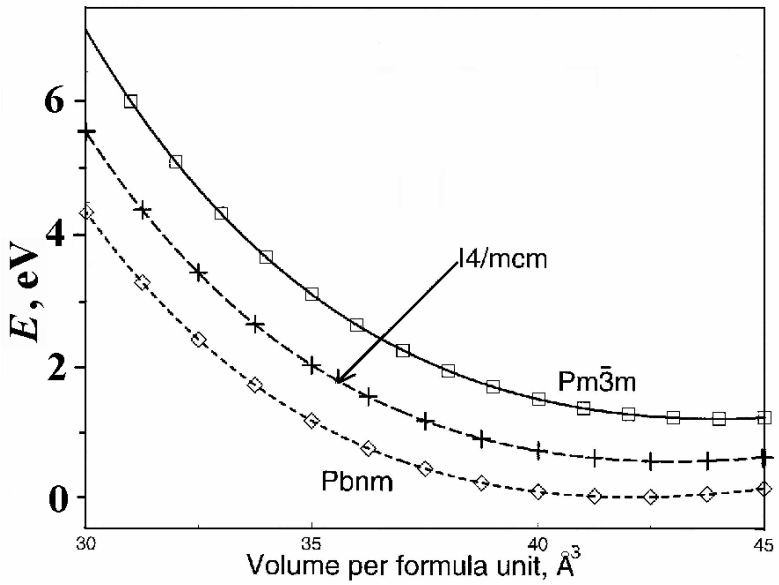

Fig. 10-6. $E(V)$ curves for the orthorhombic, tetragonal, and cubic phases of $MgSiO_3$ perovskite: GGA calculations. Minimum energy of the *Pbnm* phase is set as the reference zero. Energies are per formula unit.

Stixrude and Cohen (1993) have shown that both cubic and tetragonal phases actually correspond to local energy maxima. This has since been confirmed in many studies (e.g., Parlinsky & Kawazoe, 2000; Warren et al., 1998), which found that both tetragonal and cubic phases are dynamically unstable. The instability is due to the relatively small size of the Mg^{2+} cation, which cannot support the large cage of the ideal cubic structure – and the cage accordingly collapses.

If the transition is purely displacive, the high-symmetry cubic and tetragonal structures will be the transition states; the real structure will be dynamically disordered, hopping both ways through these barriers (see a scheme shown in Fig. 4-1). The barrier height (i.e., ΔH) will be directly related to the transition temperature, which is the temperature of the onset of the dynamical disorder. $\Delta H/k_B$ will then be a correct semiquantitative estimate of the transition temperature, and this estimate significantly exceeds the mantle temperatures.

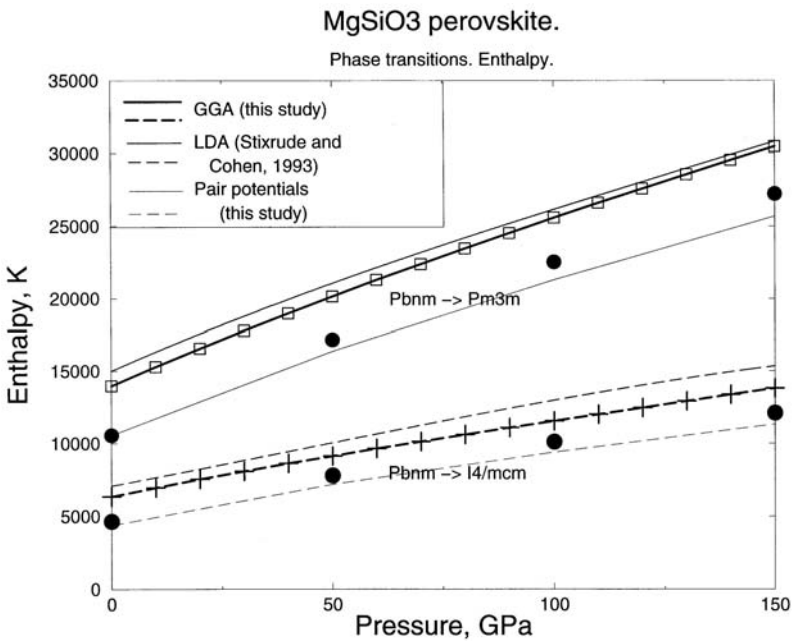

Fig. 10-7. Enthalpy differences ($\Delta H/k_B$, in units of temperature) cubic-orthorhombic and tetragonal-orthorhombic as a function of pressure. Results based on the LDA (Stixrude & Cohen, 1993) and GGA (this work) are shown along with the results based on semiclassical interatomic potentials of Oganov et al. (2000) [lines] and Matsui (1988) [solid circles].

In the other limit, the transition may be of the pure order-disorder type. In this case, the structure is also locally distorted, but all disorder is static. In this limit, there is no hopping over the barrier, because it is too high compared to k_BTc, i.e. the transition temperature is much lower than $\Delta H/k_B$. Computer simulations suggest that the $Pbnm \rightarrow Pm\bar{3}m$ transition in Mg-pv is intermediate between the pure order-disorder and displacive types. Apart from the energy of rigid rotations of the SiO_6 octahedra, there will be an important contribution from the bending of the O-Si-O angles within these octahedra. The latter contribution arises as a consequence of any static positional disorder of the O atoms. Keeping in mind that the first energy term is underestimated by the model pair potentials, at least by those of Matsui (1988) and Oganov et al. (2000) and the angle-bending terms are not present in these models at all, one expects that semiclassical simulations will give a *lower bound* to the transition temperatures. However, my semiclassical MD simulations (Fig. 10-8), as well as those of Matsui and Price (1991) and Chaplot et al. (1998) give temperatures that are way too high for the lower mantle.

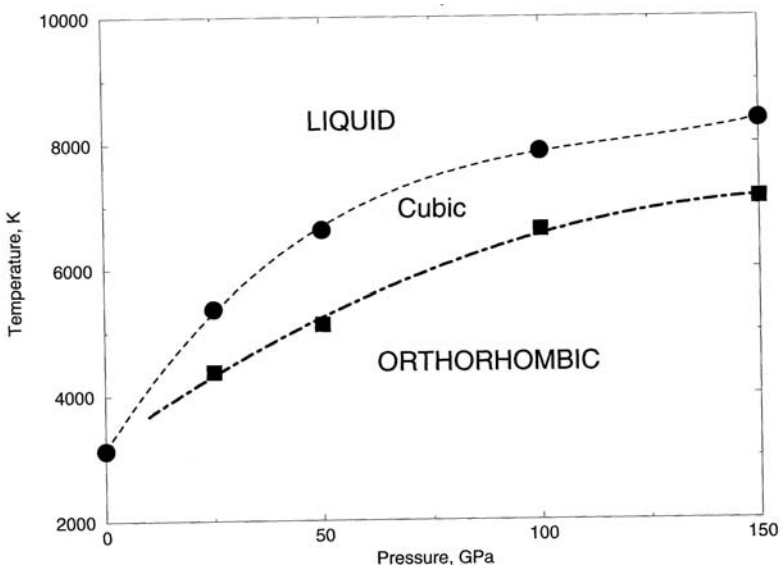

Fig. 10-8. Orthorhombic-cubic transition and melting of $MgSiO_3$ perovskite from semiclassical MD simulations. Interatomic potential model of Oganov et al. (2000) was used. These simulations used a large supercell (960 atoms) and were run for 5 ps after equilibration. The cubic phase appears at the temperatures that are too high for the lower mantle and are even above the experimental melting curve (e.g., Shen & Lazor, 1995). Introducing defects would lower the transition temperatures, but not enough to make them comparable to the mantle temperatures (Chaplot et al., 1998). The melting curve shown is an upper bound: solid→liquid transitions are strongly first-order, with large overheating effects. These effects can be reduced by introducing surfaces or by performing two-phase simulations (see Belonoshko, 2001).

In agreement with these results, *ab initio* MD simulations (Oganov et al., 2001a,b) showed no signs of any phase transition from *Pbnm* perovskite, within the mantle temperature range. These simulations were performed in the *NVT* ensemble, i.e. at constant volume[55], but with optimisation of the cell parameters. Calculating statistical averages of the stress tensor components $<\sigma_{kl}>$, it is straightforward to determine the strains e_{ij} that should be applied to the trial supercell in order to make the stress tensor hydrostatic and equivalent to the pressure p:

$$e_{ij} = -S_{ijkl}[<\sigma_{kl}>+p\delta_{kl}] \ , \qquad (10.4.1)$$

where S_{ijkl} is the elastic compliance matrix[56]. To apply (10.4.1), one needs to know the elastic constants; static elastic constants at a given volume give a reasonable approximation. Usually, the cell was fully optimised after two or three strain iterations (10.4.1). This procedure of optimising cell parameters is equivalent to finding the local free energy minimum. Optimising cell parameters at a given *pT*-

[55] Unlike the semiclassical calculations, which were performed in the *NPT*-ensemble (Parrinello & Rahman, 1981), in which fluctuations of the cell shape are included and thus there is no need to optimise the cell.

[56] Like in the discussion of the elastic constants in Chapter 3, here I use a convention that stress is positive when it is directed outwards, and strain is positive when it corresponds to expansion.

point, one can see whether the phase remains orthorhombic or has transformed, e.g. to the cubic phase (see Fig. 10-9)[57]. For the optimised cell, one can also determine the elastic constants at given p and T from stress-strain relations (Oganov et al., 2001b). Five pT-points have been studied: (38 GPa, 1500 K), (38 GPa, 2500 K), (38 GPa, 3500 K), (88 GPa, 1500 K), and (136 GPa, 4500 K). Although the simulations do show the orthorhombic distortion decrease with temperature, even at the highest temperatures probed the structure remained orthorhombic. One point (38 GPa, 3500 K) is very close to melting and had very vigorous large-amplitude thermal motion of atoms. It is remarkable that even at these conditions *Mg-pv* remained orthorhombic.

To summarise, our results and the general majority of evidence indicate stability of the orthorhombic (*Pbnm*) *Mg-pv* throughout the lower mantle. Interestingly, another group (Stixrude, 2001) recently performed *ab initio* MD simulations, very similar to mine and in the same p-T range. However, that group arrived at an opposite conclusion. Their simulations found the *Pmmn* phase, seemingly supporting the experimental findings of Shim et al. (2001). Most probably, the difference is due to less accurate pseudopotentials used by that group. This point needs further research.

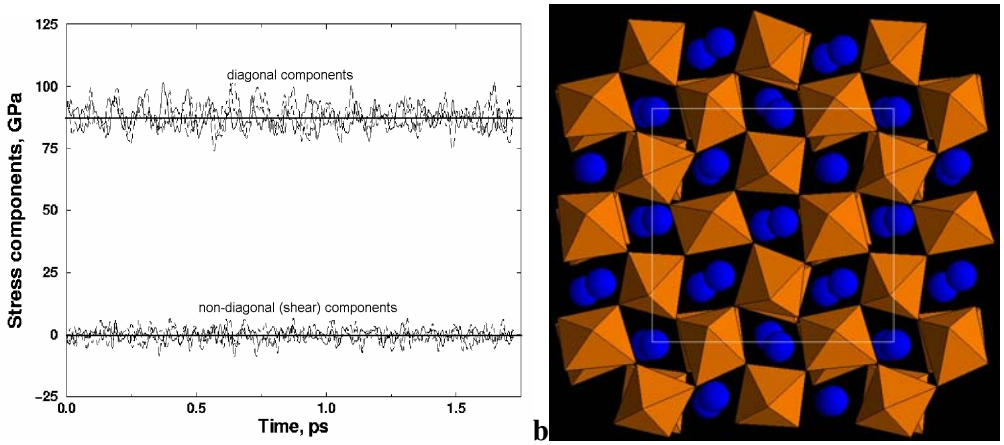

Fig. 10-9. Stress tensor and crystal structure of $MgSiO_3$ perovskite at 88 GPa and 3500 K from *ab initio* MD simulations. (a) In the optimised cell, the stress tensor is hydrostatic. In this figure, an example from a simulation at 88 GPa and 3500 K is shown. (b) A snapshot of the structure of $MgSiO_3$ perovskite at 88 GPa and 3500 K in the optimised cell. Such simulations show that the orthorhombic structure is stable throughout the lower mantle pressure-temperature regime.

10.5. Equation of state and mantle geotherm.

[57] In this way, one could have a metastable low-symmetry phase persisting in the stability domain of the high-symmetry phase. Such problems do not occur in *Mg-pv*, where the expected transitions are tricritical or even second-order.

The Grüneisen parameter was calculated using (3.7.8). The phonon pressure was calculated from the differences in stress tensors obtained in static (T = 0 K) and *ab initio* MD simulations at 500 K and 1500 K using lattice parameters optimised at 0 K. Static structure optimisation was performed at the ambient-conditions volume and at static pressures of 50, 100, and 150 GPa using the same supercell and computational conditions as in the MD simulations. The vibrational energy E_{vib} was taken as $(3n\text{-}3)k_BT$ (per supercell containing n atoms) in classical MD; this is correct to within the uncertainties of the simulations. The anharmonic contribution to E_{vib}, by (3.6.2), should be within a ~2% of $(3n\text{-}3)k_BT$ at 1500 K. The calculated $\gamma(V)$ are accurate to ~10% and show practically no temperature dependence at constant volume.

The calculated $\gamma(V)$ is given in Fig. 10-10. It is well described by the function $\gamma=\gamma_0(V/V_0)^{1.27262+1.67772\ln\frac{V}{V_0}}$, where γ_0=1.506, V_0=162.40 Å^3. At ambient conditions the calculated $\gamma_0=1.51\pm0.1$ is similar to 1.5 ± 0.2 preferred by Anderson et al. (1995). As expected, the Debye model gives poor results for $\gamma(V)$. Fig. 10-10 also shows results for MgO (Oganov et al., in preparation), which will be used below.

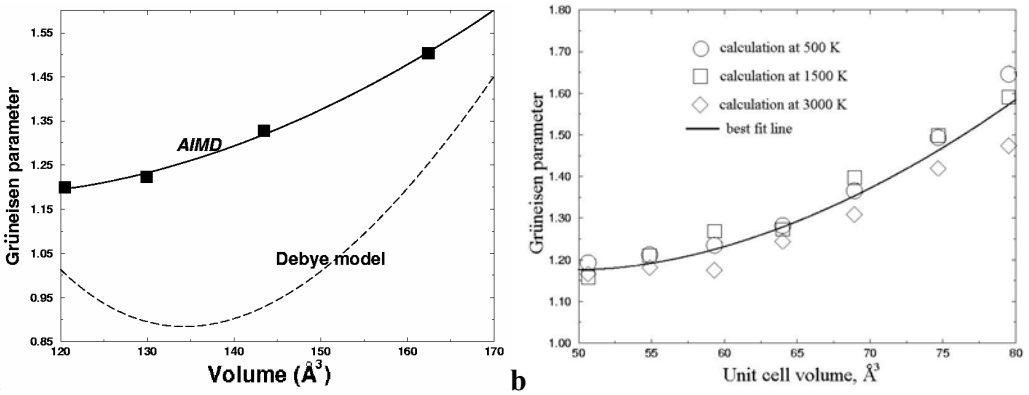

Fig. 10-10. *Ab initio* $\gamma(V)$ functions of (a) $MgSiO_3$ perovskite (Oganov et al., 2001a), (b) MgO (Oganov et al., in preparation). For MgO, a supercell with 64 atoms was used. *Ab initio* MD simulations were run in the *NVT* ensemble for 1.5 ps after equilibration, with a timestep of 1.5 fs. Γ-point was used for Brillouin zone sampling. The same GGA, pseudopotentials, and kinetic energy cutoff were used as in the calculations for *Mg-pv*.

As discussed in Chapter 3, conventional MD, based on the classical equations of motion of atoms, gives correct mode-average Grüneisen parameters even at low temperatures, where the classical approximation fails to give a correct description of the vibrational energy $E_{vib}(V,T)$ and of the EOS. The Debye model, although inaccurate in predicting $\gamma(V)$, gives excellent vibrational energies and heat capacities (Oganov et al., 2000; Anderson, 1998) above ~400 K. Fig. 10-3 illustrates this by

comparing C_V obtained by Debye model and full harmonic calculations, both of which were based on the same model of interatomic interactions (Oganov et al., 2000). Therefore, I used Debye model (based on the calculated *ab initio* static elastic constants – Table 10-4 and Fig. 10-11) to determine the first approximation to $E_{vib}(V,T)$.

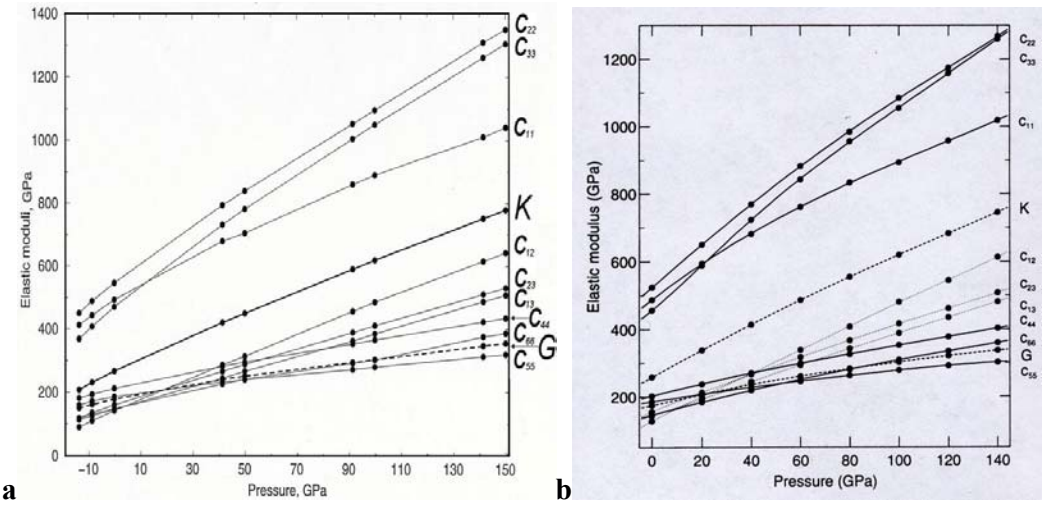

a b

Fig. 10-11. Athermal elastic constants of $MgSiO_3$ perovskite as a function of pressure. (a) GGA data of Oganov et al. (2001a) with shifted pressure scale, (b) LDA results of Karki et al. (1997). GGA calculations give $\partial G/\partial p$=1.88 at 0 GPa, close to the experimental value of 1.8 (Sinelnikov et al., 1998).

Table 10-4. Elastic properties of $MgSiO_3$ perovskite as a function of pressure (at 298 K)[a]

	Pressure (GPa)					
	0	**30**	**60**	**90**	**120**	**150**
V_0 , Å^3	162.4	148.0	138.1	130.6	124.5	119.5
C_{11}, GPa	492	629	746	851	947	1036
C_{22}	550	727	888	1044	1196	1344
C_{33}	472	661	833	995	1150	1298
C_{12}	142	246	349	449	546	639
C_{13}	148	216	287	360	433	505
C_{23}	160	237	311	385	457	528
C_{44}	213	264	309	351	394	433
C_{55}	187	221	247	272	296	319
C_{66}	154	206	249	293	338	384
K , GPa	267	379	483	583	681	775
G	180	225	261	294	325	355

a - C_{ij} values in this table were obtained by 3rd order polynomials interpolations of C_{ij} from Fig. 10-11a.

Isothermal Mie-Grüneisen EOSs, fitted by the Vinet function, are given for several temperatures in Table 10-5. Table 10-6 gives a summary of thermoelastic

parameters of $MgSiO_3$ perovskite. Comparing these tables, one can see that zero-point contribution dominates the phonon pressure at ambient conditions.

Table 10-5. *Ab initio* thermal EOS of $MgSiO_3$ perovskite.

	***T*, K**						
	static	**0**	**1500**	**2000**	**2500**	**3000**	**4000**
V_0, Å^3	160.2	162.1	167.9	170.9	174.2	177.9	187.2
K_0, GPa	279.7	269.9	228.3	210.6	192.3	173.5	134.4
K'	4.02	4.07	4.36	4.49	4.63	4.78	5.13

Table 10-6. Thermoelastic parameters of $MgSiO_3$ perovskite from theory and experiment.

Source	V_0, Å^3	K_0, GPa	K'	$(\partial K_T/\partial T)_p$, 10^{-3}GPa/K	$\frac{\partial^2 K_T}{\partial p \partial T}$, 10^{-5} K^{-1}	γ_0	q_0	α_0, 10^{-5} K^{-1}
***Ab initio* simulations**								
LDA[a]	160.74	266	4.2	-	-	-	-	-
LDA[b]	157.50	259	3.9	-	-	-	-	-
LDA[c]	162.47	257	4.02	-	-	-	-	-
LDA[d]	164.1	247	3.97	-31	32	1.63	2.0[e]	2.15
GGA	(162.4)	267	4.10	-21	15	1.51	1.27[e]	1.86
Experiment								
1[f]	162.3	259.5	3.69	-17	-	(1.4)	1.4	1.8-2.2
2[f]	(162.3)	(261)	(4)	-28	-	1.42	2.0	1.7
3[f,g]	(162.2)	(261)	(4)	-22	8	1.25	1	1.65
Exp. range	162.4±1	247-272	3.6-7	-17 to -63	-	1.3-2.2	~1-2.5	1.4-3.3

a – LAPW results of Stixrude & Cohen (1993).
b – Pseudopotential calculations of Wentzcovitch et al. (1995).
c – Pseudopotential calculations of Karki (personal communication, 1997).
d – Quasiharmonic simulations of Karki et al. (2001), based on the LDA and pseudopotential plane wave method.
e – Values given in this table correspond to the ambient conditions. Both my simulations (Oganov et al., 2001a) and those of Karki et al. (2001) found that q varies very strongly with volume.
f – 1: Fiquet et al. (2000), 2: Shim & Duffy (2000), 3: Gillet et al. (2000).
g – Work of Gillet et al. (2000), based on Raman spectroscopic measurements combined with experimental room-temperature EOS, resulted in several distinct models. Numbers given here correspond to their preferred model.

Thermal expansion was calculated as $\alpha=\gamma C_V/K_T V$. Thus calculated α is consistent (to within a few percent) with those determined directly from the *ab initio* MD optimised cell volumes at 38 GPa and 88 GPa in the temperature interval 1500-3500 K. Fig. 10-12 gives a comparison of the theoretical (Oganov et al., 2001; Karki et al., 2001) thermal expansion coefficients as a function of pressure and temperature. Several experimental results at 1 atm are also shown. Theoretical calculations are in good agreement with each other, being practically indistinguishable above 50 GPa.

The differences are significant only at low pressures and high temperatures, where the quasiharmonic approximation (used by Karki et al., 2001) is known to overestimate thermal expansion (see section 10.3 and Oganov et al., 2000). Our results clearly favour lower experimental values of thermal expansion, found in the latest experimental studies (e.g., Wang et al., 1994; Funamori et al., 1996; Fiquet et al., 2000; Shim & Duffy, 2000; Gillet et al., 2000). At ambient conditions, we calculate $\alpha=1.60*10^{-5}$ K^{-1} if Debye model is used for C_V, or $1.86*10^{-5}$ K^{-1} if the experimental value (Akaogi & Ito, 1993) is used.

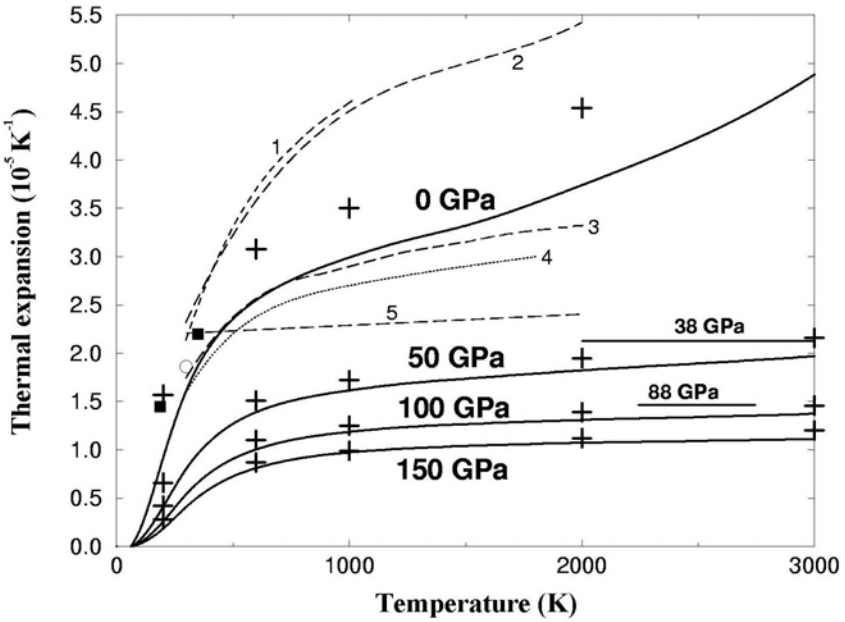

Fig. 10-12. Thermal expansion of $MgSiO_3$ perovskite. *Solid lines* – results of this study (Oganov et al., 2001a), open *circle* - calculation using γ from *ab initio* MD and experimental C_V. *Solid horizontal lines* - direct *ab initio* MD results at 38 GPa and 88 GPa between 1500 K and 3500 K. *Crosses* – calculations of Karki et al. (2001). Experimental data at 0 GPa: *squares* (Ross & Hazen, 1989), *lines* - *1* (Knittle & Jeanloz, 1986), *2* (Mao et al., 1991), *3* (Wang et al., 1994), *4* (Funamori et al., 1996), *5* (Fiquet et al., 2000).

Geophysical implications. These results have far-reaching consequences. Low thermal expansion of *Mg-pv* implies that pure-perovskite lower mantle model (Stixrude et al., 1992), is unlikely. The pure-perovskite model relied on the old high $\alpha(T)$ values of Mao et al. (1991) and Knittle and Jeanloz (1986). Low $\alpha(T)$ would imply unrealistically high temperatures needed to match the bulk modulus of *Mg-pv* and geophysical observations. This conclusion was fully supported by Karki et al. (2001) and would hardly be changed by impurities of Al and Fe, present in the mantle perovskite. *Ab initio* calculations of Brodholt (2000) have shown that Al impurity, although strongly decreasing the bulk modulus of *Mg-pv* at low pressures (in agreement with experiments of Zhang & Weidner, 1999), has practically no effect

above 30 GPa. With accurate thermoelastic parameters and EOS of *Mg-pv*, now it should be straightforward to determine the most likely composition of the lower mantle; this result would be very important for understanding the dynamics of the mantle and global chemistry of the Earth.

With the data presented here we can construct a thermal profile of the lower mantle. For the convecting lower mantle, the average temperature as a function of depth (geotherm) should increase at least adiabatically. As discussed by Jackson (1998), PREM (Dziewonski & Anderson, 1981) indicates adiabatic lower mantle, while another major global Earth's seismological model – ak135 (Kennett et al., 1995) – is consistent with large superadiabaticity in this region.

Here I construct a new adiabatic geotherm (Oganov et al., in preparation), which will serve us as a useful reference. This adiabatic geotherm is constructed on the basis of the $\gamma(V)$ functions (Fig. 10-10) of *Mg-pv* and periclase (MgO), which together account for ~90-95 vol. % of the lower mantle. The adiabatic temperature profile is expressed as the following integral:

$$T(z) = T(670\text{ km}) + \int_{z_1=670km}^{z} T\gamma(V)\left(\frac{\mathrm{d}\ln\rho}{\mathrm{d}z}\right)\mathrm{d}z \quad , \qquad (10.5.1)$$

where I use T(670 km)=1873±100 K determined from phase equilibria (Ito & Katsura, 1989) and geophysical (PREM) density profile $\rho(z)$[58]. Fig. 10-13 shows that two adiabats obtained with $\gamma(V)$ of $MgSiO_3$ and MgO (thick dashed lines) are practically indistinguishable; therefore, we have an accurately constrained adiabatic geotherm (between these two adiabats). This adiabatic geotherm is quite similar to the classical geotherms of Brown and Shankland (1981) and Anderson (1982), both of which included a small superadiabatic gradient.

Later in this chapter I consider lateral temperature variations in the lower mantle. These are extremely important for the understanding of the Earth's dynamics, but have been poorly understood to date. The breakthrough was achieved (Oganov et al., 2001b) by combining the state of the art of seismic tomography and hitherto unprecedented *ab initio* MD calculations of the elastic constants at mantle temperatures and pressures.

---

[58] PREM density profile is used instead of using theoretical equations of state of minerals. It is preferable to use as many accurate seismological data as possible to construct a good geotherm. Using mineral equations of state, on the other hand, would be useful in discriminating between different compositional models of the mantle.

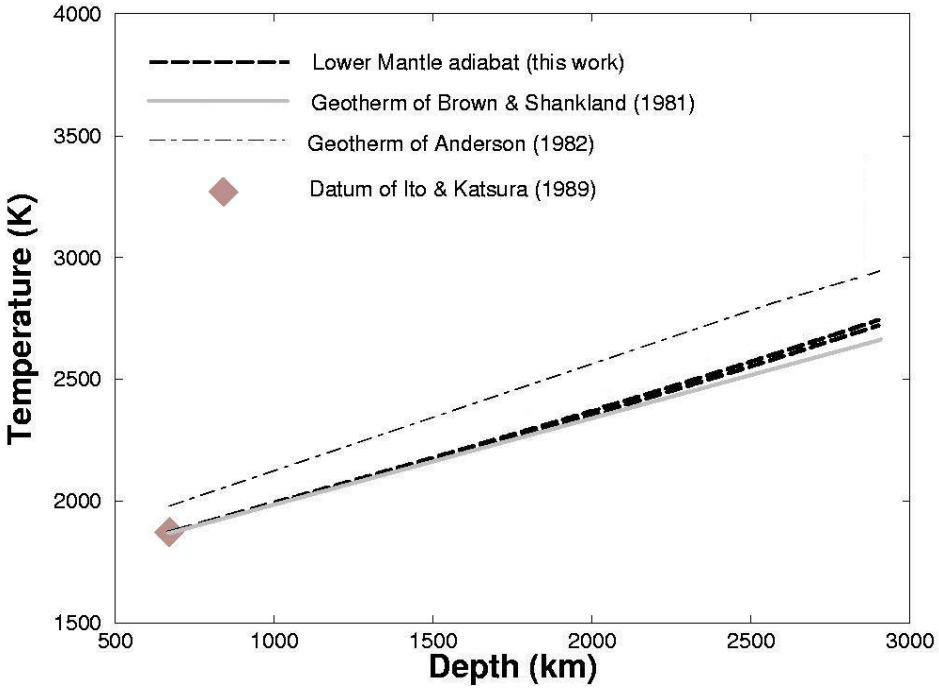

Fig. 10-13. Adiabatic geotherm (this work) in comparison with the geotherms of Brown and Shankland (1981) and Anderson (1982).

10.6. Elastic constants at mantle temperatures and pressures.

The athermal elastic constants as a function of pressure (Oganov et al., 2001a) are shown in Fig. 10-11. My results are very similar to those of Karki et al. (1997). At 1 atm, the agreement with experimental results (Yeganeh-Haeri, 1994) is remarkably good.

We were also able to perform *ab initio* MD calculations of the elastic constants of $MgSiO_3$ perovskite at lower mantle conditions – including temperature. We believe that these are the first *ab initio* MD calculations of the elastic constants of any material at non-zero temperatures. Such calculations are extremely computationally demanding. The elastic constants were calculated for the optimised supercells, from non-linear stress-strain relations with +2% and –2% strains (see Fig. 10-14).

In seismology, the relevant elastic constants are the adiabatic ones; in the *NVT*-ensemble one calculates the isothermal constants. It is easy to transform the isothermal values into adiabatic (and vice versa) using (3.10.15). The temperature

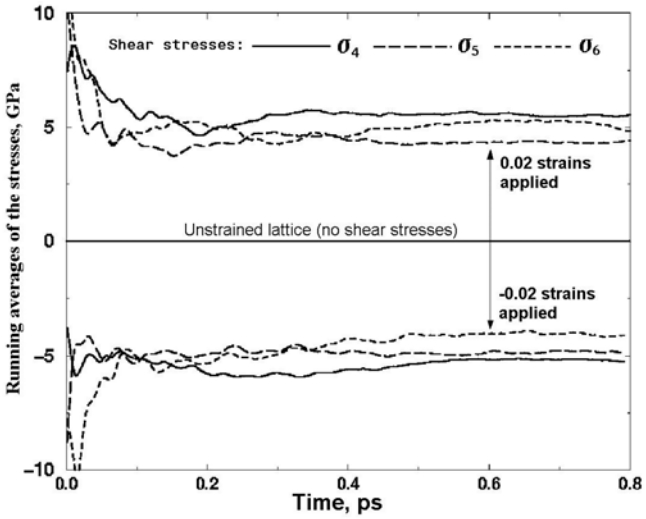

Fig. 10-14. Calculation of the elastic constants from time-averaged stresses and non-linear stress-strain relations. This example shows the calculation of the shear elastic constants (C_{44}, C_{55}, C_{66}) at 88 GPa and 3500 K.

derivatives of the stress tensor $(\partial\sigma_{ij}/\partial T)_V$, needed for this, can be directly calculated in MD simulations. The results of these calculations are shown in Table 10-7. The estimated typical uncertainties are a few percent for the elastic constants, within ~2% for the bulk and shear moduli, within 10% for α and γ, and within 20% for the derivatives (footnote 'b' to Table 10-7). The anomalous elastic constants obtained at 38 GPa and 3500 K (close to the melting curve of *Mg-pv* –see Shen & Lazor, 1995) were excluded from the analysis presented below. Note that the pressures of 38 GPa and 88 GPa in our calculations correspond to the depths of ~1,000 km and ~2,000 km, respectively.

10.7. Interpretation of seismic tomography.

One of the unresolved problems of geophysics was that $R_T = (\frac{\partial \ln V_S}{\partial \ln V_P})_T \approx 0.7$ as determined from PREM (see Anderson, 1989) is much smaller than an analogous parameter $R_p = (\frac{\partial \ln V_S}{\partial \ln V_P})_p$ determined from seismic tomography, which was found to increase from 1.7 to 2.6 between the depths of 1,000 km and 2,000 km (Robertson & Woodhouse, 1996). The striking difference between R_T and R_p has been a puzzle for geophysicists over last 15 years; Anderson (1989) suggested that it could be entirely due to intrinsic anharmonicity, to simulate which one needs to go beyond the quasiharmonic approximation and use methods such as MD or Monte Carlo. This was one of our motivations to use *ab initio* MD simulations.

Table 10-7. Elastic properties of $MgSiO_3$ perovskite at high pressures and temperatures[a,b]

Property	38 GPa, 1500 K	38 GPa, 2500 K	38 GPa, 3500 K	88 GPa, 1500 K	88 GPa, 3500 K
V, Å^3	147.63	150.83	154.08	132.55	136.48
a, Å	4.628	4.675	4.723	4.435	4.499
b, Å	4.792	4.814	4.836	4.655	4.674
c, Å	6.658	6.703	6.747	6.420	6.492
σ_1, GPa	37.9	38.0	37.0	88.1	87.8
σ_2	38.0	37.6	39.0	87.7	87.9
σ_3	37.9	37.3	38.0	88.4	88.5
p, GPa	37.9	37.6	38.0	88.1	88.1
$C_{11}^{T/S}$, GPa	601 /616	553 /579	525 /564	813 /826	749 /783
$C_{22}^{T/S}$	697 /711	629 /654	545 /578	978 /991	847 /878
$C_{33}^{T/S}$	649 /663	591 /615	545 /580	933 /945	821 /850
$C_{12}^{T/S}$	266 / 280	233 /258	222 /258	464 /477	398 /431
$C_{13}^{T/S}$	235 /249	218 /243	218 /256	348 /362	324 /356
$C_{23}^{T/S}$	251 /264	240 /265	251 /286	383 /396	364 /395
C_{44}	262	232	202	336	270
C_{55}	219	210	180	266	234
C_{66}	199	178	147	264	195
$K^{T/S}$, GPa	382.7 /396.8	349.9 /375.8	332.7 /369.5	565.7 /579.4	508.6 /542.5
G	214.3	194.9	166.2	269.7	226.9
γ	1.30	1.37	1.40	1.21	1.26
α, 10^{-5} K^{-1}	1.91	2.15	2.26	1.34	1.51

a - $\sigma_{1,2,3}$, are stress tensor components, showing that non-hydrostatic deviations from the average pressure p are very small; C_{ij} are elastic constants (T- isothermal and S- adiabatic); K and G are the Voigt-Reuss-Hill bulk and shear moduli.

b - Important derivatives: $(\partial \ln V_S/\partial T)_p$=-3.67*10^{-5} K^{-1} (38 GPa), -3.78*10^{-5} K^{-1} (88 GPa). $(\partial \ln V_P/\partial T)_p$=-2.49*10^{-5} K^{-1} (38 GPa), -1.98*10^{-5} K^{-1} (88 GPa). $(\partial \ln V_\Phi/\partial T)_p$=-1.65*10^{-5} K^{-1} (38 GPa), -0.92*10^{-5} K^{-1} (88 GPa). $(\partial \ln V_S/\partial \ln V_P)_T$=0.61 (1500 K), 0.81 (3500 K). $(\partial \ln V_S/\partial \ln V_P)_p$=1.48 (38 GPa), 1.91 (88 GPa). All errors are within 20%.

We calculate R_T=0.61-0.81 (our static simulations give 0.59-0.74) in agreement with geophysical observations. The R_p, calculated using *ab initio* MD, increases from 1.5 at the depth of 1,000 km to 1.9 at 2,000 km. These values, obtained with the full account of the anharmonic effects, are still below the geophysically measured values. Karki *et al.* (1999), using the quasiharmonic approximation, found R_p of MgO to be 1.4-1.9 in the lower mantle. The remaining deficit of R_p can be explained by significant anelasticity (Karato, 1993) throughout the lower mantle, as well as significant compositional heterogeneity (e.g., Masters et al., 2000) below 2000-2500 km.

Seismic tomography maps can be used to determine lateral temperature variations δT underlying the mantle convection (e.g., the temperature contrasts between the hot and cold mantle streams):

$$\delta T = \frac{\delta V}{V} / (\partial \ln V / \partial T)_p \quad ; \qquad (10.7.1)$$

$(\partial \ln V/\partial T)_p$ are given in Table 10-7 for different seismic velocities. To avoid the poorly known attenuation effects and minimise even poorer known compositional effects, it is better to use bulk sound velocity (V_Φ) maps.

Using seismic tomography maps of Masters et al. (2000) (with maximum velocity contrast $\frac{\Delta V_\phi}{V_\phi}$ = 1.4% at 1225 km and 2195 km), one gets (Oganov et al., 2001b) the maximum temperature contrast between the hot and cold streams increasing from 900 K to 1500 K between 1000 and 2000 km. Linear extrapolation gives ~700 K at the top and 2100 K at the bottom of the lower mantle. The root-mean square temperature variations are ~150-250 K across the lower mantle. These contrasts turned out to be large; much smaller than those of Yuen et al. (1993), but larger than those of Forte and Mitrovica (2001) or Castle et al. (2000). These values will play an important role in the future models of the Earth's mantle and its dynamics and can be used as important constraints in numerical models of the mantle convection.

If we use shear velocity maps, much smaller temperature contrasts are obtained for the 2,000 km depth and below. From the V_S maps of Masters et al. (2000) (maximum $\frac{\Delta V_s}{V_s}$ = 3.6% at 1225 km and 2195 km) we get ~1000 K throughout. Systematically lower temperature contrasts result from shear velocity maps at 2000 km depth and below. This systematic difference could be due to the hot masses, rising from the core-mantle boundary, being depleted in Fe due to a reaction (Knittle & Jeanloz, 1991) between the core and mantle, driving Fe from the silicate mantle into the metallic core. This hypothesis, supported by an independent study of Forte and Mitrovica (2001), implies that the core is still growing (although, most probably, very slowly). Minor differences in the Fe content have only a reduced effect on the bulk velocity, but are important for the shear velocities: hot Fe-depleted and cold Fe-enriched materials can have the same shear wave velocities. Lateral variations in the Fe content can explain the anticorrelation between the shear and bulk velocities observed (e.g., Masters et al., 2000) near the core-mantle boundary. However, this does not explain why the anomalies on the bulk velocity maps undergo a reversal near the core-mantle boundary (i.e. low-velocity zones at the core-mantle boundary underlay high-velocity zones of the rest of the lower mantle): such a reversal would

be more expected for the shear velocities (for which it does not happen). This puzzle still remains to be solved; whatever is the answer, it is important that the temperature contrasts obtained from the bulk velocities must be the most reliable, at least outside the anomalous core-mantle boundary region.

Our temperature contrasts are ~2-4 times smaller than estimates of Yuen et al. (1993), which were obtained using extremely uncertain extrapolations of temperature derivatives of shear wave velocities and would suggest partial melting of the lower mantle. Present results can support partial melting only near the core-mantle boundary. This is clarified in Fig. 10-15.

For the core side of the core-mantle boundary experiments of Boehler (1996) suggest T~4000 K. In good agreement with this, *ab initio* simulations (D. Alfé, personal communication) give 4100-4400 K. This gives the highest temperature in the mantle. From this and from our temperature contrasts we see that the minimum temperature of the mantle near the core-mantle boundary is 2000-2200. Using the starting temperature T(670 km) = 1873 K, core-mantle boundary temperature (4000-4400 K), our mantle adiabat and temperature contrasts, one can obtain a very interesting general picture (Fig. 10-15). Comparing this picture with experimental solidus of pyrolite determined by Zerr et al. (1998), we expect some degree of partial melting, restricted only to the lowermost ~300 km of the lower mantle. This would have important implications for the anomalous properties of the core-mantle D'' layer. The melt present in the D'' should give rise to high electrical conductivity of this layer, due to the diffusion of all ionic species in the melt. Fig. 10-15 suggests that the cold streams seem to be adiabatic throughout the lower mantle, while the hot streams are strongly superadiabatic. Below 2000 km we observe a strong asymmetry of temperatures relative to the adiabatic geotherm. The simplest way to explain this is to postulate that the average mantle temperatures are superadiabatic below 2000 km, due to the influence of the thermal boundary at 2890 km. Seismic tomography maps (Masters et al., 2000) give hot and cold anomalies as roughly equal, giving some support to this idea (in this case the superadiabatic geotherm would be ~500 K above the adiabat near the core-mantle boundary).

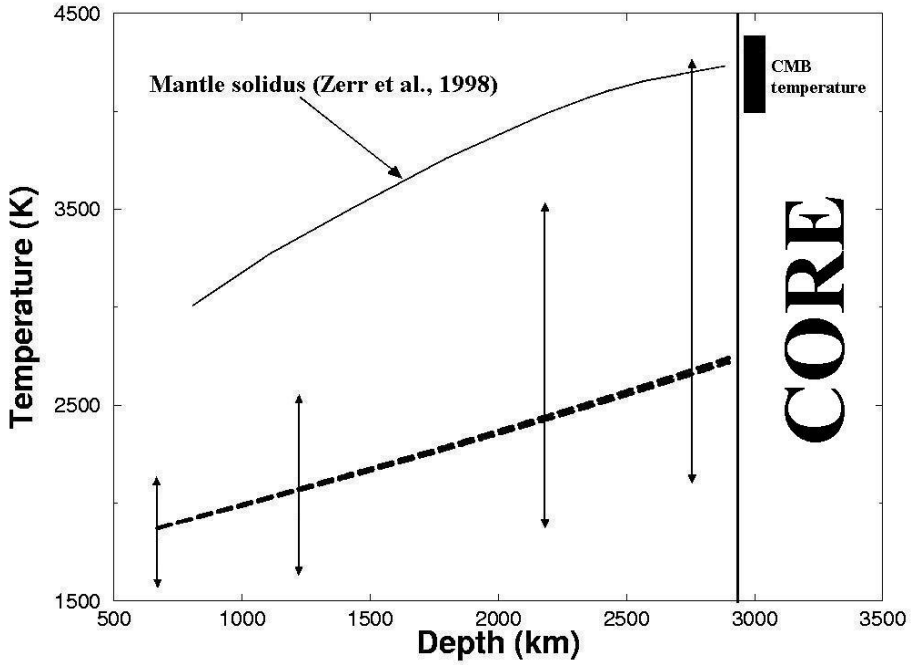

Fig. 10-15. Schematic temperature distribution in the lower mantle. Two-headed arrows indicate the maximum temperature contrasts (the lower arrow gives the lowest possible temperature at a given depth; the upper arrow gives the maximum temperature). Thick dashed curve – lower mantle adiabatic geotherm from Fig. 10-13 (depicted as two almost coinciding adiabats).

Kesson et al. (1998) estimated that lithospheric slabs should be at least ~650 K colder than surrounding mantle if they are to sink to the core-mantle boundary and at least 250 K colder to reach the depth of 1,100 km. Our maximum cold temperature anomalies suggest that most slabs should be able to reach the core-mantle boundary, but some might stop at an intermediate depth. Neutrally buoyant slabs will be dissolved by the convecting mantle; some tomographic maps show most slabs disappearing in the middle of the lower mantle (Kennett et al., 1998), while others (Masters et al., 2000) show that most slabs do reach the core-mantle boundary.

The next important step is to estimate the extent of chemical heterogeneity and anelasticity in the lower mantle and construct a 3D- mineralogical model of the Earth's mantle. With improved seismic tomography models and mineral physics data this problem can be solved in foreseeable future. I believe that computational mineral physics will play an important role in solving this and many other geologically important and exciting problems.

Chapter 11. Conclusions.

In this thesis I have presented some of the fundamentals of modern computer simulations of materials and a number of their applications to minerals. A few new equations have been derived and a new classification of phase transitions developed. Simulation methods used in this study ranged from semiclassical to quantum-mechanical and from static to lattice-dynamical and molecular dynamics. With these methods, it was possible to solve a few long-standing problems that could not be resolved experimentally. A series of unusual metastable phase transitions have been predicted for the Al_2SiO_5 polymorphs. These simulations clarified the nature of fivefold-coordinated states of Si in high-density silicates. Such issues have been addressed as high-pressure stability of the Al_2SiO_5 polymorphs, nature of anomalous antiordering in albite ($NaAlSi_3O_8$), equation of state of $MgSiO_3$ perovskite, its thermal expansion, stability and elasticity at high temperatures and pressures of the Earth's mantle, and the temperature distribution in the mantle. As clear from this list and from the list of the methods, such studies span a unique range of scales – from the subatomic scale (in quantum-mechanical simulations) and the scale of atoms and their interactions, to the scale of macroscopic crystals and their properties and, finally, to the scale of large parts of the Earth and planetary chemistry and dynamics.

The results presented in this thesis have significantly extended our understanding of the Earth and especially its mantle. However, a large number of problems still remain open, and here I mention a few. E.g., there is no commonly accepted compositional model of the lower mantle. There is no common explanation for the mid-mantle discontinuities, e.g. those at 900 km and 1200 km. Practically nothing certain is known about the core-mantle boundary region and the processes of equilibration between the core and mantle that are going on there. It is of particular importance to know whether or not large amounts of Si and K are stored in the Earth's core. The effects of Fe on mantle minerals and the spin state of Fe in these minerals are also among the important problems, but present-day computational methods cannot give a reliable description of the electronic structure of transition metal oxides and silicates. New computational methods are needed for such complicated problems.

References

Adams D.M., Hatton P.D., Heath A.E., Russell D.R. (1988). X-ray diffraction measurements on potassium nitrate under high pressure using synchrotron radiation. *J. Phys.* **C21**, 505-515.

Agoshkov V.M. (1985). Calculation of thermodynamic properties of minerals based on a model of the vibrational spectrum for silicates and oxides. *Geokhimiya*, No. 10, 1441-1454. (in Russian).

Agoshkov V.M., Kieffer S.W., McMillan P.F. (1994). Lattice dynamics and thermodynamic properties of minerals. In: *Advanced mineralogy*, v. 1, 419-430. Marfunin A.S. (editor), Springer-Verlag: Berlin.

Ahmed-Zaid I. & Madon M. (1991). A high-pressure form of Al_2SiO_5 as a possible host of aluminium in the lower mantle. *Nature* **353**, 426-428.

Ahmed-Zaid I. & Madon M. (1995). Electron microscopy of high-pressure phases synthesized from natural garnets in a diamond anvil cell : Implications for the mineralogy of the lower mantle. *Earth Planet. Sci. Lett.* **129**, 233-247.

Akaogi M. & Ito E. (1993). Heat capacity of $MgSiO_3$ perovskite. *Geophys. Res. Lett.* **20**, 105-108.

Akaogi M., Yusa H., Shiraishi K. & Suzuki T. (1995). Thermodynamic properties of alpha-quartz, coesite, and stishovite and equilibrium phase-relations at high pressures and high temperatures. *J. Geophys. Res.* **100**, 22337-22347.

Alan D.R. & Nelmes R.J. (1996). The structural pressure dependence of potassium titanyl phosphate (KTP). to 8 GPa. *J. Phys.: Condens. Matter* **8**, 2337-2363.

Alavi A., Lozovoi A., & Finnis M.W. (1999). Pressure-induced isostructural phase transition in Al-rich NiAl alloys. *Phys Rev. Lett.* **83**, 979-982.

Alberti, A., Sacerdoti, M., Quartieri, S., & Vezzalini, G. (1999). Heating-induced phase transformation in zeolite brewsterite: new 4- and 5-coordinated (Si,Al) sites. *Phys. Chem. Minerals* **26**, 181-186.

Alexandrov K.S. & Prodaivoda G.T. (1993). Elastic properties of minerals. *Crystallografiya* **38**, 214-234. (in Russian).

Alfé D., Gillan M.J., & Price G.D. (1999). The melting curve of iron at the pressures of the Earth's core from ab initio calculations. *Nature* **401**, 462-464.

Alfé D., Gillan M.J., & Price G.D. (2000). Constraints on the composition of the Earth's core from ab initio calculations. *Nature* **405**, 172-175.

Allègre C.J., Manhes G., & Göpel C. (1995a). The age of the Earth. *Geochim. Cosmochim. Acta* **59**, 1445-1456.

Allègre C.J., Poirier J.-P., Humler E., & Hofmann A.W. (1995b). The chemical composition of the Earth. *Earth Planet. Sci. Lett.* **134**, 515-526.

Allen L.C. (1989). Electronegativity is the average one-electron energy of the valence-shell electrons in ground-state free atoms. *J. Am. Chem. Soc.* **111**, 9003-9014.

Allen M.P. & Tildesley D.J. (1987). *Computer Simulation of Liquids.* Clarendon Press: Oxford, 385 pp.

Ancilotto F., Chiarotti G.L., Scandolo S., & Tosatti E. (1997). Dissociation of methane into hydrocarbons at extreme (planetary) pressure and temperature. *Science* **275**, 1288-1290.

Anders E. & Ebihara M. (1982). Solar system abundances of the elements. *Geochim. Cosmochim. Acta* **46**, 2363-2380.

Anderson D.L. (1989). *Theory of the Earth*. Blackwell Scientific Publications: Boston, 366 pp.

Anderson O.L. (1982). The Earth's core and the phase diagram of iron. *Phil. Trans. R. Soc. Lond.* **A306**, 21-35.

Anderson O.L. (1995). *Equations of state of solids for geophysics and ceramic science.* Oxford University Press: Oxford, 424 pp.

Anderson O.L. (1998). Thermoelastic properties of $MgSiO_3$ perovskite using the Debye approach. *Am. Mineral.* **83**, 23-35.

Anderson O.L., Masuda K., & Guo D.W. (1995). Pure silicate perovskite and the PREM lower mantle model: A thermodynamic analysis. *Phys. Earth Planet. Inter.* **89**, 35-49.

Angel R.J. & Ross N.L. (1996). Compression mechanisms and equations of state. *Phil. T. Roy. Soc.* **A354**, 1449-1459.

Angel R.J. (1996). New phenomena in minerals at high pressures. *Phase Transitions* **59**, 105-119.

Angel R.J. (2000). High-pressure structural phase transitions. *Reviews in Mineralogy and Geochemistry* **39** ('Transformation Processes in Minerals'), 85-104.

Angel R.J. (2001). High-pressure powder diffraction. *On-line document* (manual to EOSFIT program): http: www.ccp14.ac.uk/ccp/web-mirrors/ross-angel/ departments/ crystal/ EOSFIT/manual.pdf

Angel R.J., Allan D.R., Milletich R., & Finger L.W. (1997). The use of quartz as an internal pressure standard in high-pressure crystallography. *J. Appl. Cryst.* **30**, 461-466.

Angel R.J., Price G.D., & Yeomans J. (1985). The energetics of polytypic structures – further applications of the ANNNI model. *Acta Cryst.* **B41**, 310-319.

Angel R.J., Ross N.L., Seifert F., & Fliervoet T.F. (1996). Structural characterization of pentacoordinate silicon in a calcium silicate. *Nature* **384**, 441-444.

Apra E., Stefanovich E., Dovesi R., & Roetti C. (1991). An ab initio Hartree-Fock study of silver chloride. *Chem. Phys. Lett.* **186**, 329-335.

Arlt T. & Angel R.J. (2000). Displacive phase transitions in C-centred clinopyroxenes: spodumene, $LiScSi_2O_6$ and $ZnSiO_3$. *Phys. Chem. Minerals* **27**, 719-731.

Arlt T., Angel R.J., Miletch R., Armbruster T., & Peters T. (1998). High-pressure $P2_1/c$-$C2/c$ phase transitions in clinopyroxenes: influence of cation size and electronic structure. *Am. Mineral.* **83**, 1176-1181.

Ashcroft N.W., Mermin N.D. (1976). *Solid State Physics*. Holt, Rinehart & Winston: N.Y.

Bader (1990). *Atoms in Molecules. A Quantum Theory.* Oxford University Press: Oxford, 438 pp.

Badro J., Barrat J.-L., & Gillet P. (1996). Numerical simulation of α-quartz under nonhydrostatic compression: memory glass and five-coordinated crystalline phases. *Phys. Rev. Lett.* **76**, 772-775.

Badro J., Struzhkin V.V., Shu J., Hemley R.J., Mao H.-k., Kao C.-c., Rueff J.-P., Shen G. (1999). Magnetism in FeO at megabar pressures from X-ray emission spectroscopy. *Phys. Rev. Lett.* **83**, 4101-4104.

Badro J., Teter D.M., Downs R.T., Gillet P., Hemley R., & Barrat J.-L. (1997). Theoretical study of a five-coordinated silica polymorph. *Phys. Rev. B* **56**, 5797-5806.

Baekelandt B.G., Mortier W.J., Lievens J.L., & Schooheydt R.A. (1991). Probing the reactivity of different sites within a molecule or solid by direct comparison of molecular sensitivities via an extension of the electronegativity equalization method. *J. Am. Chem. Soc.* **113**, 6730-6734.

Baerends E.J., Gritsenko O.V. (1997). A quantum chemical view of density functional theory. *J. Phys. Chem.* **A101**, 5383-5403.

Baroni S., de Gironcoli S., Dal Corso A., Gianozzi P. (2001). Phonons and related crystal properties from density-functional perturbation theory. *Rev. Mod. Phys.* **73**, 515-562.

Baroni S., Gianozzi P., & Testa A. (1987). Green-function approach to linear response in solids. *Phys. Rev. Lett.* **58**, 1861-1864.

Barron T.H.K. & Klein M.L. (1965). Second-order elastic constants of a solid under stress. *Proc. Phys. Soc.* **85**, 523-532.

Becke A.D. (1993). Density-functional thermochemistry. 3. The role of exact exchange. *J. Chem. Phys.* **98**, 5648-5652.

Becke A.D. (2000). Simulation of delocalised exchange by local density functionals. *J. Chem. Phys.* **112**, 4020-4026.

Belikov B.P., Aleksandrov K.S., & Ryzhova T.V. (1970). *Elastic Constants of Rock-Forming Minerals.* Nauka: Moscow, 276 pp. (in Russian).

Belonoshko A.B. (2001). Molecular dynamics simulation of phase transitions and melting in $MgSiO_3$ with the perovskite structure – Comment. *Am. Mineral.* **86**, 193-194.

Belov N.V. (1947). Structure of ionic crystals and metallic phases. Soviet Academy of Sciences Press: Moscow, 237 pp. (in Russian).

Bina C.R., Navrotsky A. (2000). Possible presence of high-pressure ice in cold subducting slabs. *Nature* **408**, 844-847.

Binggeli N., Keskar N.R., & Chelikowsky J.R. (1994). Pressure-induced amorphisation, elastic instability, and soft modes in α-quartz. *Phys. Rev.* **B49**, 3075-3081.

Birle J.D. & Ehlers E.G. (1969). High-pressure phase of Al_2GeO_5. *J. Am. Ceram. Soc*. **52**, 287-288.

Birman J.L. (1966). Simplified theory of symmetry change in second-order phase transitions: application to V_3Si. *Phys. Rev. Lett.* **17**, 1216-1219.

Blöchl P.E. (1994). Projector augmented-wave method. *Phys. Rev.* **B50**, 17953-17979.

Boehler R. (1996). Melting temperatures of the Earth's mantle and core: Earth's thermal structure. *Annu. Rev. Earth Planet. Sci.* **24**, 15-40.

Born M. & Huang K. (1954). *Dynamical Theory of Crystal Lattices.* Oxford University Press: Oxford, 420 pp.

Bowley R. & Sánchez M. (1999). *Introductory Statistical Mechanics*. Second Edition. Oxford University Press, 352 pp.

Brodholt J.P. (2000). Pressure-induced changes in the compression mechanism of aluminous perovskite in the Earth's mantle. *Nature* **407**, 620-622.

Brown I.D. (1992). Chemical and steric constraints in inorganic solids. Acta Cryst. **B48**, 553-572.

Brown J.M. & Shankland T.J. (1981). Thermodynamic properties in the Earth as determined from seismic profiles. *Geophys. J. R. Astr. Soc.* **66**, 579-596.

Brown, I.D. & Altermatt, D. (1985). Bond-valence parameters obtained from a systematic analysis of the inorganic crystal structure database. *Acta Cryst.* **B41**, 244-247.

Bruce A.D. & Cowley R.A. (1981). *Structural Phase Transitions.* Francis and Taylor: London, 1981, 326 pp.

Buda F., Car R., & Parrinello M. (1990). Thermal expansion of c-Si via ab initio molecular dynamics. *Phys. Rev.* **B41**, 1680-1683.

Buerger M.J. (1961). Polymorphism and phase transformations. *Fortschr. Miner.* **39**, 9-24.

Bukowinski M.S.T. (1994). Quantum geophysics. *Ann. Rev. Earth Planet. Sci.* **22**, 167-205.

Burdett J.K. & McLarnan T.J. (1984). An orbital interpretation of Pauling's rules. *Am. Mineral.* **69**, 601-621.

Burdett J.K. (1988). Perspectives in structural chemistry. *Chem. Rev.* **88**, 3-30.

Burdett J.K. (1995). *Chemical Bonding in Solids.* Oxford University Press: N.Y., 319 pp.

Burnham C.W. (1990). The ionic model: perceptions and realities in mineralogy. *Am. Mineral.* **75**, 443-463.

Bush T.S., Catlow C.R.A., & Battle P.D. (1995). Evolutionary programming techniques for predicting inorganic crystal structures. *J. Mater. Chem.* **5**, 1269-1272.

Bush T.S., Gale JD, Catlow C.R.A., & Battle P.D. (1994). Self-consistent interatomic potentials for the simulation of binary and ternary oxides. *J. Mater. Chem.* **4**, 831-837.

Car R. & Parrinello M. (1985). Unified approach for molecular dynamics and density-functional theory. *Phys. Rev. Lett.* **55**, 2471-2474.

Carlson S., Xu Y.Q., Halenius U., & Norrestam R. (1998). A reversble, isosymmetric, high-pressure phase transition in Na_3MnF_6. *Inorg. Chem.* **37**, 1486-1492.

Carpenter M.A. & Salje E.K.H. (1998). Elastic anomalies in minerals due to structural phase transitions. *Eur. J. Mineral.* **10**, 693-812.

Carpenter M.A. & Salje E.K.H. (2000). Strain and easticity at sructural phase transitions in minerals. *In: Reviews in Mineralogy and Geochemistry* **39** ('Transformation Processes in Minerals'), 35-64.

Carpenter M.A., Salje E.K.H., & Graeme-Barber A. (1998). Spontaneous strain as a determinant of thermodynamic properties for phase transitions in minerals. *Eur. J. Mineral.* **10**, 621-691.

Castle J.C., Creager K.C., Winchester J.P., & van der Hilst R.D. (2000). Shear wave speeds at the base of the mantle. *J. Geophys. Res.* **105**, 21543-21557.

Catlow C.R.A. & Mackrodt W.C. (editors). (1982). *Computer simulation of solids.* Lecture Notes in Physics **166**, Berlin, Springer-Verlag, 320 pp.

Catlow C.R.A. & Price G.D. (1990). Computer modelling of solid-state inorganic materials. *Nature* **347**, 243-248.

Catlow C.R.A. (1977). Point defect and electronic properties of uranium dioxide. *Proc. Roy. Soc. Lond.* **A353**, 533-561.

Catlow C.R.A., Bell R.G., & Gale J.D. (1994). Computer modelling as a technique in materials chemistry. *J. Mater. Chem.* **4**, 781-792.

Catlow C.R.A., Thomas J.M., Freeman C.M., Wright P.A. & Bell R.G. (1993). Simulating and predicting crystal structures. Proc. Roy. Soc. Lond. **A442**, 85-96.

Catti M. (1986). Theoretical computation of physical properties of mantle minerals. In: *Advances in Physical Geochemistry. v.6: Geochemistry and physics of terrestrial planets*, 224-250. Ed. S.Saxena, Springer Verlag: N.Y.

Catti M. (1989). Crystal elasticity and inner strain – a computational model. *Acta Cryst.* **A45**, 20-25.

Catti M. (2001). Orthorhombic intermediate state in the zinc blende to rocksalt transformation path of SiC at high pressure. *Phys. Rev. Lett.* **87**, paper 035504.

Catti M., Pavese A., Dovesi R., Roetti C., & Causa M. (1991). Quantum-mechanical Hartree-Fock self-consistent field study of the elastic constants and chemical bonding of MgF_2 (sellaite). *Phys. Rev.* **B44**, 3509-3517.

Catti M., Valerio G., Dovesi R., & Causa M. (1994). Quantum-mechanical calculation of solid-state equilibrium $MgO + Al_2O_3 = MgAl_2O_4$ (spinel) versus pressure. *Phys. Rev.* **B49**, 14179-14187.

Cavazzoni C., Chiarotti G.L., Scandolo S., Tosatti E., Bernasconi M., & Parrinello M. (1999). Superionic and metallic states of water and ammonia at giant planet conditions. *Science* **283**, 44-46.

Ceperley D.M. & Alder B.J. (1980). Ground state of the electron gas by a stochastic method. *Phys. Rev. Lett.* **45**, 566-569.

Chandler D. (1987). *Introduction to Modern Statistical Mechanics.* Oxford University Press: N.Y., 274 pp.

Chaplot S.L. & Sikka S.K. (1993). Molecular-dynamics simulation of pressure-induced crystalline-to-amorphous transition in some corner-linked polyhedral compounds. *Phys. Rev.* **B47**, 5710-5714.

Chaplot S.L. & Choudhury N. (2001). Reply to comment on 'Molecular dynamics simulation of phase transitions and melting in $MgSiO_3$ with the perovskite structure'. *Am. Mineral.* **86**, 195-196.

Chaplot S.L., Choudhury N., & Rao K.R. (1998). Molecular dynamics simulation of phase transitions and melting in $MgSiO_3$ with the perovskite structure. *Am. Mineral.* **83**, 937-941.

Chaplot, S.L. & Choudhury, N. (2000). Phase transitions of enstatite $MgSiO_3$: a molecular dynamics study. *Solid State Comm.* **116**, 599-603.

Cheung P.S.Y. (1977). On the calculation of specific heats, thermal pressure coefficients and compressibilities in molecular dynamics simulations. *Mol. Phys.* **33**, 519-526.

Chizmeshya A.V.G., Wolf G.H., McMillan P.F. (1996). First-principles calculation of the equation-of-state, stability, and polar optic modes of $CaSiO_3$ perovskite. *Geophys. Res. Lett.* **23**, 2725-2728. (correction in: *Geophys. Res. Lett.* (1998) **25**, 711).

Choudhury N., Chaplot S.L., Rao K.R., & Ghose S. (1988). Lattice dynamics of $MgSiO_3$ perovskite. *Pramana Journal of Physics* **30**, 423-428.

Christy A.G. (1993). Multistage diffusionless pathways for reconstructive phase transitions: application to binary compounds and calcium carbonate. *Acta Cryst.* **B49**, 987-996.

Christy A.G. (1995). Isosymmetric Structural Phase Transitions: Phenomenology and Examples. *Acta Cryst.* **B51**, 753-757.

Chudinovskikh L. & Boehler R. (2001). High-pressure polymorphs of olivine and the 660-km seismic discontinuity. *Nature* **411**, 574-577.

Cohen R.E. (1987). Calculation of elasticity and high pressure instabilities in corundum and stishovite with potential induced breathing model. *Geophys. Res. Lett.* **14**, 37-40.

Cohen R.E. (1991). Bonding and elasticity of stishovite SiO_2 at high pressure: Linearized augmented plane wave calculations. *Am. Mineral.* **76**, 733-742.

Cohen R.E. (1994). Theory of crystalline SiO_2. In: *Reviews in mineralogy* **29** (‘Silica’), 369-402.

Cohen R.E. (1999). Bonding and electronic structure of minerals. In: *Miscroscopic Properties and Processes in Minerals*, NATO Science Series, v. C543. K. Wright and R. Catlow (eds.), Kluwer: Dordrecht, pp. 201-264.

Cohen R.E., Gulseren O. & Hemley R.J. (2000). Accuracy of equation-of-state formulations. *Am. Mineral.* **85**, 338-344.

Cohen R.E., Mazin I.I., Isaak D.G. (1997). Magnetic collapse in transition metal oxides at high pressure: implications for the Earth. *Science* **275**, 654-657.

Comodi P., Zanazzi P.F., Poli S., & Schmidt M. (1997). High-pressure behavior of kyanite: Compressibility and structural deformations. *Am. Mineral.* **82**, 452-459.

Coppens P. (1992). Electron density from X-ray diffraction. *Annu. Rev. Phys. Chem.* **43**, 663-692.

Coppens P. (1997). *X-ray Charge Densities and Chemical Bonding.* International Union of Crystallography Texts, **4**. Oxford University Press: Oxford, 358 pp.

Cowley R.A. (1976). Acoustic phonon instabilities and structural phase transitions. *Phys. Rev.* **B13**, 4877-4885.

d’Amour H., Schiferl D., Denner W., Schulz H., & Holzapfel W.B. (1978). High-pressure single-crystal structure determinations for ruby up to 90 kbar using an automatic diffractometer. *J. Appl. Phys.* **49**, 4411-4416.

D'Arco Ph., Causa M., Roetti C., & Silvi B. (1993a). Periodic Hartree-Fock study of a weakly bonded layer structure: brucite $Mg(OH)_2$. *Phys. Rev.* **B47**, 3522-3529.

D'Arco Ph., Freyria-Fava F., Dovesi R., & Saunders V.R. (1996). Structural and electronic properties of pyrope garnet ($Mg_3Al_2Si_3O_{12}$): an ab initio study. *J. Phys.: Condens. Matter* **8**, 8815-8828.

D'Arco Ph., Sandrone G., Dovesi R., Apra E., Saunders V.R. (1994). A quantum-mechanical study of the relative stability under pressure of $MgSiO_3$-ilmenite, $MgSiO_3$-perovskite, and MgO-periclase + SiO_2-stishovite assemblage. *Phys. Chem. Minerals* **21**, 285-293.

D'Arco Ph., Sandrone G., Dovesi R., Orlando R., & Saunders V.R. (1993b). A quantum mechanical study of the perovskite structure type of $MgSiO_3$. *Phys. Chem. Minerals* **20**, 407-414.

Dam B., Janner A., Donnay J.D.H. (1985). Incommensurate morphology of calaverite ($AuTe_2$) crystals. *Phys. Rev. Lett.* **55**, 2301-2304.

de Wijs G.A., Kresse G., Vocadlo L., Dobson D., Alfe D., Gillan M.J., Price G.D. (1998). The viscosity of liquid iron at the physical conditions of the Earth's core. *Nature* **392**, 805-807.

Dewaele A., Guyot F. (1998). Thermal parameters of the Earth's lower mantle. *Phys. Earth Planet. Inter.* **107**, 261-267.

Dick B.G. & Overhauser A.W. (1958). Theory of the dielectric constants of alkali halide crystals. *Phys. Rev.* **112**, p.90-113.

Dorogokupets P. I. (2000). Self-consistent thermodynamic functions in equations of state for minerals. *Doklady Earth Sciences* **375A**, 1459-1462.

Dorogokupets P. I. (2001). Equation of state and internally consistent thermodynamic functions of minerals. *Petrology* **9**, 534-544.

Dove M. (2002). *Structure and Dynamics*. Oxford University Press, *in press*.

Dove M.T. (1988). Molecular dynamics simulations in the solid state sciences. In: Salje E.K.H. (ed.), *Physical Properties and Thermodynamic Behaviour of Minerals.* D. Reidel: Dordrecht, NATO ASI, 501-590.

Dove M.T. (1993). *Introduction to Lattice Dynamics.* Cambridge University Press, 1993, 258 pp.

Dove M.T. (1997). Theory of displacive phase transitions in minerals. *Am. Mineral.* **82**, 213-244.

Dovesi R. (1996). Total energy and related properties. In: Quantum-mechanical ab intio calculation of the properties of crystalline materials. Pisani C. (ed.). Lecture Notes in Chemistry, v. 67, p.179-207. Springer-Verlag: Berlin.

Dovesi R., Roetti C., Freyria-Fava C., Apra E., Saunders V. & Harrison N.M. (1992). Ab intio Hartree-Fock treatment of ionic and semi-ionic compounds: state of the art. *Phil. Trans. Roy. Soc. Lond.* **A341**, 203-210.

Dovesi R., Saunders V.R., Roetti C., Causa M., Harrison N.M., Orlando R., & Apra E. (1996). CRYSTAL95 User's Manual. University of Torino: Torino.

Duan W., Wentzcovitch R.M., & Thomson K.T. (1998). First-principles study of high-pressure alumina polymorphs. *Phys. Rev.* **B57**, 10363-10369.

Dubrovinsky L.S., Dubrovinskaya N.A., & Urusov V.S. (1994). The effect of the lone electron pair on symmetry of paratellurite α-TeO_2 from computer simulation. *Doklady Russian Academy of Sciences* **334**, 441-444. (in Russian).

Dubrovinsky L.S., Saxena S.K., & Lazor P. (1998). High-pressure and high-temperature in situ X-ray diffraction study of iron and corundum to 68 GPa using an internally heated diamond anvil cell. *Phys. Chem. Minerals* **25**, 434-441.

Dubrovinsky L.S., Saxena S.K., Rekhi S. (1999). $(Mg,Fe)SiO_3$ –perovskite stability and lower mantle conditions. *Science* **285**, 983a.

Dziewonski A.M. & Anderson D.L. (1981). Preliminary Reference Earth Model. *Phys. Earth Planet. Inter.* **25**, 297-356.

Elliott S. (1998). *The Physics and Chemistry of Solids.* Wiley: Chichester, 770 pp.

Fang Z., Solovyev I.V., Sawada H., Terakura K. (1999). First-principles study on electronic structures and phase stability of MnO and FeO under high pressure. *Phys. Rev. B* **59**, 762-774.

Favot F. & Dal Corso A. (1999). Phonon dispersions: Performance of the generalized gradient approximation. *Phys. Rev.* **B60**,11427-11431.

Fedorov F.I. (1968). *Theory of elastic waves in crystals.* Plenum Press: N.Y., 375 pp.

Fiquet G. (2001). Mineral phases of the Earth's mantle. *Z. Krist.* **216**, 248-271.

Fiquet G., Andrault D., Dewaele A., Charpin T., Kunz M., & Haüsermann D. (1998). P-V-T equation of state of $MgSiO_3$ perovskite. *Phys. Earth Planet. Int.* **105**, 21-31.

Fiquet G., Dewaele A., Andrault D., Kunz M., & Le Bihan T. (2000). Thermoelastic properties and crystal structure of $MgSiO_3$ perovskite at lower mantle pressure and temperature conditions. *Geophys. Res. Lett.* **27**, 21-24.

Forte A.M. & Mitrovica J.X. (2001). Deep-mantle high-viscosity flow and thermochemical structure inferred from seismic and geodynamic data. *Nature* **410**, 1049-1056.

Foulkes W.M.C., Mitas L., Needs R.J., & Rajagopal G. (2001). Quantum Monte Carlo simulations of solids. *Rev. Mod. Phys.* **73**, 33-83.

Francis G.P. & Payne M.C. (1990). Finite basis set corrections to total energy pseudopotential calculations. *J. Phys.: Condens. Matter* **2**, 4395-4404.

Fuchs M., Bockstedte M., Pehlke E., Scheffler M. (1998). Pseudopotential study of binding properties of solids within generalised gradient approximations: The role of core-valence exchange correlation. *Phys. Rev.* **B57**, 2134-2145.

Funamori N., Yagi T., Utsumi W., Kondo T., Uchida T. (1996). Thermoelastic properties of $MgSiO_3$ perovskite determined by in situ X ray observations up to 30 GPa and 2000 K. *J. Geophys. Res.* **101**, 8257-8269.

Funamori N. & Jeanloz R. (1997). High-pressure transformation of Al_2O_3. *Science* **278**, 1109-1111.

Funamori N., Jeanloz R., Nguyen J., Kavner A., Caldwell W.A., Fujino K., Miyajima N., Shinmei T., & Tomioka N. (1998). High-pressure transformations in $MgAl_2O_4$. *J. Geoph. Res.* **103**, 20813-20818.

Gale J.D. (1996). Empirical potential derivation for ionic materials. *Phil. Mag.* **B73**, 3-19.

Gale J.D. (1997). GULP: A computer program for the symmetry-adapted simulation of solids. *J. Chem. Soc. – Farad. Trans.* **93**, 629-637.

Gale J.D. (1998). Analytical free energy minimization of silica polymorphs. *J. Phys. Chem.* **B102**, 5423-5431.

Gale J.D., Catlow C.R.A., & Mackrodt W.C. (1992). Periodic ab-initio determination of interatomic potentials for alumina. *Modell. and Simul. in Mater. Sci. and Engin.* **1**, 73-81.

Gallagher K., Sambridge M., & Drijkoningen G. (1991). Genetic algorithms: an evolution from Monte Carlo methods for strongly non-linear geophysical optimization problems. *Geoph. Res. Lett.* **18**, 2177-2180.

Ganguly P. (1993). Simple interrelationship between crystal radii, pseudopotential radii, and interatomic distances in elements. *J. Am. Chem. Soc.* **115**, 9287-9288.

Garber J.A., Granato A.V. (1975). Theory of the temperature dependence of second-order elastic constants in cubic materials. *Phys. Rev.* **B11**, 3990-3997.

Garland C.W. & Weiner B.B. (1971). Changes in the thermodynamic character of the NH_4Cl order-disorder transition at high pressures. *Phys. Rev.* **B3**, 1634-1637.

Gautron L., Kesson S.E., & Shelley J.M.G. (1997). Mineralogy of Al_2SiO_5 under the (P,T) conditions of the lower mantle. *European Union of Geoscience conference (EUG 9), 23-27 March 1997, Strasbourg (France). Abstracts, 45/1P13.*

Gavezzotti A. (1994). Are crystal structures predictable? *Acc. Chem. Res.* **27**, 309-314.

Ghose S., Choudhury, Chaplot S.L., and Rao K.R. (1992). Phonon density of states and thermodynamic properties of minerals. In: S.K. Saxena (ed.). *Advances in Physical Geochemistry: Thermodynamic data*, p. 283-314. Springer Verlag: New York.

Gillet P., Badro J., Varrel B., & McMillan P.F. (1995). High-pressure behaviour in α-$AlPO_4$: Amorphization and the memory-glass effect. Phys. Rev. **B51**, 11262-11269.

Gillet P., Daniel I., Guyot F., Matas J., & Chervin J.C. (2000). A thermodynamic model for $MgSiO_3$-perovskite derived from pressure, temperature and volume dependence of the Raman mode frequencies. *Phys. Earth Planet. Inter.* **117**, 361-384.

Gillet P., Matas J., Guyot F., & Ricard Y. (1999). Thermodynamic properties of minerals at high pressures and temperatures from vibrational spectroscopic data. In: *Miscroscopic Properties and Processes in Minerals*, NATO Science Series, v. C543. K. Wright and R. Catlow (eds.), Kluwer: Dordrecht, pp. 71-92.

Glasser L. & Catlow C.R.A. (1997). Modelling phase changes in the potassium titanyl phosphate system. *J. Mater. Chem.* **7**, 2537-2542.

Gramsch S.A., Cohen R.E., Savrasov S.Y. (2001). Metal-insulator and magnetic collapse transitions in FeO at high pressures: predictions of LDA+U. *In press.*

Grobety B. H. & Veblen D. (1995). HRTEM-study of stacking-faults and polytypism in kyanite. *Eur. J. Mineral.* **7**, 807-818.

Hahn T. and Wondratschek H. (1994). *Symmetry of crystals. Introduction to International Tables for Crystallography Vol. A.* Heron Press: Sofia, 134 pp.

Haines J., Leger J.M., & Schulte O. (1998). High-pressure isosymmetric phase transition in orthorhombic lead fluoride. *Phys. Rev.* **B57**, 7551-7555.

Hama J. & Suito K. (1996). The search for a universal equation of state correct up to very high pressures. *J. Phys. Condens. Matter* **8**, 67-81.

Hama J., Suito K., & Anderson O.L. (2000). Thermoelasticity of silicate perovskites and magnesiowüstite and its implications for the Earth's lower mantle. *Am. Mineral.* **85**, 321-328.

Harris M.J. & Dove M.T. (1995). Lattice melting at structural phase transitions. *Mod. Physics Lett.* **9**, 67-85.

Harte B., Harris J.W., Hutchison M.T., Watt G.R., Wilding M.C. (1999). Lower mantle mineral associations in diamonds from São Luiz, Brazil. In: *Mantle Petrology: Field Observations and High-Pressure Experimentation: A Tribute to Francis R. (Joe) Boyd.* The Geochemical Soc. special publication No. 6; Fei Y., Bertka C.M., Mysen B.O. (ed.), pp.125-153.

Hatch D.M. & Merrill L. (1981). Landau description of the calcite-$CaCO_3$(II) phase transition. *Phys. Rev.* **B23**, 368-374.

Heine V. & McConnell J.D.C. (1981). Origin of modulated incommensurate phases in insulators. *Phys. Rev. Lett.* **46**, 1092-1095.

Helffrich G. (2000). Topography of the transition zone seismic discontinuities. *Rev. Geophys.* **38**, 141-158.

Hemingway B.S., Robie R.A., Evans H.T.Jr., & Kerrick D.M. (1991). Heat capacities and entropies of sillimanite, fibrolite, andalusite, kyanite, and quartz and the Al_2SiO_5 phase diagram. *Am. Mineral.* **76**, 1597-1613.

Hemley R.J. & Cohen R.E. (1996). Structure and bonding in the deep mantle and core. *Phil. Trans. Roy. Soc. Lond.* **A354**, 1461-1479.

Hemley R.J., Jephcoat A.P., Mao H.K., Ming L.C., & Manghnani M.H. (1988). Pressure-induced amorphization of crystalline silica. *Nature* **334**, 52-54.

Hemmati M., Czizmeshya A., Wolf G.H., Poole P.H., Shao J., & Angell C.A. (1995). Crystalline-amorphous transition in silicate perovskites. *Phys. Rev.* **B51**, 14841-14848.

Hess A. & Saunders V. (1992). Periodic ab initio Hartree-Fock calculations of the low-symmetry mineral kaolinite. *J. Phys. Chem.* **96**, 4367-4374.

Hobbs D., Kresse G., Hafner J. (2000). Fully unconstrained noncollinear magnetism within the PAW method. *Psi-k Newsletter*, No. 41 (October 2000), 135-146.

Hohenberg P. & Kohn W. (1964). Inhomogeneous electron gas. *Phys. Rev.* **136**, B864-B871.

Holland T.J.B. & Carpenter M.A. (1986). Aluminium/silicon disordering and melting in sillimanite at high pressure. *Nature* **320**, 151-153.

Holm J.L., Kleppa O.J., & Westrum E.F. Jr. (1967). Thermodynamics of polymorphic transfiormations in silica. Thermal properties from 5 to 1070 K and pressure-temperature stability fields of coesite and stishovite *Geochim. Cosmochim. Acta* **31**, 2289-2307.

Holzapfel W.B. (1996). Physics of solids under strong compression. *Rep. Prog. Phys.* **59**, 29-90.

Holzwarth N.A.W., Matthews G.E., Dunning R.B., Tackett A.R., Zeng Y. (1997). Comparison of the projector augmented-wave, pseudopotential, and linearized augmented-plane-wave formalisms for density-functional calculations of solids. *Phys. Rev.* **B55**, 2005-2017.

Hoover W. G. (1985). Canonical dynamics: equilibrium phase-space distributions. *Phys. Rev.* **A31**, 1695-1697.

Hostettler M., Birkedal H., Schwarzenbach D. (2001). Polymorphs and structures of mercuric iodide. *Chimia* **55**, 541-545.

Hugh-Jones D.A. & Angel R.J. (1994). A compressional study of MgSiO3 orthoenstatite up to 8.5 GPa. *Am. Mineral.* **79**, 405-410.

Iglesias, M., Schwarz, K., Blaha, P., & Baldomir, D. (2001). Electronic structure and electric field gradient calculations of Al_2SiO_5 polymorphs. *Phys. Chem. Minerals* **28**, 67-75.

Iishi K., Salje E., & Werneke C. (1979). Phonon spectra and rigid-ion model calculations of andalusite. *Phys. Chem. Minerals* **4**,173-188.

International Tables for Crystallography. Vol. A, Space-Group Symmetry. (ed. Hahn Th.). Kluwer Academic Publishers: Dordrecht, 1994.

Irifune T. (1994). Absence of an aluminous phase in the upper part of the Earth's lower mantle. *Nature* **370**, 131-133.

Irifune T., Fujino K., & Ohtani E. (1991). A new high-pressure form of $MgAl_2O_4$. *Nature* **349**, 409-411.

Isaak D.G., Cohen R.E., Mehl M.J., Singh D.J. (1993). Phase stability of wüstite at high pressure from first-principles linearized augmented plane-wave calculations. *Phys. Rev. B* **47**, 7720-7731.

Ito E., Katsura T. (1989). A temperature profile of the mantle transition zone. *Geophys. Res. Lett.* **16**, 425-428.

Jackson I. & Rigden S. (1996). Analysis of P-V-T data: constraints on the thermoelastic properties of high-pressure minerals. *Phys. Earth Planet. Inter.* **96**, 85-112.

Jackson I. (1998). Elasticity, composition and temperature of the Earth's lower mantle: a reappraisal. *Geophys. J. Int.* **134**, 291-311.

Jaeger G. (1998). The Ehrenfest classification of phase transitions: introduction and evolution. *Arch. Hist. Exact Sci.* **53**, 51-81.

James R. (1979). Disorder and non-stoichiometry in rutile and corundum structured metal oxides. *UK Atomic Energy Authority Report, AERE-TP814*.

Janot C. (1994). *Quasicrystals: a Primer.* Oxford University Press: Oxford, 409 pp.

Jansen L. & Lombardi E. (1965). Three-atom and three-ion interactions and crystal stability. *Disc. Far. Soc.*, No. 40, 78-96.

Jones R.O. & Gunnarsson O. (1989). The density functional formalism, its applications and prospects. *Rev. Mod. Phys.* **61**, 689-746.

Kantorovich (1996-2001). User-friendly visualisation program for plane-wave ab initio DFT codes CASTEP/CETEP/VASP. (unpublished). See http://www.cmmp.ucl.ac.uk /~lev/codes/lev00

Kantorovich L.N. (1995). Thermoelastic properties of perfect crystals wth nonprimitive lattices. 1. General theory. *Phys. Rev.* **B51**, 3520-3534.

Karato S-i. (1993). Importance of anelasticity in the interpretation of seismc tomography. *Geophys. Res. Lett.* **20**, 1623-1626.

Karki B.B. (1997). High-pressure structure and elasticity of the major silicate and oxide minerals of the Earth's lower mantle. *PhD Thesis*, University of Edinburgh, 170 pp.

Karki B.B., Stixrude L., Clark S.J., Warren M.C., Ackland G.J., & Crain J. (1997). Elastic properties of orthorhombic $MgSiO_3$ perovskite at lower mantle pressures. *Am. Mineral.* **82**, 635-638.

Karki B.B., Warren M.C., Stixrude L., Ackland G.J., & Crain J. (1997). Ab initio studies of high-pressure structural transformations in silica. *Phys. Rev.* **B55**, 3465-3471.

Karki B.B., Wentzcovitch R.M., de Gironcoli S., & Baroni S. (1999). First-principles determination of elastic anisotropy and wave velocities of MgO at lower mantle conditions. *Science* **286**, 1705-1707.

Karki B.B., Wentzcovitch R.M., de Gironcoli S., & Baroni S. (2000a). High-pressure lattice dynamics and thermoelasticity of MgO. *Phys. Rev.* **B61**, 8793-8800.

Karki B.B., Wentzcovitch R.M., de Gironcoli S., & Baroni S. (2000b). Ab initio lattice dynamics of $MgSiO_3$ perovskite at high pressure. *Phys. Rev.* **B62**, 14750-14756.

Karki B.B., Wentzcovitch R.M., de Gironcoli S., Baroni S. (2001). First principles termoelasticity of $MgSiO_3$-perovskite: consequences for the inferred properties of the lower mantle. *Geophys. Res. Lett.* **28**, 2699-2702.

Katsnelson M.I., Sinko G.V., Smirnov N.A., Trefilov A.V., & Khromov K. Yu. (2000). Structure, elastic moduli, and thermodynamics of sodium and potassium at ultrahigh pressures. *Phys. Rev.* **B61**, 14420-14424.

Kennett B.L.N., Engdahl E.R., Buland R. (1995). Constraints on seismic velocities in the Earth from traveltimes. *Geophys. J. Int.* **122**, 108-124.

Kennett B.L.N., Widiyantoro S., & van der Hilst R.D. (1998). Joint seismic tomography for bulk sound and shear wave speed in the Earth's mantle. *J. Geophys. Res.* **103**, 12469-12493.

Kenny S.D., McConnell J.D.C., & Refson K. (2000). The *ab initio* study of the stability of low temperature Al/Si ordered albite, $NaAlSi_3O_8$. *Am. Mineral.* **84**, 1681-1685.

Kerrick, D.M. (1990). *Reviews in Mineralogy* **22**, ('The Al_2SiO_5 Polymorphs'), 406 pp.

Keskar N.R., Chelikowsky J.R., & Wentzcovitch R.M. (1994). Mechanical instabilities in $AlPO_4$. *Phys. Rev.* **B50**, 9072-9078.

Kesson S.E., Fitz Gerald J.D., & Shelley J.M. (1998). Mineralogy and dynamics of a pyrolite mantle. *Nature* **393**, 252-255.

Kesson S.E., Fitz Gerald J.D., Shelley J.M.G. (1994). Mineral chemistry and density of subducted basaltic crust at lower-mantle pressures. *Nature* **372**, 767-769.

Kieffer S.W. (1979a). Thermodynamics and lattice vibrations of minerals: 1. Mineral heat capacities and their relationship to simple lattice vibrational models. *Rev. Geophys. Space Phys.* **17**, 1-19.

Kieffer S.W. (1979b). Thermodynamics and lattice vibrations of minerals: 2. Vibrational characteristics of silicates. *Rev. Geophys. Space Phys.* **17**, 20-34.

Kieffer S.W. (1979c). Thermodynamics and lattice vibrations of minerals: 3. Lattice dynamics and an approximation for minerals with application to simple substances and framework silicates. *Rev. Geophys. Space Phys.* **17**, 35-59.

Kieffer S.W. (1980). Thermodynamics and lattice vibrations of minerals: 4. Application to chain and sheet silicates and orthosilicates. *Rev. Geophys. Space Phys.* **18**, 862-886.

Kieffer S.W. (1982). Thermodynamics and lattice vibrations of minerals: 5. Application to phase equilibria, isotopic fractionation, and high-pressure thermodynamic properties. *Rev. Geophys. Space Phys.* **20**, 827-849.

Kingma K.J., Cohen R.E., Hemley R.J., & Mao H.-k. (1995). Transformations of stishovite to a denser phase at lower-mantle pressures. *Nature* **374**, 243-245.

Kirfel A. & Eichhorn K. (1990). Accurate structure analysis with synchrotron radiation. The electron density in Al_2O_3 and Cu_2O. *Acta Cryst.* **A46**, 271-284.

Kitaigorodsky A.I. (1971). *Molecular Crystals.* (in Russian). Nauka: Moscow, 424 pp.

Knittle E. & Jeanloz R. (1986). Thermal expansion of silicate perovskite and stratfication of the Earth's mantle. *Nature* **319**, 214-216.

Knittle E. & Jeanloz R. (1987). Synthesis and equation of state of $(Mg,Fe)SiO_3$ perovskite to over 100 gigapascals. *Science* **235**, 668-670.

Knittle E. & Jeanloz R. (1991). Earth's core-mantle boundary: results of experiments at high pressure s and temperatures. *Science* **251**, 1438-1443.

Kohn W. & Sham L.J. (1965). Self-consistent equations including exchange and correlation effects. *Phys. Rev.* **140**, A1133-A1138.

Kohn W. (1999a). Nobel Lecture: Electronic structure of matter – wave functions and density functionals. *Rev. Mod. Phys.* **71**, 1253-1266.

Kohn W. (1999b). An essay on condensed matter physics in the twentieth century. *Rev. Mod. Phys.* **71**, S59-S77.

Kohn W., Meir Y., Makarov D.E. (1998). Van der Waals energies in density functional theory. *Phys. Rev. Lett.* **80**, 4153-4156.

Komada N. & Westrum E.F. (1997). Modeling lattice heat-capacity contributions by a single-parametric phonon dispersion approach. *J. Chem. Thermodynamics* **29**, 311-336.

Kresse G. & Furthmuller J. (1996a). Efficiency of ab initio total-energy caclulations for metals and semiconductors using a plane-wave basis set. *Comp. Mater. Sci.* **6**, 15-50.

Kresse G. & Furthmuller J. (1996b). Efficient iterative schemes for ab initio total-energy calculations using a plane wave basis set. *Phys. Rev.* **B54**, 11169-11186.

Kruger M.B. & Jeanloz R. (1990). Memory glass: an amorphous material formed from $AlPO_4$. *Science* **249**, 647-649.

Kubicki J.D. & Lasaga A.C. (1991). Molecular dynamics of pressure and temperature effects on $MgSiO_3$ and Mg_2SiO_4 melts and glasses. *Phys. Chem. Minerals* **17**, 661-673.

Lacks D.J. & Gordon R.G. (1995). Calculations of pressure-induced phase transitions in mantle minerals. *Phys. Chem. Minerals*, **22**, 145-150.

Landau L.D. & Lifshitz E.M. (1980). *Statistical Physics.* Part I. (Theoretical Physics, v. 5). Third edition. Moscow: Nauka, 584 pp. (in Russian).

Landau L.D. & Lifshitz E.M. (2001a). *Mechanics.* (Theoretical Physics, v. 1). Fourth edition. Moscow: Nauka, 217 pp. (in Russian).

Landau L.D. & Lifshitz E.M. (2001b). *Quantum Mechanics: non-relativistic theory.* (Theoretical Physics, v. 3). Fourth edition. Moscow: Nauka, 803 pp. (in Russian).

Le Stunff Y., Wicks C.W. Jr., Romanowicz B. (1995). P'P' precursors under Africa: evidence for mid-mantle reflectors. *Science* **270**, 74-77.

Lee I-H. & Martin R.M. (1997). Applications of the generalised-gradient approximation to atoms, clusters, and solids. *Phys. Rev.* **B56**, 7197-7205.

Leinenweber K. & Navrotski A. (1988). A transferable interatomic potential for crystalline phases in the system MgO-SiO_2. *Phys. Chem. Minerals* **15**, 588-596.

Lewis G.V. & Catlow C.R.A. (1985). Potential models for ionic oxides. *J. Phys. C.: Solid State Phys.* **18**, 1149-1161.

Lewis G.V. (1985). Interatomic potentials: derivation of parameters for binary oxides and their use in ternary oxides. *Physica*, **B&C 131**, 114-118.

Lichanot A. (2000). Hartree-Fock and density functional calculations of the elastic constants of the alkaline-earth oxides: comparison with experiment. *Solid State Commun.* **116**, 543-546.

Liu L.-G. & Bassett W.A. (1986). *Elements, Oxides, and Silicates. High-Pressure Phases with Implications for the Earth's Interior.* Oxford University Press: N.Y., 250 pp.

Liu L.-G. (1974). Disproportionation of kyanite to corundum plus stishovite at high pressure and temperature. *Earth Planet. Sci. Lett.* **24**, 224-228.

Liu L.-G. (1977). The system enstatite-pyrope at high pressures and temperatures and the mineralogy of the Earth's mantle. *Earth Planet. Sci. Lett.* **41**, 398-404.

Loubeyre P., LeToullec R., Hausermann D., Hanfland M., Hemley R.J., Mao H.K., Finger L.W. (1996). X-ray diffraction and equation of state of hydrogen at megabar pressures. *Nature* **383**, 702-704.

Louie S.G., Froyen S., & Cohen M.L. (1982). Nonlinear ionic pseudopotentials in spin-density functional calculations. *Phys. Rev.* **B26**, 1738-1742.

Lufaso M.W., Woodward P.M. (2001). Prediction of the crystal structures of perovskites using the software program *SPuDS*. *Acta Cryst.* **B57**, 725-738.

Mackrodt W.C. (1982). Defect calculations for ionic materials. In: *Computer simulation of solids*. Lecture Notes in Physics 166, Berlin, Springer-Verlag, 1982, 175-194.

Mackrodt W.C. (1988). Atomistic simulation of oxide surfaces. *Phys. Chem. Minerals* **15**, 228-237.

Madon M., Castex J., & Peyronneau J. (1989). A new aluminocalcic high-pressure phase as a possible host of calcium and aluminium in the lower mantle. *Nature* **342**, 422-424.

Mao H.K., Hemley R.J., Fei Y., Shu J.F., Chen L.C., Jephcoat A.P., Wu Y. (1991). Effect of pressure, temperature, and composition on lattice parameters and density of (Mg,Fe)SiO_3-perovskites to 30 GPa, *J. Geophys. Res.* **96**, 8069-8079.

Marton F.C. & Cohen R.E. (1994). Prediction of a high-pressure phase transition in Al_2O_3. *Am. Mineral.* **79**, 789-792.

Masters G., Laske G., Bolton H., & Dziewonski A. (2000). The relative behaviour of shear velocity, bulk sound velocity, bulk sound speed, and compressional velocity in the mantle: implications for chemical and thermal structure. In: *Earth's Deep Interior: Mineral Physics and Tomography From the Atomic to the Global Scale*, AGU Geophysical Monograph **117**, pp. 63-87. S.-i. Karato *et al.* (editors), AGU: Washington D.C.

Matsui M. & Price G.D. (1991). Simulation of the pre-melting behaviour of $MgSiO_3$ perovskite at high pressures and temperatures. *Nature* **351**, 735-737 (1991).

Matsui M. (1988). Molecular dynamics study of $MgSiO_3$ perovskite. *Phys. Chem. Minerals* **16**, 234-238.

Matsui M. (1989). Molecular dynamics study of the structural and thermodynamic properties of MgO crystal with quantum correction. *J. Chem. Phys.* **91**, 489-494.

Matsui M. (1998). Breathing shell model in molecular dynamics simulation: Application to MgO and CaO. *J. Chem. Phys.* **108**, 3304-3309.

Matsui M., Akaogi M., & Matsumoto T. (1987). Computational model of the structural and elastic properties of the ilmenite and perovskite phases of $MgSiO_3$. *Phys. Chem. Minerals* **14**, 101-106.

Matsui M., Price G.D., & Patel A. (1994). Comparison between the lattice dynamics and molecular dynamics methods – calculation results for $MgSiO_3$ perovskite. *Geophys. Res. Lett.* **21**, 1659-1662.

McCammon C. (1997). Perovskite as a possible sink for ferric iron in the lower mantle. *Nature* **387**, 694-696.

McMahan A.K. (1984). Alkali-metal structures above the s-d transition. *Phys. Rev.* **B29**, 5982-5985.

McMillan P. (2000). Jumping between liquid states. *Nature* **403**, 151-152.

McNeil L. E. & Grimsditch M. (1991). Pressure-Amorphized SiO_2 α-Quartz : An Anisotropic Amorphous Solid. *Phys. Rev. Lett.* **68**, 83-85.

Meade C., Mao H.K., Hu J.Z. (1995). High-temperature phase transition and dissociation of $(Mg,Fe)SiO_3$ perovskite at lower mantle pressures. *Science* **268**, 1743-1745.

Mendelssohn M.J., Price G.D. (1997). Computer modelling of a pressure induced phase change in clinoenstatite pyroxenes. *Phys. Chem. Minerals* **25**, 55-62.

Milman V., Winkler B., White J.A., Pickard C.J., Payne M.C., Akhmatskaya E.V., Nobes R.H. (2000). Electronic structure, properties, and phase stability of inorganic crystals: a pseudopotential plane wave study. *Int. J. Quant. Chem.* **77**, 895-910.

Mishima O. (1996). Relationship between melting and amorphization of ice. *Nature* **384**, 546-549.

Mishima O., Calvert L.D., & Whalley E. (1984). Melting of ice I at 77 K and 10 kbar: a new method for making amorphous solids. *Nature* **310**, 393-394.

Mishima O., Calvert L.D., & Whalley E. (1985). An apparently first-order transition between two amorphous phases of ice induced by pressure. *Nature* **314**, 76-78.

Monkhorst H.J. & Pack J.D. (1976). Special points for Brillouin-zone integrations. *Phys. Rev.* **B13**, 5188-5192.

Nada R., Catlow C.R.A., Dovesi R., & Pisani C. (1990). An ab-initio Hartree-Fock study of α-quartz and stishovite. *Phys. Chem. Minerals* **17**, 353-362.

Nada R., Catlow C.R.A., Dovesi R., & Saunders V. (1992). An ab initio Hartree-Fock study of the ilmenite-structured $MgSiO_3$ *Proc. Roy. Soc. Lond.* **A436**, 499-509.

Naray-Szabo St., Taylor W.H., & Jackson W.W. (1929). The structure of kyanite. *Z. Kristal.* **71**, 117-130.

Nekovee M., Foulkes W.M.C., Needs R.J. (2001). Quantum Monte Carlo analysis of exchange and correlation in the strongly inhomogeneous electron gas. *Phys. Rev. Lett.* **87**, paper 036401.

Nikoforov A.E. & Shashkin S.Yu. (1995). Computer simulation of physical properties of crystalline K_2CuF_4. *Solid State Phys* **37**, 1325-1336. (in Russian).

Nosé S. (1984). A molecular dynamics method for simulations in the canonical ensemble. *Mol. Phys.* **52**, 255-268.

Nye J.F. (1998). *Physical Properties of Crystals. Their representation by tensors and matrices.* Oxford University Press: Oxford, 329 pp.

O'Keeffe M. & Bovin J.O. (1979). Solid electrolyte behavior of $NaMgF_3$: geophysical implications. *Science* **206**, 599-600.

Oganov A. R. (1997). Energy Minimisation Modelling of Crystal Structures, Properties, and Stability of Al_2SiO_5 Polymorphs and Topaz. *M.Sc. Thesis*, Moscow State University, 132 pp.

Oganov A.R. & Brodholt J.P. (2000). High-pressure phases in the Al_2SiO_5 system and the problem of Al-phase in Earth's lower mantle: ab initio pseudopotential calculations. *Phys. Chem. Minerals* **27**, 430-439.

Oganov A.R., Brodholt J.P., & Price G.D. (2000). Comparative study of quasiharmonic lattice dynamics, molecular dynamics and Debye model in application to $MgSiO_3$ perovskite. *Phys. Earth Planet. Inter.* **122**, 277-288.

Oganov A.R., Brodholt J.P., & Price G.D. (2001a). *Ab initio* elasticity and thermal equation of state of $MgSiO_3$ perovskite, *Earth Planet. Sci. Lett.* **184**, 555-560.

Oganov A.R., Brodholt J.P., & Price G.D. (2001b). High-*P/T* elastic constants of $MgSiO_3$ perovskite: towards interpreting seismic tomography. *Nature* **411**, 934-937.

Oganov A.R., Organova N.I., & Urusov V.S. (2001c). Nature of Al-Si anti-ordering in a two-phase feldspar from Pektusan volcano. *Geochemistry International* (*in press*)

Oganov A.R., Price G.D., & Brodholt J.P. (2001d). Theoretical investigation of metastable Al_2SiO_5 polymorphs. *Acta Cryst.* **A57**, 548-557.

Oganov A.R., Urusov V.S., & Eremin N.N. (1997). Energy minimization modeling of Al_2SiO_5 polymorphs and topaz, $Al_2SiO_4F_2$. *EUG 9, 23-27 March 1997, Strasbourg (France). Abstracts, 45/1P26.*

Olbricht W., Chatterjee N.D., & Miller K. (1994). Bayes estimation - a novel approach to derivation of internally consistent thermodynamic data for minerals, their uncertainties, and correlations. 1.Theory. *Phys. Chem. Minerals* **21**, 36-49.

Organova N.I., Marsii I.M., Rozhdestvenskaya I.V., Ivanova T.I., Zakharov N.D., Nasedkin V.V., Borisovskii S.B. (1999). Structure of the K- and Na-components of two-phase feldspar from Primorskii Krai. *Crystallography Reports* **44**, 770-775.

Ortiz G. & Ballone P. (1994). Correlation energy, structure factor, radial distribution function, and momentum distribution of the spin-polarised uniform electron gas. *Phys. Rev.* **B50**, 1391-1405. (erratum: *Phys. Rev.* **B56** (1997), p. 970).

Pannetier J., Bassasalsina J., Rodriguez-Carvajal J., Caignaert V. (1990). Prediction of crystal structures from crystal chemistry rules by simulated annealing. *Nature* **346**, 343-345.

Parker S.C. & Price G.D. (1989). Computer modelling of phase transitions in minerals. *Adv. Solid St. Chem.* **1**, 295-327.

Parker S.C. & Wall A. (1991). Calculations of the radial seismic velocity/density ratio for MgO and $MgSiO_3$ perovskite at high pressure. *Geophys. Res. Lett.* **18**, 2185-2188.

Parker S.C. (1983). Prediction of mineral crystal structure. *Solid State Ionics* **8**, 179-186.

Parlinski K. & Kawazoe Y. (2000). Ab initio study of phonons and structural stabilities of the perovskite-type $MgSiO_3$. *Eur. Phys. J.* **B16**, 49-58.

Parr R.G. & Yang W. (1989). *Density-Functional Theory of Atoms and Molecules.* Oxford University Press: Oxford, 333 pp.

Parrinello M. & Rahman A. (1982). Strain fluctuations and elastic constants. *J. Chem. Phys.* **76**, 2662-2666.

Parrinello M. & Rahman A. (1981). Polymorphic transitions in single crystals: A new molecular dynamics method. *J. App. Phys.* **52**, 7182-7190.

Parthé (1996). *Elements of Inorganic Structural Chemistry. Selected Efforts to Predict Structural Features. A Course on Selected Topics.* Second Edition. K. Sutter Parthé: Lancy, 170 pp.

Pasternak M.P., Taylor R.D., Jeanloz R., Li X., Nguyen J.H., McCammon C.A. (1997). High pressure collapse of magnetism in $Fe_{0.94}O$: Mossbauer spectroscopy beyond 100 GPa. *Phys. Rev. Lett.* **79**, 5046-5049.

Patton D.C., Porezag D.V., & Pederson M.R. (1997). Simplified generalized-gradient approximation and anharmonicity: Benchmark calculations on molecules. *Phys. Rev.* **B55**, 7454-7459.

Pauling L. (1960). *The Nature of the Chemical Bond*. Ithaca, New York: Cornell University Press, 1960, 644 pp.

Payne M.C., Teter M.P., Allan D.C., Arias T.A., Joannopoulos J.D. (1992). Iterative minimization techniques for *ab initio* total energy calculations: molecular dynamics and conjugate gradients. *Rev. Mod. Phys.* **64**, 1045-1097.

Perdew J.P. & Burke K. (1996). Comparison shopping for a gradient-corrected density functional. *Int. J. Quant. Chem.* **57**, 309-319.

Perdew J.P. & Zunger A. (1981). Self-interaction correction to density-functional approximations for many-electron systems. *Phys. Rev.* **B23**, 5048-5079.

Perdew J.P., Burke K., Ernzerhof M. (1996). Generalized gradient approximation made simple. *Phys. Rev. Lett.* **77**, 3865-3868.

Perdew J.P., Kurth S. (1998). Density functionals for non-relativistic Coulomb systems. In: Joubert D.P. (ed.) *Density Functionals: Theory and Applications*. Lecture Notes in Physics, v. 500, p.8-59. Springer Verlag: Berlin.

Perdew J.P., Kurth S., Zupan A., Blaha P. (1999). Accurate density functionals with correct formal properties: a step beyond the generalized gradient approximation. *Phys. Rev. Lett.* **82**, 2544-2547.

Perdew J.P., Wang Y. (1992). Accurate and simple analytic representation of the electron-gas correlation energy. *Phys. Rev.* **B45**, 13244-13249.

Pisani C. (1996). Ab initio approaches to the quantum-mechanical treatment of periodic systems. In: Quantum-mechanical ab intio calculation of the properties of crystalline materials. Pisani C. (ed.). Lecture Notes in Chemistry, v. 67, p.47-75. Springer-Verlag: Berlin.

Poirier J.P. & Tarantola A. (1998). A logarithmic equation of state. *Phys. Earth Planet. Inter.* **109**, 1-8.

Poirier J.-P. (1999). Equations of state. In: *Miscroscopic Properties and Processes in Minerals*, NATO Science Series, v. C543. K. Wright and R. Catlow (eds.), Kluwer: Dordrecht, pp. 19-42.

Poirier J.-P. (2000). *Introduction to the Physics of the Earth's Interior.* 2nd edition. Cambridge University Press: Cambridge, 326 pp.

Polian A., Grimsditch M., & Phillipot E. (1993). Memory Effects in Pressure Induced Amorphous $AlPO_4$. *Phys. Rev. Lett.* **71**, 3143-3145.

Post J. & Burnham C.W. (1986). Ionic modeling of mineral structures and energies in the electron gas approximation: TiO_2 polymorphs, quartz, forsterite, diopside. *Am. Mineral.* **71**, 142-150.

Post J.E. & Burnham C.W. (1987). Structure-energy calculation on low and high albite. *Am. Mineral.* **72**, 507-514.

Price G.D. & Parker S.C. (1984). Computer simulations of the structural and physical properties of the olivine and spinel polymorphs of Mg_2SiO_4. *Phys. Chem. Minerals*, **10**, 209-216.

Price G.D. & Yeomans J. (1984). The application of the ANNNI model to polytypic behavior. *Acta Cryst.* **B40**, 448-454.

Price G.D. (1983). Polytypism and the factors determining the stability of spinelloid structures. *Phys. Chem. Minerals* **10**, 77-83.

Price G.D., Parker S.C., & Yeomans J. (1985). The energetics of polytypic structures – a computer simulation of magnesium silicate spinelloids. *Acta Cryst.* **B41**, 231-239.

Purton J. & Catlow C.R. (1990). Computer simulation of feldspar structures. *Am. Miner.* **75**, 1268-1273.

Purton J.A., Allan N.L., Blundy J.D. (1999). Phase transitions in disordered solids via hybrid Monte Carlo: the orthorhombic to cubic phase transition in $(Mg,Mn)SiO_3$ perovskite. *Chem. Commun.*, No. 8, 707-708.

Pushcharovsky Yu.M. & Pushcharovsky D.Yu. (1999). Geospheres of the Earth's mantle. *Geotectonics*, issue 1, 3-14. (in Russian).

Pyykko P. (1988). Relativistic effects in structural chemistry. *Chem. Rev.* **88**, 563-594.

Ralph R.L., Finger L.W., Hasen R.M., & Ghose S. (1984). Compressibility and crystal structure of andalusite at high pressure. *Am. Mineral.* **69**, 513-519.

Rao C.N.R. & Rao K.J. (1978). *Phase transitions in solids: an approach to the study of the chemistry and physics of solids.* McGraw-Hill: N.Y., 330 pp.

Rao M.N., Chaplot S.L., Choudhury N., Rao K.R., Azuah R.T., Montfrooij W.T., & Bennington S.M. (1999). Lattice dynamics and inelastic neutron scattering from sillimanite and kyanite Al_2SiO_5. *Phys. Rev.* **B60**, 12061-12068.

Rappe A.M., Rabe K.M., Kaxiras E., & Joannopoulos J.D. (1990). Optimized pseudopotentials. *Phys. Rev.* **B41**, 1227-1230.

Redfern S.A.T. (1996). High-temperature structural phase transitions in perovskite ($CaTiO_3$). *J. Phys.: Condens. Matter* **8**, 8267-8275.

Redfern S.A.T. (2000). Order-disorder phase transitions. *In: Reviews in Mineralogy and Geochemistry* **39** ('Transformation Processes in Minerals'), 105-133.

Refson K. (1988-2000). Moldy: User's Manual. http: www.earth.ox.ac.uk/ ~keith/moldy.html

Remler D.K. & Madden P.A. (1990). Molecular dynamics without effective potentials via the Car-Parrinello approach. *Mol. Phys.* **70**, 921-966.

Richardson M.F., Yang Q.-C., Novotny-Bregger E., J.D. Dunitz (1990). Conformational polymorphism of dymethyl 3,6-dichloro-2,5-dihydroxyterephthalate. II. Structural, thermodynamic, kinetic and mechanistic aspects of phase transformations among the three crystal forms. *Acta Cryst.* **B46**, 653-660.

Richet P. & Gillet P. (1997). Pressure-induced amorphisation of minerals: a review. *Eur. J. Miner.* **9**, 907-933.

Ringwood A.E. & Reid A.F. (1969). High-pressure transformations of spinels (I). *Earth Planet. Sci. Lett.* **5**, 245-250.

Ringwood A.E. (1991). Phase transformations and their bearing on the constitution and dynamics of the mantle. *Geochim. Cosmochim. Acta* **55**, 2083-2110.

Robertson G.S. & Woodhouse J.H. (1996). Constraints on lower mantle properties from seismology and mineral physics. *Earth Planet. Sci. Lett.* **143**, 197-205.

Robie R.A. & Edwards J.L. (1966). Some Debye temperatures from single crystal elastic constant data. *J. Appl. Phys.* **37**, 2659-2663.

Robie R.A. & Hemingway B.S. (1995). Thermodynamic properties of minerals and related substances at 289.15 K and 1 bar (10^5 Pascals) pressure and at higher temperatures. *U.S. Geological Survey Bulletin 2131*, Washington, 1995, 461 pp.

Romanowicz B. (2001). Can we resolve 3D density heterogeneity in the lower mantle? *Geoph. Res. Lett.* **28**, 1107-1110.

Ross N.L. & Hazen R.M. (1989). Single crystal X-ray diffraction study of $MgSiO_3$ perovskite from 77 to 400 K. *Phys. Chem. Miner.* **16**, 415-420.

Ross N.L., Shu J.-F., Hazen R. & Gasparik T. (1990). High-pressure crystal chemistry of stishovite. *Am. Mineral.* **75**, 739-747.

Salasco L., Dovesi R., Orlando R., & Causa M. (1991). A periodic ab initio extended basis set study of α-Al_2O_3. *Molec. Phys.* **72**, 267-277.

Salje E. & Werneke Ch (1982a). How to determine phase stabilities from lattice vibrations. In: *High-pressure researches in geosciences* (edited by W.Schreyer), 321-348. E. Schweizbart'sche Verlagungsbuchandlung, Stuttgart.

Salje E. & Werneke Ch. (1982b). The phase equilibrium between sillimanite and andalusite as determined from lattice vibrations. *Contrib. Miner. Petrol.* **79**, 56-67.

Salje E. (1986). Heat capacities and entropies of andalusite and sillimanite: The influence of fibrolitization on the phase diagram of the Al_2SiO_5 polymorphs. *Am. Mineral.* **71**, 1366-1371.

Salje E.K. (1993). *Phase Transitions in Ferroelastic and Co-elastic Crystals.* Cambridge University Press: Cambridge, 296 pp.

Sanders M.J., Leslie M., & Catlow C.R.A.(1984). Interatomic potentials for SiO_2. *J. Chem. Soc., Chem. Commun.* **19**, 1271-1273.

Saxena S.K., Dubrovinsky L.S., Lazor P., Cerenius Y., Häggkvist P., Hanfland M., Hu J. (1996). Stability of perovskite ($MgSiO_3$) in the Earth's mantle. *Science* **274**, 1357-1359.

Saxena SK, Dubrovinsky LS, Lazor P, Hu J.Z. (1998) *In situ* X-ray study of perovskite ($MgSiO_3$): Phase transition and dissociation at mantle conditions *Eur. J. Mineral.* **10**, 1275-1281.

Schechtman D., Blech I., Gratias D., Cahn J.W. (1984). Metallic phase with long-range orientational order and no translational symmetry. *Phys. Rev. Lett.* **53**, 1951-1953.

Schmidt M.W., Poli S., Comodi P., & Zanazzi P.F. (1997). High-pressure behavior of kyanite: Decomposition of kyanite into stishovite and corundum. *Am. Mineral.* **82**, 460-466.

Schröder U. (1966). A new model for lattice dynamics ("breathing shell model"). *Solid State Commun.* **4**, 347-349.

Seitz F. (1949). *Modern Theory of Solids.* GITTI: Moscow, 736 pp. (Russian translation).

Serghiou G., Zerr A., Boehler R. (1998). (Mg,Fe)SiO_3-perovskite stability under lower mantle conditions. *Science* **280**, 2093-2095.

Serghiou G., Zerr A., Boehler R. (1999). Response [to Dubrovinsky et al.(1999)]. *Science* **285**, 983a.

Sharma S.M. & Sikka S.K. (1996). Pressure-induced amorphization of materials. *Progr. Materials Sci.* **40**, 1-77.

Shearer P. (1990). Seismic imaging of upper-mantle structure with new evidence for a 520-km discontinuity. *Nature* **344**, 121-126.

Shen G. & Lazor P. (1995). Measurement of melting temperatures of some minerals under lower-mantle pressure. *J. Geophys. Res.* **100**, 17699-17713.

Sherman D.M. (1990). Chemical bonding and the incorporation of potassium into the Earth's core. *Geopys. Res. Lett.* **17**, 693-696.

Sherman D.M. (1991). The high-pressure electronic structure of magnesiowüstite (Mg,Fe)O – applications to the physics and chemistry of the lower mantle. *J. Geophys. Res.* **96**, 14299-14312.

Sherman D.M. (1992). Equation of state and high-pressure phase transitions of stishovite (SiO_2): ab initio (periodic Hartree-Fock) results. *J. Geopys. Res.* **98**, 11865-11873.

Shim S.-H. & Duffy T.S. (2000). Constraints on the P-V-T equation of state of $MgSiO_3$ perovskite. *Am. Mineral.* **85**, 354-363.

Shim S.H., Duffy T.S., Shen G.Y. (2001). Stability and structure of $MgSiO_3$ perovskite to 2300-kilometer depth in Earth's mantle. *Science* **293**, 2437-2440.

Silvi B. (1991). Application of quantum chemistry to geochemistry and geophysics. *J. Molec. Struct. (Theochem)* **226**, 129-145.

Silvi B., D'Arco Ph., Saunders V., & Dovesi R. (1991). Periodic Hartree-Fock study of minerals: tetracoordinated silica polymorphs. *Phys. Chem. Minerals* **17**, 674-680.

Sinelnikov Y.D., Chen G., Neuville D.R., Vaughan M.T., & Liebermann R.C. (1998). Ultrasonic shear wave velocities of $MgSiO_3$ perovskite at 8 GPa and 800 K and lower mantle composition. *Science* **281**, 677-679.

Singh D.J. (1994). *Planewaves, Pseudopotentials and the LAPW Method.* Kluwer: Boston, 115 pp.

Sirotin Yu. I. & Shaskolskaya M.P. (1975). *Fundamentals of Crystal Physics.* Nauka: Moscow, 680 pp. (in Russian).

Smrcok L. & Benco L. (1996). Ab initio periodic Hartree-Fock study of lizardite 1T. *Am. Mineral.* **81**, 1405-1412.

Sowa H. (2000). A transition path from the zinc-blende to the NaCl-type. *Z. Krist.* **215**, 335-342.

Sposito G. (1974). Landau's choice of the critical-point exponent β. *Am. J. Phys.* **42**, 1119-1121.

Stacey F.D. & Isaak D.G. (2000). Extrapolation of lower mantle properties to zero pressure: Constraints on composition and temperature. *Am. Mineral.* **85**, 345-353.

Stebbins J.F., Burnham C.W., & Bish D.L. (1993). Tetrahedral disorder in fibrolitic sillimanite : Comparison of ^{29}Si NMR and neutron diffraction data. *Am. Mineral.* **78**, 461-464.

Stebbins, J.F. & McMillan, P.F. (1989). 5- and 6-coordinated Si in $K_2Si_4O_9$ glass quenched from 1.9 GPa and 1200°C. *Am. Mineral.* **74**, 965-968.

Stewart D.B. & Wright T.L. (1974). Al/Si order order and symmetry of natural potassium feldspars, and relationship of straines cell parameters to bulk composition. *Bull. Soc. Franc. Miner. Crist.* **97**, 356-377.

Stixrude L. & Cohen R.E. (1993). Stability of orthorhombic $MgSiO_3$ perovskite in the Earth's lower mantle. *Nature* **364**, 613-616.

Stixrude L. (2001). First principles theory of mantle and core phases. *Rev. Mineral. Geochem.* **42** ('Molecular Modeling Theory: Applications in Geosciences'), 319-343.

Stixrude L., Cohen R.E., & Hemley R.J. (1998). Theory of minerals at high pressure. *Reviews in Mineralogy* **37** ('Ultrahigh-Pressure Mineralogy'), 639-671.

Stixrude L., Cohen R.E., Yu R.C., Krakauer H. (1996).
Prediction of phase transition in $CaSiO_3$ perovskite and implications for lower mantle structure. *Am. Mineral.* **81**, 1293-1296.

Stixrude L., Hemley R.J., Fei Y., & Mao H.K. (1992). Thermoelasticity of silicate perovskite and magnesiowüstite and stratification of the Earth's mantle. *Science* **257**, 1099-1101.

Stowasser R., Hoffmann R. (1999). What do the Kohn-Sham orbitals and eigenvalues mean? *J. Am. Chem. Soc.* **121**, 3414-3420.

Stuart J.A. & Price G.D. (1996). Atomistic potentials for $MgSiO_3$ with the orthorhombic perovskite structure. *Phil. Mag.* **B73**, 41-48.

Sugino O. & Car R. (1995). Ab initio molecular dynamics study of first-order phase transitions: melting of silicon. *Phys. Rev. Lett.* **74**, 1823-1826.

Sugiyama M., Endo S., & Koto K. (1987). The crystal structure of stishovite under pressure up to 6 GPa. *Miner. J.* **13**, 455-466.

Sutton A.P. (1993). *Electronic Structure of Materials.* Oxford University Press: Oxford, 260 pp.

Szotek Z., Temmerman W.M. (1993). Application of self-interaction correction to transition-metal oxides. *Phys. Rev.* **B47**, 4029-4032.

Tackley P.J. (2000). Mantle convection and plate tectonics: Toward an integrated physical and chemical theory. *Science* **288**, 2002-2007.

Terhune R.W., Kushida T., & Ford G.W. (1985). Soft acoustic modes in trigonal crystals. *Phys. Rev.* **B32**, 8416-8419.

Thijssen J.M. (1999). *Computational Physics.* Cambridge University Press: Cambridge, 546 pp.

Tossell J.A. & Vaughan D.J. (1992). *Theoretical Geochemistry: Application of Quantum Mechanics in the Earth and Mineral Sciences.* Oxford University Press: N.Y., 514 pp.

Tse J.S. & Klug D.D. (1992). Structural Memory in Pressure-Amorphized $AlPO_4$. *Science* **255**, 1559-1561.

Tse J.S. & Klug D.D. (1993). Anisotropy in the Structure of Pressure-Induced Disordered Solids. *Phys. Rev. Lett.* **70**, 174-177.

Tsirelson V.G. (1986). *Electron Crystal Chemistry*. Advances in Science and Technology, Ser. Crystal Chemistry, v. 20. Russian Institute of Scientific and Technical Information: Moscow, 261 pp. (in Russian).

Tsirelson V.G. (1993). *Chemical Bonding and Thermal Motion of Atoms in Crystals.* Advances in Science and Technology, Ser. Crystal Chemistry, v. 27. Russian Institute of Scientific and Technical Information: Moscow, 270 pp. (in Russian).

Tsuneyuki S., Matsui Y., Aoki H., & Tsukada M. (1989). New pressure-induced structural transformations in silica obtained by computer simulation. *Nature* **339**, 209-211.

Urusov V.S. & Dubrovinsky L.S. (1989). *Computer modelling of structure and properties of minerals*. Moscow State University Press: Moscow, 200 pp. (in Russian).

Urusov V.S. (1975). *Energetic Crystal Chemistry.* Nauka: Moscow, 335 pp. (in Russian).

Urusov V.S. (1987). *Theoretical Crystal Chemistry.* Moscow State University Press: Moscow, 275 pp. (in Russian).

Urusov V.S. (1993). Crystal-chemical nature of stability of complex minerals, in particular ternary oxides and ternary salts. *Geologiya i Geofisika* **34**, 92-99. (in Russian).

Urusov V.S. (1995). Semi-empirical groundwork of the bond-valence model. *Acta Crystallographica* **B51**, 641-649.

Urusov V.S., Dubrovinskaya N.A., Dubrovinsky L.S. (1990). Design of probable crystal structures of minerals. Moscow State University Press: Moscow, 129 pp. (in Russian).

Urusov V.S., Dubrovinsky L.S., Wasserman E.A., & Eremin N.N. (1994). Modelling of the structure and elastic properties of rutile-type oxides by interatomic interaction energy minimisation method. *Crystallografiya* **39**, 446-456. (in Russian).

Urusov V.S., Eremin N.N., & Oganov A.R. (1999). Modeling of structures and properties of oxide crystals by minimization of the atomization energy. *Crystallography Reports* **44**, 356-365.

Urusov V.S., Oganov A.R., & Eremin N.N. (1998). Computer simulation of structure, properties and stability of Al_2SiO_5 polymorphs. I.Ionic approximation. *Geochemistry International* **36**, 397-414.

Urusov V.S., Tauson V.L., & Akimov V.V. (1997). *Solid State Geochemistry.* GEOS: Moscow, 500 pp. (in Russian).

van Smaalen S. (1995). Incommensurate Crystal Structures. *Cryst. Rev.* **4**, 79-202.

Vanderbilt D. (1990). Soft self-consistent pseudopotentials in a generalized eigenvalue problem. *Phys. Rev.* **B41**, 7892-7895.

Vanderbilt D. (1998). First-principles theory of structural phase transitions in cubic perovskites, *J. Korean Phys. Soc.* **32**, S103-S106.

Vaughan M.T. & Weidner D.J. (1978). The relationship of elasticity and crystal structure of andalusite and sillimanite. *Phys. Chem. Minerals* **3**, 133-144.

Venkataraman G., Feldkamp L.A., & Sahni V.C. (1975). *Dynamics of Perfect Crystals.* The MIT Press: Cambridge, 517 pp.

Verhoogen J. (1980). *Energetics of the Earth.* National Academy Press: Washington, 139 pp.

Villars P., Phillips J.C., & Chen H.S. (1986). Icosahedral quasicrystals and quantum structural diagrams. *Phys. Rev. Lett.* **57**, 3085-3089.

Vinet P., Ferrante J., Smith J.R., & Rose J.H. (1986). A universal equation of state for solids. *J. Phys.* **C19**, L467-L473.

Vinet P., Rose J.H., Ferrante J., & Smith J.R. (1989). Universal features of the equation of state of solids. *J. Phys.: Condens. Matter* **1**, 1941-1963.

Vinnik L., Niu F., Kawakatsu H. (1998). Broadband converted phases from midmantle discontinuities. *Earth Planets Space* **50**, 987-997.

Vočadlo L. & Price G.D. (1996). The melting of MgO - Computer calculations via molecular dynamics. *Phys. Chem. Minerals* **23**, 42-49.

Vočadlo L., Brodholt J., Alfé D., Gillan M.J., Price G.D. (2000).
Ab initio free energy calculations on the polymorphs of iron at core conditions. *Phys. Earth Planet. Inter.* **117**, 123-137.

Vočadlo L., Price G.D., & Poirier J.-P. (2000). Grüneisen parameters and isothermal equations of state. *Am. Mineral.* **85**, 390-395.

Vogt T. & Schmahl W.W. (1993). The high-temperature phase transition in perovskite. *Europhys. Lett.* **24**, 281-285.

Vosko S.H., Wilk L., Nusair M. (1980). Accurate spin-dependent electron liquid correlation energies for local spin density calculations: a critical analysis. *Can J. Phys.* **58**, 1200-1211.

Wall A. (1988). Lower mantle minerals: computer simulation and analogue studies. *PhD Thesis*, University of London.

Wallace D.C. (1998). *Thermodynamics of Crystals.* Dover Publications: N.Y., 484 pp.

Wang Y. & Perdew J.P. (1991). Correlation hole of the spin-polarized electron gas, with exact small-vector and high-density scaling. *Phys. Rev.* **B44**, 13298-13307.

Wang Y., Guyot F., & Liebermann R.C. (1992). Electron microscopy of (Mg,Fe)SiO_3 perovskite: evidence for structural phase transitions and implications for the lower mantle. *J. Geophys. Res.* **97**,12327-12347.

Wang Y., Guyot F., Yeganeh-Haeri A., Liebermann R.C. (1990). Twinning in $MgSiO_3$ perovskite. *Science* **248**, 468-471.

Wang Y., Li J., Yip S., Phillpot S., & Wolf D. (1995). Mechanical instabilities of homogeneous crystals. *Phys. Rev.* **B52**, 12627-12635.

Wang Y., Yip S., Phillpot S., & Wolf D. (1993). Crystal instabilities at finite strain. *Phys. Rev. Lett.* **71**, 4182-4185.

Warren M.C., Ackland G.J., Karki B.B., & Clark S.J. (1998). Phase transitions in silicate perovskites from first principles. *Miner. Mag.* **62**, 585-598.

Warren M.C., Redfern S.A.T., & Angel R.J. (1999). Change from sixfold to fivefold coordination of silicate polyhedra: Insights from first-priciples calculations of $CaSi_2O_5$. *Phys. Rev.* **B59**, 9149-9154.

Watson G.W., Wall A., Parker S.C. (2000). Atomistic simulation of the effect of temperature and pressure on point defect formation in $MgSiO_3$ perovskite and the stability of $CaSiO_3$ perovskite. *J. Phys. – Cond. Matter* **12**, 8427-8438.

Welch D.O., Dienes G.J., Paskin A. (1978). A molecular dynamical study of the equation of state of solids at high temperature and pressure. *J. Phys. Chem. Solids* **39**, 589-603.

Wentzcovitch R.M., Karki B.B., Karato S., & da Silva C.R.S. (1998). High pressure elastic anisotropy of $MgSiO_3$ perovskite and geophysical implications. *Earth Planet. Sci. Lett.* **164**, 371-378.

Wentzcovitch R.M., Martins J.L., Price G.D. (1993). Ab initio molecular dynamics with variable cell shape: application to $MgSiO_3$. *Phys. Rev. Lett.* **70**, 3947-3950.

Wentzcovitch R.M., Ross N.L., & Price G.D. (1995). Ab initio study of $MgSiO_3$ and $CaSiO_3$ perovskites at lower-mantle pressures. *Phys. Earth Planet. Inter.* **90**, 101-112.

White J.C. & Hess A.C. (1993). Periodic Hartree-Fock study of siliceous mordenite. *J. Phys. Chem.* **97**, 6398-6404.

Will G., Bellotto M., Parrish W., & Hart M. (1988). Crystal structures of quartz and magnesium germanate by profile analysis of synchrotron-radiation high-resolution powder data. *J. Appl. Cryst.* **21**, 182-191.

Wilson K.G. (1983). The renormalization group and related phenomena. *Rev. Mod. Phys.* **55**, 583-600.

Winkler B. & Buehrer W. (1990). Lattice dynamics of andalusite: prediction and experiment. *Phys. Chem. Minerals* **17**, 453-461.

Winkler B. & Dove M.T. (1992). Thermodynamic properties of $MgSiO_3$ perovskite derived from large-scale molecular dynamics. *Phys. Chem. Minerals* **18**, 407-415.

Winkler B. & Milman V. (1997). Polymorphism of CsI. *J. Phys.: Condens. Matter* **9**, 9811-9817.

Winkler B., Dove M.T., & Leslie M. (1991). Static lattice energy minimization and lattice dynamics calculations on aluminosilicate minerals. *Am. Mineral.* **76**, 313-331.

Winter J.K. & Ghose S. (1979). Thermal expansion and high-temperature crystal chemistry of the Al_2SiO_5 Polymorphs. *Am. Mineral.* **64**, 573-586.

Winters R.R., Serghiou G.C., & Hammack W.S. (1992). Observation and explanation of the reversible pressure-induced amorphization of $Ca(NO_3)_2/NaNO_3$. *Phys. Rev.* **B46**, 2792-2797.

Wood B.J. & Rubie D.C. (1996). The effect of alumina on the phase transformations at the 660-kilometer discontinuity from Fe-Mg partitioning experiments. *Science* **273**, 1522-1524.

Xu Y., Shankland T., Poe B.T. (2000). Laboratory-based electrical conductivity in the Earth's mantle. *J. Geophys. Res.* **105**, 27865-27875.

Yagi T. & Funamori N. (1996). Chemical composition of the lower mantle inferred from the equation of state of $MgSiO_3$ perovskite. *Phil. Trans. R. Soc. Lond.* **A354**, 1371-1384.

Yagi T., Mao H.K., & Bell P.M. (1982). Hydrostatic Compression of Perovskite-Type $MgSiO_3$. In: *Advances in Physical Geochemistry* v.**2**, 317-325. Saxena S.K. (editor), Springer Verlag: Berlin.

Yang H., Downs R.T., Finger L.W., Hazen R.M., & Prewitt C.T. (1997a). Compressibility and crystal structure of kyanite, Al_2SiO_5, at high pressure. *Am. Mineral.* **82**, 467-474.

Yang H., Hazen R.M., Finger L.W., Prewitt C.T., & Downs R.T. (1997b). Compressibility and crystal structure of sillimanite, Al_2SiO_5, at high pressure. *Phys. Chem. Minerals* **25**, 39-47.

Ych C.-Y., Lu Z.S., Froyen S., & Zunger A. (1992). Predictions and systematisations of the zinc-blende-wurtzite structural energies in binary octet compounds. *Phys. Rev.* **B45**, 12130-12133.

Yeganeh-Haeri A. (1994). Synthesis and re-investigation of the elastic properties of single-crystal magnesium silicate perovskite. *Phys. Earth Planet. Inter.* **87**, 111-121.

Yeomans J.M. (1992). *Statistical Mechanics of Phase Transitions.* Oxford University Press: Oxford, 168 pp.

Yuen D.A., Čadek O., Chopelas A., & Matyska C. (1993). Geophysical inferences of thermal-chemical structures in the lower mantle. *Geophys. Res. Lett.* **20**, 899-902.

Zen E-an. (1969). The stability relations of the polymorphs of aluminium silicate: a survey and some comments. *Am. J. Sci.* **267**, 297-309.

Zerr A., Diegler A., Boehler R. (1998). Solidus of Earth's deep mantle. *Science* **281**, 243-246.

Zhang J.Z. & Weidner D.J. (1999). Thermal equation of state of aluminum-enriched silicate perovskite. *Science* **284**, 782-784.

Zhang L., Ahsbahs H., Kutoglu A., & Hafner S.S. (1992). Compressibility of grunerite. *Am. Mineral.* **77**, 480-483.

Zhang Y., Yang W. (1998). A challenge for density functionals: self-interaction error increases for systems with a noninteger number of electrons. *J. Chem. Phys.* **109**, 2604-2608.

Zhao Y., Weidner D.J., Parise J.B., Cox D.E. (1993). Thermal expansion and structural distortions of perovskite – data for $NaMgF_3$ perovskite. *Phys. Earth Planet. Inter.* **76.** Part I, 1-16; part II, 17-34.

Zharkov V.N. & Kalinin V.A. (1968). *Equations of State of Solids at High Pressures and Temperatures.* Nauka: Moscow, 312 pp. (in Russian).

Zunger A. (1980). Systematisation of the stable crystal structures of all AB-type binary compounds: a pseudopotential orbital-radii approach. *Phys. Rev.* **B22**, 5839-5872.

Zupan A., Blaha P., Schwarz K., & Perdew J.P. (1998). Pressure-induced phase transitions in solid Si, SiO_2, and Fe: Performance of local-spin-density and

generalized-gradient-approximation density functionals. *Phys. Rev.* **B58**, 11266-11272.

Appendix. List of publications.

Papers:

1. Oganov A.R. (1996). A find of rhombohedral pyrite crystals. *Proc. Russ. Miner. Soc.*, No.1, 65-69. (in Russian)
2. Urusov V.S., Oganov A.R., Eremin N.N. (1998). Computer simulation of structure, properties and stability of Al_2SiO_5 polymorphs. I.Ionic approximation. *Geochem. Int.* **36**, 397-414.
3. Urusov V.S., Eremin N.N., Oganov A.R. (1999). Modeling of structures and properties of oxide crystals by minimization of the atomization energy. *Cryst. Rep.* **44**, 356-365.
4. Oganov A.R., and Brodholt J.P. (2000). High-pressure phases in the Al_2SiO_5 system and the problem of Al-phase in Earth's lower mantle: *ab initio* calculations. *Phys. Chem. Minerals* **27**, 430-439.
5. Oganov A.R., Brodholt J.P., Price G.D. (2000). Comparative study of quasiharmonic lattice dynamics, molecular dynamics and Debye model in application to $MgSiO_3$ perovskite. *Phys. Earth Planet. Inter.* **122**, 277-288.
6. Oganov A.R., Brodholt J.P., Price G.D. (2001a). *Ab initio* elasticity and thermal equation of state of $MgSiO_3$ perovskite. *Earth Planet. Sci. Lett.* **184**, 555-560.
7. Oganov A.R., Brodholt J.P., Price G.D. (2001b). The elastic constants of $MgSiO_3$ perovskite at pressures and temperatures of the Earth's mantle. *Nature* **411**, 934-937.
8. Oganov A.R., Organova N.I., Urusov V.S. (2001c). Nature of Al-Si anti-ordering in a two-phase feldspar from the Pektusan volcano. *Geochem. Int.* (*in press*)
9. Oganov A.R., Price G.D., Brodholt J.P. (2001d). Theoretical investigation of metastable Al_2SiO_5 polymorphs. *Acta Cryst.* **A57**, 548-557.

Abstracts:

1. Oganov A.R. (1996). Theoretical modelling of structure and physical properties of minerals: Al_2SiO_5 polymorphs. *Bull. Student Sci. Soc.* (Moscow State University), p.26. (in Russian)
2. Oganov A.R., Urusov V.S., Eremin N.N. (1997). Computer simulation of structure, properties and stability of Al_2SiO_5 polymorphs. Ionic approximation. *Spectroscopy, X-ray and Crystal Chemistry of Minerals. International Conference.* 30.09-2.10.1997, Kazan, Russia. Abstracts, p.21-22 (in Russian).
3. Urusov V.S., Eremin N.N., Oganov A.R. (1997). Electronegativity equalisation method in computer modelling of crystals. *Spectroscopy, X-ray and Crystal Chemistry of Minerals. International Conference.* 30.09-2.10.1997, Kazan, Russia. Abstracts, p.33-34 (in Russian).
4. Oganov A.R., Urusov V.S., Eremin N.N. (1997). Energy minimisation modelling of Al_2SiO_5 polymorphs and topaz, Al_2SiO_4F. *9th European Union of Geosciences meeting (EUG-9)*, 23-27.03.1997, Strasbourg, France. Collected Abstracts, 45/1P26.
5. Urusov V.S., Oganov A.R. (1998). Theoretical study of crystal structure, elastic properties and alpha-beta-transformation of quartz. *1st Russian National Conference on Crystal Chemistry.* 24-29.05.1998, Chernogolovka, Russia. Collected Abstracts (in Russian), No.2-40, p.140.
6. Urusov V.S., Oganov A.R. (1998). Average structure and limits of miscibility in solid solution series corundum (Al_2O_3)-eskolaite (Cr_2O_3): a computer modelling study. *1st Russian National Conference on Crystal Chemistry.* 24-29.05.1998, Chernogolovka, Russia. Collected Abstracts (in Russian), No.2-41, p.141.

7. Oganov A.R., Urusov V.S., Eremin N.N. (1998). Theoretical study of alpha-beta-transformation of quartz. *XVIII European Crystallographic Meeting (ECM-18)*, 16-20.08.1998, Prague, Czech Republic. Collected Abstracts, p.177-178.
8. Oganov A.R., Brodholt J.P. (1999). High-pressure phases in Al_2SiO_5 system and the problem of Al-phase in Earth's lower mantle : *ab initio* pseudopotential calculations. *Journal of Conference Abstracts*, v. 4, No. 1, p.655. European Union of Geosciences meeting (EUG-10), 28.03-1.04.1999, Strasbourg, France. Abstract L08:4P/01:PO.
9. Oganov A.R., Urusov V.S., Catti M. (1999). Solid solution properties from point defect energetics. *Journal of Conference Abstracts*, v. 4, No. 1, p.655. European Union of Geosciences meeting (EUG-10), 28.03-1.04.1999, Strasbourg, France. Abstract L08:4P/02:PO.
10. Oganov A.R., Brodholt J.P., Price G.D. (1999). High-pressure crystal chemistry of in Al_2SiO_5: *ab initio* pseudopotential calculations. *International Union of Crystallography meeting (IUCr'99)*, 4-13.08.1999, Glasgow, UK. Collected Abstracts., abstract No. P05.OE.002, p.18.
11. Oganov A.R., Price G.D., Brodholt J.P. (1999). High-pressure phases in the Al_2O_3-SiO_2 system and the problem of aluminous phase in the lower mantle : an *ab initio* study. *The Deep Earth. EURESCO conference.* Maratea, Italy, 11-16 September 1999. Collected Abstracts.
12. Oganov A.R., Brodholt J.P., Price G.D. (2000). Simulating Phase Transitions and Thermoelasticity of Mantle Minerals. *XIX European Crystallographic Meeting (ECM-19)*, 25-31 August 2000, Nancy, France. Collected Abstracts, p.142.
13. Oganov A.R., Brodholt J.P., Price G.D. (2000). Ab initio thermoelasticity of $MgSiO_3$ perovskite : towards interpreting seismic tomography. *Mineralogical Society of America, Short Course 'Transformation Processes in Minerals', abstracts.* Cambridge, U.K., 1-2 September 2000.
14. Oganov A.R., Brodholt J.P., Price G.D. (2000). Equation of state and elasticity of $MgSiO_3$ perovskite at high temperatures from *ab initio* molecular dynamics: towards interpreting seismic tomography. *Goldschmidt 2000 Conference*, Collected Abstracts CD. Oxford, U.K., 3-8 September 2000.
15. Oganov A.R., Brodholt J.P., Price G.D. (2000). Thermoelasticity of $MgSiO_3$ Perovskite in the Earth's Lower Mantle from *Ab Initio* Molecular Dynamics. *American Geophysical Union Fall 2000 meeting*, San Francisco (U.S.A.), 15-19 December 2000. Collected abstracts, abstract V71B-26.
16. Oganov A.R., Brodholt J.P., Price G.D. (2000). Thermoelasticity of $MgSiO_3$ Perovskite: from Wavefunctions to high-*P/T* Elasticity and Interpretation of Seismic Tomography. *Mantle Materials, Processes, and Products. Winter Meeting of the Mineralogical Society of Great Britain and Ireland*, Durham, 3-5 January 2001. Collected abstracts.
17. Oganov A.R., Brodholt J.P., Price G.D. (2000). *Ab initio* elasticity and thermal equation of state of $MgSiO_3$ perovskite. *Psi-k Newsletter*, No. 43, p. 85.
18. Oganov A.R. and Brodholt J.P. (2001). High-pressure phases in the Al_2SiO_5 system and the problem of Al-phase in Earth's lower mantle: *ab initio* calculations. *Psi-k Newsletter*, No. 44, p. 99.
19. Oganov A.R., Brodholt J.P., Price G.D. (2001). Quantum Mechanics of the Earth's Mantle. // Density Functional Theory for the Study of Complex Oxides. School and Workshop, The Royal Institution of Great Britain, 14-18 May 2001. Collected Abstracts.
20. Oganov A.R., Brodholt J.P., Price G.D. (2001). The elastic constants of MgSiO3 perovskite at pressures and temperatures of the Earth's mantle. *Psi-k Newsletter*, No. 45, p. 64.

21. Oganov A.R., Price G.D., Brodholt J.P. (2001). Theoretical investigation of metastable Al_2SiO_5 polymorphs. *Psi-k Newsletter*, No. 45, p. 65.
22. Oganov A.R. (2001). Quantum mineralogy of the Earth's mantle. *XX European Crystallographic Meeting (ECM-20)*, 25-31 August 2001, Cracow, Poland. Collected abstracts, abstract SIG_5-M3-O3.